

Optimisation of Deep Vibratory Compaction as Liquefaction Mitigation Measure

von

Sparsha Sinduri Nagula

Herausgegeben von

J. Grabe

Technische Universität Hamburg
Institut für Geotechnik und Baubetrieb

License: This work is licensed under the Creative Commons Attribution-NonCommercial 4.0 International License. To view a copy of this license, visit <http://creativecommons.org/licenses/by-nc/4.0/> or send a letter to Creative Commons, PO Box 1866, Mountain View, CA 94042, USA.

DOI: <https://doi.org/10.15480/882.3945>

ORCID: Sparsha Sinduri Nagula

<https://orcid.org/0000-0002-1645-2103>

Veröffentlichungen des Instituts für
Geotechnik und Baubetrieb

50

Herausgeber:

Univ.-Prof. Dr.-Ing. Jürgen Grabe
Technische Universität Hamburg
Institut für Geotechnik und Baubetrieb
Harburger Schloßstraße 20
D – 21079 Hamburg
e-mail: *grabe@tuhh.de*

ISBN-13: 978-3-936310-52-8 (Erstausgabe)

Druckerei

Druckzentrum Neumünster GmbH
Rungestraße 4
24537 Neumünster

In derselben Reihe erschienen:

1. J. Grabe (Hrsg.), 2000: Verbrennungsrückstände. Tagungsband, ISBN 3-936310-00-9
2. J. Grabe (Hrsg.), 2001: Schaden- und Risikomanagement im Tiefbau. Tagungsband, ISBN 3-936310-01-7
3. J. Grabe, 2003. Bodenmechanik und Grundbau. ISBN 3-936310-03-3
4. J. Grabe (Hrsg.), 2003: Euronormen in der Geotechnik – Was ändert sich? Tagungsband, ISBN 3-936310-04-1
5. J. Grabe (Hrsg.), 2003: Bodenverdichtung, Experimente - Modellierung - Geräteentwicklung - Baustellenberichte - F+E-Bedarf. Tagungsband, ISBN 3-936310-05-X
6. M. Kelm, 2004: Numerische Simulation der Verdichtung rolliger Böden mittels Vibrationswalzen. Promotion, ISBN 3-936310-06-8
7. J. Grabe (Hrsg.), 2004: Kaimauern - Messungen und Numerik. Tagungsband, ISBN 3-936310-07-6
8. J. Stein, 2005. Experimentelle und numerische Untersuchungen zum Düsenstrahlverfahren. Promotion, ISBN 3-936310-09-2
9. J. Grabe (Hrsg.), 2005: Grenzschicht Wasser und Boden - Phänomene und Ansätze. Tagungsband, ISBN 3-936310-10-6
10. J. Grabe (Hrsg.), 2005: FEM in der Geotechnik - Qualität, Prüfung, Fallbeispiele. Tagungsband, ISBN 3-936310-11-4
11. B. Mardfeldt, 2006: Zum Tragverhalten von Kaikonstruktionen im Gebrauchszustand. Promotion, ISBN 3-936310-12-2
12. J. Grabe (Hrsg.), 2006: Optimierung in der Geotechnik - Strategien und Fallbeispiele. Tagungsband, ISBN-13: 978-3-936310-13-9
13. T. Bierer, 2007: Bodenschwingungen aus Straßenverkehr auf unebener Fahrbahn im Zeitbereich - experimentelle und theoretische Untersuchungen. Promotion, ISBN-13: 978-3-936310-14-6
14. J. Grabe (Hrsg.), 2007: Bemessen mit Finite-Elemente-Methoden. Tagungsband, ISBN-13: 978-3-936310-15-3
15. K.-P. Mahutka, 2008: Zur Verdichtung von rolligen Böden infolge dynamischer Pfahleinbringung und durch Oberflächenrüttler. Promotion, ISBN-13: 978-3-936310-16-0
16. J. Grabe (Hrsg.), 2008: Seehäfen für Containerschiffe zukünftiger Generationen. Tagungsband, ISBN-13: 978-3-936310-17-7

17. F. König, 2008: Zur zeitlichen Traglastentwicklung von Pfählen und der nachträglichen Erweiterung bestehender Pfahlgründungen. Promotion, ISBN-13: 978-3-936310-18-4
18. S. Henke, 2008: Herstellungseinflüsse aus Pfahlrammung im Kaimauerbau. Promotion, ISBN-13: 978-3-936310-19-1
19. J. Grabe (Hrsg.), 2009: Spundwände – Profile, Tragverhalten, Bemessung, Einbringung und Wiedergewinnung. Tagungsband, ISBN-13: 978-3-936310-20-7
20. J. Dührkop, 2009: Zum Einfluss von Aufweitungen und zyklischen Lasten auf das Verformungsverhalten lateral beanspruchter Pfähle in Sand. Promotion, ISBN-13: 978-3-936310-21-4
21. O. Möller, 2009: Zum Langzeit-Kompressionsverhalten weicher organischer Sedimente. Promotion, ISBN-13: 978-3-936310-22-1
22. J. Grabe (Hrsg.), 2011: Ports of container ships of future generations. Tagungsband, ISBN-13: 978-3-936310-23-8
23. S. Kinzler, 2011: Zur Parameteridentifikation, Entwurfs- und Strukturoptimierung in der Geotechnik mittels numerischer Verfahren. Promotion, ISBN-13: 978-3-936310-24-5
24. G. Qiu, 2012: Coupled Eulerian Lagrangian Simulations of Selected Soil-Structure Problems. Promotion, ISBN-13: 978-3-936310-25-2
25. X. Ma, 2013: Nutzung der oberflächennahen Geothermie mittels Energiepfählen und Erdwärmesonden. Promotion, ISBN-13: 978-3-936310-26-9
26. J. Grabe (Hrsg.), 2013: Proceedings of the Conference on Maritime Energy COME 2013. Tagungsband, ISBN-13: 978-3-936310-28-3
27. J. Grabe (Hrsg.), 2013: Bemessen mit numerischen Methoden. Tagungsband, ISBN-13: 978-3-936310-29-0
28. T. Pucker, 2013: Stoffmodell zur Modellierung von stetigen Materialübergängen im Rahmen der Optimierung geotechnischer Strukturen. Promotion, ISBN-13: 978-3-936310-30-6
29. S. Henke, 2013: Untersuchungen zur Pfropfenbildung infolge der Installation offener Profile in granularen Böden. Habilitation, ISBN-13: 978-3-936310-31-3
30. J. Grabe (Hrsg.), 2014: Ports for Container Ships of Future Generations. Tagungsband, ISBN-13: 978-3-936310-32-0
31. J. Grabe (Hrsg.), 2014: Offshore Basishäfen, Tagungsband, ISBN-13: 978-3-936310-33-7

32. C. Rudolph, 2015. Untersuchungen zur Drift von Pfählen unter zyklischer, lateraler Last aus veränderlicher Richtung. Promotion, ISBN-13: 978-3-936310-34-4
33. J. Grabe (Hrsg.), 2015: Morphodynamics 2015, Tagungsband, ISBN-13: 978-3-936310-35-1
34. T. Hamann, 2015: Zur Modellierung wassergesättigter Böden unter dynamischer Belastung und großen Bodenverformungen am Beispiel der Pfahleinbringung. Promotion, ISBN-13: 978-3-936310-36-8
35. B. Schümann, 2015: Beitrag zum dynamischen Dreiphasenmodell für Boden auf Basis der Finite-Elemente-Methode, Promotion, ISBN-13: 978-3-936310-37-5
36. M. Milatz, 2015: Untersuchungen zum Einfluss der Kapillarität auf das hydraulisch-mechanische Verhalten von granularer Tragschichten für Verkehrswege. Promotion, ISBN-13: 978-3-936310-38-2
37. H. Kaya, 2016: Bodenverschleppung und Spaltbildung infolge der Einbringung von Profilen in Dichtungsschichten aus Ton. Promotion, ISBN-13: 978-3-936310-39-9
38. J. Grabe (Hrsg.), 2017: Proceedings of the Conference on Maritime Energy COME 2017. Tagungsband, ISBN-13: 978-3-936310-40-5
39. B. Kocak, 2017: Zur numerischen Modellierung von hydraulisch-mechanisch gekoppelten Prozessen in gesättigten granularen Böden mittels Smoothed Particle Hydrodynamics. Promotion, ISBN-13: 978-3-936310-41-2
40. K. Siegl, 2017: Zur Pfahldynamik von gerammten Großrohrpfählen und der daraus resultierenden Wellenausbreitung in Wasser und im Meeresboden. Promotion, ISBN-13: 978-3-936310-42-9
41. J. Grabe (Hrsg.), 2017: Numerical Methods in Geotechnics. Tagungsband, ISBN-13: 978-3-936310-43-6
42. J. Grabe (Hrsg.), 2018: Digitale Infrastruktur und Geotechnik (DIG 2018). Tagungsband, ISBN-13: 978-3-936310-44-3
43. D. Osthoff, 2018: Zur Ursache von Schlosssprengungen und zu einbringbedingten Lageabweichungen von Spundwänden. Promotion, ISBN-13: 978-3-936310-45-0
44. E. Heins, 2018: Numerical based identification of the pile-soil interaction in terms of the axial pile bearing capacity. Promotion, ISBN-13: 978-3-936310-46-7
45. K.-F. Seitz, 2021: Zur Topologieoptimierung von geotechnischen Strukturen und zur Tragfähigkeitssteigerung des Baugrunds durch Scherfugenverfestigung. Promotion, ISBN-13: 978-3-936310-47-4
46. D. Plenker, 2021: Physical and numerical investigations of the dynamic interaction of saturated granulates and fluid. Promotion, ISBN-13: 978-3-936310-48-1

47. J. Grabe, J. O. Backhaus, P. Vogel 2021: Bauprojektmanagement. Skriptum, ISBN-13: 978-3-936310-49-8
48. M. Kanitz, 2021: Experimental and numerical investigations of particle-fluid systems in geotechnical engineering. Promotion, ISBN-13: 978-3-936310-50-4
49. J. O. Backhaus, 2021: A methodology for the numeric time-cost Forecast and pareto optimisation of large injection projects in tunneling. Promotion, ISBN-13: 978-3-936310-50-4

„Tough times don't last, tough people do.“

Robert Schuller

Rahul Dravid you continue to inspire me...

Dedicated to Brownie

Editor's Preface

Die Verflüssigung locker gelagerter Sande hat meist katastrophale Folgen, siehe beispielsweise Niigata, Japan, 1964. Auslöser können Erschütterungen oder Erdbeben sein. Teilweise reichen schon minimale Störungen, wie lokale Eingriffe am Böschungsfuß oder Veränderungen des Grundwasserstands durch Niederschläge. Eine Möglichkeit zur Stabilisierung solcher Gebiete ist die Verdichtung der Sande durch das Verfahren der Rütteldruckverdichtung. Wenn es sich um große Gebiete handelt, wie beispielsweise bei den Kippen der ostdeutschen Tagebaue, werden sogenannte unterirdische Verdichtungsstreifen im Raster hergestellt. In Cottbus werden von der Lausitzer Energie Bergbau AG (LEAG) besonders große und leistungsstarke Rüttler eingesetzt. Ein naheliegendes Ziel ist die Optimierung der Tiefenverdichtung hinsichtlich des Rasterabstandes, der Rüttlerfrequenz, des Verdichtungsprozesses und der Rütteldauer. Der Verdichtungserfolg kann derzeit lediglich indirekt anhand von vorher und nachher durchgeführten Sondierungen beurteilt werden. Daher ist eine wesentliche Zielsetzung der Forschung die Ableitung von Kennwerten, die den Verdichtungserfolg arbeitsparallel anzeigen können. Mit der vorgenannten Thematik befasst sich die vorliegende Doktorarbeit von Frau Sinduri Nagula. Ihre Arbeit ist von hoher wirtschaftlicher und gesellschaftlicher Relevanz, da es weltweit etliche Gebiete mit verflüssigungsgefährdeten, locker gelagerten Sanden gibt.

Zielsetzung der Arbeit von Frau Sinduri Nagula ist die Bearbeitung folgender übergeordneter Forschungsfragen, siehe Kapitel 3, Seite 36:

- *Research has shown that none out of field measurements, model tests and numerical simulations alone can completely help better understand factors affecting deep vibrations compaction. A package involving all three needs to be developed as it would be an ideal solution to further our existing knowledge about deep vibratory compaction.*
- *Develop a numerical framework capable of simulating the entire deep vibratory compaction process as close as possible to reality. Preciseness of numerical framework majorly depends on the choice of constitutive model used to model soil behavior. Hence, a well justified choice needs to be made with robustly calibrated material parameters. The developed numerical framework needs to be well validated before it can be used for further analysis.*
- *Identify and analyse factors affecting deep vibratory compaction in depth other than the primary ones studied till date via model tests and numerical simulations.*
- *Identify easily obtainable on-line compaction control parameters by means of model tests. Followed by verification of numerical simulations to be used to develop an optimization routine based on the chosen control parameter to design compaction process in any sand under consideration.*
- *Efficiency of deep vibratory compaction for liquefaction mitigation needs to be accessed by seismic numerical simulation of saturated sand before and after deep vibratory compaction. A coupled constitutive model based on the u-p-formulation needs to be identified in order to predict soil response of saturated sand.*

In Kapitel 1 führt Frau Sinduri Nagula in die Thematik und Motivation ihrer Arbeit ein. Der Stand der Wissenschaften zur Rütteldruckverdichtung, zur numerischen Modellierung des Verfahrens, zur on-line Kontrolle der Verdichtung und zur Verbesserungswirkung im Hinblick auf die Reduktion der Verflüssigungsfahr wird in Kapitel 2 dargestellt. Somit ist der Ausgangspunkt ihrer Dissertation beschrieben.

In Kapitel 3 leitet sie den Forschungsbedarf ab, stellt sie ihre Ziele vor und die von ihr gewählte methodische Vorgehensweise.

Die Grundlagen der von ihr durchgeführten Experimente und verwendeten numerischen Methoden werden in Kapitel 4 behandelt. Hervorzuheben ist die Konstruktion und der Bau eines Minirüttlers, siehe Bild 4.1 und 4.2. Bild 4.3 zeigt den von ihr benutzten Versuchsstand. Des Weiteren hat sie Zugang zu Messdaten eines Versuchsfeldes im Cottbusser Tagebau. Dort stehen sehr locker gelagerte Kippenböden an. Die LEAG in Verbindung mit dem Fachbüro GMB GmbH setzen einen eigens entwickelten V48 Rüttler zur Verdichtung der Kippenböden bis in 60 m Tiefe ein, siehe Bild 4.6 und 4.7.

Frau Sinduri Nagula beschreibt in Abschnitt 4.3 die von ihr verwendete Finite-Elemente Methode. Sie verwendet die von Dassault Systemes zur Verfügung gestellte Programmierung der CEL Methode, um die durch den Rüttler verursachten großen Bodenverformungen im Boden abbilden zu können. Sie kann dazu auf vorhergehende Arbeiten des Institutes u. a. von Heins et al. (2015) und Qiu (2012) zurückgreifen. Sie verwendet die Version ABAQUS 6.14. Für den verwendeten Sand bestimmt sie nachfolgend die Parameter der Gleichung 4.2, um aus dem simulierten Spannungszustand und der Lagerungsdichte auf den Sondierwiderstand einer Drucksonde schließen zu können. Damit kann sie die im Feld gemessenen Sondierwiderstände mit den numerisch simulierten Werten vergleichen. In Abschnitt 4.5 beschreibt sie des Weiteren das von ihr verwendete Materialmodell, nämlich die Hypoplastizität mit der Erweiterung der intergranularen Dehnungen nach Niemunis und Herle (1997). Die Bestimmung der Parameter zur Beschreibung der intergranularen Dehnungen wird in Abschnitt 4.5.3 dargestellt, siehe Tab 4.5 und Tab 4.6.

Kapitel 5 behandelt die numerische Modellierung der Tiefenverdichtung mit Rüttlern. Sie vergleicht in Abschnitt 5.1 die Finite-Elemente-Modellierung nach Lagrange (ABAQUS Explicit) mit der CEL Methode, bei der der Rüttler als Lagrange-Gebiet und der Boden als Euler Gebiet abgebildet werden. Es zeigt sich, dass die Bodenverformungen so groß sind, dass bei der Lagrange-Modellierung des Bodens es zu einem Abbruch des Rechnungsgangs kommt. Sie untersucht des Weiteren den Einfluss der gewählten Diskretisierung bei der CEL Modellierung, siehe Bild 5.3.

In Abschnitt 5.2 stellt sie die von ihr durchgeführten Versuche mit dem Modellrüttler dar und vergleicht die Ergebnisse mit den Ergebnissen der CEL Simulationen. Bild 5.11 zeigt eine gute Übereinstimmung. In Abschnitt 5.3 behandelt sie die Messungen im Versuchsfeld der LEAG AG. Dazu bestimmt sie numerisch die Parameter der Gleichung 5.2. Bild 5.22 zeigt erneut eine zufriedenstellende Übereinstimmung der gemessenen und simulierten Sondierwiderstände vor und nach der Verdichtung. Das Bild 5.23 zeigt den Vergleich der am Rüttler gemessenen maximalen Beschleunigungen mit den simulierten Beschleunigungen. Der Vergleich kann aufgrund der Filterung der realen Daten nur bedingt durchgeführt werden. Anzumerken ist eine Schwäche des numerischen Modells, denn es wird keine energetische Betrachtung gezogen, ob der reale Hydraulikmotor überhaupt in der Lage ist, die zur Verdichtung des Bodens benötigte Energie zur Verfügung zu stellen. Bei dicht

gelagerten Böden ist zu bezweifeln, ob der Prototyp die Rüttlerfrequenz aufrechterhalten kann.

Die den Verdichtungserfolg beeinflussenden Faktoren werden in Kapitel 6 systematisch untersucht. Es handelt sich hierbei um die Frequenz, die Lagerungsdichte, die Kornverteilungslinie des zu verdichtenden Bodens, der Form des Rüttlers, des Verdichtungsprozesses, des Rasterabstands und des Sättigungsgrades.

In Kapitel 7 befasst sie sich mit on-line Verdichtungskontrolle. Sie stellt fest, dass die Schwingungsamplitude des Rüttlers ein geeignetes Maß für die erzielte Verdichtung ist. Der Phasenwinkel, wie von Fellin (2000) vorgeschlagen, scheint sich dagegen in Abhängigkeit der Verdichtung nicht ausreichend signifikant in Abhängigkeit der erzielten Verdichtung zu ändern, siehe Bild 7.4. Sie diskutiert auch die neuesten Erkenntnisse von Nagy (2019), siehe Bild 7.5.

In Abschnitt 7.3 folgert sie, dass eine Regelung nach dem Parameter „Amplitude“ zu einer wesentlichen Reduktion der Verdichtungszeit führt. Diese aus Versuchen und den numerischen Simulationen abgeleiteten Erkenntnisse sind für die zukünftige Entwicklung von Tiefenrüttlern von wesentlicher Bedeutung. In Kooperation mit der University of Colorado Boulder, USA, untersucht sie den Effekt der Verdichtung auf das Verflüssigungspotential von locker gelagerten, wassergesättigten Sanden infolge Erdbeben. Zur Verfügung stehen ihr hierfür Ergebnisse aus Zentrifugenversuchen, die von Kirkwood und Dashti (2019) durchgeführt wurden. Bild 8.11 zeigt zunächst den Vergleich der numerisch simulierten und in der Zentrifuge gemessenen Setzungen. Die Übereinstimmung gelingt erstaunlich gut. Die Bilder 8.21ff zeigen die Verbesserung des Verflüssigungspotentials durch Verdichtung auf.

In Kapitel 9 beantwortet Frau Sinduri Nagula zusammenfassend die von ihr in Kapitel 3 aufgestellten Forschungsfragen und gibt einen Ausblick.

Frau Sinduri Nagula hat mit ihren experimentellen und numerischen Untersuchungen einen wesentlichen wissenschaftlichen Beitrag zum Stand der Wissenschaft in der Geotechnik, insbesondere für den Spezialtiefbau und für die Bodendynamik, geleistet.

Frau Sinduri Nagula hat bereits mehrfach in qualitätsgesicherten, renommierten Fachzeitschriften publiziert, was für die hohe Qualität ihrer wissenschaftlichen Arbeit spricht. Hier sind insbesondere ihre Beiträge in den Zeitschriften *Computer and Geotechnics*, *Soil Dynamics and Earthquake Engineering* und in der britischen *Geotechnique* zu nennen. Des Weiteren hat sie mehrfach auf internationalen Tagungen vorgetragen. Ihre Publikationen sind ein Beleg für ihre außerordentliche Leistung.

Ich bin mir sicher, dass Frau Sinduri Nagula eine große wissenschaftliche Karriere vor sich hat. Dafür wünsche ich ihr alles Gute. Ich würde mich freuen, wenn wir auch weiterhin im Austausch bleiben.

Hamburg 11.10.2021

Jürgen Grabe

Author's Preface

The current world population ranges around 7 Billion and is ever increasing; the rising population has created huge demand of land for various infrastructure facilities. This has pushed the engineering community to use land which previously in history was considered unsuitable for any construction. Soil liquefaction caused by earthquake loading is a major threat to infrastructure. Loose saturated sands when subjected to seismic loading develop high excess pore water pressures and shear strains that may lead to soil liquefaction. Deep vibratory compaction method is an established ground improvement technique for granular soils. The lack of analytical design methodology and dependence on field experience of past projects inhibits the efficient use of deep vibratory compaction. I as a doctoral researcher at Institute of Geotechnical Engineering and Construction Management, TUHH, Hamburg carried out my research work in two-fold steps, first being validation of numerical simulation of deep vibratory compaction based on the results of model tests and field measurements followed by parametric study and optimization of the technique.

It gives me great pleasure to thank all the people who have contributed in making my doctoral journey, a memorable one. Firstly I would like to thank Prof. Dr. -Ing. Jürgen Grabe for granting me an opportunity to pursue my PhD and off course his support and incessant encouragement throughout. I would like to thank him specifically for the confidence he showed in me and for letting me free to independently tread on my research path.

I would also like to take this opportunity to thank Prof. Dr.-Ing. Marcus Rutner and Prof. Dr. techn. Dietmar Adam for reviewing my thesis and for the insightful discussion and feedback. I am sure this would only help me evolve into a better researcher. It would be incomplete if I do not thank Prof. Dr. -Ing. Günter Rombach for chairing my PhD defence and ensuring that it was a perfect show.

Before I continue on my gratitude list, the first person I would like to thank would be Dr. Hans Stanford for being around right from the time I had to apply for doctoral scholarship to giving me critical value addition for the rebuttal of my last journal paper at the institute. I wish and hope that we would continue to be in touch both scientifically and personally.

The research journey of a geotechnical engineer is incomplete without a visit to the laboratory. I too had the opportunity to perform some cliché and some innovative geotechnical tests and what made them interesting was my interaction with Markus Banduch. The first time we met, we both did not speak each other's language but we connected just in a few minutes and I so wish this continues to stay so. And trust me when I say that noone understand geotechnical tests as Marek, you certainly are my geotech genius. My doctoral work required me to re-create a model vibrator at a scaled level and a lot of it's credit goes to Patrick Mayanja for his incredible designing skills and to TUHH workshop for their amazing construction skills. Lastly would like to thank Göta Bürkner for the quintessential feedback on the various soils I analysed as part of my work.

It would be unfair if I do not thank the illustrious students with whom I had the opportunity to work with. Marie, Lars, Justus and Michael your work was an invaluable contribution to my dissertation. Thank you so much for it and I wish good luck in your future endeavours.

I guess most would agree that the decision to do a PhD is an adventurous one but I went one step ahead and decided to do it from Germany, at a point of time when I could speak no German and was completely new to the culture. I am sure I would have caved in to the stress (pun intended) had I not met my wonderful colleagues at the institute. I can still recollect being the only international colleague when I joined and how some of my colleagues went the extra mile to make me feel one among them. Dominik you have been my first acquaintance and first friend and I cannot thank you enough for it. Time rolled and I ended up finding some amazing friends with whom I could have a critical technical discussion and the same time blurt out my PhD frustrations. Alex, Onne, Evelyn and Marius you have been those wonderful people. Alex thanks and a big hug for all the technical discussions and bakchodi, I thoroughly enjoyed it and wish that this continues. As they say you get the best when you expect it the least, I found a great student, colleague and friend at the institute in the form of Micha. We started off as he being my student and ended up being great friends. You made me feel home Micha and thank you so much for it. It is rightly said when the phrase reads birds of same feather flock together, Rahul and I were these birds. Obviously we have known each other since long and this helped us strike a nice chord as colleagues. In fact to be true, had it not been for Rahul I am sure I would not be writing this and wrapping up my dissertation. Thank you for everything Rahul, I owe you big time.

Being 8000 km away from home may sound exciting but was not always fun. I completely relied on my support system which included my taken for granted forever friends. Prem, the random conversations we had both virtually and physically, kept my spirit high. Ankit I can undoubtedly state that you have always been around and I cannot thank you enough for it. Sam you have been my soul-friend both in terms of my professional and personal endeavour. Thank you with all my heart, is all I have to say. Debo, I know I need not thank you but we know it well that I would not have made it this far if not for your good wishes. You are my only constant. Bhoomi and Piyush, life changed for good once you both moved to Hamburg. The good humour and the splendid time we spent together would always be cherished. I look forward to many such memories. Amiya, I still continue to thank you for convincing me to take 'Leap of Faith' and go in for this PhD.

PhD has been a long sail and I had to anchor from time to time and these anchors were in the form my dearest family members. They have been a constant source of inspiration and made sure that I made till the end. I cannot thank you all enough.

The journey of (PhD) life is sweeter when travelled with a dog. To all my furry friends, I love you as unconditionally as you love me.

"You do not meet people by accident but there is always a reason or a blessing", for me you have been both of them. Kartik you have been my constant reason to better myself and also a blessing, making my life even more beautiful.

Maa and Papa, you are my roots and also the wind under my wings. I am because of you!

Hamburg 13.10.2021

Sparsha Sinduri Nagula

Schlagwörter:

Tiefenvibrationsverdichtung, CEL, 1g Physikalische Modelltests, Seismische Analyse, Parametrische Studie, Sand, Vibrator, Verflüssigung, Amplitudengesteuerte Verdichtung, Hypoplastisch, Zentrifugentest

Keywords:

Deep Vibration Compaction, CEL, 1g Physical Model tests, Seismic Analysis, Parametric Study, Sand, Vibrator, Liquefaction, Amplitude Controlled Compaction, Hypoplastic, Centrifuge Test

Optimisation of Deep Vibratory Compaction as Liquefaction Mitigation Measure

Vom Promotionsausschuss der
Technischen Universität Hamburg
zur Erlangung des akademischen Grades
Doktor-Ingenieur(in) (Dr.-Ing.)

genehmigte Dissertation

von
Sparsha Sinduri Nagula

aus
Nagpur, India

2021

1. Gutachter: Univ.-Prof. Dr.-Ing. Jürgen Grabe
2. Gutachter: Univ.-Prof. Dr.-Ing. Marcus Rutner
3. Gutachter: Univ.-Prof. Dr. techn. Dietmar Adam

Tag der mündlichen Prüfung: 08.10.2021

Contents

1	Introduction	1
2	State of Art	5
2.1	Deep Soil Compaction: Deep Vibratory Compaction	5
2.1.1	Methodology for Deep Vibratory Compaction	6
2.1.2	Suitability of Deep Vibratory Compaction	8
2.1.3	Factors affecting Deep Vibratory Compaction	11
2.1.4	Extent and Degree of Deep Vibratory Compaction	12
2.1.5	Principle behind Deep Vibratory Compaction	13
2.1.6	Geotechnical Investigation of Soil	15
2.2	Physical Modelling and Field Testing of Deep Vibratory Compaction	16
2.3	Analytical and Numerical Models of Deep Vibratory Compaction	19
2.4	On-line Compaction Control during Deep Vibratory Compaction	26
2.5	Liquefaction Mitigation Potential of Deep Vibratory Compaction	29
3	Research Questions and Objectives	35
3.1	Research Gap	35
3.2	Research Gap Motivated Objectives	36
3.3	Methodology	37
3.4	Flow of Thesis	38
4	Principles of Experimental and Numerical Methods	41
4.1	1g Physical modelling	41
4.1.1	Fabrication of model vibrator	41
4.1.2	Experimental Set up	42
4.1.3	Granular Material	43
4.1.4	Methodology	43
4.2	Deep Vibratory Compaction: Field Trials	45
4.2.1	Project Description	46
4.2.2	Kippen Sand	48
4.2.3	On-Field Measurements	50
4.3	Numerical Framework	51
4.3.1	CEL Deep Vibratory Compaction Model	52
4.3.1.1	Model Definition	53
4.3.1.2	Simulation Methodology	54
4.3.2	FE CPT Model	55
4.3.2.1	Model Definition	55
4.3.2.2	Simulation Methodology	56

4.4	Plane Strain Lagrangian framework for Seismic Analysis	57
4.4.1	Model Definition	57
4.4.2	Simulation Methodology	58
4.5	Constitutive Model for Sand	58
4.5.1	Hypoplastic Model with Intergranular Strains	59
4.5.2	Determination of Hypoplastic Model Parameters	61
4.5.2.1	Hypoplastic Model Parameters	65
4.5.3	Determination of Intergranular Strain Parameters	65
4.5.3.1	Intergranular Strain Parameters	68
4.5.4	Calibration of Parameters	71
5	Validation of Numerical Framework for Deep Vibratory Compaction	75
5.1	Comparison of Classical FE and CEL	75
5.1.1	Classic Lagrangian (FE) Framework	75
5.1.2	CEL Framework	77
5.1.3	Comparison of Frameworks	77
5.2	1g Model Measurements and Simulations	78
5.2.1	1g Model Measurements	78
5.2.1.1	Ground Vibration Measurement with a Geophone	79
5.2.2	1g Model Test Simulations	81
5.2.2.1	CEL Model for 1g Model Test	81
5.2.2.2	1g Model Simulation Steps	82
5.2.2.3	CPT Correlation for Hamburger sand	82
5.2.2.4	Comparison of 1g Model Test and Simulations Results	84
5.2.2.5	Spatial and Temporal Insight into 1g Model Test	85
5.3	Cottbus Field Measurements and Simulations	88
5.3.1	Cottbus Field Measurements	89
5.3.1.1	CPT and Machine Parameters	89
5.3.2	Cottbus Field Deep Vibratory Compaction Simulations	90
5.3.2.1	CEL Model and Simulation Methodology for Field Deep Vibratory Compaction	90
5.3.2.2	CPT Correlation for Kippen Sand	91
5.3.2.3	Comparison of Cottbus Field Measurements and Simulations Results	92
5.3.2.4	Comparison of Machine Data	94
5.3.2.5	Spatial and Temporal Insight into Field Deep Vibratory Compaction	94
6	Understanding Factors Affecting Deep Vibratory Compaction	99
6.1	Frequency	99
6.1.1	1g Model Test Results for Frequency	99
6.1.2	Numerical Simulations Results for Frequency	101
6.1.2.1	Deep Vibratory Compaction Simulations at Field Scale	101

6.2	Relative Density and Stress State	102
6.2.1	Numerical Simulations Results for Relative Density and Stress State	104
6.2.1.1	Effect of Relative Density in Field Scale Simulations . . .	104
6.2.1.2	Effect of Stress State in Field Scale Simulations	105
6.3	Granular Material	107
6.3.1	Numerical Simulations Results for Granular Material	107
6.3.1.1	1g Model Test Simulation Results	110
6.3.1.2	Field Scale Simulation Results	111
6.4	Shape of Vibrator Probe and Friction	111
6.4.1	Numerical Simulations Results for Vibrator Shape and Friction . . .	112
6.4.1.1	Effect of Different Vibrator Probes in Field Scale Simulations	114
6.4.1.2	Influence of Friction in Field Scale Simulations	114
6.5	Compaction Process	116
6.5.1	Numerical Simulation Results for Compaction Process	116
6.5.1.1	Effect of Compaction Process in Field Scale Simulations .	117
6.6	Spacing and Compaction Grid	118
6.6.1	Numerical Simulation Results for Spacing and Compaction Grid . .	119
6.6.1.1	Effect of Spacing in Field Scale Simulations	119
6.6.1.2	Effect of Compaction Grid in Field Scale Simulations . . .	120
6.7	Soil Saturation	122
6.7.1	Performance of Coupled Hypoplastic Model to Model Saturated Kip- pen Sand	124
6.7.2	Numerical Simulation Results with Saturated Soil	127
6.7.3	Development of Void Ratio and Pore Pressure in Field Scale Simu- lations	127
6.7.4	Influence of Permeability in Field Scale Simulations	131
6.7.5	Variation of Void Ratio with Consolidation in Field Scale Simulations	134
7	Optimisation of Deep Vibratory Compaction: Compaction Control	137
7.1	1g Model Tests	137
7.1.1	Measurement of Amplitude and Phase Angle	138
7.1.2	Identification of Control Parameter: Variation of Amplitude and Phase Angle with Compaction	140
7.1.3	Calculation of the reaction stiffness according to Nagy (2019) . . .	142
7.1.4	Compaction with and without Control	144
7.2	Numerical Simulations	144
7.2.1	Code to Control Simulations	146
7.2.1.1	Simulation Steps	147
7.2.2	Validation of Numerical Framework based on Amplitude Controlled Model Tests	149
7.2.3	Compaction Simulation with and without Control	149
7.3	Extension to Field: Conceptualization	151

8	Liquefaction Mitigation of Deep Vibratory Compaction	153
8.1	Plane Strain Lagrangian framework	153
8.1.1	Numerical Model and Methodology	153
8.1.2	Validation of Plane Strain Model	154
8.1.2.1	Seismic Centrifuge Test	154
8.1.2.2	Comparison of Centrifuge and Numerical Results	159
8.2	Mitigation Potential of Deep Vibratory Compaction	163
8.2.1	Before Deep Vibratory Compaction	163
8.2.2	After Deep Vibratory Compaction	165
9	Inference and Perspective	173
9.1	Key Research Answers	173
9.2	Future Scope	177
	References	179
	Appendix A Design of Model Vibrator	193
	Appendix B Results of Experimental Tests	205
B.1	Grain size distribution of Hamburger sand	205
B.2	Grain density of Hamburger sand	207
B.3	Maximum and minimum void ratio of Hamburger sand as per DIN 18126	209
B.4	Critical friction angle of Hamburger sand	211
B.5	CRS oedometer test of loose Hamburger sand	213
B.6	CRS oedometer test of dense Hamburger sand	215
B.7	Static triaxial test of loose Hamburger sand	217
B.8	Static triaxial test of dense Hamburger sand	219
B.9	Stress path controlled triaxial test of Hamburger sand for intergranular strain parameters	221
B.10	Grain size distribution of Kippen sand	223
B.11	Water content of Kippen sand	225
B.12	Organic content of Kippen sand	227
B.13	Maximum and minimum void ratio of Kippen sand as per DIN 18126	229
B.14	Critical friction angle of Kippen sand	231
B.15	CRS oedometer test of Kippen sand	233
B.16	Static triaxial test of loose Kippen sand	235
B.17	Static triaxial test of dense Kippen sand	237
B.18	Stress path controlled triaxial test of Kippen sand for intergranular strain parameters	239
	Appendix C Details of field V48 vibrator	241
	Appendix D VUAMP: Amplitude controlled CEL simulations	243

1 Introduction

The current world population ranges around 7 Billion and is ever increasing; the rising population has created huge demand of land for various infrastructure facilities. This has pushed the engineering community to use land which previously in history was considered unsuitable for any construction. Soil liquefaction caused by earthquake loading is a major threat to infrastructure. Figure 1.1 depicts the devastating effect of liquefaction of saturated sand. Loose saturated sands when subjected to seismic loading develop high excess pore water pressures and shear strains that may lead to soil liquefaction. This has led to the evolution of various ground improvement techniques. The methods range from extensive mechanical compaction of existing soil to replacement of soil with stiffer columns of material to enhance its bearing capacity and liquefaction mitigation. Granular soils are mainly improved by imparting mechanical forces which lead to densification of the soils. Deep vibratory compaction method is an established ground improvement technique for granular soils. This technique is used to improve the properties of loose to medium dense granular soils by compacting deep layers of the soil and therefore reducing settlements, increasing the vertical bearing capacity and aiding in liquefaction mitigation.



Figure 1.1: Liquefaction induced damage in the 1964 Niigata, Japan Earthquake (Elnashai and Di Sarno, 2008)

The method involves a vibrator probe (Fig.1.2) penetrating to the desired installation depth and the generated shear waves in the soil due to vibrations of the probe leading to the compaction of the soil. The lack of analytical design methodology and dependence on field experience of past projects to ascertain liquefaction mitigation potential inhibits the efficient use of deep vibratory compaction. Vibrator-soil interaction and factors affecting compaction hold the key to improving the method. CPT field measurements before and after compaction help analyse the efficiency of deep vibratory compaction. Data from the



Figure 1.2: Deep vibration compaction probe at work in Silbersee, North Germany

accelerometers in the vibrator aid in understanding the vibrator soil interaction; however, field measurements alone cannot provide sufficient information to optimise the process (Triantafyllidis and Kimmig, 2019). Extensive field trials demand additional financial and temporal resources. Field measurements also lack adequate control on test conditions. Physically modelling at 1g can provide insight but cannot realistically capture stress state conditions. Considering the above mentioned lacunae, numerical simulations can help one understand the various physical processes the soil undergoes during compaction (Arnold and Herle, 2009). Numerical models developed to date have neither been able to realistically capture the entire compaction process nor have they been validated. Hence, a combination of physical modelling, field measurements and numerical simulations would help analyse deep vibratory compaction. Followed by seismic numerical simulations of saturated sand compacted by deep vibratory compaction to analyse the feasibility and effectiveness of this method for mitigating the liquefaction hazard and its consequences. The research work outlined in this thesis is twofold, first being validation of numerical simulation of deep vibratory compaction based on the results of model tests and field measurements followed by parametric study and optimization of the technique. Second leg of the work aims at studying the effectiveness of deep vibratory compaction as liquefaction mitigation measure. The deep vibratory compaction technique was numerically simulated in Coupled Eulerian and Lagrangian (CEL) computational framework. The numerical simulations were validated based on the results of model tests in the laboratory and measurement data from the field. Model tests were performed with an in-house fabricated mini vibrator. Parametric analysis varying the machine parameters, drainage

and type of granular material were performed to study its effect on the compaction process. The results of the numerical and physical model studies were used to identify on-line compaction control parameters. The same was used to design an optimization algorithm to control the compaction process, which would eventually lead to efficient compaction process. In the end, numerical simulations of loose saturated sands under seismic loading were investigated and the improvement in the liquefaction potential of the saturated sands after subjection to deep vibratory compaction was analysed.

2 State of Art

During planning of a construction project, geotechnical investigations are carried out. Based on the determined soil parameters, the suitability of soil for withstanding the planned construction is commented upon. If the properties of soil do not meet the necessary load bearing requirements, there are three possible solutions:

1. Soil is exchanged and replaced by a more stable one. This measure is seldom economical due to the high transport costs.
2. Deep foundations such as piles are used to transfer load to stable soil layers at deeper depths.
3. The properties of existing soil are improved.

The methods for improving soil properties are divided into two different subgroups by Sondermann and Kirsch (2017). On the one hand, all measures which include introducing a more stable material into existing soil, are described as reinforcing measures. This can be sand in the form of compaction columns or a cement suspension by means of jet grouting. The second subgroup of soil improvement includes compaction/densification measures. Deep vibratory compaction is one such method. Deep vibratory compaction was devised by Johann Keller company in 1930s in Germany (Sondermann and Kirsch, 2017). Deep vibratory compaction is an established ground improvement technique for granular materials. It densifies loose sands by means of shear and compressive deformation processes imparted by the horizontal vibrations of a vibrator probe at the required soil depth. It is used to improve the properties of loose to medium dense granular soils by compacting deep layers, leading to reduced settlement and increased bearing capacity (Mitchell, 1982; Massarsch, 1991; Massarsch, 1999). In addition, it aids in liquefaction mitigation (Kumar et al., 2010). It gained increasing importance in recent years due to its high economic efficiency and capacity to improve large volumes of soil. The development and modifications made to the method over the decades is detailed by Kirsch and Kirsch (2017).

2.1 Deep Soil Compaction: Deep Vibratory Compaction

Deep vibratory compaction is one of the methods for deep soil compaction. Deep soil compaction includes compaction of soil between 2-30 m depth. This includes compaction with retractable vibrators, top-mounted vibrators, compaction piles, the dynamic compaction with drop weights and blasting compaction. The aim of such compaction techniques is to cause shearing through oscillations and vibrations in order to reinitiate relocation of soil grains to a denser and compact state. This increases the density, angle of friction and stiffness of soil. As a result, soil bearing capacity improves, settlement and permeability of the ground is lowered (Fellin, 2000).

Deep vibratory compaction initiates rearrangement of soil grains as mentioned before. Deep vibratory compaction creates a horizontal force on the soil grains and changes the soil arrangement. Relocation of the soil grains leads to an increase in storage density and volume reduction. Reduction in soil volume, leads to lowering of the ground surface. Thus, soil exhibits a higher angle of friction and an increased stiffness modulus (Fellin, 2000). This leads to an increased load carrying capacity and lower subsidence. Deep vibratory compaction in some granular materials can lead to a 5 to 8° increase in angle of friction (Fellin, 2000).

2.1.1 Methodology for Deep Vibratory Compaction

The deep vibratory compaction technique uses a vibrator probe made generally of steel, with diameters ranging approximately 0.3 m to 0.5 m. The vibroflot consists of an unbalanced mass inside a steel tube; this mass rotates around the vertical axis of the compactor, generating oscillations in the vibrator (Figure 2.1). These oscillations create a centrifugal force that is imparted to the soil. Resulting shear waves lead to soil compaction. The vibroflot typically functions between 15 and 60 Hz, with a maximum amplitude of 3 mm to 21 mm at the toe of the vibrator (Fellin, 2000). In order to develop the necessary compression energy a motor with 50 to 150 kW power is usually used (Sondermann and Kirsch, 2017). The weight of the vibrator body is usually between 820 and 4400 kg. The vibroflot is attached to extendable stay tube via elastic coupling (Figure 2.1). The elastic coupling provides cushioning effect to the stay tubes from the vibrations created by the vibroflot (Sondermann and Kirsch, 2017). The other end of the stay tube is pinned to a crane resting on ground surface. In order to ease penetration of vibroflot into the ground, pressurised air or water is used at tip of the probe in order to loosen the soil. Following that the penetration of the probe takes place under its self weight and in some special cases additional activating force is added through the supporting crane. The arrangement and the number of air/water outlets can vary depending on the device type. The vibroflot is driven electronically or hydraulically. The following parameters of the vibroflot are decisive for the success of compaction (Kirsch and Kirsch, 2017):

- Probe amplitude
- Vibrator frequency
- Centrifugal force
- Power of vibroflot
- Number and placement of air/water nozzles

Deep vibratory compaction begins with the vibroflot being guided to the required target depth. The weight of the vibroflot and stay tubes is sufficient to mitigate the penetration in most of the cases as described earlier. Injection of air or water during lowering of vibroflot makes the penetration easier in stiffer soils (Nendza, 2006). When the target depth is reached, the air or water supply is stopped. Following this compaction by the vibroflot begins. According to Fellin (2000) there are primarily two compaction procedures which are as follows:

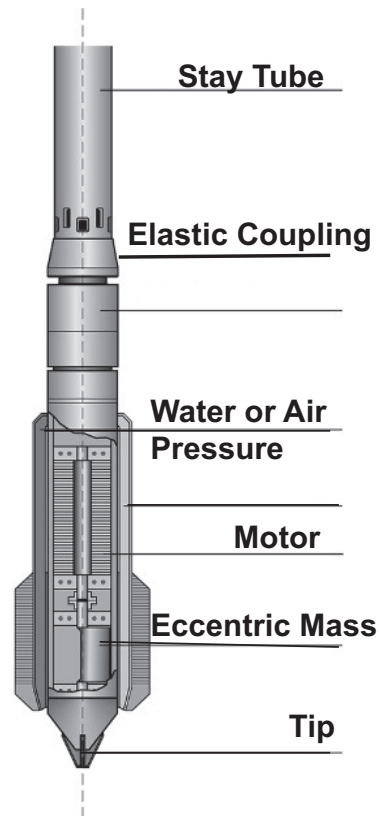


Figure 2.1: Schematic representation of vibroflot (Sondermann and Kirsch, 2017)

- The gradual pulling
- The pilgrim step

In the first procedure, the vibroflot is pulled up in stages. After 30 to 60 s vibration time at a certain depth, the probe is pulled up by 0.3 to 1 m. This method has been found to be more suitable for cohesionless soils (Nagy, 2019). In pilgrim step method, the vibrator is pulled up (0.3 to 1 m) and pushed down (0.15 to 0.5 m) in a sequence while the probe is vibrating. This method has been found to be more suitable for granular soils with fines and lightly cemented soils (Nagy, 2019). The pilgrim step method is discussed in detail in the following chapters. During compaction of the soil, its volume decreases leading to a settlement on soil surface. According to Sondermann and Kirsch (2017), settlement to the order of 5 to 15 % of highest compaction depth can occur. In order to maintain ground surface level and to also fill in void created due to compaction, additional material is added. The addition of material also ensures that the vibrator probe is in constant contact with the ground. This is necessary to ensure transfer of energy between vibroflot and soil which leads to compaction. Medium to coarse sand with a grain diameter of 0.2 to 2 mm is used as additional filling material (Fellin, 2000). Additional filling material of approximately 0.4 to 0.8 tonne per m of compaction depth is required. In certain scenarios quantity of filling material used as an indirect quality control measure. Deep vibratory compaction method cannot compact soil close to ground surface till 3-5 m depth (Fellin, 2000). Soil

close to ground surface is generally re-compacted by other compaction techniques. This is usually executed using a vibratory roller. Compaction by deep vibratory compaction can hence be categorised into the following steps (Nagy, 2019). Penetration of vibroflot into the soil to required depth followed by compaction by vibrations. Addition of filler material to compensate for void created by settlements soil. Finally is marked by the re-densification of soil near surface.

Compaction by deep vibratory compaction demands creation of a huge homogeneously compacted area. In order to achieve this, compaction is carried out on the basis of specific compaction grid. The distribution of compaction points in the grid is decided as per local conditions. Compaction in a grid is composed of two stages. As part of the first stage compaction is carried out as per a triangular or rectangular grid, called as "primary grid". In the second step, compaction is carried out at diagonal points of the original grid, called as "secondary grid". The optimal distance between compaction points depends on the soil and vibroflot properties and is usually between 2.5-5 m. Nagy (2019) states that the minimum distance between the compaction points should be 1.4 m.

2.1.2 Suitability of Deep Vibratory Compaction

The limits of applicability of deep vibratory compaction for compaction of soils depends on various factors. These factors must be well understood, in order to access if the technique would be a feasible ground improvement method and above all financially profitable. To quote an example, deep vibratory compaction cannot be used for all types of soil and beyond a certain depth it loses its effectiveness. In summary, the following aspects must be accessed:

Soil type The type of soil to be improved has a decisive influence on the selection of deep vibratory compaction as compaction method. The compressibility of soil is most often defined on the basis of its grain size distribution. As a general rule, coarse-grained soils with a high potential for self-compaction can be optimally compressed by deep vibratory compaction. Hence, it can be stated that the use of deep vibratory compaction is limited to non-cohesive, granular materials. In the case of cohesive soils, the existing cohesion prevents compaction by vibrations of the vibrator. Kirsch and Kirsch (2017) broadly classify granular soils on the basis of their compactability by deep vibratory compaction method in Table 2.1. It can be observed that not all granular soils can be efficiently compacted and that the grain size distribution of the soil has a decisive influence on the achievable compaction success. Even a comparatively small amount of silt or clay can reduce or even prevent the dynamic compaction effect. The suitability can be accessed primarily by studying the grain size distribution of the soil. The range of application is defined by limit curves as shown in Figure 2.2 after Witt (2017a) and by Figure 2.3 after Mitchell (1982) and Thorburn (1975). In principle, the more soils are closer to the fine-grain area (red line) in Figure 2.2, the more difficult they are to compact by deep vibratory compaction. According to Mitchell (1982) in Figure 2.3 soil with fines content higher than 20-25 % cannot be vibrocompacted due to the cohesive properties of the soil. It should be noted that the range described by Mitchell (1982) in Figure 2.3 for coarse sand and gravel is not accurate and experience on field has showed that these soils can be effectively compacted by deep vibratory compaction. In Figure 2.2 as one approaches the green line,

Table 2.1: Suitability assessment of granular soils for vibro compaction (Kirsch and Kirsch, 2017)

Soil type	USCS	Comment on suitability for deep vibratory compaction
Gravel, well graded	GW	Well suited for vibro compaction, potential penetration difficulties with less powerful machines
Gravel, poorly graded	GP	If $d_{60}/d_{10} \leq 2$ compaction only marginal (trial compaction recommended)
Gravel, silty or clayey	GM, GC	Compaction not possible if clay content $> 2\%$ and silt content $> 10\%$
Sand, well graded	SW	Ideally suited
Sand, poorly graded	SP	If $d_{60}/d_{10} \leq 2$ compaction only marginal (trial compaction recommended)
Sand, silty	SM	Compaction inhibited if silt content $> 8\%$
Sand, clayey	SC	Compaction inhibited if clay content $> 2\%$

the soil is composed of coarser grains and bigger particles. The coarser soils make the penetration of vibroflot difficult, reducing the effectiveness of the compaction method. Uniformly graded gravel and cobble significantly impair penetration. Soil with particle diameter greater than 100 mm can be nearly impossible to penetrate (FGSV, 1979). Grain shape also influences the compaction behaviour. Soils with an angular shape (edge length > 50 mm) substantially reduce the effectiveness of deep vibratory compaction. It is to be noted that zone of application depicted in Figure 2.2 can vary, as they are determined empirically and are partly dependent on the kind of vibroflot used. Brown (1977) defined

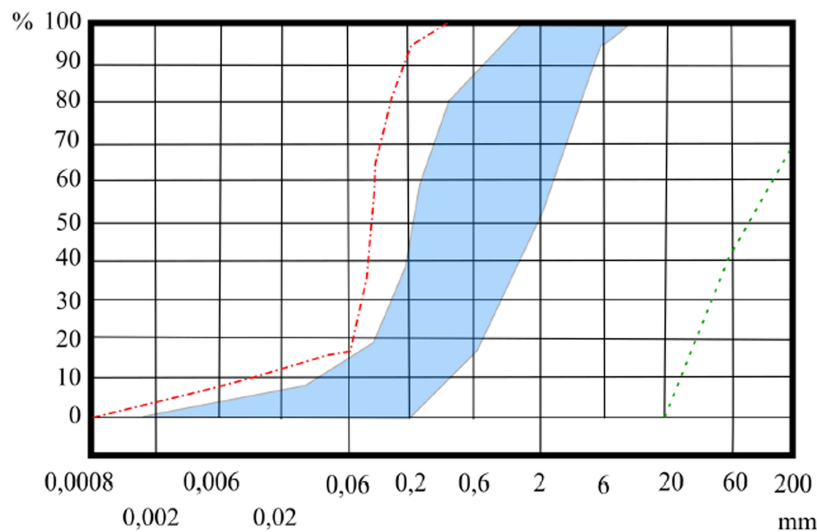


Figure 2.2: Limits for application of deep vibratory compaction as per grain size distribution of soil (Witt, 2017a)

a suitability factor based on the particle size distribution for assessment of compactability of soils. The suitability factor SN is defined by Equation 2.1

$$SN = 1.7 \left(\frac{3}{d_{50}^2} + \frac{1}{d_{20}^2} + \frac{1}{d_{10}^2} \right)^{0.5} \quad (2.1)$$

where, d_{50} , d_{20} and d_{10} correspond to the grain diameter at corresponding percentage fines as mentioned in bracket.

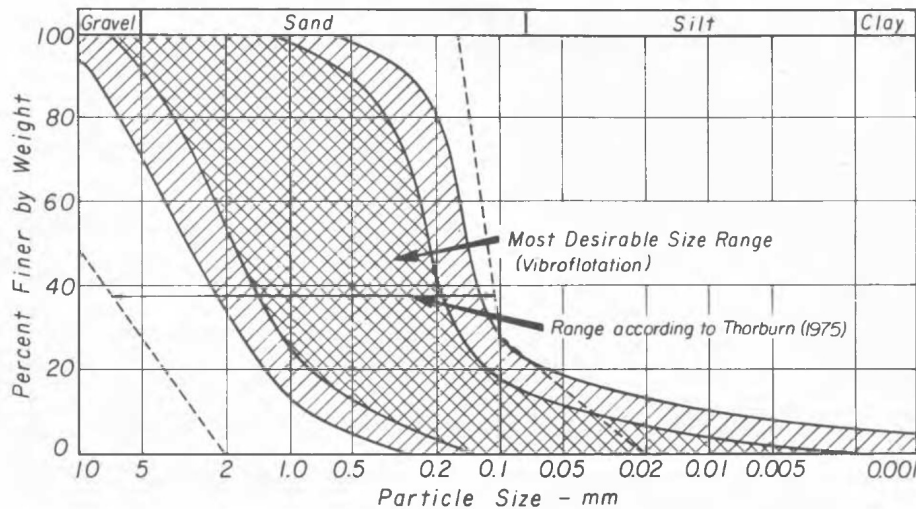


Figure 2.3: Range of suitability as per grain size distribution for using deep vibration as compaction method (Mitchell, 1982; Thorburn, 1975)

The smaller the suitability factor, the better the soil is suitable for compaction with deep vibratory compaction. Soils with a suitability factor over 50 cannot be compacted with deep vibratory compaction.

In brief, various researchers have quoted several maximum permissible fine fraction (fine = grain diameter $d < 0.06$ mm) in soil to be suitable to be compacted by deep vibratory compaction. Kirsch (1979) quotes fines below 15 %, Brown (1977) fines below 20 % and Thorburn (1975) fines below 30 % as the maximum limit.

Soil Permeability The hydraulic permeability of the soil to be compacted is decisive, as it influences the compressibility of soil. According to Massarsch (1999), the permeability of the soil to be compacted should be sufficiently large to allow the rapid reduction of the excess pore water pressure caused due to vibrations of probe to allow rearrangement of soil grains possible. According to Kirsch and Kirsch (2017), effectiveness of deep vibratory compaction is negligible in soils with permeability lower than $k = 1 \times 10^{-5}$ m/s. Simons and Kahl (1987) suggest suitability of soil for compaction by deep vibratory compaction on the basis of permeability of the soil. They suggest that the permeability of soil should be greater than 1.03 m/s. Higher permeability ensures that there is no generation of excess pore water pressure due to vibrations in saturated soils or due to added water during penetration of vibroflot. Development of excess pore water pressures hinders the re-arrangement of soil particles and soil can attain a denser state only after the excess pore pressure dissipate. As presence of fines reduces permeability both the factors are intertwined and both affect the usability of deep vibratory compaction for compaction of soils with fines.

Soil Depth The usual compaction depths for vibration compression are between 3 up to 25 m. In extreme cases, these can also be extended to a depth of 30 m (Fellin, 2000). The layers near the surface cannot be compacted by deep vibratory compaction as they tend to loosen than compaction due to less overburden. At depths beyond 40 m, deep vibratory compaction process becomes less economical because the difficulty in penetra-

tion of vibroflot increases tremendously (Fellin, 2000). Skin friction between the vibrator including the stay tubes and soil accumulates with increasing depth. The necessary force to push the vibrator into the ground increases, making the penetration uneconomical. On the whole, Nendza (2006) and Fellin (2000) suggest that deep vibratory compaction can be economically used to compact soil till depths of 25 m below ground level. In certain exceptional cases it can be used up to 35 m (Fellin, 2000) or 50 m (Nendza, 2006).

2.1.3 Factors affecting Deep Vibratory Compaction

According to Fellin (2000), the vibroflot essentially influences compaction and in addition the existing soil, compaction workflow and used backfill material determines the success of deep vibratory compaction. There is no clear connection between the vibrator data (e.g. mass, frequency and centrifugal force) and the compression achieved. Increased use of deep vibratory compaction in recent years shows that every soil is different in the way it reacts to dynamic loads. According to Fellin (2000), low frequency (30 to 70 Hz) and large amplitude (5 to 10 mm) leads to best compaction in sandy soils. On the other hand, no such correlation exists for gravel soils (Simons and Kahl, 1987). The quality of deep vibratory compaction cannot be assessed on the basis of the machine data alone. Every soil behaves differently. It is not necessary stronger vibrators lead to better compaction. Field trials from the Bauer Spezialtiefbau GmbH showed that vibroflots with greater impact force lead to better compaction at centre of compaction but the effect reduced with increasing radial distance. The same applies to the vibrator frequency. Higher frequencies result in better compaction at vibration centre, but loses its effect with radial distance. In brief, vibroflots with high frequency and impact force make compaction flow easy and also ease the penetration of vibroflot into the soil and on the whole deliver good compaction effect. Deep vibratory compaction leads to best compaction in very loose sands with groundwater. Efficient deep vibratory compaction requires soil to be compacted to have sufficient permeability so that the soil could consolidate unhindered (Brown, 1977). Presence of silt, clay and organic additions dampen vibration. Presence of high percentage of fines in sands can lead to formation of loose agglomerates which can hinder re-arrangement of soil into denser state (Fellin, 2000). In contrast, coarse-grained soils such as gravel, dense sand and cemented sand layers reduce the rate of penetration of vibroflot and render deep vibratory compaction uneconomical (Fellin, 2000). In brief, soils with a medium to dense relative density ($0.3 < I_D < 0.7$) are harder to compact than soils with a loose storage density ($I_D < 0.3$).

It was mentioned prior that compaction workflow also affects compaction efficiency. Two types of compaction processes namely gradual pulling method and pilgrim step method have been discussed in preceding section. The compaction time at each depth is determined based on the power consumption of the vibrator motor. According to the power consumption concept, with progressing compaction, resistance to movement of vibrator increases eventually leading to increased power consumption. Machine operator decides compaction time at each depth depending on the variation of power consumed. Vibration time for such compaction process at each depth varies between 30 and 60 s. In the pilgrim step method, the vibrator is pulled up and pushed down in sequence to execute compaction. Compaction at each depth is carried out for a pre decided time. Compaction

time in the pilgrim step method is heavily dependent on the soil type. Simons and Kahl (1987) suggest compaction time of 120 s in all kinds of soils as it ensures complete compaction.

Type of filler material used to compensate for voids created due to compaction also affects compaction success. Type of filler material used depends heavily on the existing soil. Soils with high self-healing potential, that is property of soil to independently flow to fill in voids created by compaction, need no filler material. In scenarios where filler material is to be used, medium and coarse sand are preferred. Filler material that is too coarse or too flattened leads to wedging and hinders flow of material (Brown, 1977). On the other hand, very fine material does not sink into the ground to fill in the created voids (Brown, 1977). The amount of the filling material varies between 10 - 15 % of total volume of soil compacted.

2.1.4 Extent and Degree of Deep Vibratory Compaction

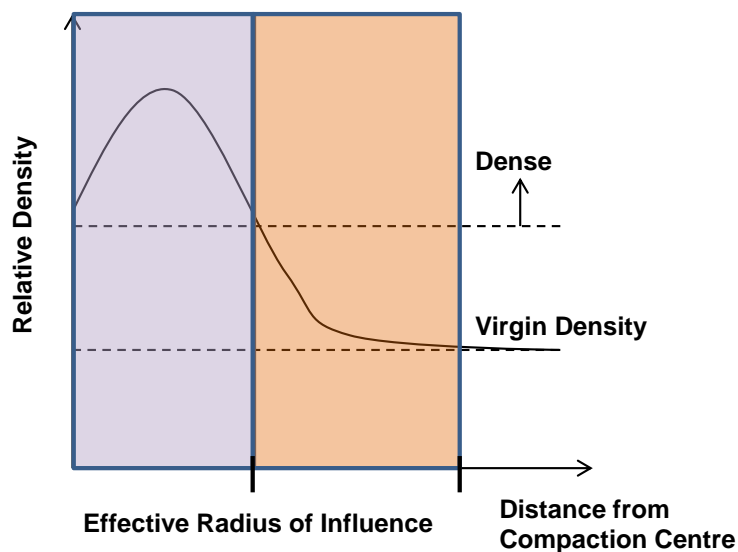


Figure 2.4: Qualitative variation of relative density with radial distance from vibrator after deep vibratory compaction

Compaction effect by deep vibratory compaction at a certain point depends on the radial distance of the point from vibration centre. The effective radius describes the radial distance around compaction centre where soil reaches required denser state (Figure 2.4). Radius of influence describes radial distance around compaction centre where increase in relative density compared to the virgin soil is observed (Figure 2.4). Grid spacing is primarily decided on the basis of effective radius. Two grid patterns are popular namely, rectangular grid and triangular grid (Figure 2.5). Rectangular grid is preferred for building single foundations and triangular grid for compacting large areas (Fellin, 2000). In Figure 2.5 point *W* corresponds to the centre of the triangle (square) between the individual compaction points. It is the farthest point from the vibrating source. The distance r

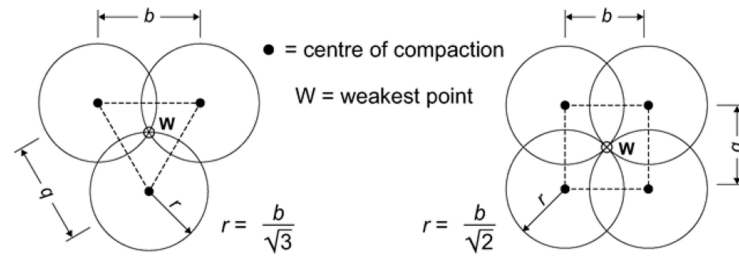


Figure 2.5: Types of deep vibratory compaction grids (Kirsch and Kirsch, 2017)

between point of vibration and centre point depends on the grid spacing as described in Equation 2.2

$$\begin{aligned} \text{Triangular: } r &= \frac{b}{\sqrt{3}} \\ \text{Rectangular: } r &= \frac{b}{\sqrt{2}} \end{aligned} \quad (2.2)$$

where, b is grid spacing.

Nendza (2006) suggests that in large projects, Cone Penetration Test (CPT) should be carried out at various radial distances after deep vibratory compaction in order to determine if required compaction occurs at point W as shown in Figure 2.5 and accordingly choose the grid spacing for the compaction project.

Figure 2.6 describes the variation of relative density with increasing radial distance to compaction centre for various kinds of soils. It is evident that they all describe a similar trend but no specific correlation can be developed. Frequency of compaction and centrifugal force (also called impact force) imparted by the vibroflot influence the extent and degree of compaction. The imparted centrifugal force can be evaluated by Equation 2.3

$$F = m e_m \omega^2 \quad (2.3)$$

where, F = centrifugal force, m = mass of eccentric weights, e_m = eccentricity of masses and ω = angular frequency.

Equation 2.3 shows that it is possible to create same centrifugal force with different frequencies and unbalance masses. This would make one to conclude that all such combinations would lead to similar compaction effect. But, in reality the compaction extent of all such combinations lies in a certain bandwidth as depicted in Figure 2.7 (Nendza, 2006). The probable reason could be that extent and degree is sensitive to both frequency and impact force depending on the type of soil being compacted. Fellin (2000) states best compaction is achieved at lower frequency and higher centrifugal force.

2.1.5 Principle behind Deep Vibratory Compaction

The prerequisite for the compaction of soils is the rearrangement of their grain structure. It is generally believed that soil particle rearrangement occurs as a result of liquefaction

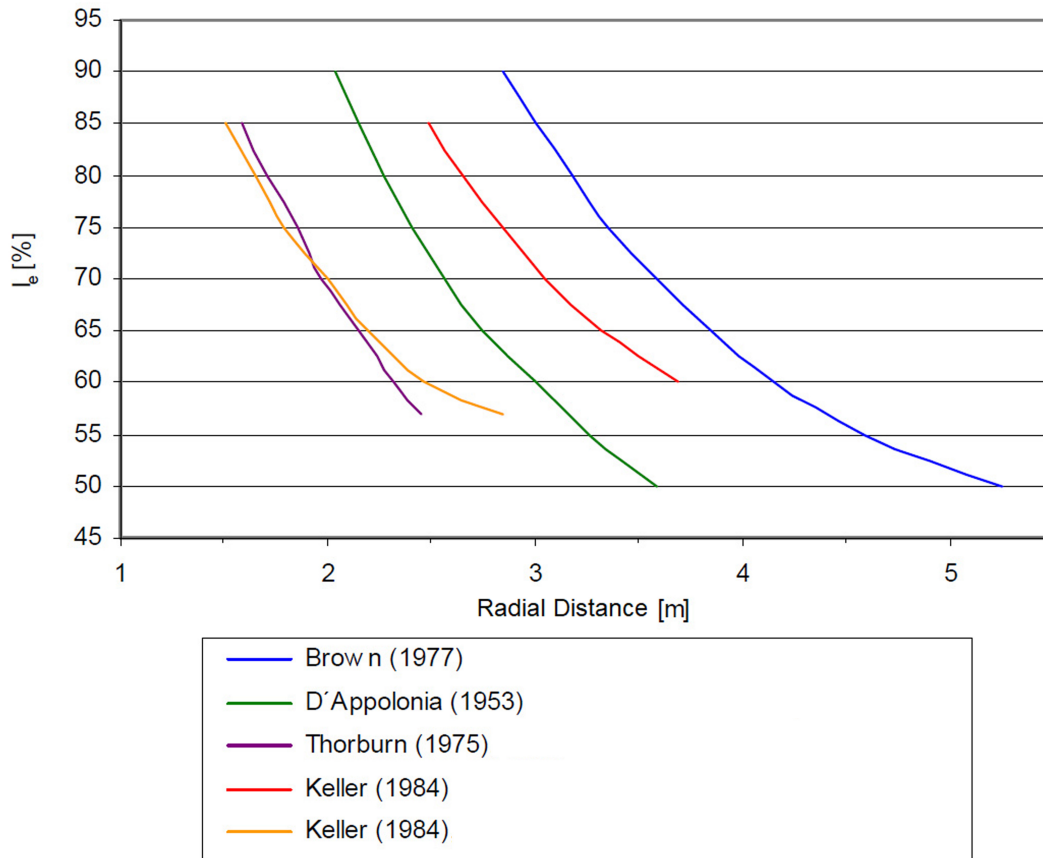


Figure 2.6: Variation of relative distance with radial distance from vibrator after Brown (1977), d'Appolonia (1954) and Thorburn (1975) from Nendza (2006)

in saturated soils and fluidization in dry soils. Bernatzik (1947) states that impact force imparted by the vibroflot to the soil leads to an increase in the excess pore water pressure in saturated soils and high particle acceleration in dry soils. This leads to loss of shear stress and grain to grain tension, making rearrangement of soil particles into a denser state possible. Simons and Kahl (1987) also explain that build up of excessive pore water pressures also hinder immediate rearrangement of soil particles and may not lead to desirable results in all scenarios. It is to be noted that liquefaction is not a prerequisite for grain rearrangement. Vibrations due to motion of vibroflot travel equally in fully saturated soils as well as in dry soils. Kutzner (1962) carried out deep vibratory compaction on glass spheres and found that compression effect in the water saturated case was similar to completely dry case. Rodger (1979) attributes acceleration of grain particles leading to fluidization of dry soils eventually leading to compaction. As soon as accelerations becomes 0.5 g, the shear strength of the soil is reduced and compression begins as depicted in Figure 2.8. At an acceleration of 1.5 g soil reaches a state of fluidization. It is to be noted that no compaction occurs in the fluidized zone. According to Rodger (1979) fluidization occurs in the immediate vicinity of the vibroflot hence, soil just around the vibroflot is not compacted. Compaction is observed with increasing radial distance from

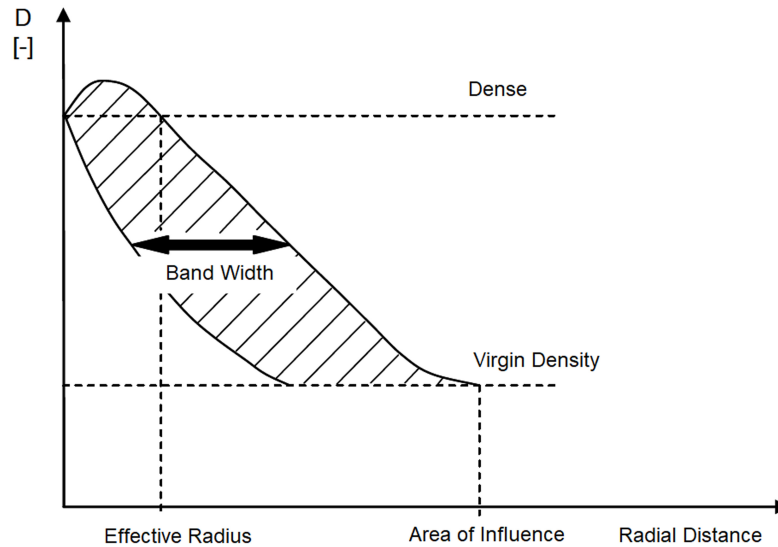


Figure 2.7: Compaction efficiency bandwidth created by same centrifugal force for a combination of frequencies and unbalanced forces (Nendza, 2006)

the vibroflot (Figure 2.8). With increasing radial distance optimal acceleration (0.5-1.5 g) range is reached which facilitates compaction. With further increase in radial distance no compaction is observed as acceleration generated in this zone is too weak to lead to any soil rearrangement. The main difference is that soil rearrangement in dry soils is immediate whereas in saturated soils it occurs after dissipation of excess pore water pressures (Fellin, 2000). Though dry and saturated soils behave similar, partially saturated soils behave slightly differently. Capillary forces can induce apparent cohesion which inhibit grain rearrangement (Kutzner, 1962).

2.1.6 Geotechnical Investigation of Soil

In the previous sections, various factors affecting success of deep vibratory compaction have been discussed. The selection and success of deep vibratory compaction as ground improvement method relies heavily on nature of soil to be compacted. Hence, it is necessary to carry out a detailed geotechnical investigation before executing the compaction. The following parameters need to be determined in order to access if deep vibratory compaction would be a suitable method to compact soil under consideration.

- Grain size distribution and quantity of fine grain fraction
- Storage density
- Hydraulic permeability
- Risk of grain fragmentation
- Cohesion or Cementation

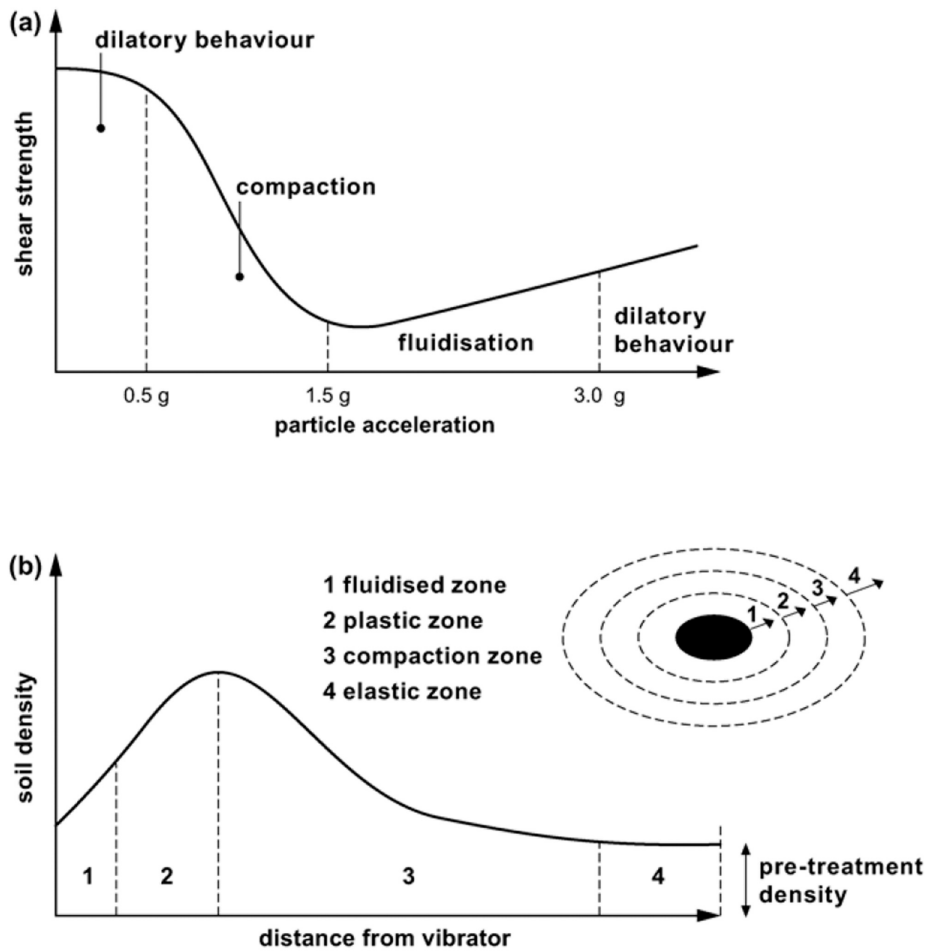


Figure 2.8: Acceleration generated due to deep vibratory compaction around vibrator and the corresponding zones (Rodger, 1979)

The relevant properties of the filler material if to be used, must also be determined. Filler material must be sufficiently hard and chemically inert. Kirsch and Kirsch (2017) recommend carrying out field trials in order to determine success of compaction on site.

2.2 Physical Modelling and Field Testing of Deep Vibratory Compaction

Various investigations have been carried out over the years in form of field measurements and physical tests with surface model vibrators in order to better understand and improvise compaction surface compactors which induce compaction by means of vertical vibrations. The effect of frequency and amplitude of surface compactors on compaction of granular soils has been studied by various researchers (Arnold and Herle, 2009; Wersäll et al., 2013; Wersäll et al., 2015; Wersäll et al., 2017). Field measurements, model tests and numerical simulations have been performed to study compaction by surface compactors (Grabe, 1992;

Adam, 1996; Kelm, 2004; Wang et al., 2007; Wersäll et al., 2013; Kenneally et al., 2015; Chen et al., 2015; Wersäll et al., 2015; Wersäll et al., 2017). On the other hand very few investigations have been carried out to analyse deep compaction by deep vibratory compaction. This section would briefly introspect works from the past which have tried to better understand deep vibratory compaction and study the underlying factors affecting its success.

Morgan and Thomson (1983) carried out extensive large-scale experimental investigations involving deep vibratory compaction. Deep vibratory compaction was carried out with three types of vibroflots in loose sand. The compaction process was carried out as per pilgrim step method as described before. Various sensors were installed in soil and on the vibroflot. Light penetrometer was used in order to access success of compaction. Figure 2.9 depicts the variation of vibrator amplitude and penetrometer resistance after compaction at various depths for a particular vibroflot. Outcome of the work was used to develop correlation between vibroflot amplitude and achieved density after compaction. Development of analytical model to determine soil parameters from vibroflot movement was suggested.

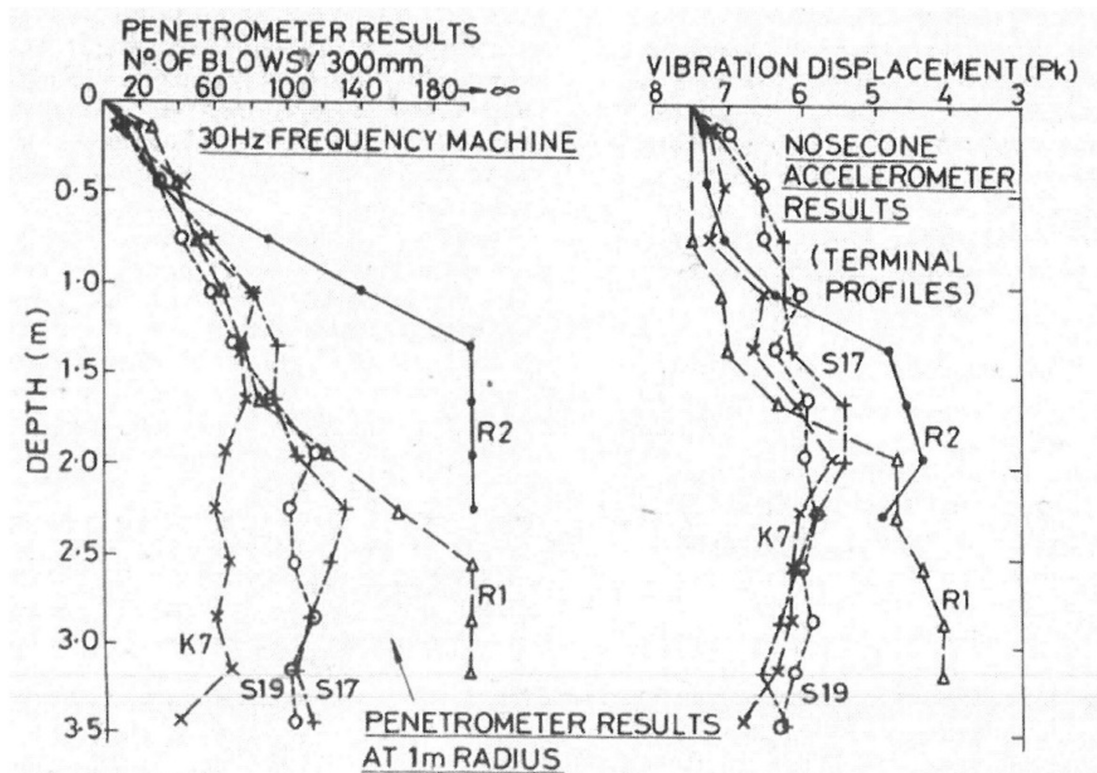


Figure 2.9: Variation of penetrometer resistance after compaction and vibrator amplitude during compaction with depth (Morgan and Thomson, 1983)

Massarsch and Fellenius (2002) and Massarsch and Fellenius (2005) performed field measurements before and after compaction in the form of Cone Penetration Test (CPT) data and during deep vibratory compaction as ground vibration measurements. Figure 2.10 describes increase in tip resistance and sleeve friction after compaction (Massarsch and

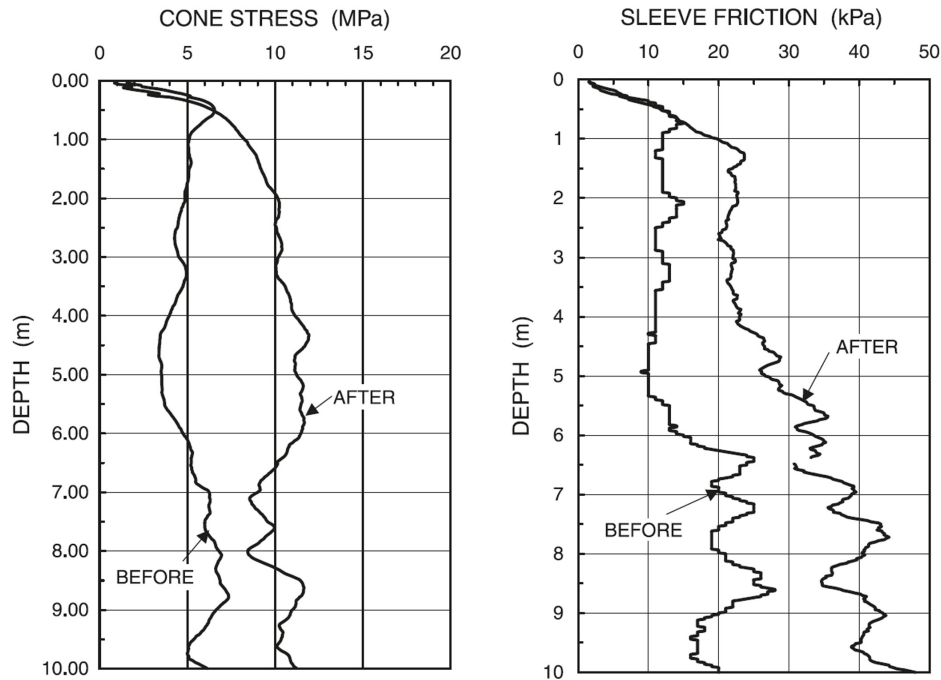


Figure 2.10: CPTu measurements in form of cone resistance (left) and sleeve friction (right) before and after deep vibratory compaction (Massarsch and Fellenius, 2002)

Fellenius, 2002). Similar increase in CPT values after deep vibratory compaction was observed in field by Bo et al. (2005) and Robertson (2016). CPT measurements after compaction were executed over a course of time and it was observed that the soil gained strength over time even after the dissipation of all excess pore water pressures (Massarsch and Fellenius, 2005). This mechanism is yet to be fully understood and one possible explanation could be the readjustment of a heterogeneous stress state to a homogenous one with time, leading to rearrangement of soil particles. CPT measurements also indicate an increase in effective horizontal stress after compaction due to repeated vibration cycles. Sleeve friction measurements were used to estimate lateral earth pressure coefficient after compaction (Massarsch and Fellenius, 2005). Flat dilatometers (DMT) were used by Balachowski and Kurek (2016) in order to verify increase in horizontal stress after deep vibratory compaction. Figure 2.11 depicts increase in horizontal stress index and the constrained Modulus after deep vibratory compaction in sand up to 8 m depth. Karray et al. (2010) performed modal analysis of surface waves (MASW) in order to access degree of compaction achieved by deep vibratory compaction and dynamic compaction at the foundation level of Péribonka dam. Figure 2.12 describes the distribution of shear wave velocity profiles over vertical planes before and after the compaction work. It can be clearly observed that loose pockets of soil layers have been compacted up to depth of 30-40 m. The work also highlights the advantage of using non-intrusive geophysical methods to access success of compaction over large spread of area.

Nendza (2006) and Nendza et al. (2008) conducted 1g model tests with 1:3 scaled model vibrator. Accelerometers were installed on the model vibrator and pore water pressure sensors were installed in the soil. Tests were carried out in water saturated medium sand.

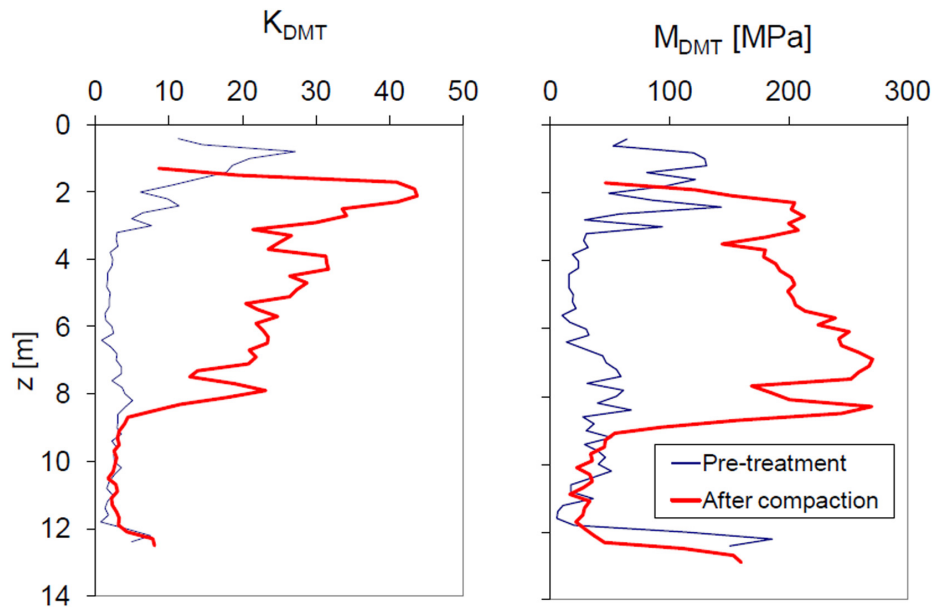


Figure 2.11: Increase in horizontal stress index (left) and the constrained modulus (right) after deep vibratory compaction (Balachowski and Kurek, 2016)

Effect of compaction frequency, eccentric vibrator mass, vibration depth and vibrator amplitude on extent and degree of compaction was assessed. It was found that frequency of vibration and vibrator amplitude had a significant influence on the success of compaction.

2.3 Analytical and Numerical Models of Deep Vibratory Compaction

Extensive field trials demand additional financial and temporal resources. Considering the lack of such trials, numerical simulations can help one understand the various physical processes the soil undergoes during compaction. Also field measurements alone cannot provide sufficient information to optimise the process. Deep vibratory compaction is a complex process making its numerical simulation a tough goal to achieve. Effort has been made in the past few decades to develop analytical and numerical models to better understand vibrator soil interaction and to estimate extent and degree of compaction. Fellin (2000) investigated deep vibratory compaction using analytical and numerical models. Analytical solutions were derived for movement of vibrator in air and soil. The developed analogy was used to develop theoretical relationship between vibrator movement and soil parameters using principles of soil dynamics. Analytical solutions developed by Wolf (1994) for vibrations in foundation resting on soil and Makris and Gazetas (1993) for pile vibrations were used to back calculate soil parameters on the basis of vibrator movement. The work was successful in demonstrating that theoretically vibrator movement in terms of amplitude and phase angle (phase difference between movement of tip of vibrator and

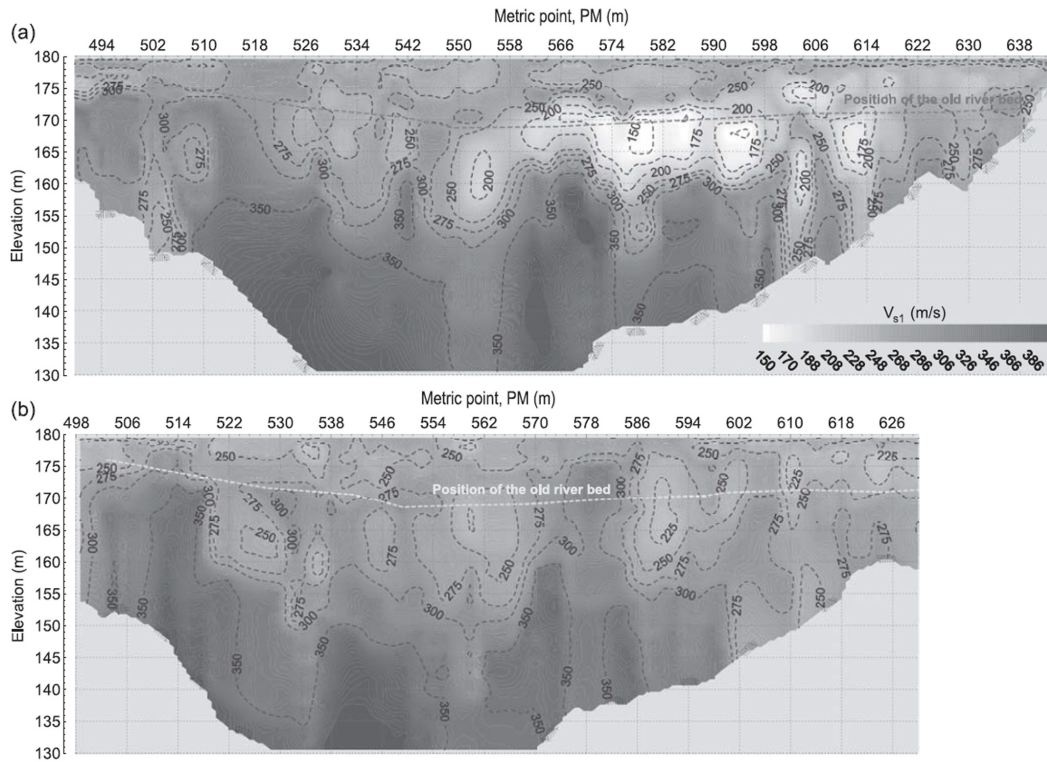


Figure 2.12: Shear wave velocity profiles over vertical planes at foundation level of Péribonka dam before and after compaction (Karray et al., 2010)

eccentric mass) can be associated with progress of compaction and may serve as an on-line compaction control parameter. Fellin (2000) also developed a 2D hypoplastic model to study the change in soil density by an expanding cylindrical cavity model and wave propagation in shock capturing numerical model. The vibrator's frequency of rotation, also referred to as compaction frequency, was found to be an important parameter controlling the degree and radial extend of compaction (Fellin, 2000). The increase in soil density around compaction point was studied as part of the numerical simulations. Fellin (2000) suggested that in order to better understand factors affecting deep vibratory compaction both large scale experimental studies and numerical simulations are necessary. On the basis of above described theoretical investigations, Fellin et al. (2000) and Fellin et al. (2003) carried out large-scale experiments to develop an on-line control system based on vibrator movement. Fellin (2000) suggested that vibrator frequency played an important role in optimizing deep vibratory compaction. Following this Wehr (2005) conducted theoretical analyses on the basis of models developed by Fellin (2000) in order to determine an optimised compaction frequency for deep vibratory compaction. Wehr (2005) found that soil underwent best compaction when the soil-vibrator system was in resonance. In order to be able to identify resonance frequency, the vibroflot should be equipped to operate at various frequencies in field.

Kessler et al. (2006) simulated the strain paths during deep vibratory compaction in various finite element models using an elastic material law as depicted in Figure 2.13. Detailed 3D numerical simulation of deep vibratory compaction is extremely demanding in terms of

modelling and computational costs. Hence, Kessler et al. (2006) simulated deep vibratory compaction using an axial-symmetric thin planar soil section, and compared the outcomes to a full 3D model. The axial-symmetric model could not capture shear distortion of soil which substantially contributes to compaction. The disc-shaped 3D model was suggested as a reasonable simplification.

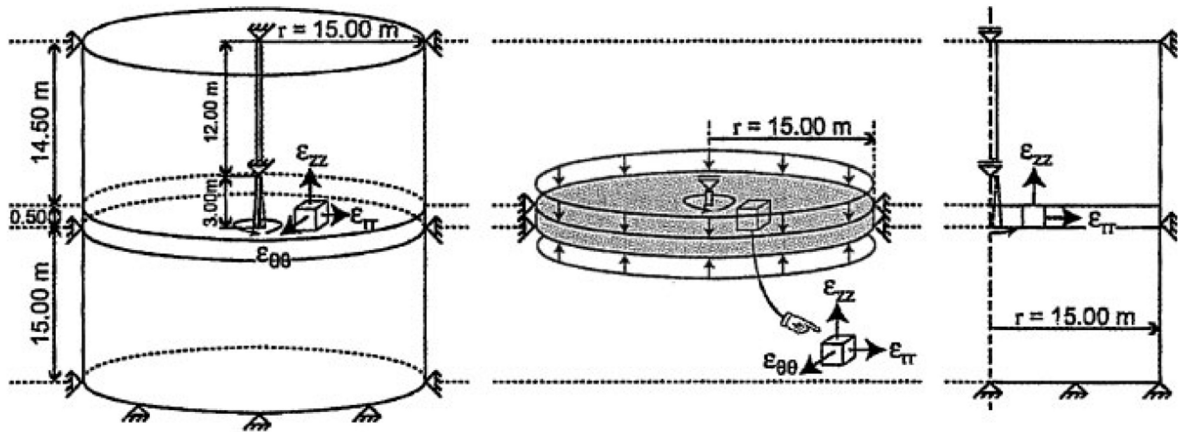


Figure 2.13: Types of FE models for deep vibratory compaction: Full 3D model (left), 3D disc-shaped soil section (middle) and axisymmetric model (right) after Kessler et al. (2006)

Cudmani et al. (2006) presented a procedure for the estimation of the grid spacing. They used a hypoplastic infinite cylindrical cavity soil model with a prescribed radial stress component. For a given set of machine parameters the model predicted density changes at different radial distances from the vibrator. The predicted densities could be converted into cone penetration resistance that are expected after the compaction. The required grid spacing could be evaluated by comparing the predicted cone resistances with the specified values.

It has been highlighted that shear strain amplitude plays an important role in determining extent of compaction. In order to capture the effect of shear strain amplitude, Arnold and Herle (2009) determined strain paths on the basis of elastic finite element (FE) analysis. Strain amplitude-dependent stiffness was determined at varying radial distance from the vibrator by carrying out subsequent iterations. Following that the obtained strain paths were used to control single element simulations using hypoplasticity with intergranular strains. The calculated compaction profiles showed three zones as depicted in Figure 2.14. The work concluded that the hypoplastic constitutive model with intergranular strain was capable to capture compaction effect.

Schmitter and Adam (2017) attempted to study the effect of frequency on compaction using a disc-shaped 3D model under elastic regime. Variation of machine parameters such as amplitude of vibrator and phase angle between vibrator tip and eccentric mass with time was predicted (Figure 2.15). It can be observed that vibrator amplitude is not proportional to applied frequency and peaks around 42 Hz. Maximisation of vibrator amplitude hints at resonance and existence of optimal frequency of compaction. The outcomes of numerical

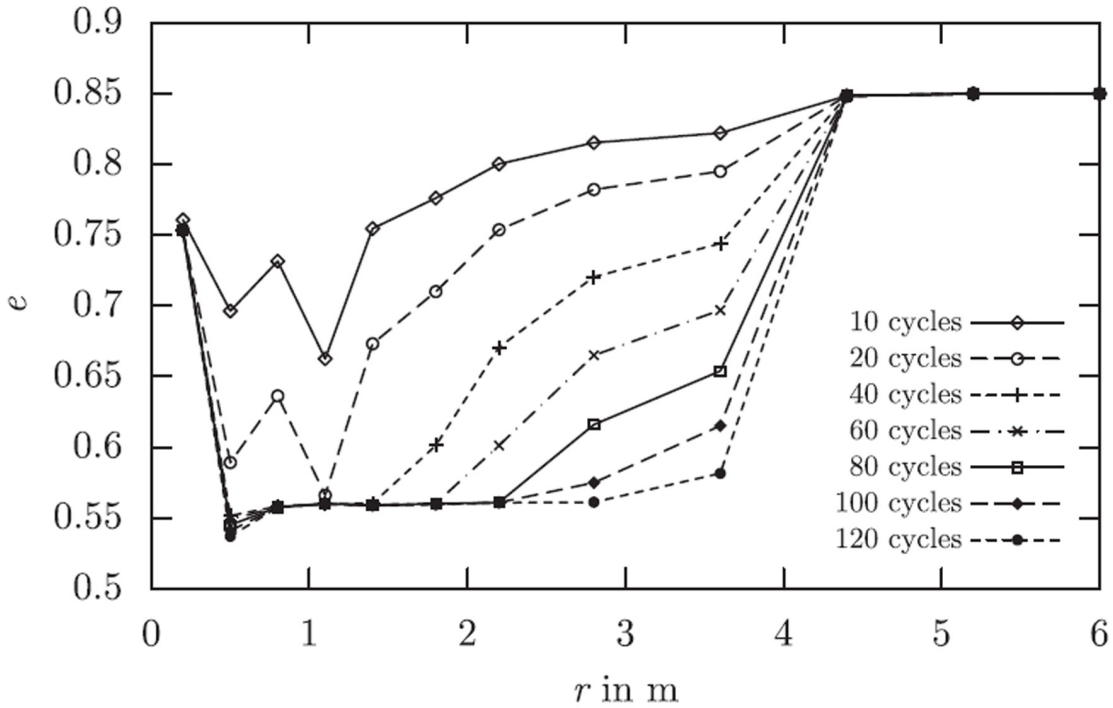


Figure 2.14: Evolution of void ratio along radial distance from the vibrator after deep vibratory compaction after Arnold and Herle (2009)

simulations were imported to a lumped parameter model composed of two discrete spring-dashpot systems and a lumped mass subjected to a rotating force. The analytical model was then used to predict variation in soil parameters with time. A 3D model based on

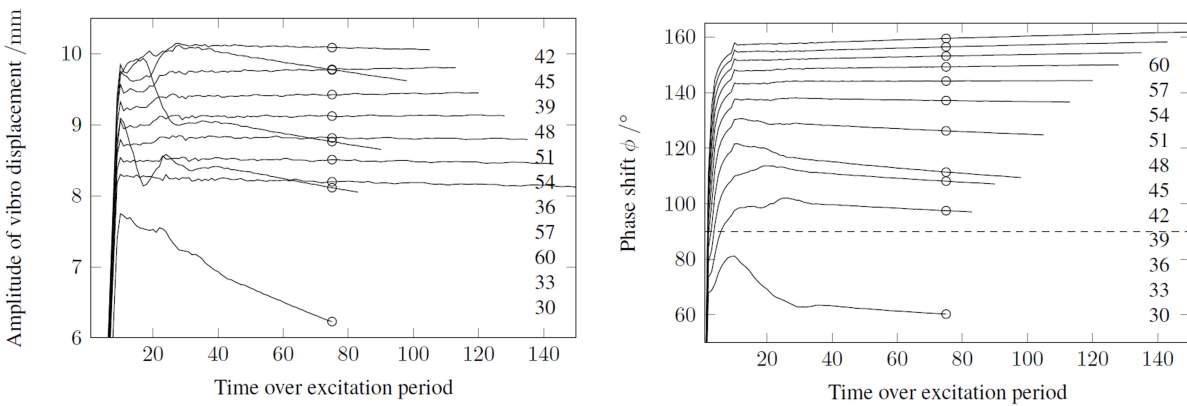


Figure 2.15: Variation of vibrator amplitude (left) and phase angle (right) with compaction time as obtained from numerical simulations (Schmitter and Adam, 2017)

the Coupled Eulerian-Lagrangian (CEL) approach was developed to model deep vibratory compaction as classical finite element (FE) model suffered from excessive deformations limiting simulation of deep vibratory compaction to only few cycles of loading (Henke et al., 2012). Parametric study was conducted to understand the effect of frequency, centrifugal force and amplitude of the vibrator on the efficiency of compaction (Henke et al., 2012). Soil was modelled as an Eulerian domain with hypoplastic constitutive model according to Wolffersdorff (1996) with the extension of intergranular strains according to Niemunis and Herle (1997). The vibrator was modelled as a simplified cylinder and frequencies/centrifugal forces corresponding to recommendations by Fellin (2000) were applied. Radius of influence of about 1.5 to 2 m was observed way above the range observed by Fellin (2000) (0.60 m to 1.70 m). Parametric studies showed that vibration frequency had a significant influence on the compaction range. Compaction at lower frequency lead to better spread as shear waves with a larger wavelength have a larger radius of influence (Mahutka et al., 2007). Henke et al. (2012) strongly recommend that the numerical framework needs to be validated against field measurements.

Grabe et al. (2015) and Heins et al. (2015) carried out further numerical investigations with CEL model and compared the results of the same to a classical FE model for saturated sand. In the CEL model the impact force could be directly applied to the tip of the vibrator. On the other hand, in the FE model the impact force had to be applied to soil segments at varying degree which would be in contact with vibrator. Figure 2.16 compares void ratio around vibrator after compaction for both the numerical models and it can be observed that both yield similar results for dry soil. In saturated soil, the compaction effect is marginal (Figure 2.17) and this could be due to the development of excess pore water pressure that hinder soil rearrangement (Heins et al., 2015). Heins et al. (2015) found the CEL framework to be better as compared to classical FE model as it could simulate more cycles of loading without issue of excessive deformations.

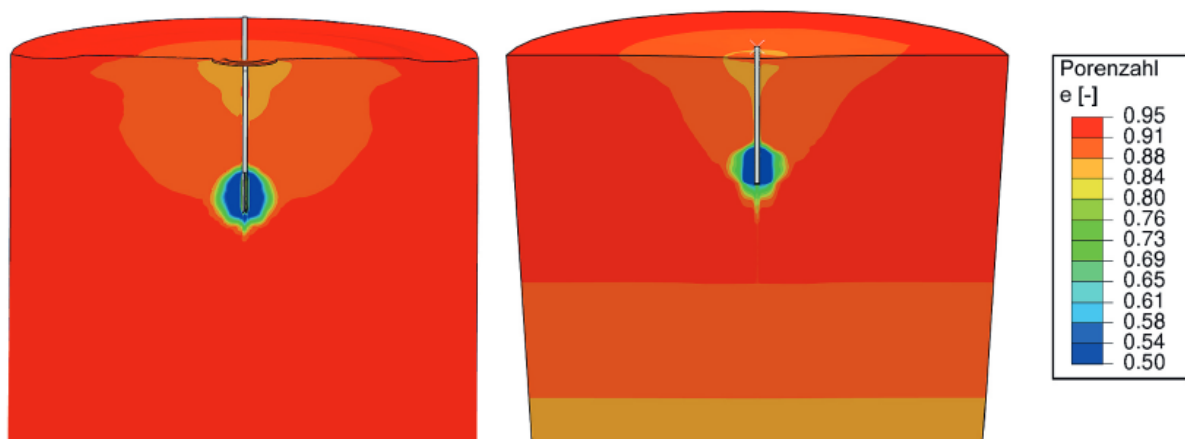


Figure 2.16: Comparison of void ratio distribution as obtained from CEL model (left) Classical FE model (right) (Heins et al., 2015)

Chmelnizkij et al. (2017) compared results from two different numerical frameworks based on CEL and Material Point Method (MPM). Soil was modelled by hypoplastic model

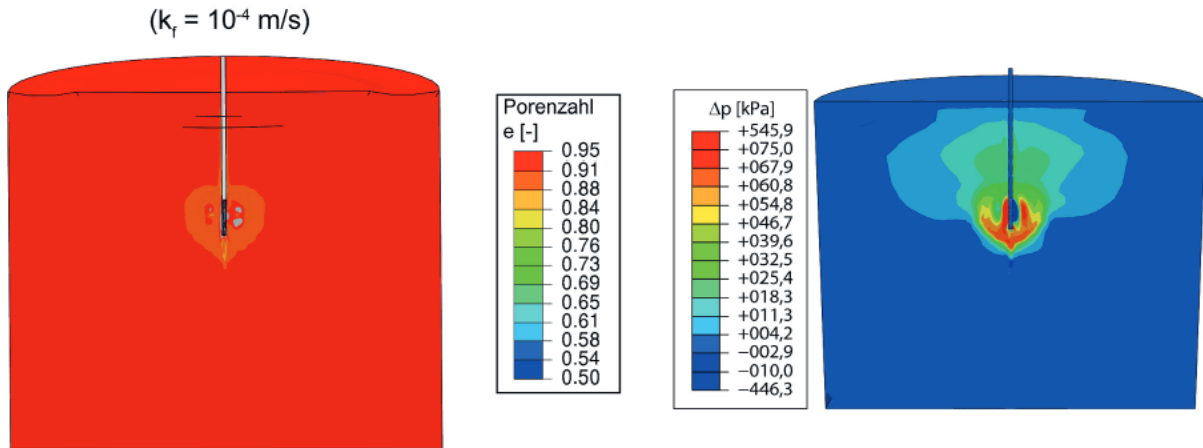


Figure 2.17: Void ratio distribution (left) and excess pore water pressure (right) in saturated soil as per results from CEL simulations (Heins et al., 2015)

with intergranular strain extension. Figure 2.18 compares void ratio contours from both the frameworks and it can be observed that both predict zone of compaction around the vibrator. The variation can be attributed to difference in discretization.

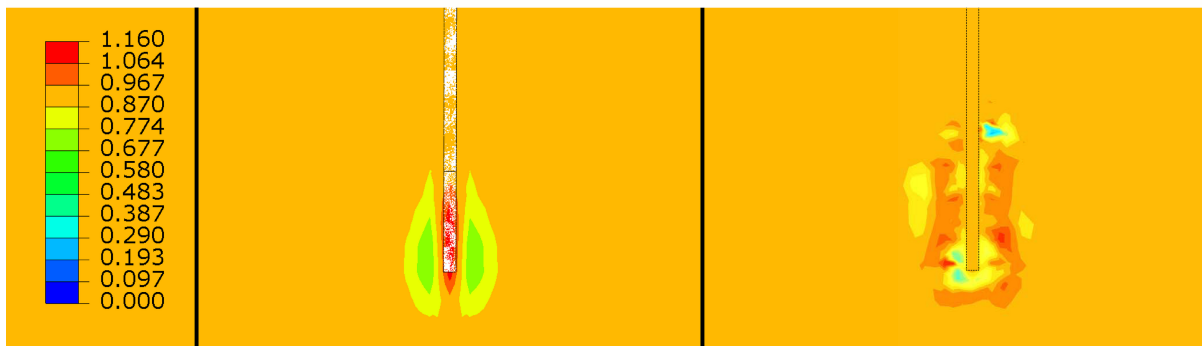


Figure 2.18: Comparison of void ratio distribution around vibrator after 20 load cycles between CEL model (left) MPM model (right) (Chmelnizkij et al., 2017)

Triantafyllidis and Kimmig (2019) developed an analytical and numerical model to estimate spacing of compaction points in a grid in order to attain a predefined post compaction density. They used a disc-shaped 3D hypoplastic model to calculate total strain amplitude during four cycles of deep vibratory compaction. The estimated total strain was then used as input for a simplified high cycle accumulation model to predict the relative density changes due to a large number of compaction cycles. The method can be used on construction sites where amplitude of vibrations in soil around compaction point can be used to estimate magnitude of densification. Figure 2.19 depicts the evolution of void ratio around vibrator with loading cycles as predicted by the high cycle accumulation model.

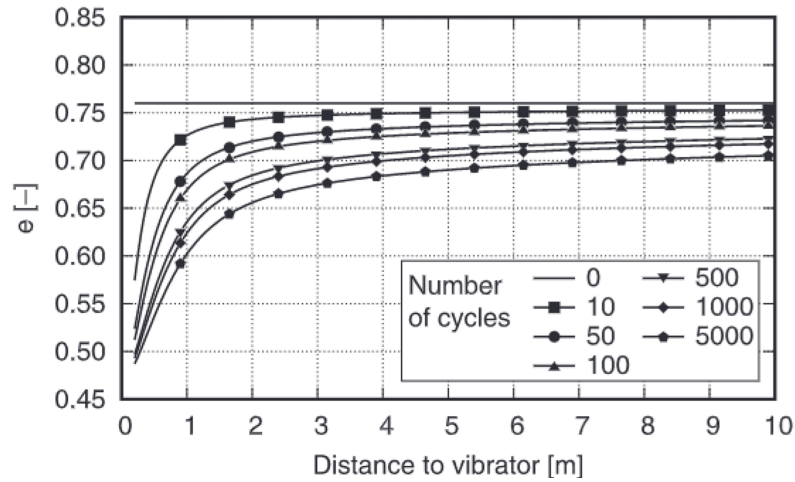


Figure 2.19: Development of void ratio around vibrator with increasing number of loading cycles as predicted by high cycle accumulation model (Triantafyllidis and Kimmig, 2019)

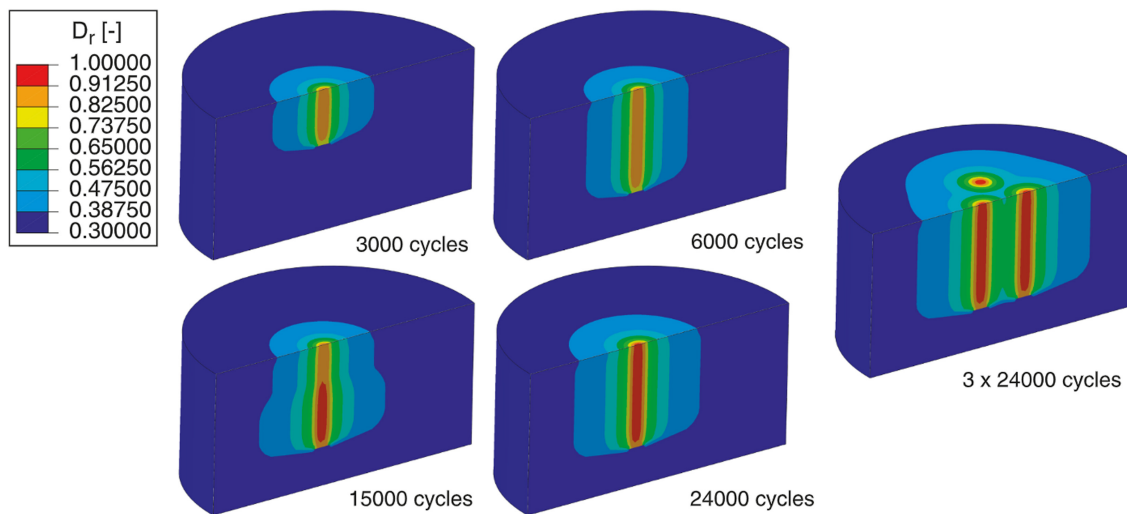


Figure 2.20: Prediction of relative density zone with loading cycles as per high cycle accumulation model in a triangular grid of 5 m spacing (Triantafyllidis and Kimmig, 2019)

The accumulation model was used to predict zone of compaction in terms of achieved relative density for a triangular compaction grid with three points at 5 m spacing (Figure 2.20).

2.4 On-line Compaction Control during Deep Vibratory Compaction

Recording change in relative density at the respective depth during compaction process is currently not possible with existing measurements techniques. In order to access success of compaction during compaction, indirect methods have been adopted. Various vibroflot parameters and process parameters that can be recorded and processed during compaction have been used to access compaction success. Some of them are as follows:

- Current consumed and oil pressure over time of the vibrator
- Quantity of filler material
- Time consumed per compaction point
- Total energy consumption per compression point

Industry has been using these parameters to infer the compression success. Density increase can be estimated from the amount of filler material used and magnitude of surface soil settlement before and after settlement (Fellin, 2000). But, the method is imprecise because density distribution in the soil is heterogeneous. As information from machine and process parameters is dubious, CPT measurements need to be carried out before and after compaction in order to access its success. But in certain scenarios development of excess pore water pressures in saturated soils may not lead to immediate densification which can be captured by CPT measurements. One has to make measurements over time in order to access compaction success and such wait time may not be feasible in all scenarios (Sondermann and Kirsch, 2017). Afifi and Woods (1971) and Wichtmann and Triantafyllidis (2005) found that gain in soil stiffness may last up to years due to various reasons such as improvement in macro-interlocking of soil grains, chemical cementation of grain contacts and biological causes. Also CPT measurements and other probing techniques can only be carried out at some spatial points and cannot capture compaction quality of huge compacted areas. It is also to be noted that all probing techniques or geophysical tests which can access success of compaction need to be carried out after compaction. If the carried out compaction does not lead to desired results, additional cost and time needs to be invested in order to design a new compaction methodology. All these reasons lead to the need to develop a reliable and scientifically supported on-line compaction control methodology which can access success of compaction during compaction itself. Fellin (2000) was first to identify variation of amplitude of vibrator with compaction and potential of it to be related to change in soil parameters. Based on Fellin (2000), Nendza (2006) tried to develop on-line control parameters on the basis of physical tests with model vibrator. Nendza (2006) developed model vibrator with accelerometers and a trigger. The trigger sent a block signal when the eccentric mass passed over it. The trigger was fixed to vibrator body, so the trigger signal could specify the position of the rotating eccentric mass at a specific point in time. Data from the orthogonal accelerometers were used to determine movement of the vibrator tip in time. The phase angle was determined as the angle between location of vibrator tip and eccentric mass at a particular instant of time. Figure

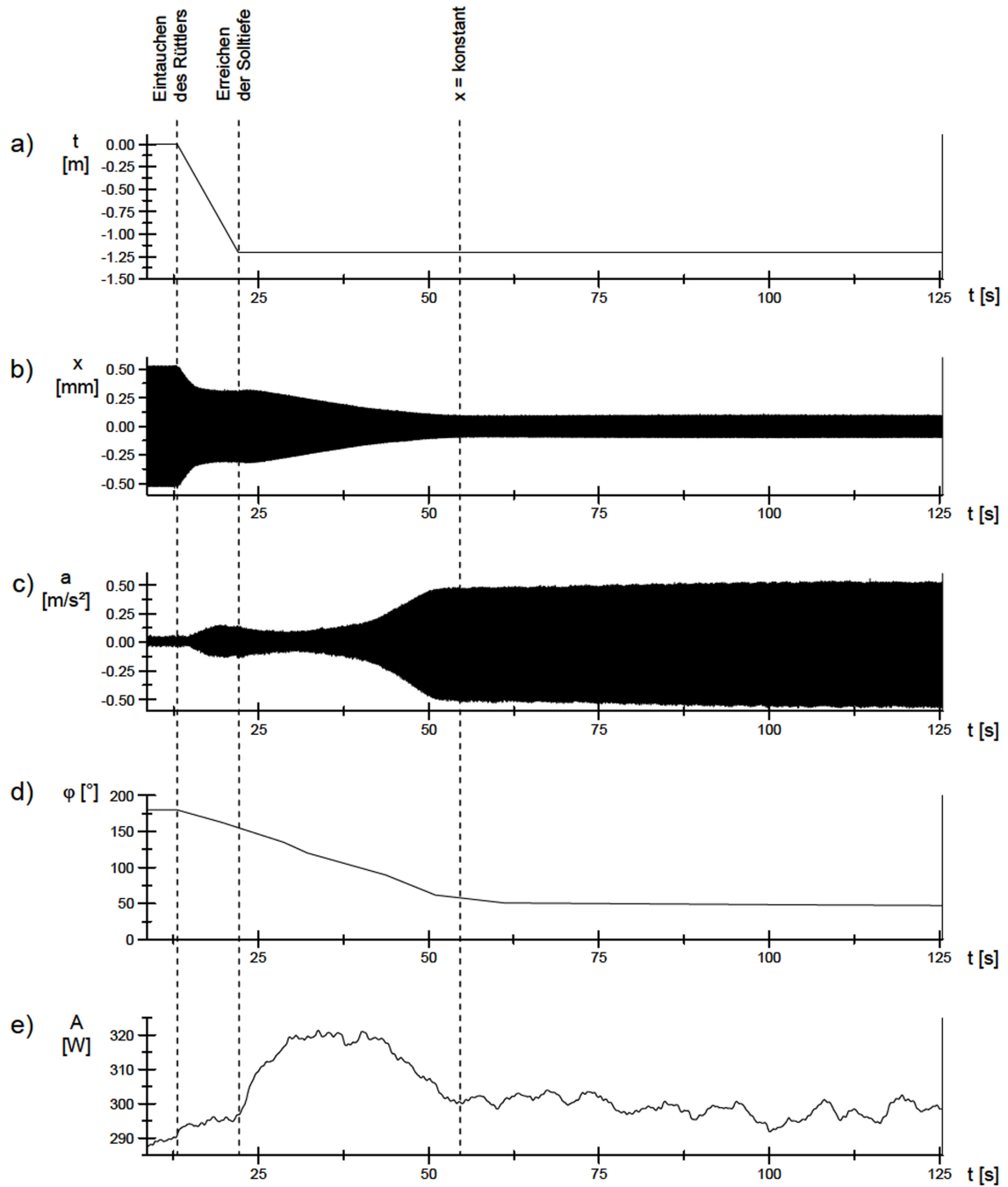


Figure 2.21: Variation of vibrator (a) depth (b) amplitude (c) acceleration (d) phase angle and (e) current consumed with compaction time in 1g model tests (Nendza, 2006)

2.21 depicts variation of depth, amplitude, phase angle and power consumed by vibrator with compaction time. Both amplitude and phase angle were found to decrease with

compaction time and eventually reached a constant value marking end of compaction. The amplitude was found to reach its limit value marginally before phase angle reached its limit value. Nendza (2006) also demonstrated how variation of relative density could be evaluated by calibration of measured values with complete knowledge of the soil parameters. The work found that the limit value of the amplitude could potentially be used as compaction termination criterion for on-line control. Massarsch and Fellenius (2005) suggested control of compaction frequency in order to facilitate better spread of vibrations eventually leading to efficient compaction. Geophones were installed on soil surface to record surface wave velocity at varying frequency. Figure 2.22 depicts the recorded particle vertical velocity at various frequencies. Soil is said to undergo best compaction when frequency is at resonance frequency of the soil-vibrator system. Resonance is marked by peak in the particle velocity diagram as shown in Figure 2.22. The suggested concept claims that best compaction occurs at resonance (15 Hz in this case) and measurement of particle velocity can be used as an on-line compaction control technique. Massarsch (2016) demonstrated that penetration speed of vibroflot into the soil also indirectly verifies compaction. Penetration speed is substantially lowered in compacted soil compared to non-compacted soil and this can be used as an indirect methodology to verify if soil compaction at a certain location in a compaction grid. Fellin et al. (2000) and Fellin et

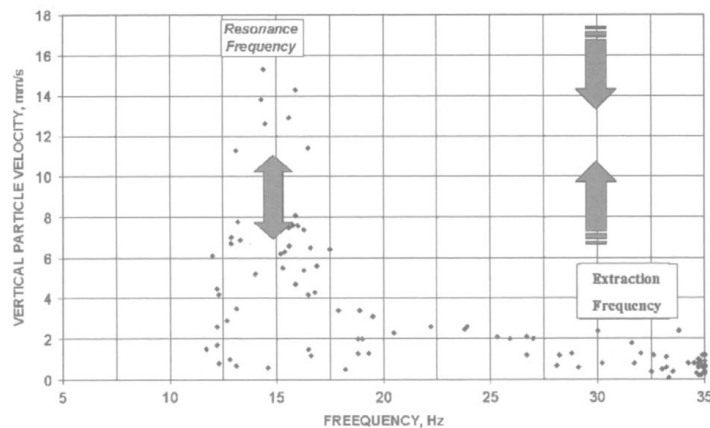


Figure 2.22: Particle velocity as recorded by geophone during deep vibratory compaction and penetration of vibroflot on field Massarsch and Fellenius (2005)

al. (2003) first identified displacement amplitude of the vibrator probe to be an effective on-line compaction control parameter and was used by Nagy (2019) and Nagy and Adam (2019) to optimise the deep vibratory compaction in gravel on the basis of field trials. According to Nagy (2019), the compression process is divided into two sections. At the beginning of compaction soil exhibits contracting behaviour. The grain structure of the soil is rearranged and void ratio reduces. This leads to more contact area between soil grains. After reaching a certain threshold the soil stops exhibiting contractive behaviour and tends to be more dilatant. The tendency to increase in volume is hindered by lateral constraints and leads to the development of high effective stress. Due to the increased effective stress, soil reaction stiffness also increases significantly. Increased soil stiffness substantially reduces vibrator amplitude and also alter phase angle of the vibrator. Nagy

(2019) suggested that shift from contractant to dilative behaviour marks completion of compaction. Figure 2.23 highlights the transition from contractant to dilatant behaviour by dashed line. It can be observed that the transition cannot be precisely captured by amplitude or phase angle behaviour. Therefore, Nagy (2019) suggested reaction stiffness to be used as an effective control parameter. Reaction stiffness can be calculated on the basis of vibrator amplitude and phase angle and is described in detail in Chapter 7.

2.5 Liquefaction Mitigation Potential of Deep Vibratory Compaction

Soil liquefaction is by definition a reduction in the shear strength and shear stiffness of the soil due to the increasing pore water pressure in saturated non-cohesive soils due to cyclical or transient loading (Kramer, 1996). Liquefaction leads to a state of almost zero effective stress in the grain structure thus converting the soil into a quasi-liquid state. According to Kramer (1996), the following boundary conditions must exist in order for a soil to liquefy:

- Saturated soil without cohesion
- Dynamic (cyclical or transient) loading
- Undrained conditions

Earthquakes often lead to soil liquefaction under appropriate boundary conditions. They lead to considerable permanent deformations in the liquefied soil and consequently structural damage. Idriss and Boulanger (2008), Kramer (1996), Seed and Idriss (1967) and Youd and Hoose (1976) have accounted for numerous cases of damage that have been caused due to soil liquefaction resulting from earthquakes.

In the past, efforts have been made to understand the liquefaction phenomenon on the basis of large-scale experiments and field measurements. Owing to the high cost of large-scale tests and lack of availability of field data coupled with recent advancement in the field of numerical modelling, a shift has been observed. The prediction of liquefaction triggering requires the use of a coupled stress-field analysis with a suitable elasto-plastic constitutive model (Taiebat et al., 2009). At a basic level, researchers have numerically modelled the free-field 1-D seismic response of saturated soils to predict propagation of accelerations, pore pressure generation, and resulting volumetric settlements (Ramirez et al., 2018). The liquefaction prediction capability of various constitutive models has previously been evaluated by comparing the simulation results to element level tests or centrifuge experimental results for saturated soils (Ramirez et al., 2018; Arulanandan and Scott, 1993; Taiebat et al., 2007; Kutter et al., 2015; Jeremić et al., 2008; Tasiopoulou et al., 2015; Shahir et al., 2012a). Research has noted that the choice of the constitutive model plays a critical role in capturing the soil response under seismic loading (Jeremić et al., 2008). The efficiency of the chosen model to capture changes in soil porosity and permeability during seismic event holds the key.

On the whole, loose granular soils with a high proportion of fines tend to liquefy under abrupt shear stress. This leads to the development of excessive pore water pressures and

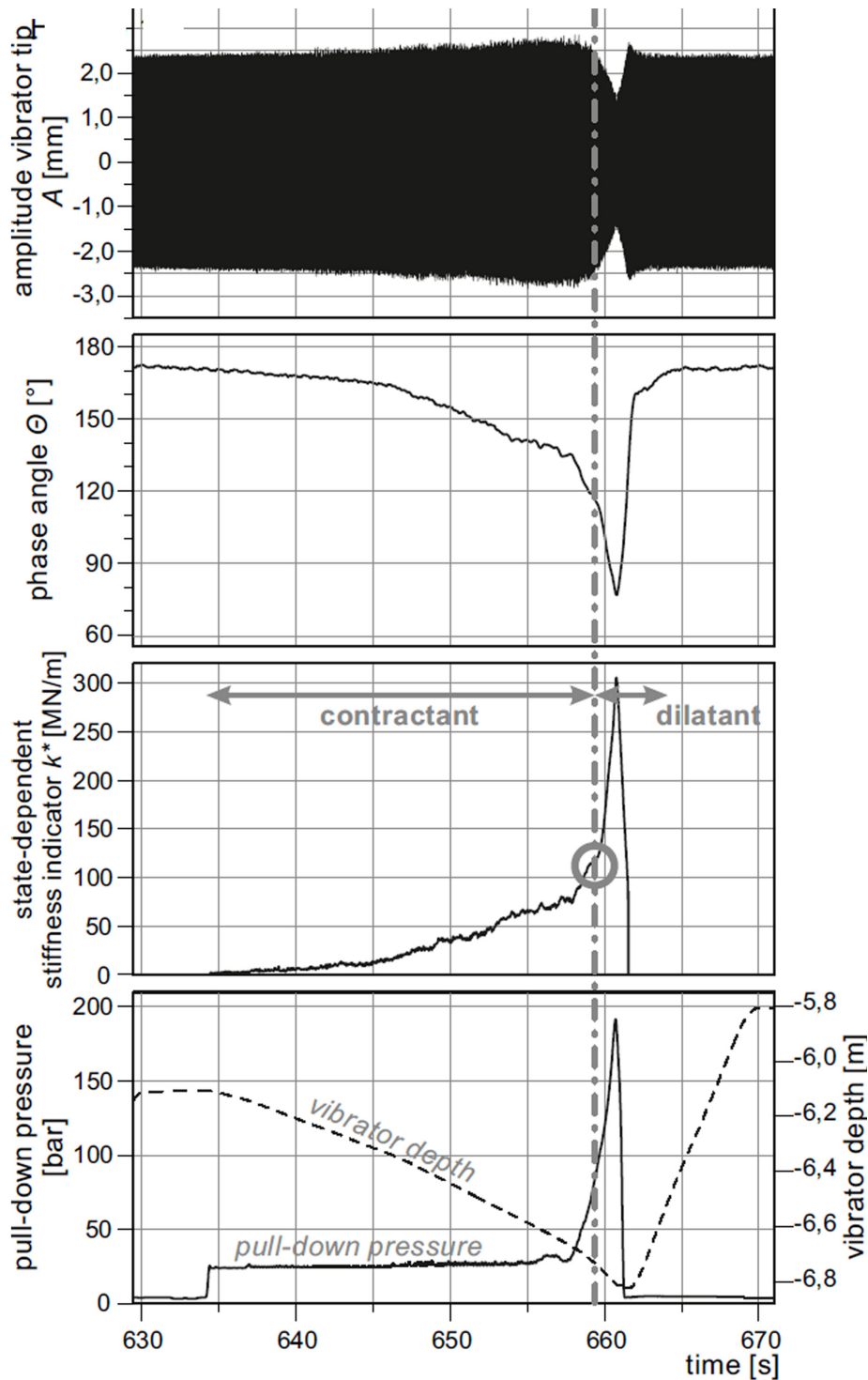


Figure 2.23: Variation of vibrator amplitude (top), phase angle (2nd from top), soil reaction stiffness (2nd from bottom) and depth/pressure (bottom) with time during compaction of granular soil on field (Nagy, 2019)

eventually may lead to complete loss of effective stresses. In such scenarios deep vibratory compaction can serve as an effective ground improvement technique to mitigate liquefac-

tion in loose granular materials with fines. Deep vibratory compaction increases relative density due to closer arrangement of soil grains leading to reduction in soil void ratio. Since, liquefaction potential depends highly on initial relative density of soil, compaction by deep vibratory compaction can nullify liquefaction potential of a loose granular soil deposit. The increased storage density in loose sand reduce the tendency of the soil to liquefy (Fellin, 2000). Massarsch and Fellenius (2002) state that increase in horizontal stress state after deep vibratory compaction also aids in improving the soils liquefaction potential. Iai et al. (1994) and Yasuda et al. (2006) documented numerous case studies from Japan where vibro compacted soil delivered better seismic performance compared to unimproved sites nearby.

It is often difficult to obtained undisturbed sample of granular material from field in order to determine their liquefaction potential. Hence, Cyclic Resistance Ratio (CRR) (Figure 2.24) is determined based on Standard Penetration Test (SPT) and CPT and is used to determine the liquefaction potential of saturated sand under consideration before and after deep vibratory compaction (Kirsch and Kirsch, 2017).

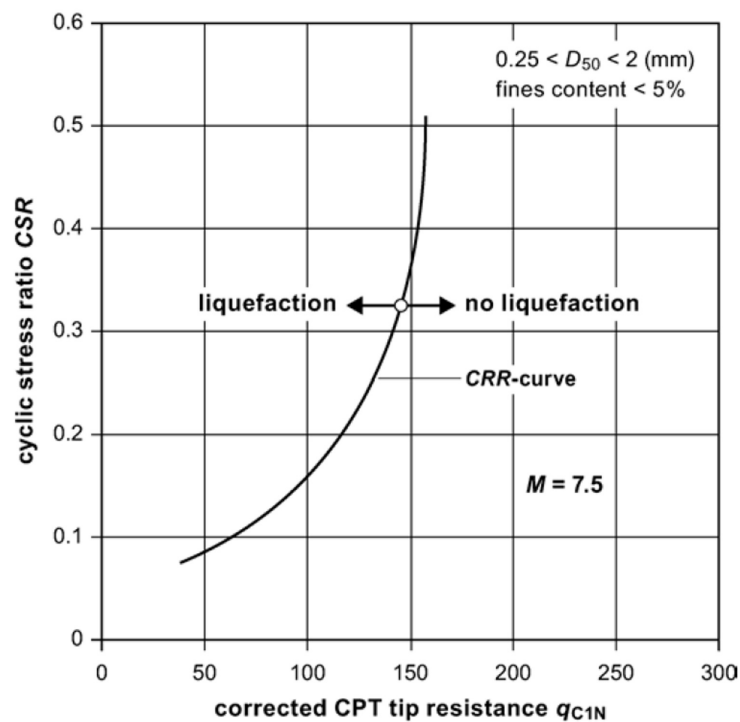
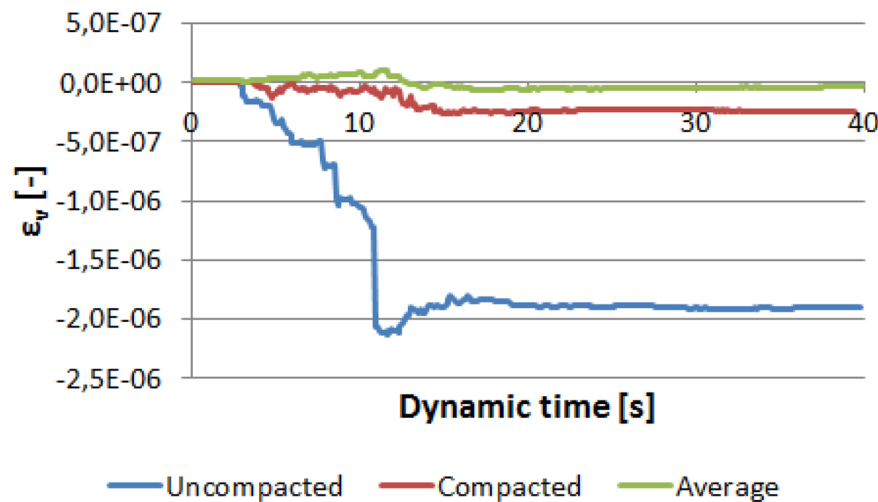


Figure 2.24: Identification of liquefaction potential of saturated soils based on CRR from CPT data (Kirsch and Kirsch, 2017)

Massarsch and Fellenius (2005) suggest that the vibroflot itself can be used as a tool to judge if compaction has reduced liquefaction potential. In the first compaction pass the saturated sand prone to liquefaction would liquefy due to the vibrations. But once the first pass is completed, the same soil does not undergo liquefaction in the second compaction pass due to densification indicating that the soil has become more resistant to liquefaction. Vranckx (2017) conducted seismic analysis on plane strain model in FE domain with sat-

urated sand before and after deep vibratory compaction. The actual compaction by deep vibratory compaction was not simulated but change in relative density after compaction was assumed and same was simulated. In order to take into account the heterogeneous densification by deep vibratory compaction, varying relative density over soil domain was assumed as per various compaction grid spacing. The seismic simulations were performed in PLAXIS commercial geotechnical software hence, were not able to capture realistic liquefaction. Instead compressive volumetric strain was considered as an indicator for liquefaction. Figure 2.25 depicts the volumetric strain before and after compaction for a grid spacing of 3.11 m and it is clearly evident that compaction leads to substantial reduction in compressive volumetric strains indicating betterment of liquefaction potential of the sand. Vranckx (2017) indicated that deep vibratory compaction may not be suitable to mitigate liquefaction in soils against earthquakes with Richter scale magnitudes of 7.5 or higher.



Depth 9 m, $x = 0$ m

Figure 2.25: Volumetric strain before and after deep vibratory compaction in saturated sand during seismic loading as obtained by simulations by Vranckx (2017)

Practising geotechnical engineers state that as fines content increase, the effectiveness of deep vibratory compaction to compact the soil reduces. It has been discussed earlier that researchers have proposed various maxima for permissible fines content in granular material to be compacted by deep vibratory compaction. The existence of fines becomes even more critical when deep vibratory compaction is performed to reduce liquefaction potential. The soil may be marginally compacted but may not really be safeguarded against liquefaction due to presence of fines, which remain unaffected due to compaction. This encourages development of a framework to identify if a particular soil under consideration can be benefited by deep vibratory compaction against liquefaction. Feasibility of deep vibratory compaction to serve as a liquefaction mitigation measure is mainly based on past field experience and field CPT/SPT trials in some cases, with uncertain seismic loading and soil conditions (Kirsch and Kirsch, 2017). Numerical simulations of deep vibratory compaction

and seismic analysis of saturated sand would help analyse the feasibility and effectiveness of this method for mitigating the liquefaction hazard and its consequences (Massarsch and Fellenius, 2002).

3 Research Questions and Objectives

The previous chapter discussed work that has been carried out by various researchers in the field of deep vibratory compaction over years. Holding that as base this chapter tries to enlist in brief the research gap that exists and draws motivation from it to frame the research questions which would be addressed in this work. The last half of the chapter would like to throw light on the basic methodology adopted in order to seek answers for the raised questions. This is followed by description of the outline of the thesis.

3.1 Research Gap

Deep vibratory compaction method is an established ground improvement technique for granular soils. This technique is used to improve the properties of loose to medium dense granular soils by compacting deep layers of the soil and therefore reducing settlements, increasing the vertical bearing capacity and aiding in liquefaction mitigation. The lack of analytical design methodology and dependence on field experience of past projects for design and to ascertain liquefaction mitigation potential inhibits the efficient use of deep vibratory compaction. Vibrator–soil interaction and factors affecting compaction hold the key to improving the method. Researchers over the years have tried to better understand physical processes involved and factors affecting deep vibratory compaction by means of field measurements, physical model tests and numerical simulations. Nonetheless their contributions also pave way for areas of improvement and highlight specific avenues that need to be better analysed and understood. In this section, the lacuna in the field of deep vibratory compaction would be put forward keeping in mind the already conducted research discussed in the previous chapter as a baseline.

CPT field measurements are commonly carried out before and after compaction to help analyse the efficiency of compaction. Data from the accelerometers in the vibrator and geophones installed on ground surface aid in understanding the vibrator–soil interaction; however, field measurements alone cannot provide sufficient information to optimise the process (Triantafyllidis and Kimmig, 2019). Field measurements are difficult to realize in homogenous loose sands, and there is a lack of adequate control of the test conditions in the field. Extensive field trials also demand additional financial and temporal resources.

Numerical simulations can help one understand the various physical processes the soil undergoes during compaction (Arnold and Herle, 2009). Attempts have been made to simulate the deep vibratory compaction process various numerical frameworks in the past. Unfortunately, none have been able to simulate the entire deep vibratory compaction process using an elasto-plastic constitutive model. Research to date has noted that the choice of the constitutive model and calibration of parameters play a critical role in capturing the soil response under dynamic loading. Constitutive model chosen to simulate

granular material behaviour under both deep vibratory compaction and seismic loading should be able to capture variation of void ratio with time as that would hold key to capturing the compaction effect. The numerical frameworks used till date have not been able to replicate the soil-vibrator interaction realistically and have suffered from excessive deformations. Numerical simulations have always been compared to a black box hence, making its validation extremely critical. Validation of numerical frameworks has not been achieved till date hence, questioning the whole ideology of using the concept of numerical simulations for optimising deep vibratory compaction.

The previous works have primarily focused on understanding the primary factors affecting deep vibratory compaction via numerical simulations but have not aimed at optimising the process using an on-line compaction control mechanism. Currently used on-line compaction control parameters such as power, current consumed and quantity of additional granular material are imprecise and fallible (Fellin, 2000). The real-time increase in density of soil with progress of compaction cannot be realised and hence identification of an effective online control parameter for the optimisation of compaction process is necessary. It is also to be ascertained if such online control would lead to better compaction. Fellin (2000), Nendza (2006), Nagy (2019) and Nagy and Adam (2019) have identified amplitude and calculated soil reaction stiffness as probable on-line compaction control parameters by means of field trials and model tests. But it has already been mentioned that field trials may not be feasible in all scenarios and also each soil to be compacted could react differently to the chosen on-line compaction control parameter.

The deep vibratory compaction method is gaining popularity as a liquefaction mitigation measure for granular materials. But feasibility of deep vibratory compaction to serve as a liquefaction mitigation measure is mainly based on past field experience which are very few as discussed in the previous chapter. Field measurements in the form of CPT are common in order to identify efficacy of deep vibratory compaction to mitigate liquefaction. But it is important to note that all the correlations based out of CPT are empirical hence, cannot fully predict performance of soil under realistic seismic loading. In the past, effort has been made to understand the liquefaction phenomenon on the basis of large-scale experiments and field measurements. Owing to the high cost of large-scale tests and lack of availability of field data coupled with recent advancement in the field of numerical modelling, a shift has been observed. But effort to understand liquefaction mitigation potential of deep vibratory compaction by means of numerical simulations has not been carried out.

3.2 Research Gap Motivated Objectives

Following enlisting of gaps in research, this section would like to bring forth some of the key objectives which this work would try to answer in its due course.

1. Research has shown that none out of field measurements, model tests and numerical simulations alone can completely help better understand factors affecting deep vibratory compaction. A package involving all three needs to be developed as it would be an ideal solution to further our existing knowledge about deep vibratory compaction.
2. Develop a numerical framework capable of simulating the entire deep vibratory compaction process as close as possible to reality. Preciseness of numerical framework majorly

depends on the choice of constitute model used to model soil behaviour. Hence, a well justified choice needs to be made with robustly calibrated material parameters. The developed numerical framework needs to be well validated before it can be used for further analysis.

3. Identify and analyse factors affecting deep vibratory compaction in depth other than the primary ones studied till date via model tests and numerical simulations.
4. Identify easily obtainable on-line compaction control parameter by means of model tests. Followed by verification with numerical simulations which can later be used to develop an optimisation routine based on the chosen control parameter to design compaction process in any sand under consideration.
5. Efficiency of deep vibratory compaction for liquefaction mitigation needs to be accessed by seismic numerical simulation of saturated sand before and after deep vibratory compaction. A coupled constitutive model based on the $u - p$ formulation needs to be identified in order to predict soil response of saturated sand.

3.3 Methodology

The research work outlined in this thesis is twofold, first being validation of numerical simulation of deep vibratory compaction based on the results of model tests and field measurements followed by parametric study and optimization of the technique. Second leg of the work aims at studying the effectiveness of deep vibratory compaction as liquefaction mitigation measure.

A combination of physical modelling, field measurements and numerical simulations was integrated to analyse deep vibratory compaction. Deep vibratory compaction was used to compact an open-cast mine deposit using a V48 vibrator. Field measurements including CPT and accelerometer data from the vibrator were used to study the process. Model tests under controlled lab conditions can provide insight into the various physical processes granular materials undergo during deep vibratory compaction. Hence, a model vibrator was fabricated to perform 1 g physical model tests. The effectiveness of compaction by model vibrator was evaluated in terms of CPT before and after compaction. Physically modelling at 1g can provide insight but cannot realistically capture stress state conditions. Considering this lacuna, numerical simulations can help one understand the various physical processes the soil undergoes during compaction. Numerical models developed to date have neither been able to realistically capture the entire compaction process nor have they been validated. The deep vibratory compaction technique was numerically simulated in Coupled Eulerian and Lagrangian (CEL) computational framework. Choice of hypoplastic model with intergranular strains to capture granular material behaviour was justified. Results from the model tests and field measurements were used to facilitate validation. The validation was followed by a parametric study in which the following were evaluated in terms of their effects on the extent and degree of compaction: frequency, relative density, shape of vibrator, spacing of compaction points, saturation of sand layer, nature of compaction process and type of sand. 1g model tests were used to identify on-line compaction control parameter. Compaction efficiency in model tests using an on-line control parameter were compared to ones without it. Once the feasibility of using amplitude as

control parameter was established at 1g model test level, the same was verified at realistic stress state conditions by means of numerical simulations. The same was used to design an optimization algorithm to control the compaction process, which would eventually lead to efficient and optimised compaction. This was followed by seismic numerical simulations of saturated sand compacted by deep vibratory compaction to analyse the feasibility and effectiveness of this method for mitigating the liquefaction hazard and its consequences. A coupled $u - p$ stress-field formulation analysis based on the hypoplastic constitutive model was used to model saturated soil behaviour. The seismic analysis of saturated sand was modelled under plane strain conditions using the Lagrangian approach. Results of a 1D seismic centrifuge test performed at the University of Colorado Boulder, USA on a layered saturated sand deposit was used to validate the seismic response under 1D shaking. The validated framework was used to analyse the efficiency of reduction in soil void ratio after deep vibratory compaction for liquefaction mitigation for different kinds of sands.

3.4 Flow of Thesis

The thesis is structured in line with the previously described research objectives and methodology. Chapter 1 and 2 have already highlighted the need for this study and also described what has been done in the past and what needs to be done.

Chapter 4 thoroughly and lucidly describes experimental and numerical methods adopted in this work ranging from field measurements to seismic numerical framework. It outlines the design and development of the scaled down model vibrator. It clearly describes the 1g physical test setup and the procedure followed to conduct the model tests. Details about the characterisation of granular soil used in the model tests is included. The chapters also details the deep vibratory compaction field measurements carried out in Cottbus, Germany including project details, type of vibroflot used, soil compacted, compaction methodology. CEL framework used to model deep vibratory compaction and classical FE plane strain model to perform seismic analysis are well described. Determination and calibration of material parameters of the hypoplastic model with intergranular strain for all the granular soils used in this work is also described. Special attention is paid to verify the performance of the coupled $u - p$ hypoplastic model to capture undrained soil behaviour under cyclic loading.

Chapter 5 firstly compares the efficiency of CEL framework as compared to classical FE framework and enlists pros and cons of each. This is followed by validation of the CEL framework against field measurements and 1g model test results.

Following validation of the CEL framework, Chapter 6 describes in detail the parametric study performed to understand the effect of frequency, relative density, type of granular material, shape of vibrator, nature of compaction process, spacing and type of compaction grid and soil saturation/permeability on deep vibratory compaction.

Chapter 7 identifies an on-line compaction control parameter by means of 1g model tests and tries to quantify its efficiency in improvising and optimising compaction. Following this the validity of the control parameter is verified at realistic stress state conditions via numerical simulations. Details regarding development of an optimisation routine which can control simulations on the basis of identified control parameter are included.

Chapter 8, the last leg of the thesis discusses the liquefaction mitigation efficacy of deep vibratory compaction by means of numerical simulation results. It highlights the suitability of deep vibratory compaction to eradicate liquefaction in certain kinds of granular soils. It also identifies certain kind of soils where this method may not be suitable to completely eradicate liquefaction.

Chapter 9 presents the major findings of the thesis in a nut shell and also presents perspective to further this work in order to be able to create an impactful deliverable for the industry.

4 Principles of Experimental and Numerical Methods

The research work involved 1g physical modelling, field measurements and numerical simulations. The chapter describes in detail the principles and methodology adopted to develop and execute the aforementioned tasks.

4.1 1g Physical modelling

1g model tests were conducted using an in-house fabricated mini deep vibratory compactor under controlled conditions on a granular material. The tests were conducted at different frequencies of vibration to analyse the effect of the same on the degree and extent of compaction. In order to access the success of compaction, CPT tests are performed on the sand before and after compaction.

4.1.1 Fabrication of model vibrator

The mini vibrator design is based on the S-vibrator commonly used for deep vibratory compaction. The design of the model vibrator was based on patents by Bilfinger and Berger Bauktiengesellschaft (1982), Köcher (2000), Köcher (2001), Berg and Köcher (2003), and Berg and Köcher (2009). The dimensions of the mini vibrator were to be scaled down as per the available test tank and accordingly it was decided for the vibrator to have a maximum diameter of 0.04 m. The other dimensions of the mini vibrator were to be scaled down accordingly. The scaling laws proposed by Wood (2004) were used in this work. The linear dimensions of the vibrator were scaled by a factor of $\lambda = 13.15$. The mini vibrator consisted of a steel tube with a diameter of 0.038 m and a length of 0.34 m, which was pin jointed to a stay tube of a similar diameter and a length of 0.24 m.

It can be observed Figure 4.1 that the vibrator had a pointed tip and wings at the bottom, to aid penetration into the soil. The vibrator housed an eccentric mass made of brass weighing 0.675 kg. The eccentric mass maintains a constant eccentricity of 7.213 mm from the central vertical axis of the vibrator. Patent filed by Berg and Köcher (2009) was used as basis for the design of the eccentric mass. The mass and eccentricity was chosen so as that the centrifugal force created by the rotating mass maintains scaling factor of $\lambda = 13.15$.

It is common amongst real-life vibrators also to have a fixed mass and eccentricity. The mass was connected to a motor through an internal shaft. The vibroflot typically functions between 15 and 60 Hz (Massarsch and Fellenius, 2005). Hence, an EC-max 30 motor from Maxon was chosen that could be operated in the working range of 10 Hz to 66 Hz. An

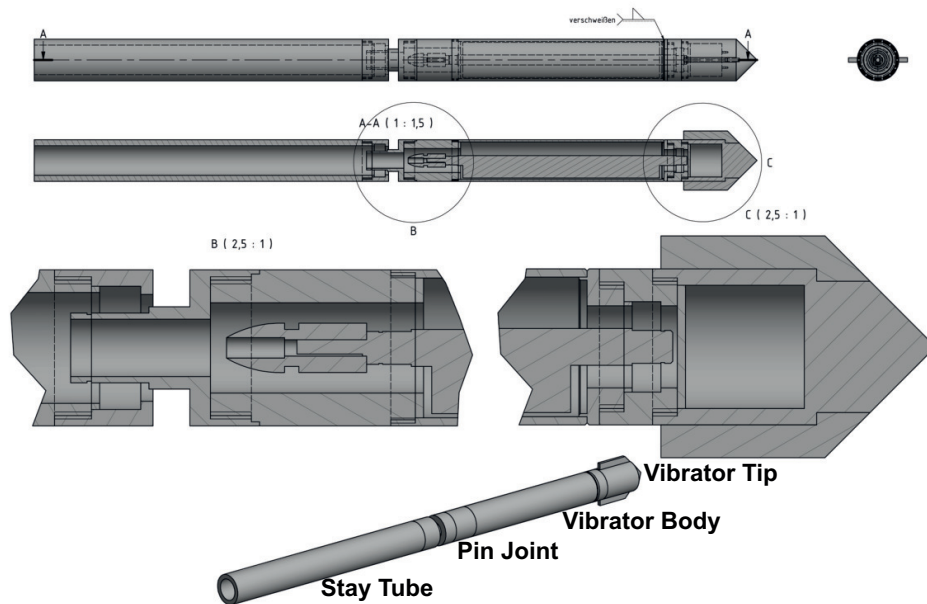


Figure 4.1: A segment of AutoCAD design displaying the model vibrator used in 1g model tests

accelerometer was installed at the tip of the vibrator to record the acceleration of the vibrator during operation. Figure 4.2 depicts the fabricated model vibrator with various components. The detailed design drawings of the vibrator are attached in Appendix A.

4.1.2 Experimental Set up

The tests were conducted under 1g stress state conditions. To reduce hydro-mechanical errors, tests were conducted under dry conditions, rather than in saturated sands where time scaling would play an important role. Tests were conducted in a steel cylindrical test tank. The test tank measured 1 m in diameter and 1.1 m in height, as shown in Figure 4.3. The test tank could be moved horizontally over the tracks as shown in Figure 4.3. The test frame consisted of a motor-controlled connection rig that could be connected to the cone penetrometer and vibrator. The rig could be controlled by a motor to move up and down at required rate. The test stand was equipped with an automated sand filling system. The test tank is filled with sand from a secondary overhead container. The sand trickled from the overhead container through a funnel (hard plastic tube) into the test tank. The overhead tank could be moved vertically (up/down) at a controlled rate, while the sand was deposited from the overhead tank into the test tank. The rate of movement of the overhead tank was controlled to ensure that sand of a fairly uniform density was deposited in the test tank.

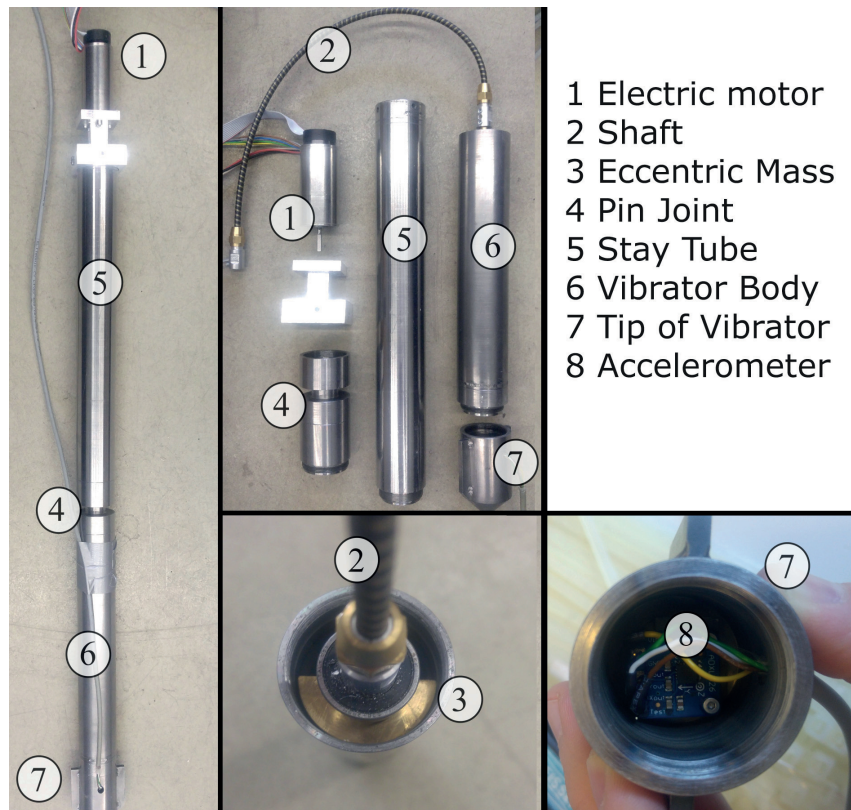


Figure 4.2: Fabricated model vibrator enlisting its various components

4.1.3 Granular Material

Hamburger sand was used as the granular media in the 1g model tests. The Hamburg sand is a medium-sized coarse sand. Most of the grains consist of quartz (80%) and low proportion of feldspar. In addition, it visually showed remnants of lime and heavy minerals. The grain size of the sand varied between 0.4 mm and 1 mm, which was confirmed by sieve analysis. The grain size distribution of Hamburger sand is as depicted in Figure 4.4 was determined as per DIN 18123 (1996). The grain density (ρ_s) was determined to be 2.64 g/cm^3 determined. The maximum and minimum number void ratio was determined according to DIN 18136 and tabulated in Table 4.1. The other important basic physical properties are as enlisted in Table 4.1. The detailed test results can be found in Appendix B. The suitability of the sand for compaction using the deep vibratory compaction method was ascertained based on the grain size distribution determined by Mitchell (1982).

4.1.4 Methodology

Trials were made to determine the rate at which the storage tank should be raised to have a uniform loose sand deposit. Once the rate was identified, the same procedure was used to deposit the sand in the tank for all tests to avoid discrepancies. Sand was deposited until a depth of 0.1 m below the top of the tank, at an average relative density of 0.2 for all the tests unless otherwise stated. The process of compaction using the model

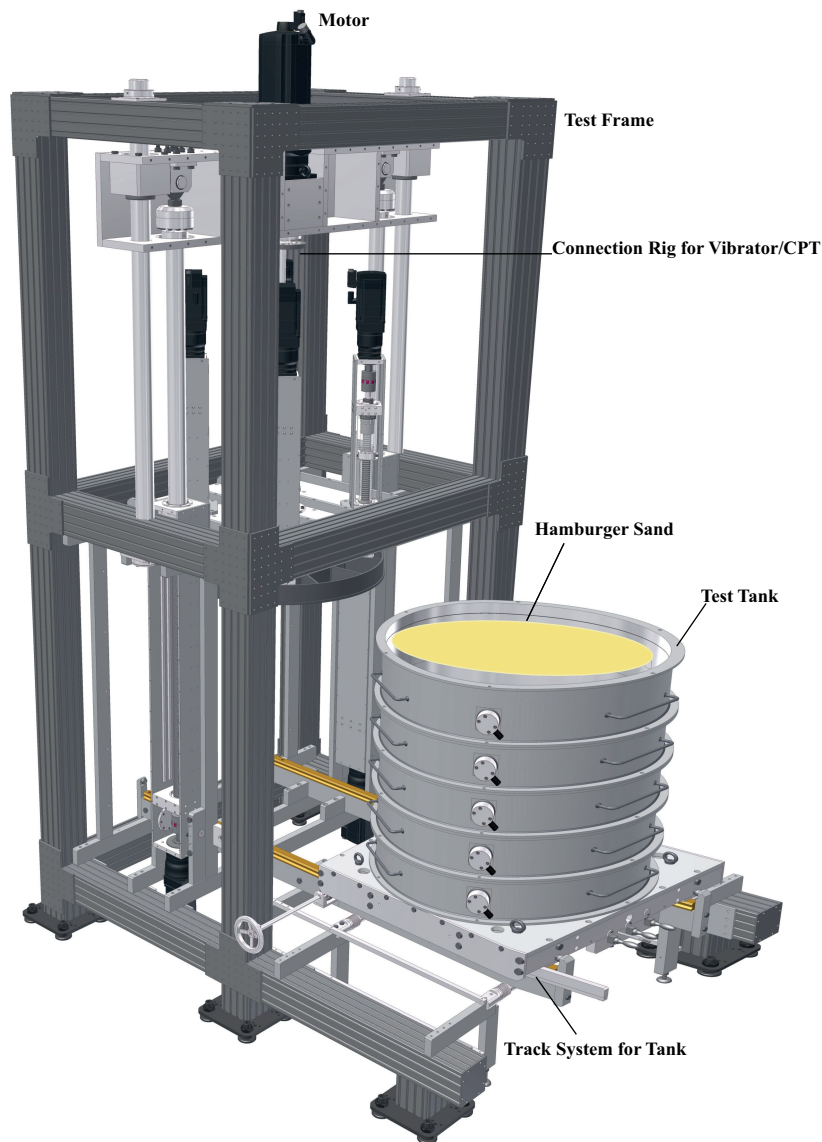


Figure 4.3: Schematic representation of 1g model test tank with various parts

vibrator involved two primary processes. First, the vibrator penetrated into the sand and second, the vibrator produced horizontal oscillations at the required depth. The vibrator is connected to the connection rig and is driven vertically down into the sand in the test tank. The penetration of the vibrator into the granular material layer is normally executed at higher frequencies (Massarsch and Fellenius, 2005). Hence, in all the tests, the vibrator penetrated into the sand at a frequency of 45 Hz, followed by compaction at the required depth at different frequencies. It should be noted that no water pressure was used to aid the penetration of the vibrator into the sand, unlike real-field conditions. Tests were conducted at compaction frequencies of 15, 30, 45 and 60 Hz. This range was chosen in accordance with the frequency range used for deep vibratory compaction in the field. The

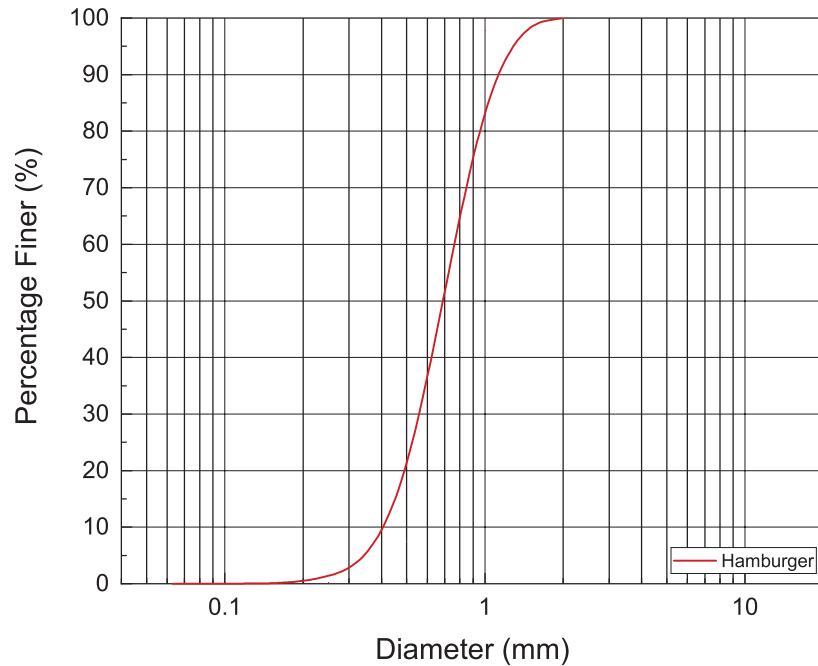


Figure 4.4: Grain size distribution of Hamburger sand used in 1g model tests and numerical simulations

model vibrator was penetrated into the sand layer at the centre of the test tank to a depth of 35 cm from the top of the sand layer. In certain tests compaction was carried out at two depths of 50 and 25 cm from the top of the tank. After reaching the required depth, the frequency of the compactor was set to the required compaction frequency and was vibrated for a time period of 30 s. It was expected that the operational frequency of the vibrator during the compaction process would be different than the set target value due to resistance from the sand. The operational frequency and the acceleration of the tip of the vibrator were recorded through the vibrator motor and installed accelerometer, respectively. The operational frequency was adjusted until the target frequency was reached during the process of compaction. After compaction, the vibrator was withdrawn at a frequency of 45 Hz. A geophone was installed at a radial distance of 250 mm from the centre of the tank to record the ground vibrations during compaction. CPTs were performed before and after compaction. Mini CPT with a diameter of 16 mm was mounted on the test frame rig and driven into the sand at a rate of 20 mm/s. CPT with a cone area of 2 cm² was used to substantially reduce size and boundary effects. CPT results were recorded at the centre of the compaction point and at radial distances of 70 mm, 140 mm and 250 mm from the centre. The CPT was conducted before compaction in order to ensure the presence of a fairly homogeneous sand fill in the test tank.

4.2 Deep Vibratory Compaction: Field Trials

Deep vibratory compaction was used to compact an open-cast mine deposit using a V48 vibrator. Field measurements including CPT and accelerometer data from the vibrator

Table 4.1: Basic physical properties of Hamburger sand used in 1g model tests and numerical simulations

Property	Value
Gradation	Poor
e_{\min}	0.526
e_{\max}	0.813
Friction Angle	32°
Density max	1.736 kg/m^3
Density min	1.462 kg/m^3
Particle Size	0.4 - 1 mm
D_{10}	0.51 mm
C_u	1.47

were used to study the process and validate the numerical framework.

4.2.1 Project Description



Figure 4.5: Deep vibratory compaction in action in test field at Cottbus, Germany (GMB GmbH, 2017b)

At the end of the coal mining in the Cottbus-Nord opencast mine in December in 2015, it was decided to develop the area as Germany's largest artificial lake called as Cottbus Baltic Sea. The area around the lake was planned to be compacted by deep vibratory compaction. Deep vibratory compaction was chosen to compact the residual granular material called as Kippen sand, in order to create dense and strong soil strata. The compacted surrounding would provide sufficient support to the artificial lake. Huge areas could be compacted

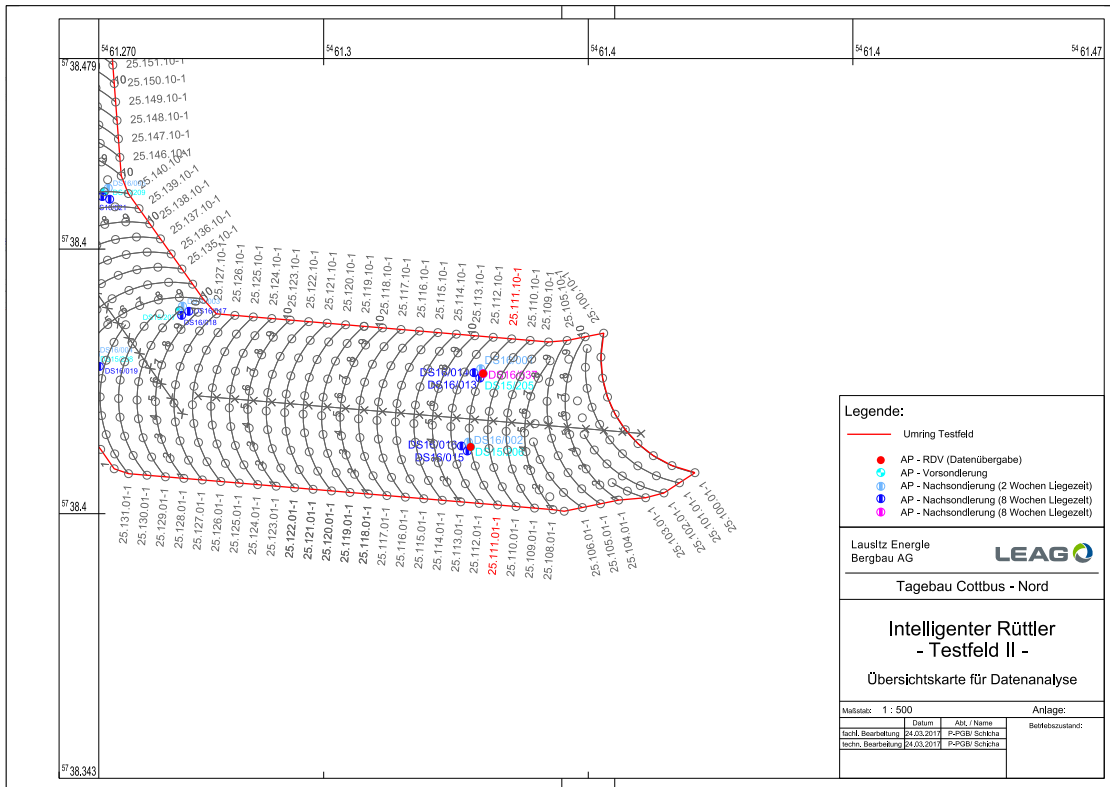


Figure 4.6: Location of the two compaction points which were part of field measurements in Cottbus, Germany (GMB GmbH, 2017b)

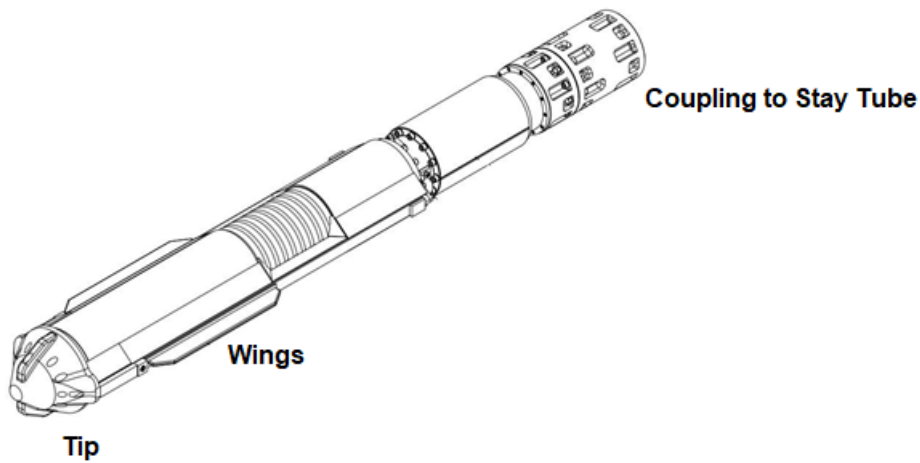


Figure 4.7: Schematic representation of V48 vibrator used for deep vibration compaction in Cottbus, Germany (GMB GmbH, 2017b)

by this process which would ensure no risk of flow failure of this loose residual material. With the gradual rising of ground water level due to the development of artificial lake, the granular residual material would also be prone to landslides and liquefaction if left under loose density. Deep vibratory compaction whose results are discussed in this work

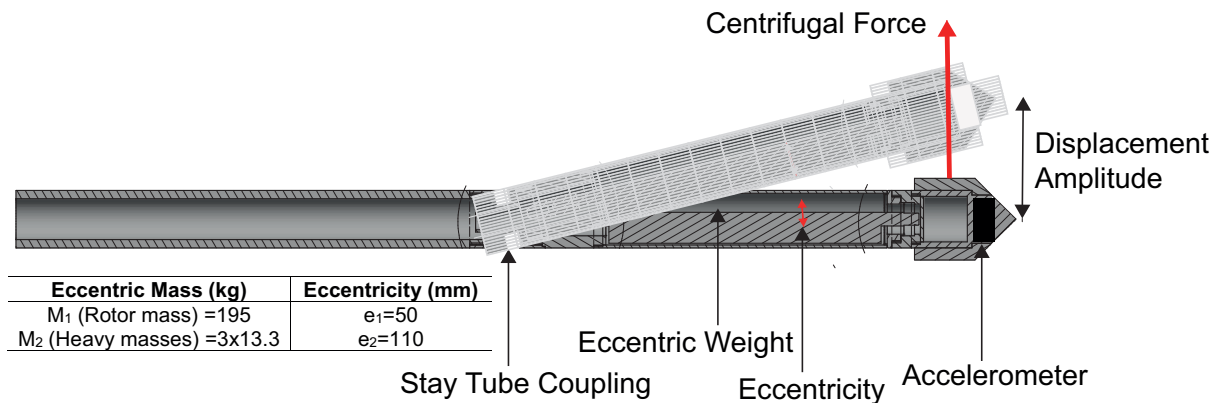


Figure 4.8: Schematic sketch of V48 vibrator with various components and sensors

was carried out as part of compaction process on a test area of approximately 8311 m² with 771 compaction points forming a grid with spacing of 3.5 m. Figure 4.5 depicts deep vibratory compaction at test field. In this work field measurements were carried out for two compaction points namely AP16015 and AP16013 (Figure 4.6(a)), in co-operation with GMB GmbH, Cottbus, Germany. Deep vibratory compaction was carried out based on the pilgrim step method. The compaction process is described in detail in the following sections. A V48 type vibrator probe produced by Vibro and SKM GmbH, Germany was used to execute deep vibratory compaction (Figure 4.7). The GMB GmbH-type Liebherr LR1300 crane system was used to support the stay tube, which was connected via an elastic coupling to the vibrator probe (Figure 4.7). The vibrator was 5 m long and of 0.47 m diameter with radial wings near the tip as shown in (Figure 4.7). The vibrator had a fixed eccentric mass and eccentricity; hence, the centrifugal force applied by the vibrator varied with frequency. The details of the eccentric mass and eccentricity are described in Figure 4.8. The vibrator was pre-installed with an accelerometer in order to evaluate the displacement amplitude of the vibrator (Figure 4.8). To log data during compaction, the vibrator was equipped with various sensors. Data loggers logged power consumed, operational frequency, temperature of vibrator, maximum and minimum acceleration of the vibrator, depth of operation and time log of the process during compaction. Further details on the hardware and software involved with the vibrator can be found in GMB GmbH (2017b).

4.2.2 Kippen Sand

The Kippen sand is a residual granular material, an outcome of Lignite extraction in the Cottbus region over the past few decades. The residual material following coal extraction was dumped in open pits. The extraction and transport significantly influenced the physical properties of the residual material. The main difference between the Kippen soil and the natural soil is its loose storage and associated high deformation potential (Geß, 2009). Kippen sand was a fine and medium sand with well-rounded grains. Three batches (5 kg per batch) of the Kippen soil were extracted from field in order to determine its physical

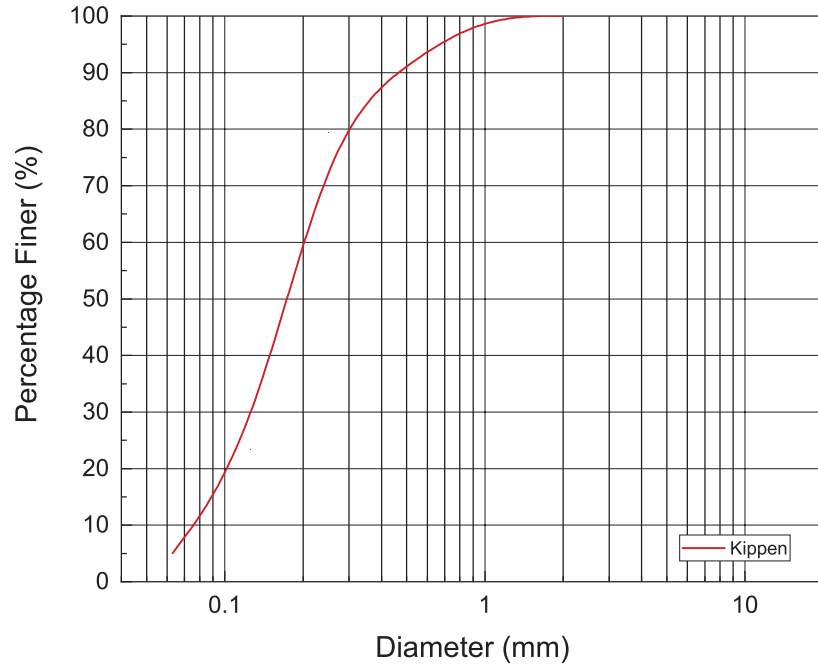
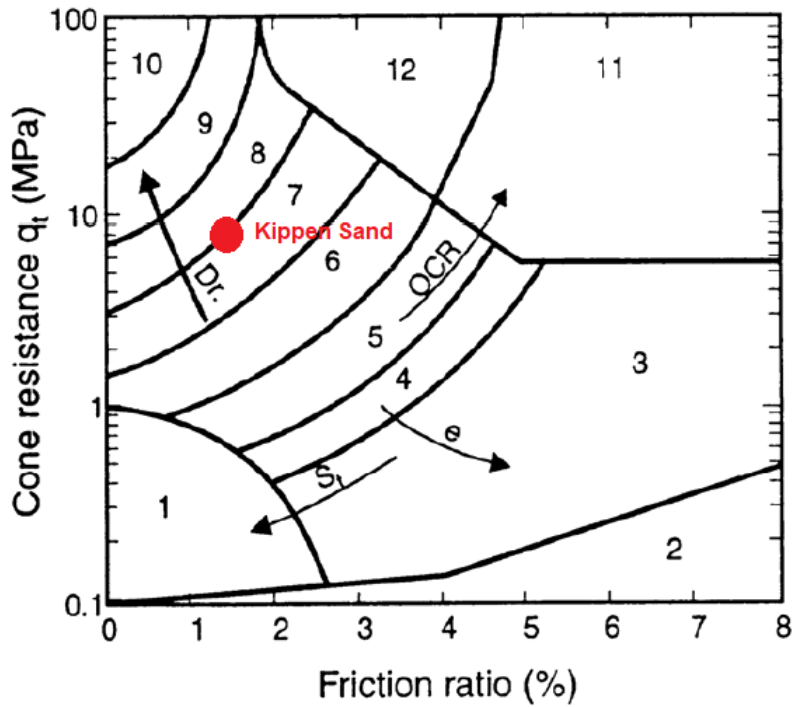


Figure 4.9: Grain size distribution of Kippen sand found at deep vibration compaction test site in Cottbus, Germany

properties and material parameters. The particle size distribution of Kippen sand was determined in accordance with DIN EN ISO 17892-4 (formerly DIN 18123) and is depicted in Figure 4.9. It can be observed from that the material consisted of roughly 7-8 % fines. The other basic physical properties of Kippen sand are tabulated Table 4.2. The detailed test results for Kippen sand can be found in Appendix B. CPT-u tests measuring both cone resistance and sleeve resistance according to DIN EN ISO 22476-1 were carried out to access the site condition. The CPT measurements are discussed further in the following chapters. Figure 4.10 maps the in-situ soil condition on a typical soil behaviour plot based on the averaged cone resistance and friction ratio measured on field and it can be observed that the Kippen sand is mostly lies in domain of silty sands.

Table 4.2: Basic physical properties of Kippen sand found at deep vibration compaction test site in Cottbus, Germany

Property	Value
Gradation	With Fines
e_{\min}	0.672
e_{\max}	1.116
Friction Angle	31°
D_{10}	0.08 mm
C_u	2.25
k	$2.52 \times 10^{-5} \text{m/s}$



Zone	Soil Behavior Type
1	Sensitive fine grained
2	Organic material
3	Clay
4	Silty Clay to clay
5	Clayey silt to silty clay
6	Sandy silt to clayey silt
7	Silty sand to sandy silt
8	Sand to silty sand
9	Sand
10	Gravelly sand to sand
11	Very stiff fine grained*
12	Sand to clayey sand*

* Overconsolidated or cemented

Figure 4.10: Effectiveness of deep vibration compaction to compact Kippen sand based on soil behaviour map by Robertson (1990)

4.2.3 On-Field Measurements

Deep vibratory compaction was carried out between 25 and 3 m depth. The groundwater in the area was located 33 m below surface. The vibrator was initially penetrated to a depth of 25 m. Water was used to ease the penetration of the vibrator to the required depth. A water volume of approximately 0.5 to 1 m³/m depth of compaction was used during the virgin penetration of vibrator probe to 25 m. Once the vibrator probe reached the required depth, water injection from tip of the vibrator was stopped, and water was injected from

the lateral sides of the vibrator at a slow rate of 1 litre/min during compaction. The pilgrim step method (Figure 4.11) involved stationary compaction for 23 s at a specific depth; next, the vibrator was pushed down 0.5 m in 6 s, then pulled up 1 m in 7 s. The total time of compaction at each depth was 36 s. No additional external vertical force was applied during the pushing down or pulling up of the vibrator. The loose sand between 25 m and 3 m depth was compacted in steps of 0.5 m. Additional Kippen sand was added from the top using a wheel loader to compensate for the volume deficit of sand created by compaction. Volume of additional sand was not recorded. The entire compaction process was carried out at an average frequency of 30 Hz and with an average centrifugal force of 520 kN. CPT-u tests measuring both cone resistance and sleeve resistance according to DIN EN ISO 22476-1 were conducted both before and after deep vibratory compaction at a radial distance of 0.5 m from the centre of the compaction point. Two sets of CPT-u tests were conducted three months after compaction in order to ensure repeatability. Large amounts of data were collected during field measurements and in the following chapters; only results that were used for validation of the numerical framework are discussed. Additional details on the performed field measurements can be found in GMB GmbH (2017b).

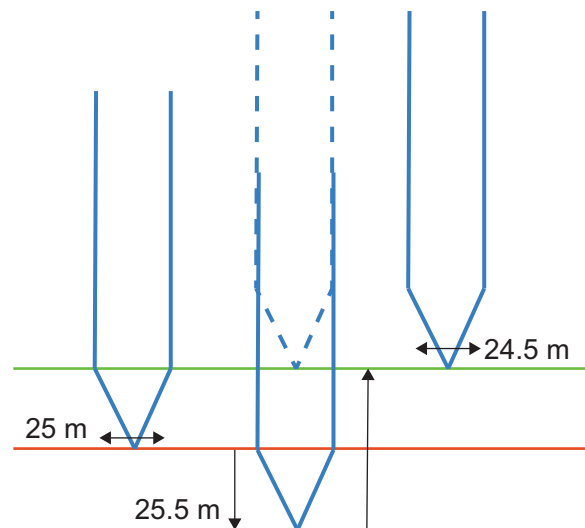


Figure 4.11: Schematic of Pilgrim Step method of deep vibration compaction

4.3 Numerical Framework

The numerical modelling is based on mathematical models for soil and soil-structure interaction. It basically involves solving of linear and non-linear systems of equations. In comparison to conventional calculation methods, numerical simulation is a complex method. In this work the finite element method (FEM) was used to study the vibrator-soil interaction, develop CPT correlation based on simulation and seismic simulation to study liquefaction mitigation. The following section discusses the basics of various numerical frameworks, modelling techniques and simulation methodology.

4.3.1 CEL Deep Vibratory Compaction Model

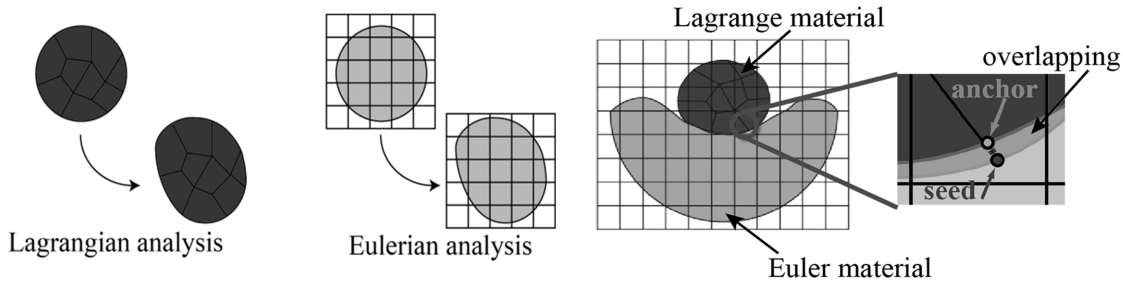


Figure 4.12: Deformation of a continuum in a Lagrangian and an Eulerian analysis with illustration of the penalty contact method (Qiu, 2012)

Simulation of the entire deep vibratory compaction process involves large-scale deformations. CEL framework has previously been successfully used to model large-scale deformations (Dassault Systemes, 2014; Qiu, 2012). CEL formulation combines the advantages of Lagrangian analysis with those of a Eulerian formulation. A characteristic of the Lagrangian formulation is the deformable mesh that moves with the material. The movement of the continuum is described as a function of time and material coordinates (Figure 4.12). In Eulerian analysis, the movement of the continuum is formulated by a function of time and spatial coordinates; hence, the mesh remains undeformed (Figure 4.12). The material moves through the mesh and each element receives a degree of filling (EVF = Eulerian Void Fraction). The movement is described using a function of spatial coordinates and time. It is possible that more than one material is assigned to an Eulerian element in the sense that partial filling is allowed. The filling level (EVF) of an element can be between 1 and 0. The shape and movement of the body is detected via the filling level of the individual elements. Eulerian formulation allow modelling of void elements which can be used to accommodate heaving of soil near surface during large deformation processes such as deep vibratory compaction. Eulerian formulation helps avoid errors due to geometric non-linearities, non-linear boundary conditions and large deformations. One of the disadvantages of this approach as observed by Brown et al. (2002) is a finer degree of discretization as compared to Lagrangian approach. The contact algorithm between Lagrangian object and Eulerian region is based on the penalty method, which assumes a hard pressure-overclosure behaviour (Dassault Systemes, 2014). It allows small penetrations of the Eulerian material into the Lagrangian object (Figure 4.12). When the Lagrangian element penetrates into the Eulerian region, the material displaces and void is created. This contact provision enables the method to be effectively used to model deep vibratory compaction process. The normal contact in normal direction is defined as hard contact and only compressive stresses can be transmitted. The tangential contact is assumed linear elastic and ideal plastic according to Coulomb's law of friction. The shear stress is considered proportional to the normal stress with friction coefficient μ . Work of Henke et al. (2012), Heins et al. (2015), Chmelnizkij et al. (2017) and Nagula and Grabe (2020) demonstrate the usefulness of CEL method to model deep vibratory compaction

process. Dynamic CEL analysis in addition to spatial discretization also requires time discretization. In this work, direct explicit time integration was used. With the explicit time integration, the discretization of time is finer. At the same time the number of arithmetic operators per time increment is lower, which reduces the computational effort per calculation step. The explicit integration is therefore suitable for dynamic processes. The explicit FEM is numerically stable as long as a critical time increment is not exceeded. The critical time step is derived from the minimum element length and current dilatatory wave velocity. ABAQUS 6.14 Explicit enabled with CEL framework was used to model deep vibratory compaction in this work (Dassault Systemes, 2014).

4.3.1.1 Model Definition

A 3D CEL-based model with 66304 hexahedral elements was created (Figure 4.13). The

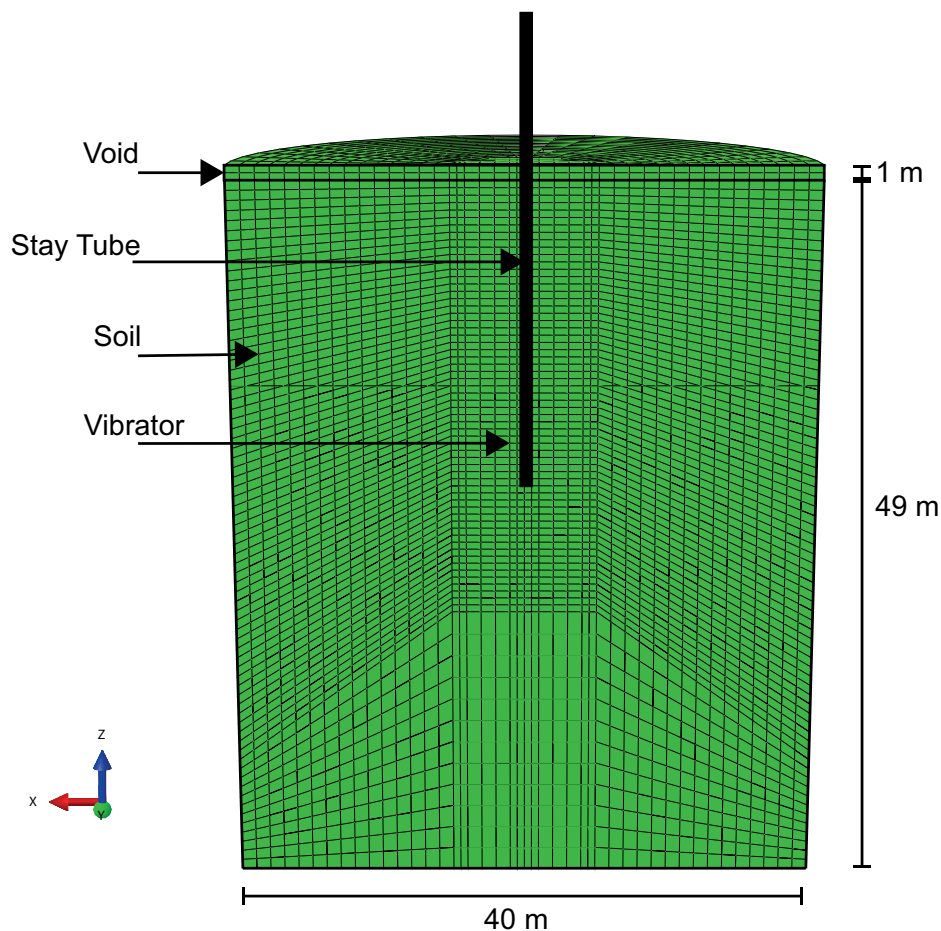


Figure 4.13: Section of 3D finite element model based on CEL to simulate deep vibratory compaction at realistic stress state

soil body was modelled as an Eulerian domain with a diameter of 40 m and height of 50 m. The chosen dimensions of the model ensured no boundary effect on the simulation results. 5 m radial distance around the axis of rotation of the vibrator was finely discretized with finite elements of length $0.1xd$, d corresponding to the diameter of the vibrator as per

Kaya and Grabe (2015). A 1 m high void area was created above the soil to allow the flow of material into this space during the simulation. The external lateral boundaries were restrained against horizontal movement. The bottom boundary of the model was restrained against vertical movement. The vibrator was modelled as a 5 m long, 0.47 m diameter cylindrical Lagrangian body, wished-in-place at required depth. The shape of the vibrator was simplified for computational efficiency. The effect of shape of vibrator is discussed the following chapters. The vibrator was vertically hinged (pinned connection) to a stay tube of the same diameter, and the bottom tip was free to move in the horizontal plane ($x \sim y$). The stay tube was pinned at its upper end to replicate real-life clenching of the tube to a crane. To replicate the vibrations of the vibrator, centrifugal force applied by the vibrator in x and y directions (horizontal plane) was calculated based on the variables in Equation 4.1, and was idealized to act at the tip of the vibrator (Schmitter and Adam, 2017; Chmelnizkij et al., 2017; Nagula and Grabe, 2020) (Figure 4.8).

$$F = m e_m \omega^2 \quad (4.1)$$

where, F = centrifugal force, m = mass of eccentric weights, e_m = eccentricity of masses and ω = angular frequency.

A sinusoidal amplitude for the corresponding operational frequency was applied to the central node at the tip of the vibrator in x and y directions to simulate circular horizontal vibration. As the vibrator is pinned at the top, and sinusoidal nodal forces are applied at the bottom; this imitates a pendulum-like motion with zero amplitude at the top and maximum horizontal amplitude at the tip. The vertical displacement of the vibrator due to vibration is neglected.

Contact between the vibrator and soil was modelled according to Coulomb's friction law (Henke et al., 2012; Grabe et al., 2015; Chmelnizkij et al., 2017). To simplify, the tangential friction coefficient between vibrator and soil was assumed to be zero (Chmelnizkij et al., 2017). The choice of considering no friction between soil and vibrator is justified in Chapter 5. In some specific cases friction between vibrator and soil was considered which would be highlighted in the corresponding sections. The vibrator and stay tube were modelled as a linear elastic material with the properties of steel.

4.3.1.2 Simulation Methodology

The deep vibratory compaction process was carried out using the pilgrim step method as described in the previous sections. The following simulation steps were created to model the compaction process.

1. Initial Phase: Initial state parameters were calculated based on the K_0 -stress state. K_0 (Earth pressure co-efficient at rest) was determined as per equation by Jaky (1944) for loose sand under consideration. It should be noted that the penetration effect of the vibrator into the soil was not considered due to computational limitations. Water injection was used in-field for penetration of the vibrator into the soil; however, this was not simulated during the numerical modelling.

2. Compaction Phase: The vibrator was wished-in-place at required depth. In order to replicate the vibrations of the vibrator, nodal forces in x and y directions (horizontal plane) were calculated based on eccentric mass, eccentricity of vibrator and frequency. The

centrifugal force was idealised to act at the tip of the vibrator as described earlier. The calculated force was applied with a sinusoidal amplitude as per the considered frequency to the tip of the simulated vibrator. A compaction time of 23 s (similar to in-field compaction time) was considered for each compaction depth unless otherwise stated.

3. Push Down Phase: After 23 s of compaction, the vibrator (while vibrating) was pushed down 0.5 m in 6 s.

4. Pull Up Phase: The vibrator was pulled up 1 m in 7 s. Displacement boundary condition was defined in order to execute the push down and pull up phases in simulations. Steps 2, 3 and 4 were repeated until compaction for required depth in step heights of 0.5 m was completed.

The numerical calculation steps considered a linear bulk viscosity of 0.42 and quadratic bulk viscosity of 1.2 as per the work of Kelm (2004) and Hamann et al. (2015). A time-scaling factor (which determines the number of time steps in ABAQUS) of 0.4 was chosen after multiple iterations.

4.3.2 FE CPT Model

It has been highlighted in the preceding sections that efficiency of deep vibratory compaction in compacting the sand was ascertained by means of CPT measurements before and after compaction. The CPT results would be used to validate the numerical models. Deep vibratory compaction simulation does not directly yield us the CPT tip resistance values and hence an indirect method was adopted in this work to estimate the tip resistance values. A CPT model was used to evaluate the coefficients of Equation 4.2, which would help convert the numerical simulation results in terms of the vertical stress and void ratio to the CPT tip resistance values.

$$q_c = a P_a \left[\frac{\sigma'_v}{P_a} \right]^b \exp^c I_D \quad (4.2)$$

where, q_c = CPT tip resistance, σ'_v = Effective vertical stress, I_D = Relative density, P_a = Reference pressure (1 kPa) and a , b and c are constants.

This relation can be used to indirectly estimate the CPT tip resistance values if the vertical stress and void ratio are known (Grabe and König, 2004; Grabe and Milatz, 2014). Equation 4.2 needs to be calibrated for the sand under consideration, and hence, a CPT model was set to determine the coefficients of the equation for required sand. CPT was modelled using the Zipper technique based on a Lagrangian FE axisymmetric model as the model was computationally less demanding. This made possible simulation of large number of iterations for the determination of co-efficients of tip resistance equation in shorter amount of time.

4.3.2.1 Model Definition

The numerical simulation of the CPT requires simulation of large relative displacements between the cone and the soil. The CPT hence, was simulated based on the Zipper technique in a Lagrangian axisymmetric model (Cudmani, 2001; Grabe and König, 2004). This method involved modelling a frictionless tube with a diameter of 1 mm along the

axis of symmetry of the numerical model over which the cone slid to establish a contact between the soil and cone. An axisymmetric model with a radius of 1 m and height of 1 m was created as shown in Figure 4.14. A cone with a diameter of 16 or 36 mm (D_{cone}) (as used in the 1g model tests or field measurements) was modelled as a rigid body with a rigid tip to distinguish the tip resistance from the total resistance. The lower edge of the model was completely fixed. The right edge of the model was fixed laterally. At the beginning of the simulation, the cone was pre-installed at a depth of $5D_{cone}$. The vertical stress on the soil layer was simulated as an external surface load, as shown in Figure 4.14. This ensured a homogeneous stress state with uniform void ratio in the entire soil. The soil was discretized with 6039 CAX4R 4 noded elements. The mesh is made fine in the proximity of the cone penetration. The sand was considered dry (drained) in all the simulations. An implicit integration scheme in ABAQUS Standard 6.14 was used.

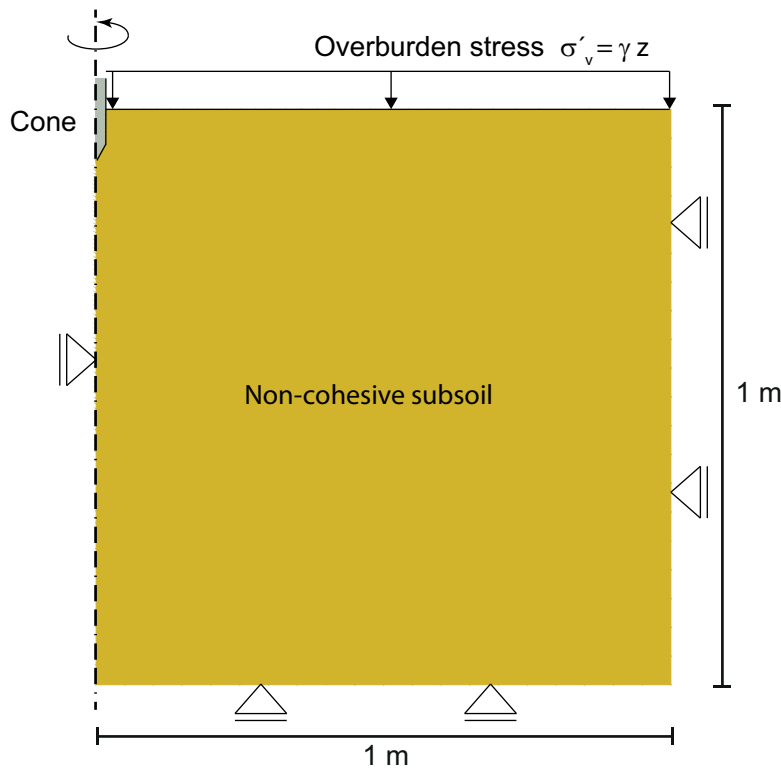


Figure 4.14: FE model to simulate CPT test

4.3.2.2 Simulation Methodology

Different initial state conditions were simulated in terms of the initial void ratio and vertical stress, and the corresponding tip resistance under each case was estimated. The simulation of CPT was sequenced as per the following steps.

1. **Initial Phase:** Activation of model geometries, contact conditions and boundary conditions. The CPT was wished-in-place at a depth of $5D_{cone}$.
2. **Stress State:** The initial stress state in terms of the effective vertical stress and initial void ratio was activated.

3. CPT Penetration: The cone was penetrated into the soil at a displacement rate of 20 mm/s until a constant tip resistance was reached.

4.4 Plane Strain Lagrangian framework for Seismic Analysis

In order to analyse the efficiency of deep vibratory compaction for liquefaction mitigation, seismic analysis of saturated sand before and after compaction was performed. Seismic analysis required the numerical model boundaries to be non-reflective meaning they should absorb the impending waves rather than deflecting them back into the model. This is necessary to replicate the free-field boundary as existing in natural ground. The CEL approach cannot be used to model the behaviour of saturated sand under seismic loading due to the unavailability of appropriate boundary conditions (Nielsen, 2006). The liquefaction behaviour of saturated sands under seismic loading was modelled using the Lagrangian approach under plane strain conditions. Characteristic of the Lagrangian formulation is the deformable mesh which moves with the material meaning that the movement of a continuum is described as a function of time and material coordinates. This approach is well developed and gave the flexibility of using appropriate boundary conditions in order to model seismic loading.

4.4.1 Model Definition

A plane strain model of 50 m height and 40 m width was created in the Lagrangian domain (Figure 4.15). It is common to use a single element column to model the free-field condition under seismic loading. Nonetheless, in this work the stress state in the soil after deep vibratory compaction from CEL simulation was mapped to the plane strain model in order to realistically map the efficiency of deep vibratory compaction for liquefaction mitigation. Hence, a larger domain was chosen to model the soil. The bottom of the model was completely fixed in the vertical direction to model a fixed rigid half-space. A lateral periodic boundary condition was imposed by constraining the opposite nodes on lateral boundaries to undergo the same displacement. This boundary condition is reasonable for strong 1D shaking since the energy dissipation in the soil due to hysteretic damping (particularly when liquefiable) supersedes the energy radiation from the side boundaries. It is to be noted that the periodic boundary condition provides exact results in case of level ground with a free surface subjected to 1D base shaking without any structure (Gudehus et al., 2004). The maximum allowable element size at each depth was determined as per Ramirez et al. (2018). Maximum allowable element size was determined at each depth based on the small-strain shear wave velocity of the soil obtained empirically from Seed and Idriss (1967) and Menq (2003) and the maximum frequency content of the applied base motion. Linear bulk viscosity of 0.42 and quadratic bulk viscosity of 1.2 as per the work of Kelm (2004) and Hamann et al. (2015) were assumed as in the CEL model and no additional dampening was introduced. A time scaling factor (which determines the number of time steps in ABAQUS) of 0.2 was chosen after multiple iterations.

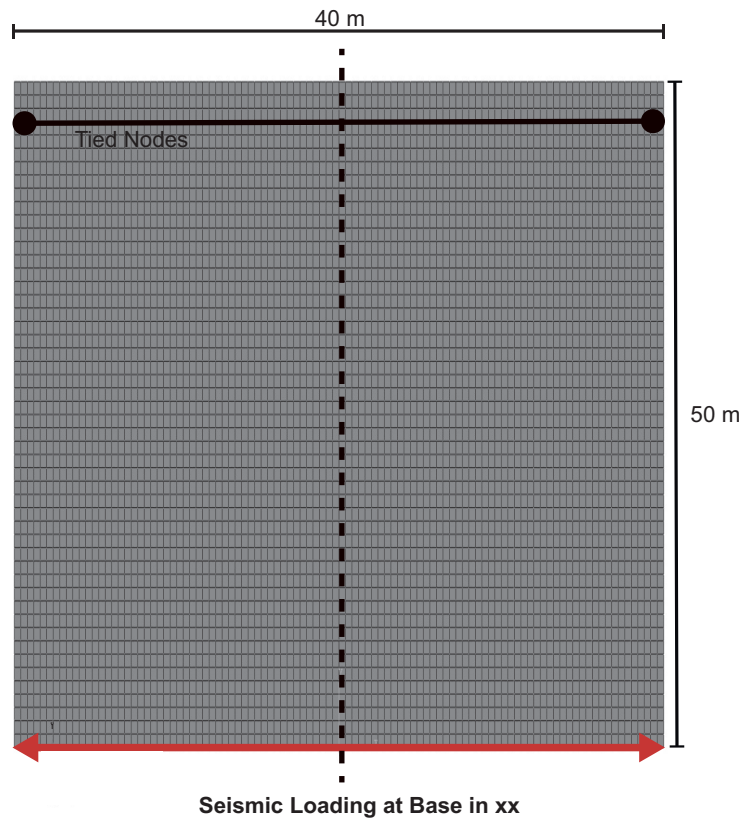


Figure 4.15: 40 x 50 m plane strain model to perform seismic analysis

4.4.2 Simulation Methodology

The seismic loading was applied in the form of horizontal (xx) acceleration time histories. Two kinds of earthquake loading were considered, which are further discussed under relevant sections. The acceleration time history under consideration was applied as input to the base of the numerical model. The sequence of seismic analysis simulations to model the behaviour of saturated sand before and after compaction was as follows:

1. **Phase I:** Loose saturated sand in a plane strain domain was subjected to seismic loading in order to simulate excess pore pressure generation and softening.
2. **Phase II:** The corresponding state developed in soil after deep vibratory compaction (as described before) was exported to the plane strain model. The model with the modified state was subjected to seismic loading. The liquefaction mitigation capacity of deep vibratory compaction was monitored.

4.5 Constitutive Model for Sand

Research has noted that the choice of the constitutive model plays a critical role in capturing the soil response under dynamic processes and seismic loading (Jeremić et al., 2008).

The efficiency of the chosen model to capture changes in soil porosity and permeability during seismic event holds the key. The material behaviour of the sand in this work was modelled by the hypoplastic model developed by Kolymbas (1991) and Kolymbas (1985) and Kolymbas (1991) and Wolffersdorff (1996) and further extended for intergranular strain by Niemunis and Herle (1997). The model is suitable for capturing the dependency of granular materials on pressure and void ratio (Niemunis and Herle, 1997). The model can handle phenomenon such as dilatancy, contractancy, material softening, the dependency of stiffness and strength on the pressure and void ratio, as well as different stiffness for loading, unloading and reloading. Densification is primarily related to the reduction in void spaces in soil; hence, the chosen constitutive model should include the void ratio as a state parameter. The hypoplastic model does include the void ratio as a state variable, hence making it ideal to simulate the compaction processes. Qui et al. (2011) used the hypoplastic model to simulate pile penetration, hence validating the feasibility of the model to function under dynamic loading. The suitability of the hypoplastic model to simulate vibro-compaction has been based on the successful usage of the model to simulate different densification problems as per Arnold and Herle (2009) and Heins et al. (2015).

Wegener and Herle (2012), Mašín (2014) and Wichtmann et al. (2019) have discussed the shortcomings of the hypoplastic model with intergranular strain in modelling cyclic mobility phenomena under undrained conditions. Wichtmann et al. (2019) found the hypoplastic model to perform better compared to other models in predicting maximum stress ratio and strain accumulation under drained (dry) conditions. Wichtmann et al. (2019) concluded that the intergranular strain anisotropy (ISA) model (Fuentes and Triantafyllidis, 2015) is best suited to capture the behaviour of saturated sands under cyclic loading. However, the stability of the ISA model in a finite element (FE) framework (as a VUMAT with $u - p$ formulation if modelling saturated sands in ABAQUS) and performance of the model to capture the densification-related boundary value problem has not been evaluated. Wichtmann et al. (2019) suggest that the hypoplastic model with intergranular strain can be used without major compromise on strain accumulation under undrained conditions for problems with strains below 5 %. Due to successful use of a hypoplastic model to simulate densification problems and lack of access to a verified ISA routine in FE framework, the authors used the former in this work. However, the authors did some primary simulations using the ISA model and have compared the results of same with hypoplastic model. The detailed results are discussed in the next chapter. The hypoplastic model was developed as a VUMAT (user subroutine to define material behaviour) to be used in the explicit numerical framework of ABAQUS. The index, oedometer, triaxial and dynamic tests with strain reversal were performed for the determination of hypoplastic material parameters (Herle and Gudehus, 1999).

4.5.1 Hypoplastic Model with Intergranular Strains

The hypoplastic model describes the mechanical behaviour of granular materials. The model assumes that granular materials are arranged in the form of simple granular skeleton and their state is defined by certain basic properties such as effective stress and void ratio. The hypoplastic model is well suited to model the non-linear and inelastic behaviour of dry granular soils. The first version of the hypoplastic model was formulated by Kolym-

bas (1991). The most widely used version was developed by Wolffersdorff (1996). Since the behaviour of granular materials is non-linear even at small strain levels the model developed some problems under small scale cyclic loading under which an increased accumulation of strains was observed. In order to rectify the effect of ratcheting, Niemunis and Herle (1997) enhanced the model with the intergranular strain concept.

The hypoplastic model describes the stress state change of a simple granular skeleton. The granular framework is defined by the following properties:

- The state of the granular material is defined by the stress tensor and the void ratio.
- The grains are robust and are assumed to undergo no internal deformation or fracturing.
- The assembly of the grain skeleton is bound by an upper and lower void ratio depending on the existing mean effective pressure hence, macro pores are accounted for.
- Deformations under similar boundary conditions are identical.
- It is assumed that granular materials are rate independent.

In the hypoplastic model (Wolffersdorff, 1996) the objective stress rate tensor $\dot{\sigma}$ is defined as a tensor valued function h of the effective Cauchy stress σ , the deformation rate D and the void ratio e as in Equation 4.3:

$$\dot{\sigma} = h(\sigma, D, e) \quad (4.3)$$

The function h is first order homogenous with respect to strain rate and directionally homogenous with respect to stress. Hence the formulation is able to describe both elastic and plastic deformations. The detailed description regarding the development and mathematical properties of the hypoplastic model can be found in Kolymbas (1988) and Kolymbas (1991), Wu et al. (1996), Gudehus (1996), Bauer (1996).

The hypoplastic model estimates deformations due to the rearrangement of granular skeleton under regular loading effectively but leads to accumulation of deformation on being subjected to excessive small amplitude stress cycles called as ratcheting. Hence, the hypoplastic model was extended and the intergranular strain parameters were introduced. The extended model took into account the behaviour of the granular material under small strains due to change of direction of stress or strain path. The intergranular strain extension leads to the addition of the intergranular strain tensor (δ) which stores the most recent deformation history and also leads to an increase in the incremental stiffness ($E = dT/d\epsilon$) of the material on change in direction of deformation (D). The extended model states that if the state of stress and density of the material at point * (Figure 4.16) is similar even after being subjected to different deformation histories as indicated in Figure 4.16, a reversal in direction of deformation would lead to a variable increase in incremental stiffness depending on the nature of the reversal. A 180° reversal as indicated in Figure 4.16 (top left), would lead to an increase in stiffness according to $E_R = m_R E_0$ and a 90° reversal (middle left) would lead to an increase in stiffness as per $E_T = m_T E_0$ where m_R and m_T are intergranular strain parameters and E_0 is the asymptotic stiffness which the

material inherits after long monotonic shearing in similar state. After being subjected to sufficient deformation (ϵ_{SOM}), the effect of change in direction of deformation is swept out of memory which is marked by the constancy of the incremental stiffness. The elastic range R , describes the strain range over which the stiffness of the material is strain independent. The size of the elastic range R is assumed to be constant irrespective of the state of stress and void ratio as indicated in Figure 4.16 (right) but whereas the magnitude of the elastic stiffness varies as per the stress state and void ratio. The intergranular strain model includes two other exponents β_χ and χ which govern the decay of $E_{R/T}$ after the change in deformation direction.

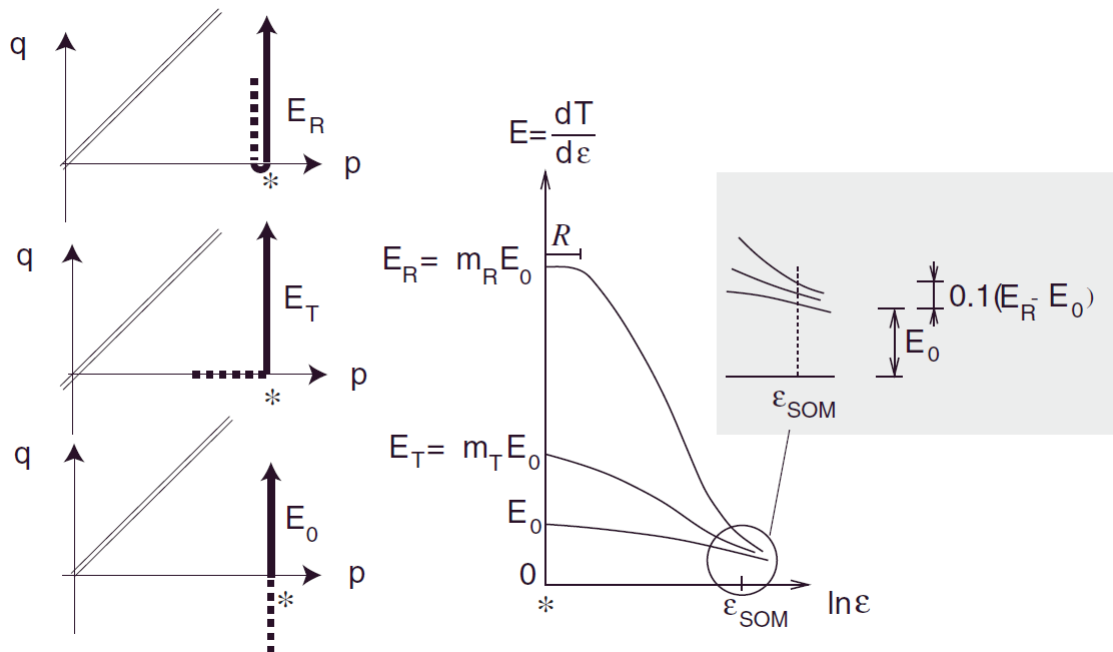


Figure 4.16: Incremental stiffness as per intergranular strain concept according to change in direction of deformation (Niemunis and Herle, 1997)

4.5.2 Determination of Hypoplastic Model Parameters

The hypoplastic model without the intergranular strain parameter predominantly consists of 8 parameters. All of the parameters are closely related to the geometric and material constants of the grains and hence can be determined by standard index tests. The determination of Hypoplastic model parameters requires a series of triaxial and oedometer tests.

The first set of parameters consist of the limiting void ratios e_{i0} , e_{c0} and e_{d0} corresponding to the upper bound, critical state and lower bound void ratio at zero pressure. These parameters are estimated from the minimum and maximum void ratio values of the granular material which are determined by standard index tests. The critical angle ϕ_c determines

the resistance of the granular material in monotonic shearing in critical state. It is evaluated from drained triaxial tests or by the determination of angle of repose. In this work the critical friction angle was determined by both the approaches. The parameters granulate hardness h_s and exponent n describe the isotropic compression of loose sands under increasing effective mean pressure as Equation 4.4:

$$e = e_0 \exp \left[- \left(\frac{3p'}{h_s} \right)^n \right] \quad (4.4)$$

where, e = Void ratio, e_0 = Max void ratio, p' = Effective mean pressure, h_s = Granulate hardness, n = Exponent.

n reflects the curvature of the compression curve whereas h_s governs the slope. They are determined from isotropic compression tests on loose samples of granular materials. Since, placement of granular material under very loose condition in an isotropic compression test is difficult, h_s and n are obtained by one dimensional oedometer test. The exponent α governs the peak friction angle and also indirectly influences the dilatancy of the material and is calibrated with the results of drained triaxial tests on dense samples. The parameter exponent β which governs the stiffness of the granular materials is calibrated from oedometer or triaxial test data on dense samples.

The material parameters for 6 different kinds of sands namely Hamburger, Kippen, Ottawa, A1, A2, A3 and A5, which have been used in this work, were evaluated by performing laboratory experiments on the sand samples. The basic physical properties and grain size distribution of the 6 sands are as tabulated in Table 4.3 and Figure 4.17. In order to perform laboratory experiments, 15 kg of Kippen sand was extracted from a borehole near the compaction point on field. Rest of the sands are all naturally existing sands and procured from field. Triaxial samples of sand of 50 mm diameter and a height of 125 mm were prepared using vacuum suction method. Standard oedometer samples of 70 mm diameter and 20 mm height were prepared. Dense and loose samples according to the maximum and minimum density of the sands as per Table 4.3 were prepared with sufficient quantity of water in case of saturated samples, in order to ensure complete saturation of the sample during testing. This helped analyse the effect of initial density on the material properties of various sands.

The critical friction angle (ϕ_c) was determined based on the test method suggested by Cornforth (1973). A funnel filled with soil was slowly lifted releasing the soil on a flat surface. The angle made by the cone on the flat surface, gave the value of the critical friction angle. In order to compare the results, critical friction angle was also determined using the results of static triaxial test data.

In order to determine h_s and n , one dimensional compression oedometer test was performed on dry samples. The test was different from a standard oedometer test, the sample was loaded at a constant deformation rate of 0.25 mm/min and the corresponding axial load developed was recorded. h_s and n were evaluated using the relations described below. The bulk modulus given by Equation 4.5

$$K = -\dot{p}' / \left(\frac{\dot{e}}{1+e} \right) \quad (4.5)$$

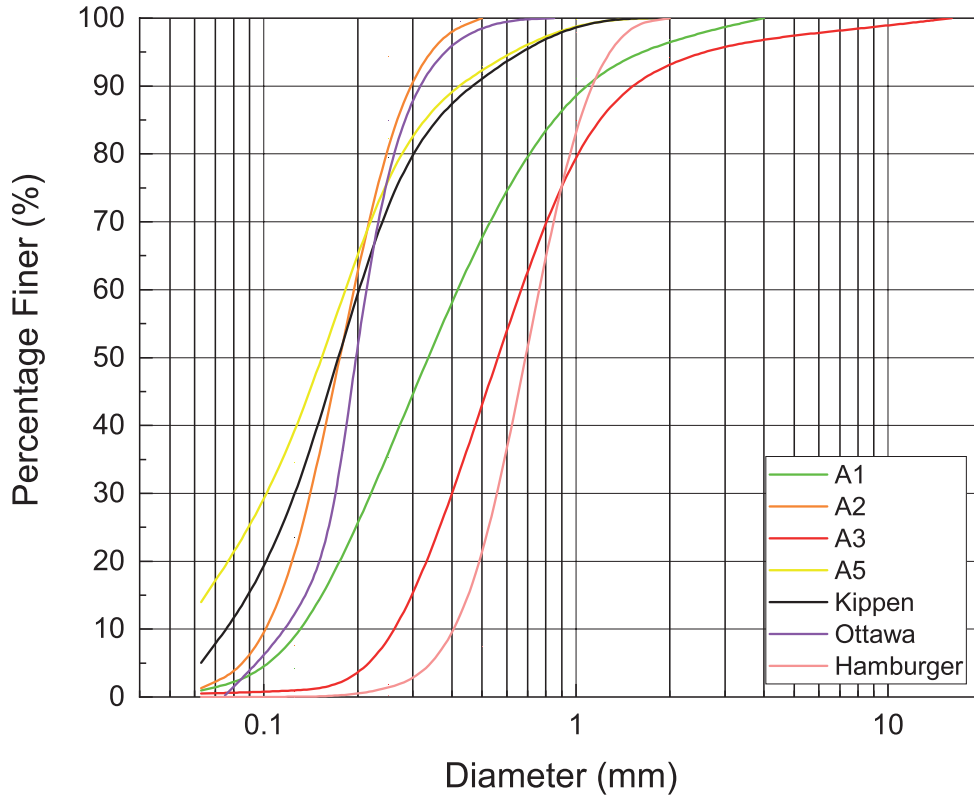


Figure 4.17: Grain size distribution of A1, A2, A3, A5, Kippen, Ottawa and Hamburger sands used in numerical simulations

where, \dot{p}' = rate of change of mean pressure, \dot{e} = rate of change of void ratio and other terms as described earlier, can be expressed with the help of Equation 4.4 as Equation 4.6

$$K = \frac{1}{3} \frac{h_s}{n} \left(1 + \frac{1}{e}\right) \left(\frac{3p'}{h_s}\right)^{1-n} \quad (4.6)$$

where, the terms are as described earlier.

When Equation 4.5 was compared to conventional bulk modulus Equation 4.7

$$K = \frac{p'(1+e)}{C_c} \quad (4.7)$$

where, C_c = Compression index, the following relation was generated in the form of Equation 4.8

$$h_s = 3p' \left(\frac{ne}{C_c}\right)^{1/n} \quad (4.8)$$

Considering two load points on the oedometer compression curve p_1 and p_2 and corresponding compression indexes and void ratios, the exponent n was evaluated from Equation 4.8 to form Equation 4.9.

$$n = \frac{\ln\left(\frac{e_1 C_{c2}}{e_2 C_{c1}}\right)}{\ln\left(\frac{p_2}{p_1}\right)} \quad (4.9)$$

Table 4.3: Basic physical properties of A1, A2, A3, A5, Kippen, Ottawa and Hamburger sands used in numerical simulations

Sand	e_{max}	e_{min}	C_u
Kippen	1.116	0.672	2.25
Hamburger	0.813	0.526	1.47
Ottawa	0.82	0.53	1.45
A1	0.8	0.38	3.45
A2	1	0.51	1.43
A3	0.72	0.47	2.1
A5	1.12	0.67	2.4

The granulate hardness h_s was then evaluated according to the value of n . Further details can be found in Herle and Gudehus (1999). Typically the h_s and n are determined by compression tests on initially loose samples but in order to study the variation of the parameters with density, compression test with initial dense samples were also carried out.

The limiting void ratio e_{d0} was determined as per standard minimum void ratio index test according to DIN 18126. e_{c0} was considered equal to maximum void ratio as per Herle (1998). Hence maximum void ratio was found according to the standard index test as per DIN 18126 (1996). The e_{i0} was approximated to be around 1.2 times e_{max} (Herle and Gudehus, 1999).

Exponent α describes the effect of density on the peak friction angle of the granular material. The determination of α required determination of peak friction angle, dilatancy angle at a particular density by means of drained triaxial test. The values were then used to determine the value of α using the following Equation 4.10.

$$\alpha = \frac{\ln \left[6 \frac{(2+K_p)^2 + a^2 K_p (K_p - a - \tan \vartheta_p)}{a(2+K_p)(5K_p - 2) \sqrt{4 + 2(1 + \tan \theta_p)^2}} \right]}{\ln \left(\frac{e - e_d}{e_c - e_d} \right)} \quad (4.10)$$

$$K_p = \frac{1 + \sin \varphi_p}{1 - \sin \varphi_p} \quad (4.11)$$

$$a = \frac{\sqrt{3} (3 - \sin \varphi_c)}{2\sqrt{2} \sin \varphi_c} \quad (4.12)$$

where, ϕ_p = Peak friction angle, ϑ_p = Dilatancy angle, ϕ_c = Critical friction angle, e = Void ratio, e_d = Min void ratio and e_c = Max void ratio

Further details about the determination of α can be found in Herle (1998) and Karcher (2003).

Exponent β controls the increase of the pressure dependent stiffness with increasing density. The increase of stiffness is predominant in dense specimens and hence the parameter is important for evaluation of stiffness in dense specimens. The factor was determined

after the determination of all the other parameters of the hypoplastic model. Stiffness modulus along with the void ratio of the material in dense and loose state was determined from oedometer test data. Following this β was evaluated using the following Equation 4.13

$$\beta = \frac{\ln\left(\beta_0 \frac{E_2}{E_1}\right)}{\ln\left(\frac{e_1}{e_2}\right)} \quad (4.13)$$

$$\beta_0 = \frac{3 + a^2 - a\sqrt{3}f_{d1}}{3 + a^2 - a\sqrt{3}f_{d2}} \quad (4.14)$$

$$f_d = \frac{e - e_d}{e_c - e_d} \quad (4.15)$$

where, subscript 1 stands for loose and 2 for dense, E = Stiffness modulus and the other terms are as described earlier.

The exponents α and β are dependent on the value of h_s and n and need to be calibrated in tandem (Bauer, 1996).

4.5.2.1 Hypoplastic Model Parameters

The hypoplastic model parameters of the 6 sands are as tabulated in Table 4.4. Some of the parameters are amiss because not all laboratory tests could be conducted due to lack of required quantity of sand. It can be observed that the material parameters of the sands vary with their physical properties. The friction angle marginally increased with increasing C_u of sands which was also observed by Herle and Gudehus (1999). It can be observed that h_s and n were not only dependent on the physical properties of sands but also on the initial density of the granular material. Figure 4.18 depicts a sample evaluation of h_s and n from oedometer compression test results from two sets of data points (average of A-B and D-E) for dense and loose samples using Equation 4.8 and Equation 4.9. It can be observed that the nature of the curves for dense and loose sample vary and hence the parameters h_s and n vary as per the initial density of sand. It can also be observed by comparing values in Table 4.4 and 4.3 that n is closely related to the granulometric property of the sands and increases with reducing C_u (Schultze and Moussa, 1961). h_s on the other hand is found to increase with increasing C_u . The minimum void ratio e_{d0} decreases with increasing C_u due to filling of voids with smaller particles (Youd, 1972). Sand A5 is an anomaly and negates the above stated trend. The probable reason can be due to the presence of excessive finer particles (more than 13 %), which do not allow the sand to reach a lower void ratio owing to difficulty in compaction. α governs the dependence of peak friction angle on density and hence was found to be related to the granulometric property of sands (Mogami and Yoshikoshi, 1968; Koerner, 1970; Holubec and D'Appolonia, 1973). α marginally increased with increasing ϕ_c which is indirectly related to C_u .

4.5.3 Determination of Intergranular Strain Parameters

Intergranular strain parameters are comparatively difficult to evaluate and require dynamic tests or static tests with strain reversal (Niemunis and Herle, 1997) to be performed. The

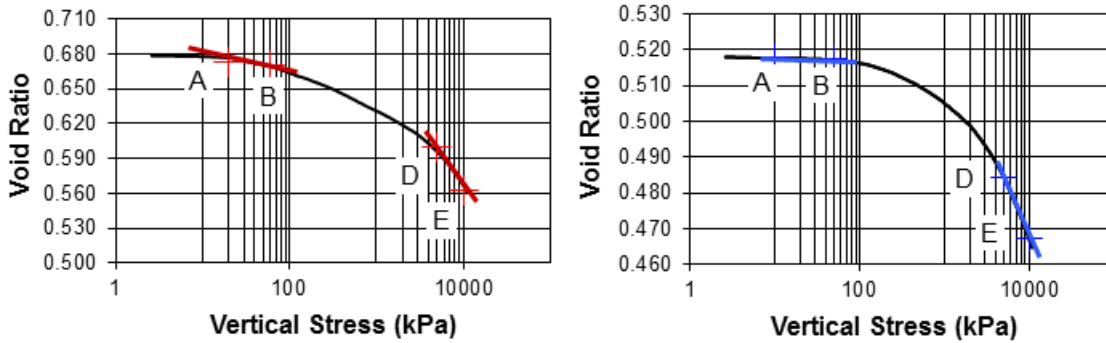


Figure 4.18: Determination of h_s and n considering average of two load points (A-b and D-E) on the oedometer compression curve and corresponding compression indexes and void ratios for loose sample (left) and dense sample (right) using 4.8 and Equation 4.9

parameters as determined by Niemunis and Herle (1997) for Hochstetten sand has been seen to work quite reasonably well for finite element simulations and hence not much work has been done on the determination of these parameters. However recently researchers have observed by means of dynamic and cyclic tests on Karlsruhe and Zbraslav sand that the intergranular strain parameters are density and stress state dependent (Manual, 2007). This called for the need of identifying a simple and effective method of determination of the parameters. In this work stress path controlled static triaxial tests have been used to determine the intergranular strain parameters m_R , m_T and R . The experimental test results were calibrated as per Niemunis and Herle (1997) to attain the exponential parameters.

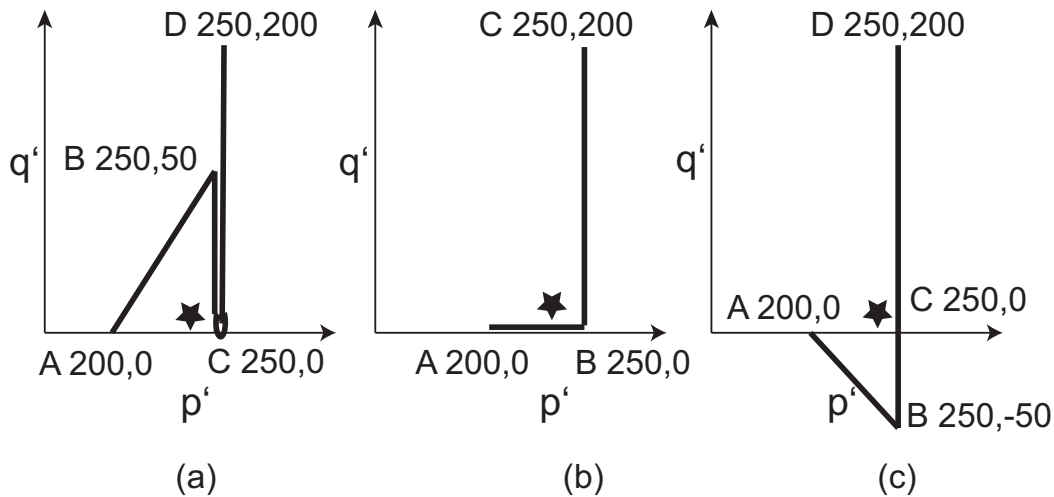
Simple static triaxial tests were performed in order to determine the intergranular strain parameters m_R , m_T and R . Stress path control method of testing was employed in order to subject the material to strain reversal after being subjected to different deformation histories. The tests were performed in the automated stress path module of the GDS (GDS Instruments, Hampshire, United Kingdom) Triaxial Testing System (GDSTTS). Since the speculated strain ranges are low and need to be measured accurately, on sample GDS Linear Variable Differential Transformer (LVDT) local strain transducers were installed. These LVDTs can measure small strains and are well suited for small strain stiffness measurements.

GDS Triaxial Testing System equipped with automated stress path module is based on the classic Bishop and Wesley type stress path triaxial cell which directly controls the stress on the sample. The sand sample was cast at the required density and was placed in the triaxial chamber with the on sample LVDTs as described in the preceding section. The sample was installed with extension load cap, in order to ensure that the sample could even be subjected to extension/tension during loading. The sample was first made to undergo saturation ramp at a radial pressure of 410 kPa and back pressure of 400 kPa. Samples were ensured to have a B-check value of at least 0.98 in order to ensure satisfactory saturation. The samples were then subjected to isotropic consolidation at pressure 100 kPa or 200 kPa. The two different consolidation pressures were chosen in

Table 4.4: Hypoplastic model parameters of sands

	ϕ_c	h_s	n	α	β	e_{d0}	e_{c0}	e_{i0}
Kippen	31	137 _L	0.18 _L	0.273	1.02	0.672	1.116	1.283
Hamburger	31	4500 _L	0.19 _L	0.166	0.218	0.526	0.813	0.935
Ottawa	30	2100 _L	0.23 _L	0.25	1	0.53	0.82	0.94
A1	33.7	580 _L 853 _D	0.32 _L 0.48 _D	0.04	2.76	0.38	0.8	0.92
A2	32.3	800 _L 2277 _D	0.31 _L 0.43 _D	0.03	2.51	0.51	1	1.15
A3	33	405 _L 436 _D	0.43 _L 0.6 _D	0.04	1.52	0.47	0.72	0.82
A5	32.9	17 _L 79 _D	0.32 _L 0.68 _D	0.0007	6.03	0.67	1.12	1.28

L= Loose, D= Dense

Figure 4.19: Stress paths used in triaxial tests for a) 180° b) 90° and c) 0° reversal (values indicate the applied q and p')

order to study the variation of the intergranular strain parameters with varying initial stress state conditions. The stress path controlled testing enabled the sample to be driven to desired p' (mean stress) and q' (deviatoric stress) stresses as depicted in Figure 4.19. The module ensured independent linear control of p' and q' on the sample; hence the samples were subjected to stress paths as depicted in Figure 4.19. Sand samples were subjected to three kinds of stress paths 1) 180° strain reversal 2) 90° strain reversal 3) no reversal, which are described further in detail. The points marked with * in Figure 4.16 have the same density and void ratio. This was ensured in the experimental tests by casting similar samples (dense or loose) and subjecting them to the same preliminary consolidation stages and ensuring that the samples reached the same stress state point at start of the test. The samples were subjected to initial consolidation pressure of 100

kPa or 200 kPa pressure as described earlier and corresponding q' and p' for the different tests are marked in brackets in Figure 4.19. In order to study the effect of density on the intergranular strain parameters, the tests described in the preceding sections were performed both on loose and dense samples.

- **180° reversal:** The sample was made to undergo preliminary stages of saturation and consolidation as described in the preceding section. At the start of the stress path module the sample was subjected to $q' = 0$ kPa and $p' = 100$ kPa (excluding back pressure) marked as point A in Figure 4.19(a). The q' and p' stresses were then linearly increased to reach 50 and 150 kPa (Point B Figure 4.19(a)), followed by reduction of q' to 0 kPa at constant p' of 150 kPa to reach point C (Figure 4.19(a)). This stage marked extension of the sample as q' was reduced. As soon as q' reached 0 kPa, the stress paths were programmed to make a 180° reversal. The q' was increased to reach 200 kPa at constant p' of 150 kPa to reach point D (Figure 4.19(a)). This stage marked the compression of the sample as q' was increased hence the material underwent a 180° deformation reversal from extension to compression leading to the evaluation of the E_R which is ratio of incremental stress to strain after 180° strain reversal.
- **90° reversal:** After consolidation, the material was subjected to further isotropic consolidation by increasing p' to reach a value of 150 kPa as depicted in Figure 4.19(b) (Point B). The sample was then subjected to monotonic shearing by an increase of q' to reach a value of 200 kPa at constant p' of 150 kPa to reach point C (Figure 4.19(b)). This change from isotropic consolidation to compression marked a 90° reversal leading to the evaluation of E_T .
- **0° reversal:** The sample was made to undergo extension after consolidation by reducing q' to reach -50 kPa and by increasing p' to 150 kPa to reach point B (Figure 4.19(c)). The sample was then subjected to monotonic shearing by increasing q' to reach 200 kPa at constant p' of 150 kPa. The incremental stiffness E_0 was evaluated after the stress path crossed point C (Figure 4.19(c)).

The values of R , β_χ and χ were determined from the stress path results as discussed in the following section.

4.5.3.1 Intergranular Strain Parameters

The evaluation of the intergranular strain parameters revealed that they are stress state sensitive and varied according to the density of the granular material. The following section describes the variation of the intergranular strain parameters with stress state and initial density of the granular material.

- **Variation of stiffness with reversal in deformation path**

The variation of the stiffness after the deformation path reversal as described in Figure 4.19 was evaluated. It was observed in Figure 4.20 that the incremental stiffness was highest after a 180° reversal followed by stiffness for 90° reversal. Eventually

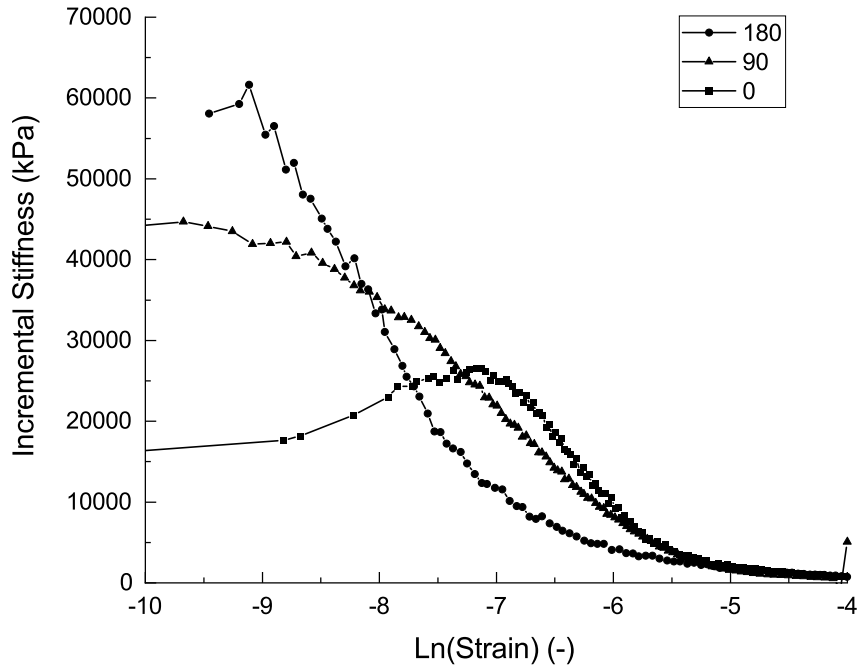


Figure 4.20: Variation of stiffness after 180°, 90° and 0° reversal for A5 sand

the incremental stiffness values decreased with increasing deformation and asymptotically reached a constant value which was equivalent to the stiffness under no deformation path reversal. The strain ϵ_{SOM} beyond which the effect of deformation path reversal was negligible are as tabulated in Table 4.5. It was observed that for all sands m_R was found to be 1.5 - 2.5 times m_T (Table 4.5)

- **Variation of stiffness with nature of sand**

Figure 4.21 describes the variation of the stiffness after 180° reversal for 5 sands. The stiffness was higher for pure sands with higher coefficient of uniformity. Sands A3 and A5 are found to be outliers and this can be probably be justified by the presence of more amount of fines (13 %) in A5 soil and more percentage fraction of gravel in A3 (Figure 4.17). Hence it can be suggested that stiffness parameters not only depend on the index properties of the sand but also on the nature of particles present in the granular material (Biryaltseva et al., 2016). The presence of gravel and fines leads to substantial changes in the stiffness parameters of the sand.

- **Variation of stiffness with stress state**

The dependence of the incremental stiffness on the stress state for A3 sand can be observed in Figure 4.22. It can be observed that the stiffness values increased with increasing consolidation pressure. This observation showed that the intergranular strain parameters are stress state sensitive and are not unique to the granular material.

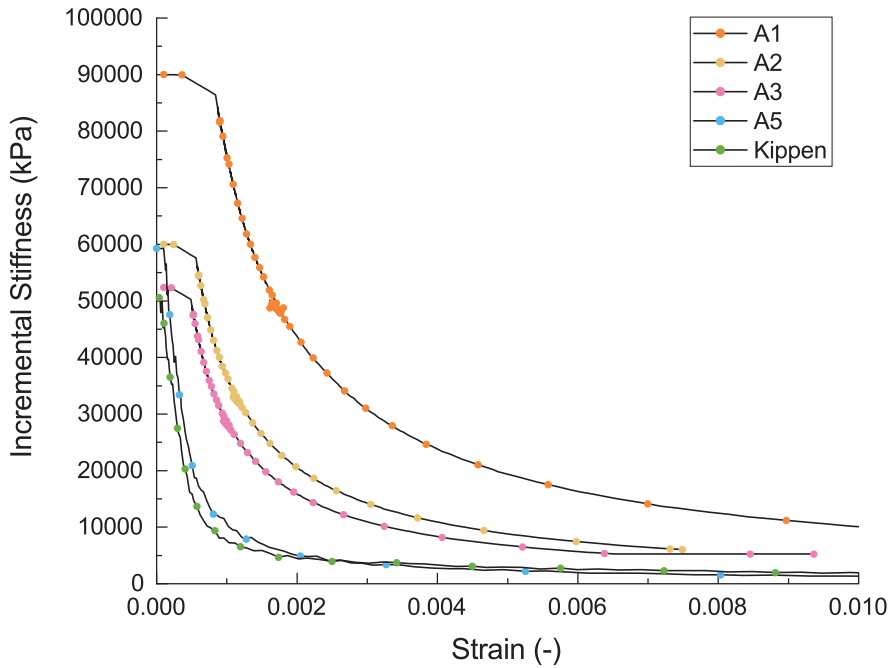


Figure 4.21: Stiffness variation for A1, A2, A3, A5 and Kippen sand after 180° reversal (dense state)

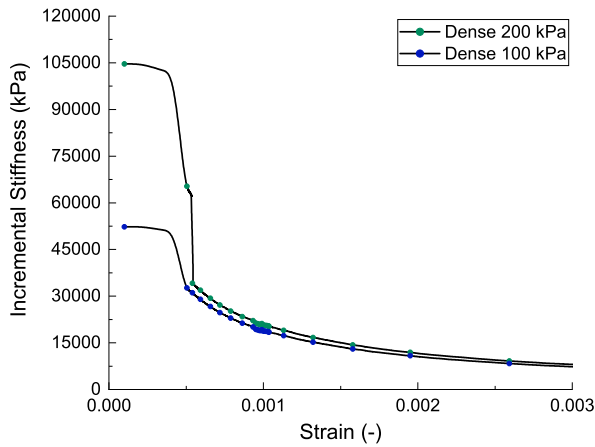


Figure 4.22: Variation of stiffness with stress state after 180° reversal for A3 sand

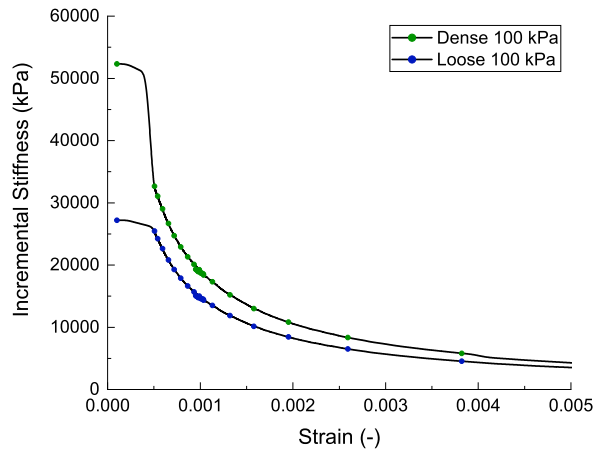


Figure 4.23: Variation of stiffness with density after 180° reversal for A3 sand

- **Variation of stiffness with density**

The incremental stiffness varied as per the density of A3 sand as can be observed in Figure 4.23. Sand in denser state showed higher stiffness values than in loose state suggesting that the corresponding intergranular strain parameters are density dependent.

- **Elastic strain range (R)**

The elastic strain range R is defined as the strain until which the stiffness of the material remains constant after deformation reversal. The values of R for 4 sands are as tabulated in Table 4.5. It is interesting to observe that R is neither sensitive to the nature of the granular material nor to the stress state and density. It can be observed that as suggested by Niemunis and Herle (1997), the value of R can be closely approximated to 0.0001.

- **β_χ and χ**

β_χ and χ which define the decay of $m_{R/T}$ were calibrated using the experimental results and are as tabulated in Table 4.5 for varying initial densities.

- **Intergranular strain parameters**

Table 4.5 tabulates all the intergranular strain parameters for two different initial density conditions for an initial consolidation pressure of 100 kPa. The intergranular stiffness coefficients were found to be highly sensitive to density, whereas as other parameters were found to be density independent.

Table 4.5: Intergranular strain parameters of sands

Sand	m_R	m_T	R	β_χ	χ	ϵ_{SOM}
Kippen	3.69	2.78	0.00012	0.3	6	0.00028
Hamburger	2	5	0.0001	0.5	5	0.0001
Ottawa	2	5	0.0001	0.5	6	-
A1	6.6 _L	4.25 _L	0.0001	0.7	1	0.0003
	3.26 _D	0.48 _D		0.6	1	0.00024
A2	8.68 _L	4.44 _L	0.00011	0.5	2	0.0005
	5.48 _D	3.65 _D		0.6	2	0.0004
A3	5.35 _L	0.47 _L	0.0001	1	1	0.00011
	2.91 _D	2.25 _D		1	1	0.00013
A5	2 _L	4 _L	0.0001	0.35	5	-
	3.69 _D	2.78 _D				

L= Loose, D= Dense

4.5.4 Calibration of Parameters

It has been discussed in the earlier sections that the parameters are sensitive to initial stress and density state. Hence, the calibration of parameters is important, so as to best predict material behaviour over a wide range of stress states. A routine was written in MATLAB (R2019a) to calibrate certain hypoplastic model parameters. The parameters which described the physical attributes of sand such as friction angle, minimum and maximum void ratios were held constant whereas, the other parameters which were found to be density and stress state dependent were varied. The parameters were varied in the range suggested by Herle and Gudehus (1999) and iterations were run until best predictions were

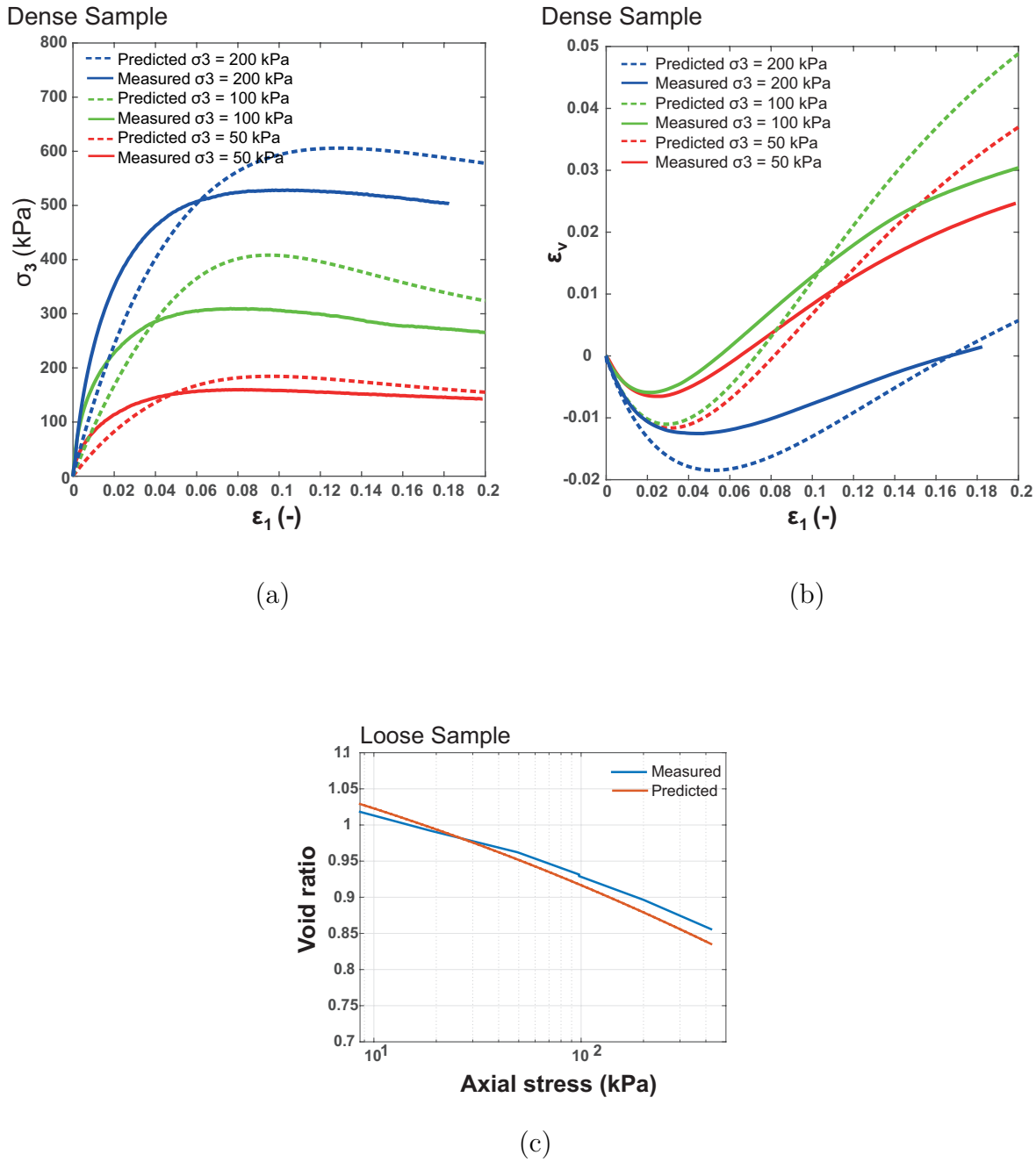


Figure 4.24: Measured and predicted values for monotonic triaxial test (a,b) and oedometer (c) for Kippen sand

obtained. Figure 4.24 compares the model predictions after calibration (as evaluated by MATLAB routine) with experimental results for Kippen sand. The material parameters were calibrated against static triaxial and static oedometer tests. The calibrated model parameters for all the sands are as tabulated in Table 4.6. It can be observed that the parameters such as friction angle and void ratios have been kept constant as obtained from experimental tests. Deep vibratory compaction is a highly cyclical process hence, it is not

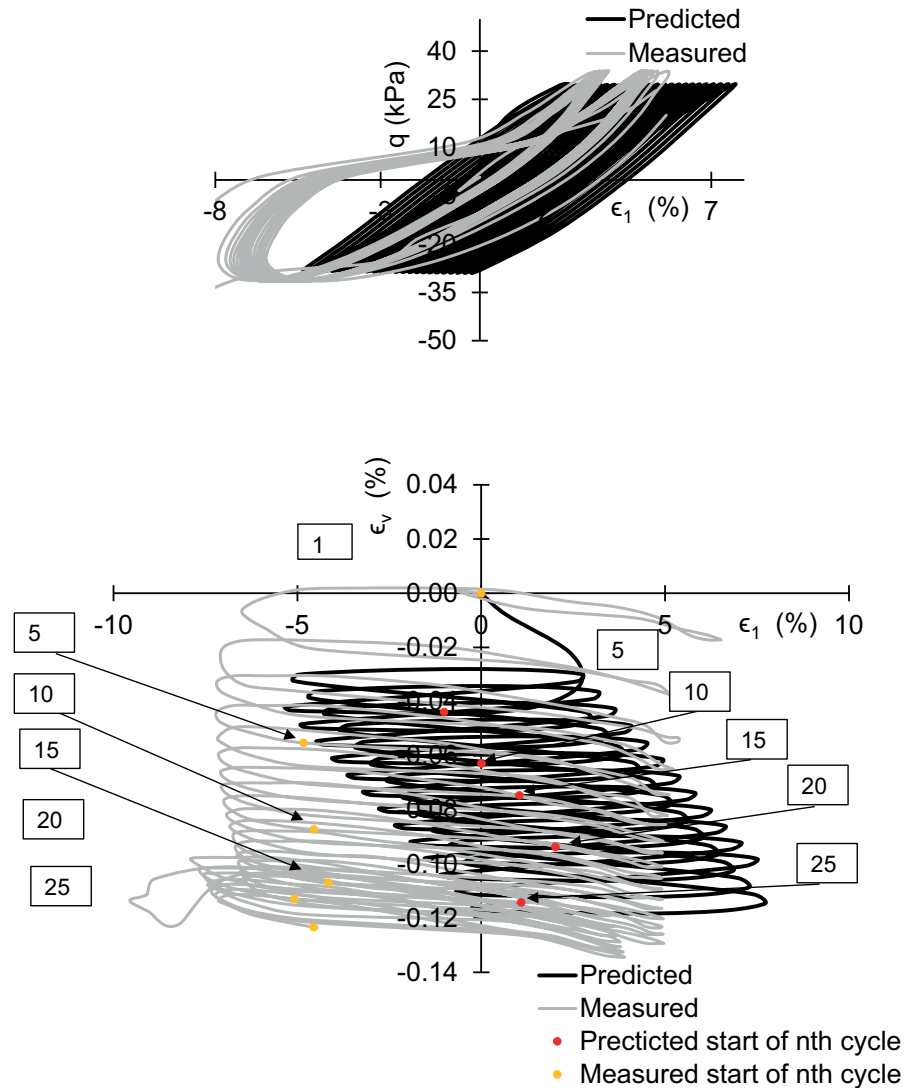


Figure 4.25: Measured and predicted values for the development of axial strain with loading cycles (top) and the accumulation of volumetric strain (bottom) for drained cyclic triaxial test with 25 loading cycles at 0.02 Hz for Kippen sand

sufficient to verify its performance for monotonic loading paths such as static triaxial tests. The performance of the constitutive model under cyclic loading is more appropriate hence, numerical predictions for cyclic tests were compared to experimental results for Kippen sand using the calibrated material parameters (Table 4.6). In order to determine the efficiency of the hypoplastic model with intergranular strains to model cyclic behaviour, Figure 4.25 compares predicted and measured curves for the development of axial strain with 25 loading cycles for the drained cyclic triaxial test performed at 0.02 Hz. Figure 4.25 compares the accumulation of volumetric strain with loading cycles for the drained case. The magnitude of accumulated strains and number of cycles as indicated in Figure 4.25 are in good agreement hence; it can be asserted that modelled time can be compared to real time. This conclusion is important as it validates comparison of simulation time to

real time, making simulation of field deep vibratory compaction process more authentic.

Table 4.6: Calibrated hypoplastic model parameters of sands

	ϕ_c	h_s	n	α	β	e_{d0}	e_{c0}	e_{i0}	m_R	m_T	R	β_χ	χ
Kippen	31	195	0.168	0.243	1.03	0.672	1.116	1.283	3.69	2.78	0.00012	0.3	6
Hamburger	31	4000	0.29	0.164	0.218	0.526	0.813	0.935	2	5	0.0001	0.5	5
Ottawa	30	2000	0.22	0.25	1	0.53	0.82	0.94	2	5	0.0001	0.5	6
A1	33.7	552	0.36	0.04	2.76	0.38	0.8	0.92	6.6	4.25	0.0001	0.7	1
A2	32.3	980	0.36	0.03	2.51	0.51	1	1.15	8.68	4.44	0.00011	0.5	2
A3	33	410	0.47	0.04	1.52	0.47	0.72	0.82	5.35	0.47	0.0001	1	1
A5	32.9	37	0.4	0.0007	6.03	0.67	1.12	1.28	2	4	0.0001	0.35	5

5 Validation of Numerical Framework for Deep Vibratory Compaction

Validation is imperative to numerical modelling. In order to validate the developed framework, the results were validated against 1g model tests and field measurements. A mini model vibrator was fabricated to conduct 1g deep vibratory compaction model tests in sand as described in the previous chapter. CPT was performed before and after compaction to determine the degree of compaction and these results were used to validate the numerical framework. As part of field measurements, deep vibratory compaction was used to compact an open-cast mine deposit using a V48 vibrator. Field measurements in the form of CPT and accelerometer data from the vibrator were used to validate the numerical framework. CEL based framework as described in previous chapter was used to simulate the 1g model tests and field compaction process. The feasibility of CEL framework to simulate the deep vibratory compaction process was validated based on this comparison which is discussed in detail in this chapter. In addition to this the chapter also compares two different numerical frameworks namely classic Lagrangian and CEL. The comparison helps reason and validate choice of CEL framework to model deep vibratory compaction process.

5.1 Comparison of Classical FE and CEL

Numerical simulations of the deep vibratory compaction technique was carried out using the Coupled Eulerian Lagrangian (CEL) approach. The process that is being simulated involved large scale deformations and hence, the choice was made after rigorous analysis. Two different numerical frameworks, classic Lagrangian and CEL were chosen and identical simulations were carried out using both frameworks. Special attention was paid to make the two simulations in the different frameworks to be as similar as possible in terms of model dimensions, boundary conditions, constitutive material law and integration schemes used. This section first briefly describes the models created in each framework and then aims at comparing the results from each one of them.

5.1.1 Classic Lagrangian (FE) Framework

ABAQUS 6.14 Explicit enabled was used to model deep vibratory compaction in classical FE regime (Dassault Systemes, 2014). A 3D Lagrangian model with a diameter of 40 m and height of 50 m consisting 307228 hexahedral elements was created to model soil domain (Figure 5.1). The external lateral boundaries were restrained against horizontal movement. The bottom boundary of the model was restrained against vertical movement.

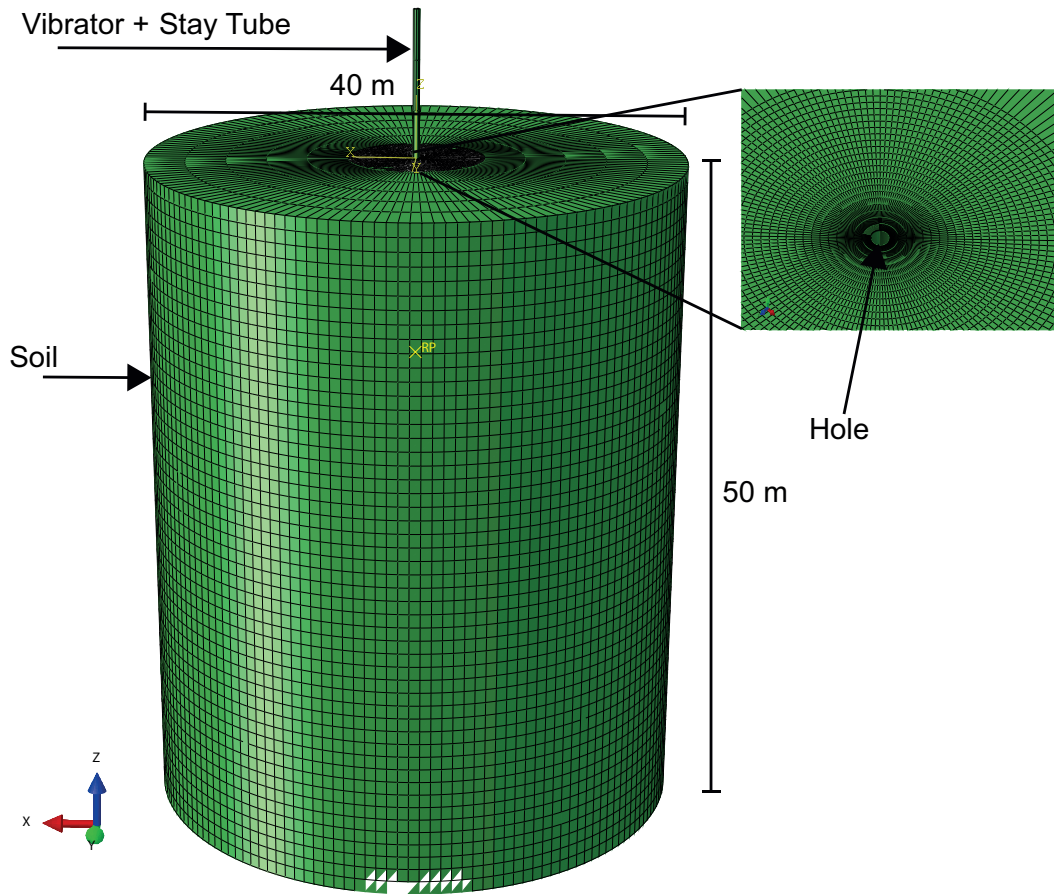


Figure 5.1: 3D classic Lagrangian finite element model for deep vibratory compaction simulation

The vibrator was modelled as a 5 m long, 0.47 m diameter cylindrical Lagrangian body. The vibrator was vertically hinged (pinned connection) to a stay tube also modelled a Lagrangian body of the same diameter and length of 26 m. The bottom end of the vibrator was free to move in the horizontal plane ($x - y$). A cylindrical soil domain of 0.47 m similar to the diameter of the vibrator and height of 21 m was cut out of the main soil domain (See Figure 5.1). This void was created in order to insert the Lagrangian vibrator-stay tube body into the soil domain. This facilitated the vibrator to be wished-in-place at required depth of 21 m at start of the simulation. The stay tube was pinned at its upper end to replicate real-life clenching of the tube to a crane. The numerical calculation steps considered a linear bulk viscosity of 0.42 and quadratic bulk viscosity of 1.2 as per the work of Kelm (2004) and Hamann et al. (2015). A time-scaling factor (which determines the number of time steps in ABAQUS) of 0.4 was chosen after multiple iterations similar to the CEL model was explained in the previous Chapter 4. Soil domain was modelled using the hypoplastic with intergranular strains constitutive law, which has already been

described in detail in the previous Chapter 4.

5.1.2 CEL Framework

The CEL model has been described and discussed in detail in Chapter 4. In this case the vibrator along with the stay tube was wished in place at a depth of 21 m as in the classical Lagrangian model. The mesh of the soil domain was made finer with 259092 hexahedral elements to have a discretization as similar as possible to the FE model.

5.1.3 Comparison of Frameworks

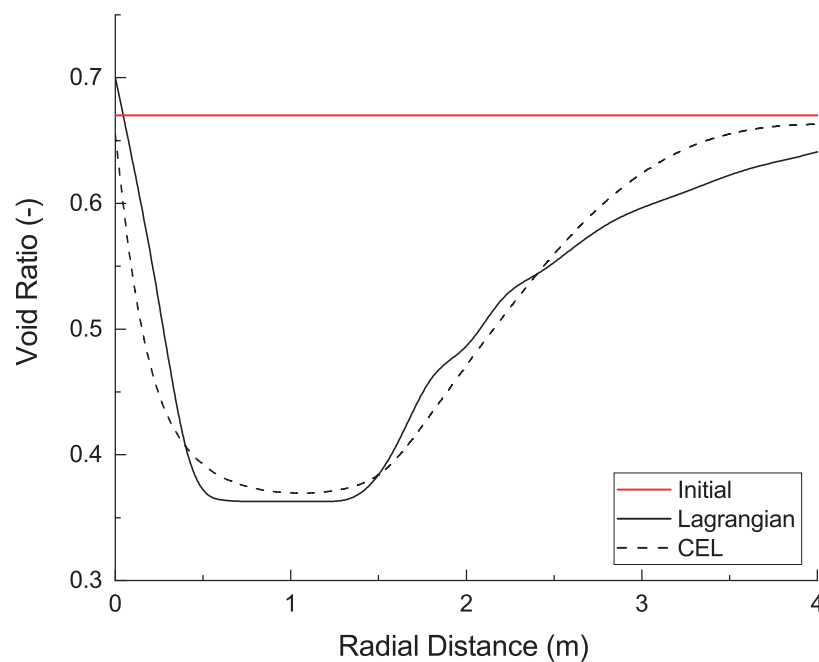


Figure 5.2: Comparison of void ratio variation with radial distance around vibrator as obtained classic FE and CEL frameworks

Simulation in both frameworks were carried out for a single compaction step at a constant depth of 21 m for 15 s. The compaction time was limited to 15 s as the classical Lagrangian simulation failed at this stage due to large deformations, hence, no further simulation was possible. In order to replicate the vibrations of vibrator, sinusoidal nodal forces of 520 kN were applied in x and y directions at the tip of vibrator for both the simulations at constant frequency of 30 Hz. Material parameters of Hamburger sand as per Table 4.6 were considered to model the soil domain in both frameworks. The vibrator and stay tube were modelled as a linear elastic material with the properties of steel in both frameworks. Figure 5.2 describes the variation of void ratio with radial distance at the tip of vibrator for both scenarios. It can be well observed that the results are comparable qualitatively and magnitude of void ratio change is of the same range. The difference in results can well be explained by the variation in discretization of the models. While the FE framework finely discretized the soil domain with 307228 elements, the CEL model had 259092 elements.

Classical Lagrangian FE is a well established method and has been used over years for simulation of various dynamic geotechnical processes but nonetheless its usage is limited in cases of excessive deformations (Qiu et al., 2011). The CEL formulation can in such cases be used to model scenarios that involve large deformations. CEL-based model with 66304 hexahedral elements led to results that converged to results from CEL model with 259092 elements (Figure 5.3). This convergence supported the choice of 66304 element model to model complete deep vibratory compaction process with affordable computational effort.

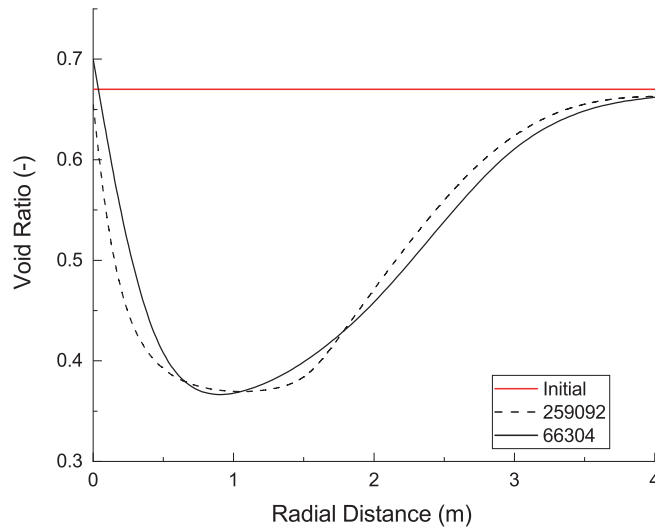


Figure 5.3: Comparison of void ratio variation with radial distance around vibrator as obtained from CEL model with 259092 and 66304 elements

Following validation of choice of CEL framework over other numerical frameworks to model deep vibratory compaction process. The following sections would discuss the accuracy and validity of the CEL model to capture the process. CEL framework was used to simulate the 1g model test and field deep vibratory compaction process. The results from numerical framework was then compared to actual measurements and the precision of simulations to capture the process was analysed and commented upon. Firstly 1g model tests are simulated and its results are compared followed by the simulation of field deep vibratory compaction process.

5.2 1g Model Measurements and Simulations

In this section the 1g model test measurements and simulations would be discussed for a better understanding of the compaction process.

5.2.1 1g Model Measurements

Details about the methodology used to conduct the 1g model tests has already been discussed in Chapter 4. CPT tests were performed at three radial distances from the centre of the compaction point to study the extent of compaction. Figure 5.4 depicts

the maximum tip resistance values for various frequencies at various radial distances. In Figure 5.4, it can be observed that maximum compaction was observed at 70 mm and minimum compaction was obtained at a distance of 250 mm. It can also be observed that the extent of compaction is greater at higher frequencies than at lower frequencies with the same vibrator mass and eccentricity. Figure 5.4 shows that the degree of compaction is maximized at 45 and 60 Hz. Detailed analysis on the effect of frequency on compaction and reason behind higher tip resistance at 70 mm radial distance for compaction at 45 Hz in Figure 5.4 are discussed in the following section. The maximum tip resistance is recorded at a radial distance of 250 mm at 60 Hz, and as the frequency decreases, the recorded tip resistance also decreases (Figure 5.5). The tip resistance values at 250 mm for frequencies of 15 and 30 Hz are similar, indicating that compaction at lower frequencies leads to a negligible compaction at larger radial distances (Figure 5.5).

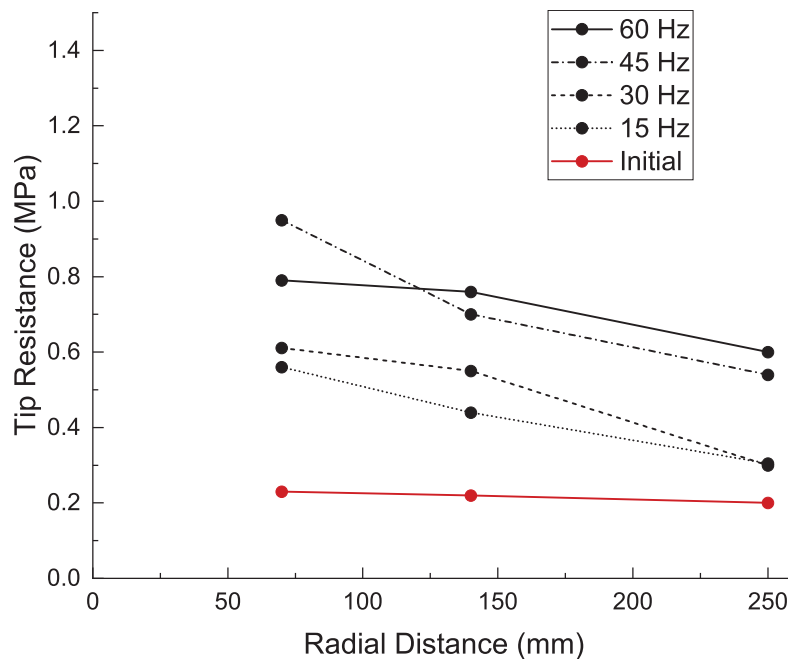


Figure 5.4: Maximum tip resistance at various radial distances for different compaction frequencies in model tests with model vibrator

5.2.1.1 Ground Vibration Measurement with a Geophone

The resonance of the vibrator-soil-system leads to an increase in ground vibrations (Masarsch and Fellenius, 2005), and hence, measurement of the ground vibrations can provide useful insight into the effect of the frequency on compaction. To study the effect of the frequency on the ground vibrations, a geophone was installed on top of the sand layer at a distance of 250 mm away from the centre of the compaction point in the test tank. Figure 5.6 describes the increase in the particle velocity amplitude with increasing frequency. The tip resistance at a radial distance of 250 mm in Figure 5.5 can be studied in tandem with the maximum particle velocity, and it can be observed that both the tip resistance and maximum particle velocity are low at frequencies of 30 and 15 Hz.

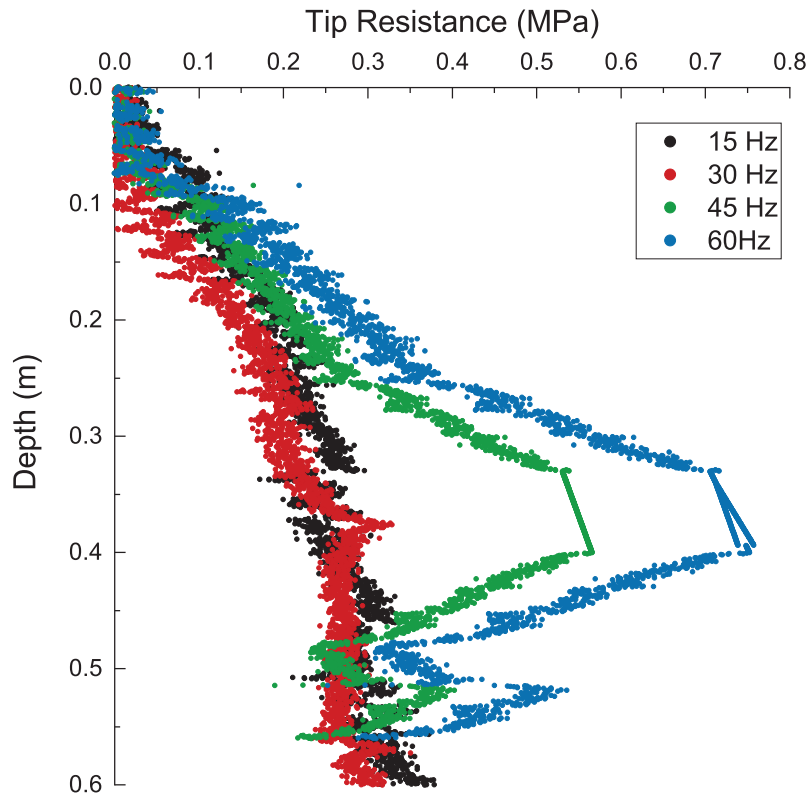


Figure 5.5: Tip resistance for various compaction frequencies at 250 mm radial distance from model vibrator in model tests

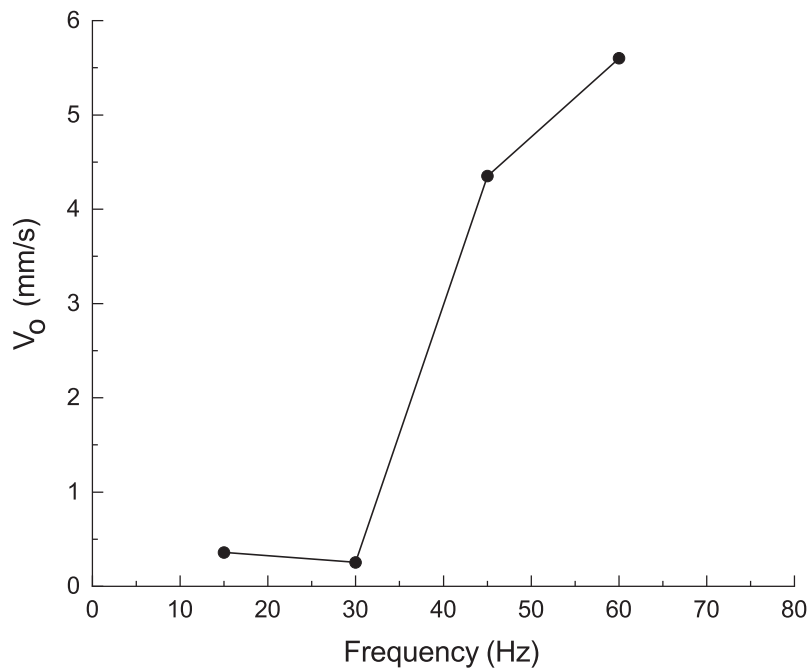


Figure 5.6: Variation of maximum RMS value of particle velocity amplitude with frequency at 250 mm radial distance in model tests

5.2.2 1g Model Test Simulations

The following sections would describe the CEL model created to simulate the 1g model tests and would also compare the simulation results to experimental measurements.

5.2.2.1 CEL Model for 1g Model Test

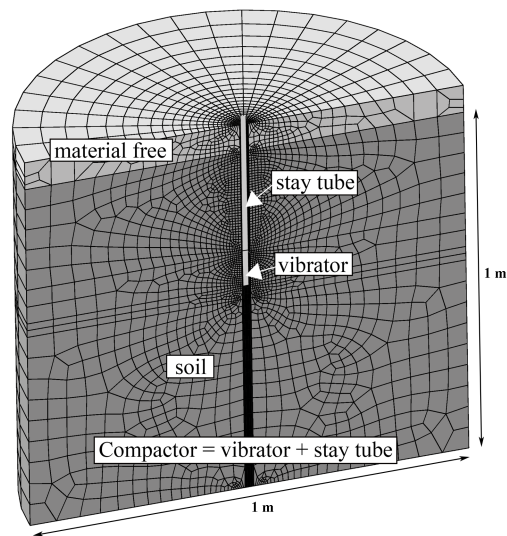


Figure 5.7: Section of CEL model to simulate 1g model test

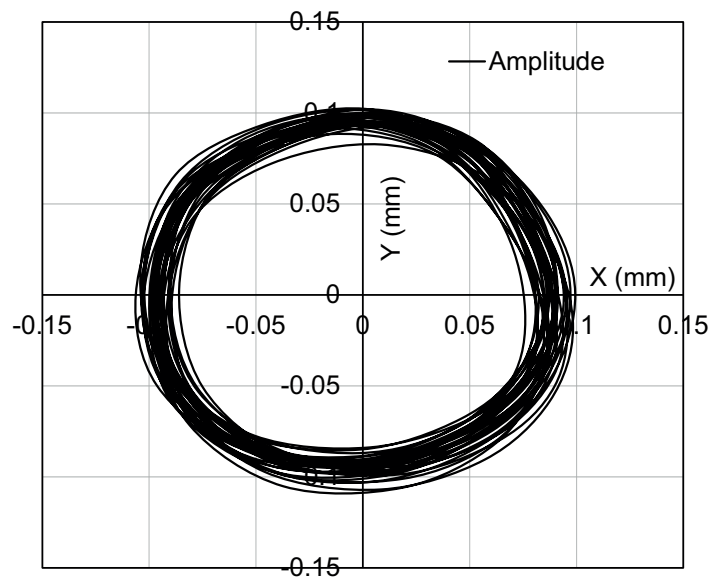


Figure 5.8: Movement of tip of the vibrator for compaction frequency of 30 Hz in model test

A 3D cylindrical model with a height of 1.1 m and radius of 0.5 m was created with 3010 hexahedral elements. The dimension of the model were made identical to the test tank used for the 1g model tests as described in Chapter 4. The top 0.1 m of the domain was modelled as a void area (similar to the model tests) to allow for the movement of material into the area during the simulations. The external lateral boundaries were restrained against horizontal movement. The bottom boundary of the model was restrained against vertical movement. The vibrator was modelled as wished-in-place at a depth of 0.35 m in the sand domain, as depicted in Figure 5.7. The vibrator was modelled as a rigid body with a length of 0.34 m and diameter of 0.038 m connected to a stay tube of a similar diameter and length of 0.24 m. The stay tube was modelled as a rigid body. To replicate the vibrations of the vibrator, nodal displacements in the x and y directions (horizontal plane) were applied at the tip of the vibrator. The displacements were evaluated by double integrating the acceleration data recorded by the accelerometer during the tests. Figure 5.8 shows the movement of the vibrator (displacement) during compaction at an operational frequency of 30 Hz, and it can be observed that the movement of the vibrator was nearly circular. The contact between the vibrator and the soil was modelled according to Coulomb's friction law. As a simplification, the tangential friction coefficient between the vibrator and the soil was assumed to be zero (Chmelnizkij et al., 2017). Soil domain was modelled using the hypoplastic model parameters of Hamburger sand (sand which was used to conduct model tests) as enlisted in Table 4.6. The vibrator and stay tube were modelled as a linear elastic material with the properties of steel.

5.2.2.2 1g Model Simulation Steps

ABAQUS Explicit formulation was used to simulate 1g model test deep vibratory compaction process. The process of penetration and withdrawal of the vibrator in soil was not modelled due to the higher computational demand. A time scaling factor (which explicitly determines the number of time steps in ABAQUS) of 0.5 was chosen after multiple iterations. The simulation included two primary steps. The initial step was where the geostatic forces according to the K_0 condition were activated with sand at an initial relative density of 0.2 as in model test and the vibrator was modelled as fixed in place at a depth of 0.35 m in the sand. The K_0 condition assumption was validated by measuring the tip resistance values before and after the penetration of vibrator. The results showed a marginal influence of penetration on the in-situ stresses. The second step modelled the vibration process of the vibrator at the required depth similar to the model tests. The nodal amplitudes as calculated from the model tests were activated at the tip of the vibrator as described earlier to simulate the vibration process. A vibration duration of 30 s was modelled similar to the 1g model tests.

5.2.2.3 CPT Correlation for Hamburger sand

Efficiency of deep vibratory compaction in 1g model tests was ascertained by means of CPT measurements before and after compaction. The CPT results would be used to validate the numerical model. Deep vibratory compaction simulation does not directly yield us the CPT tip resistance values and hence a CPT model was created to develop CPT correlation for sand under consideration as described in Chapter 4. The CPT simulations were carried

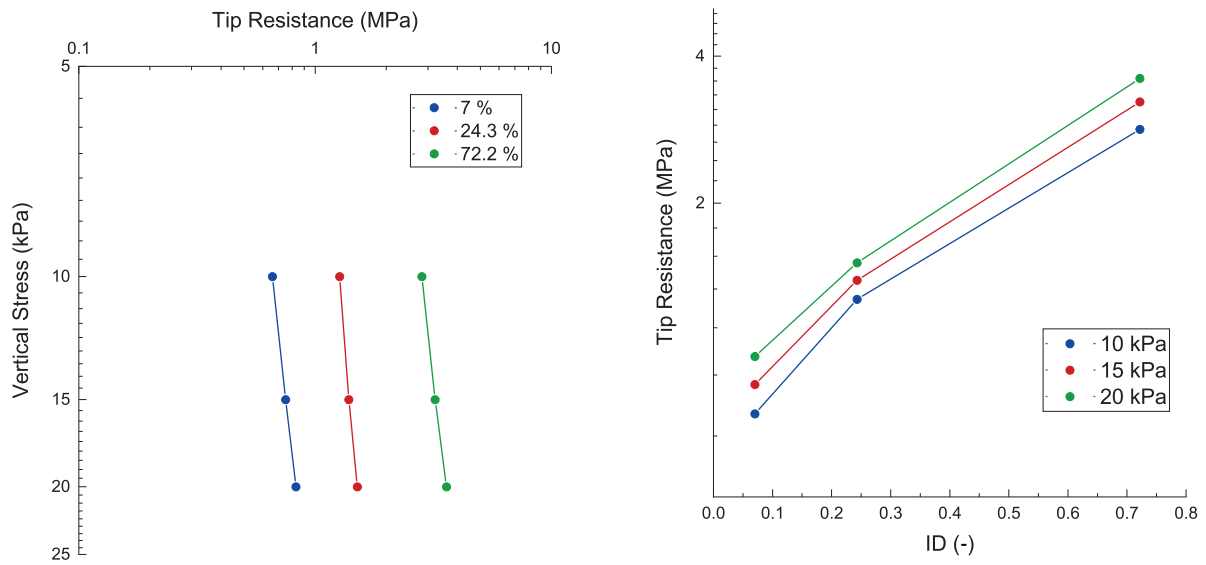


Figure 5.9: Tip resistance variation with vertical stress (left) and relative density (right) for Hamburger sand as obtained from CPT simulations

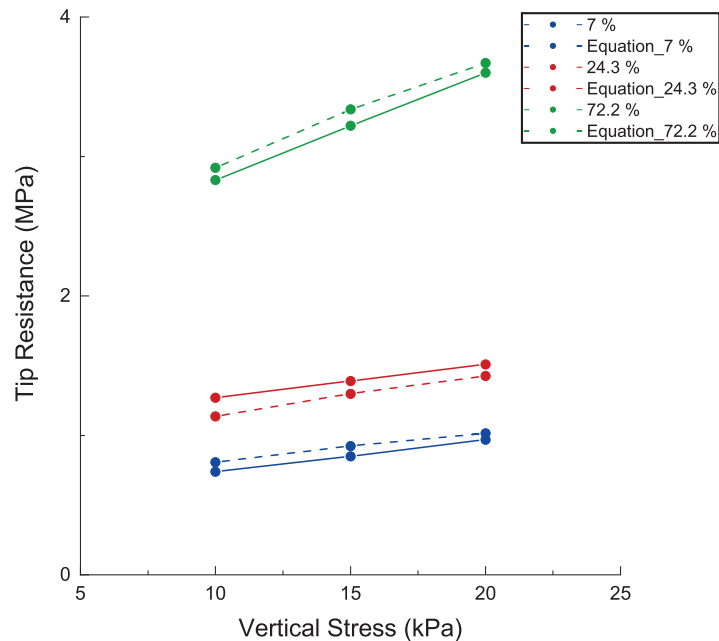


Figure 5.10: Comparison of tip resistance values as obtained from developed CPT relation for Hamburger sand at various relative densities

out for three different relative densities (ID) and vertical stresses (σ'_v) in the range of stress states, as expected in the 1g model tests. The tip resistance values (q_c) obtained for the various initial conditions are depicted in Figure 5.9. The tip resistance is plotted against the vertical stress in double logarithmic form (Figure 5.9 (left)) and against the relative density in half logarithmic form (Figure 5.9 (right)). The simulation results were used to

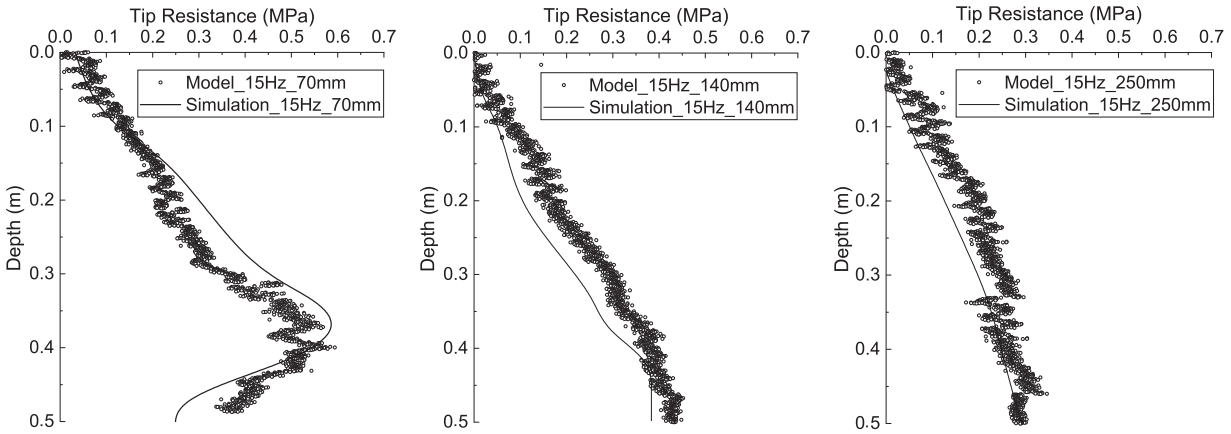
determine the constants of Equation 4.2 to derive the following Equation 5.1.

$$q_c = 329.2 P_a \left[\frac{\sigma'_v}{P_a} \right]^{0.33} \exp^{1.97 I_D} \quad (5.1)$$

where, the terms are as described for Equation 4.2. Figure 5.10 compares the results of the tip resistance values from the CPT model against the values obtained by the above equation. It can be observed that the developed equation can accurately estimate the tip resistance values.

5.2.2.4 Comparison of 1g Model Test and Simulations Results

The numerical simulations indicated a decrease in the void ratio around the vibrator after deep vibratory compaction. The developed CPT correlation (Equation 5.1) was used to obtain the tip resistance values (q_c) from the void ratio and vertical stress values as obtained from numerical simulations at required radial distances. Figure 5.11 compares the q_c values at 15, 30 and 45 Hz obtained from 1g model tests and numerical simulations. The simulation results fit the 1g model test results fairly well. The simulated CPT values exhibit no fluctuation unlike the model test values, as they have been derived from the CPT equation. The results are observed to fit better at lower frequencies than at higher frequencies. The simulation results can be observed to overestimate the tip resistance values, probably owing to the pronounced damping effect at higher frequencies in the 1g model tests, which was not effectively captured by the numerical model.



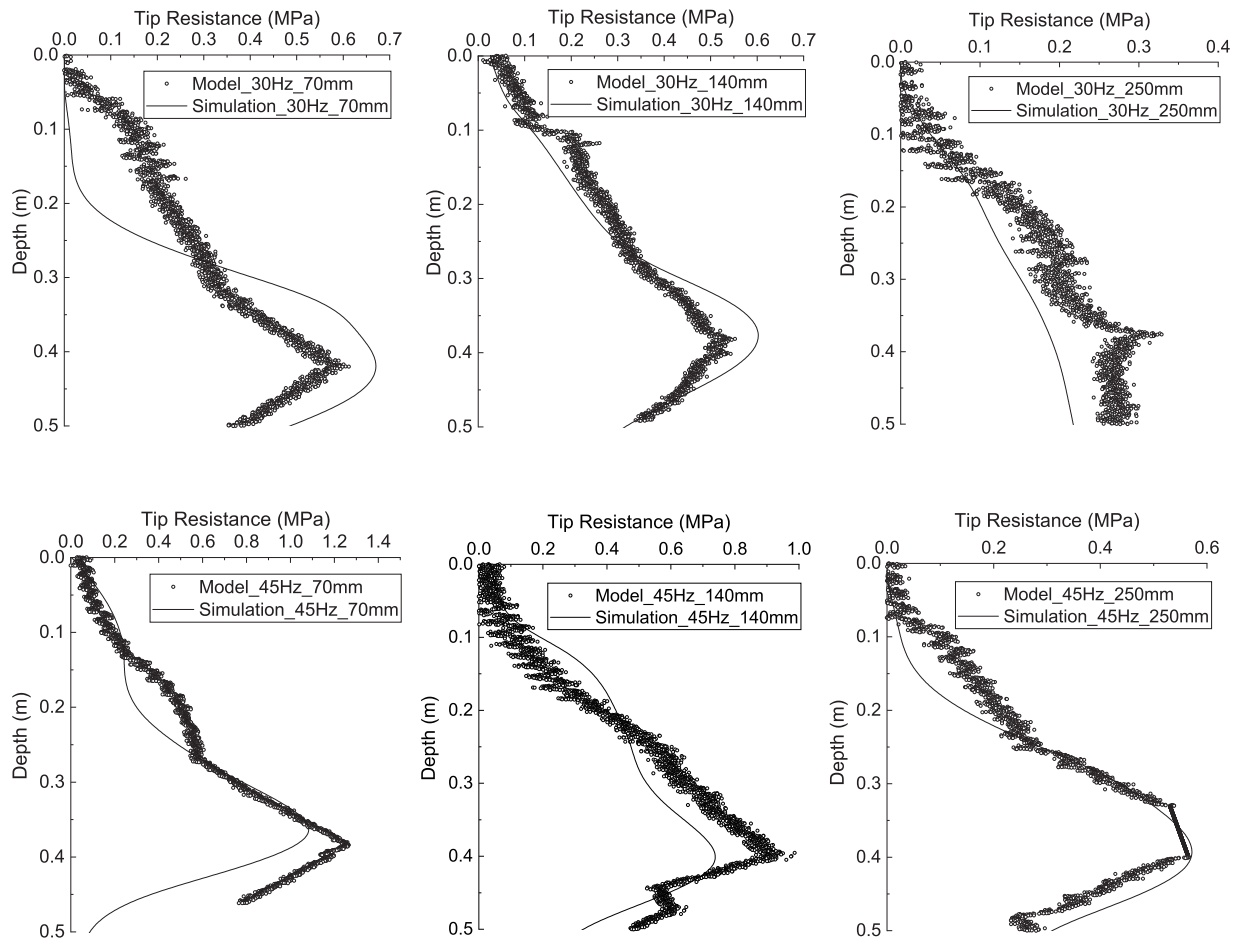


Figure 5.11: Comparison of tip resistances from 1g model tests and numerical simulations at compaction frequency of 15, 30 and 45 Hz

5.2.2.5 Spatial and Temporal Insight into 1g Model Test

It has been observed in the preceding section that 1g model tests facilitated measurements only in the form of CPT values and geophone data. The numerical simulations results have already been compared to CPT values from model tests in order to validate the numerical framework in Chapter 5. In this section other aspects of numerical simulation results would be discussed and its advantages over model tests would also be highlighted. The numerical results provide a holistic spatial and temporal insight into the process which was not possible in case of the model tests.

Figure 5.12 describes the development of the void ratio around the tip of the vibrator at a depth of 0.35 m after compaction at 45 Hz for Hamburger sand (sand used in model tests). Three zones of compaction as per Kirsch and Kirsch (2017) were observed, which are difficult to observe in 1g model tests. Majority of the researchers (Kessler et al., 2006; Schmitter and Adam, 2017) till date have considered soil as an elastic medium and hence have not been able to capture this phenomenon. The first zone, just around the vibrator, shows zero or negative compaction (no reduction or increase in the void ratio) due to

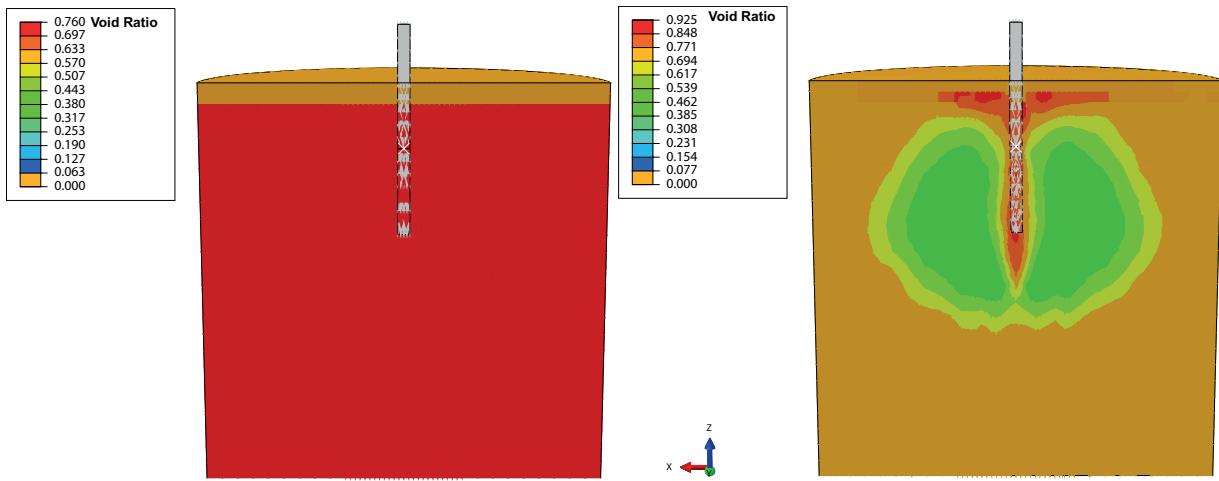


Figure 5.12: Contour of void ratio around vibrator before (left) and after (right) at compaction frequency of 45 Hz for Hamburger sand as obtained from simulation

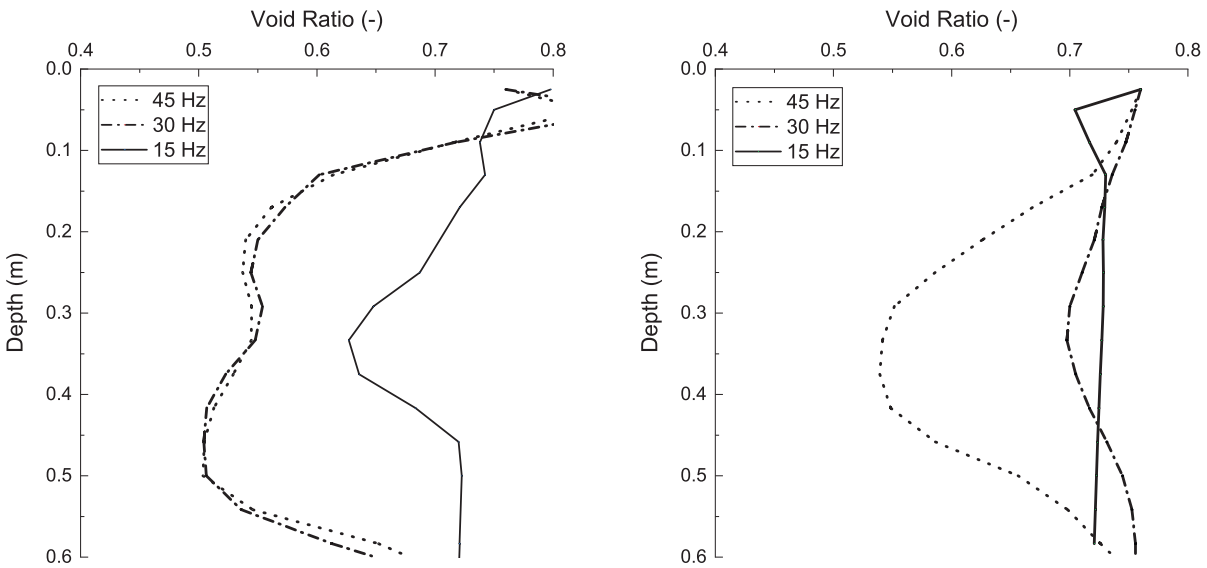


Figure 5.13: Variation of void ratio with depth for different compaction frequencies at radial distance of 70 mm (left) and 250 mm (right) for Hamburger sand as obtained from simulation

dilatancy because of the large strain amplitudes. The second zone, slightly farther from the vibrator, shows compaction (reduction in the void ratio) as the strain amplitudes are too small to create dilatancy. In the third zone, approximately 0.3 m from the vibrator, the strain amplitudes are negligible and do not cause any compaction (void ratio similar to that of virgin sand). The decrease in the void ratio as compaction progressed was found to increase with frequency (Figure 5.13), and the same is observed in the 1g model tests in terms of a higher tip resistance. The void ratio at a frequency of 30 and 45 Hz at a radial distance of 70 mm is similar (Figure 5.13 (left)), which is also observed in the form of the

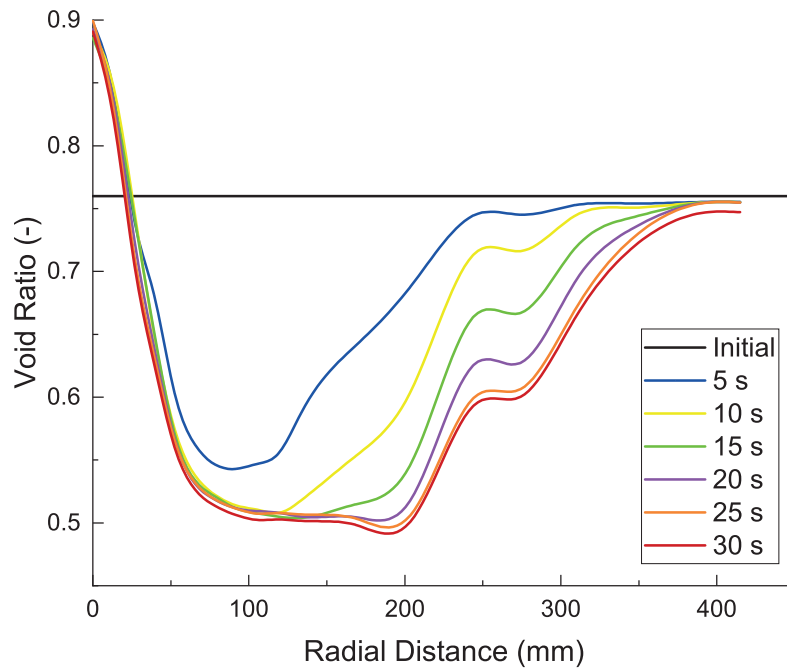


Figure 5.14: Evolution of void ratio along radial distance with time at compaction frequency of 30 Hz for Hamburger sand as obtained from simulation

similar tip resistances from the 1g model test results (Figure 5.4). At a radial distance of 250 mm, there is hardly any reduction in the void ratio at 15 and 30 Hz compared to that at 45 Hz (Figure 5.13 (right)), which is also observed in the case of the 1g model test results (Figure 5.4).

Numerical simulations help analyse the temporal variation of compaction which is difficult to observe in the model tests. Figure 5.14 depicts the evolution of the void ratio with time for a compaction frequency of 30 Hz, and it can be seen that the compaction is nearly stagnant after 25 s. The results captured realistic compaction time unlike (Arnold and Herle, 2009), which predicted faster compaction rates. It can be observed that no compaction occurs beyond 25 s and hence, this can be used to design an optimised compaction time and unlike current practice, not follow a standard compaction time based on past field experiences. Numerical simulations can be carried out for the granular material under consideration and an effective compaction time can be determined.

In addition, the numerical simulation results also help visualize changes in stress state before and after compaction in the entire soil domain which may not be possible to achieve in any form of physical measurements. Figures 5.15 and 5.16 depict the vertical and horizontal stress contour in the $x - z$ plane before and right at the end of compaction. It is to be noted that at the end of compaction the vibrator is still in motion and impacting centrifugal forces on the surrounding soil and hence an increase in both vertical and horizontal stress is observed around the vibrator in direction of the applied centrifugal force at that instance. It can also be observed in Figure 5.16 that there is an overall increase in magnitude of compressive horizontal stress throughout the soil domain. The increase in horizontal stresses in soil after deep vibratory compaction has also been observed by Massarsch and Fellenius (2002). Figure 5.17 describes the density contour and it also

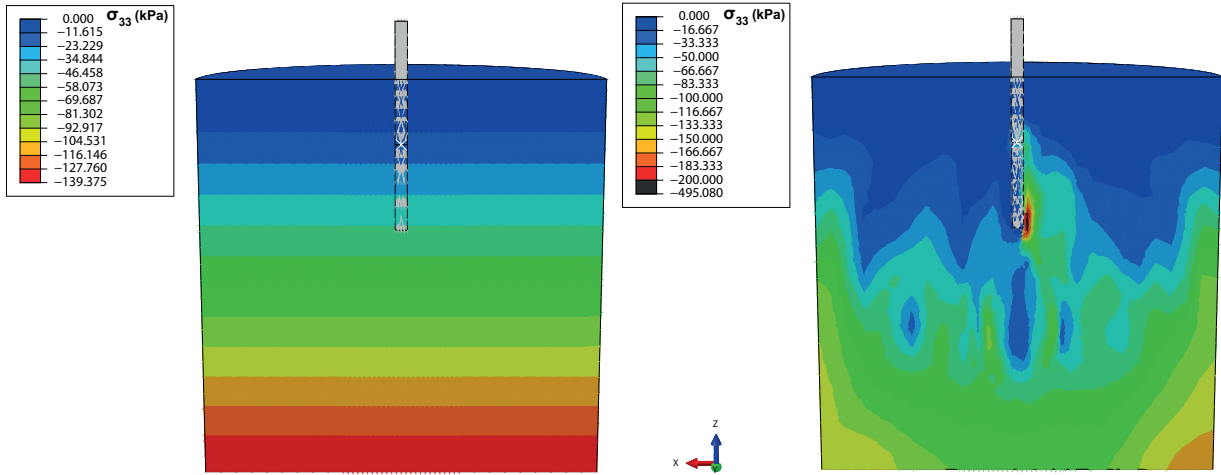


Figure 5.15: Contour of vertical stress (σ_{33}) around vibrator before (left) and at end of (right) compaction at compaction frequency of 45 Hz for Hamburger sand as obtained from simulation

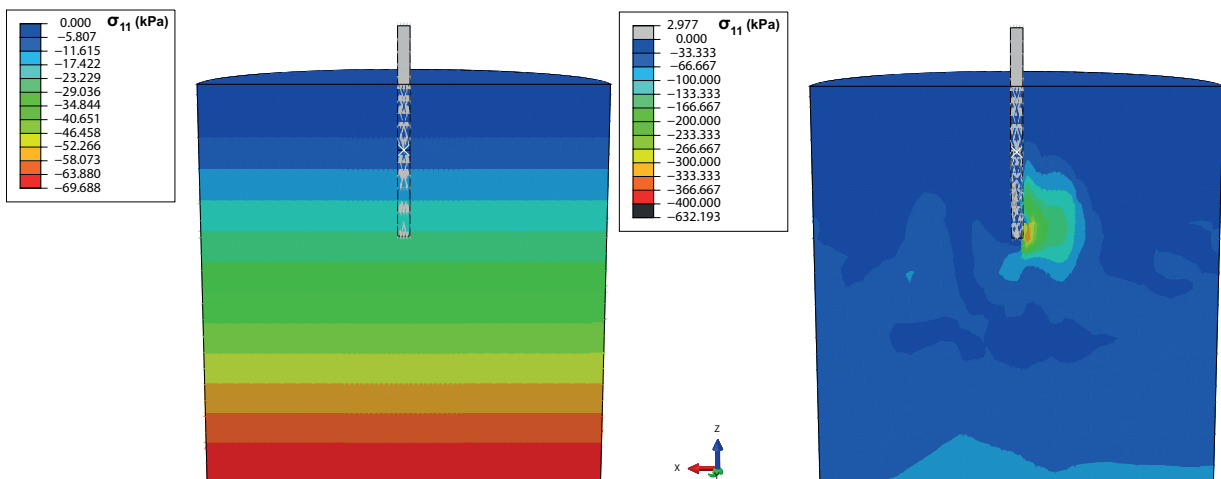


Figure 5.16: Contour of horizontal stress (σ_{11}) around vibrator before (left) and at end of (right) compaction at compaction frequency of 45 Hz in a numerical model test of Hamburger sand

confirms the existence of zones of compaction around the vibrator. The zone closest to vibrator undergoes loss of density while the vibrator is still in motion and as the radial distance increases an increase in density compared to the virgin density is observed.

5.3 Cottbus Field Measurements and Simulations

In this section, Cottbus measurements and simulations would be discussed for a better understanding of the compaction process at realistic stress state conditions.

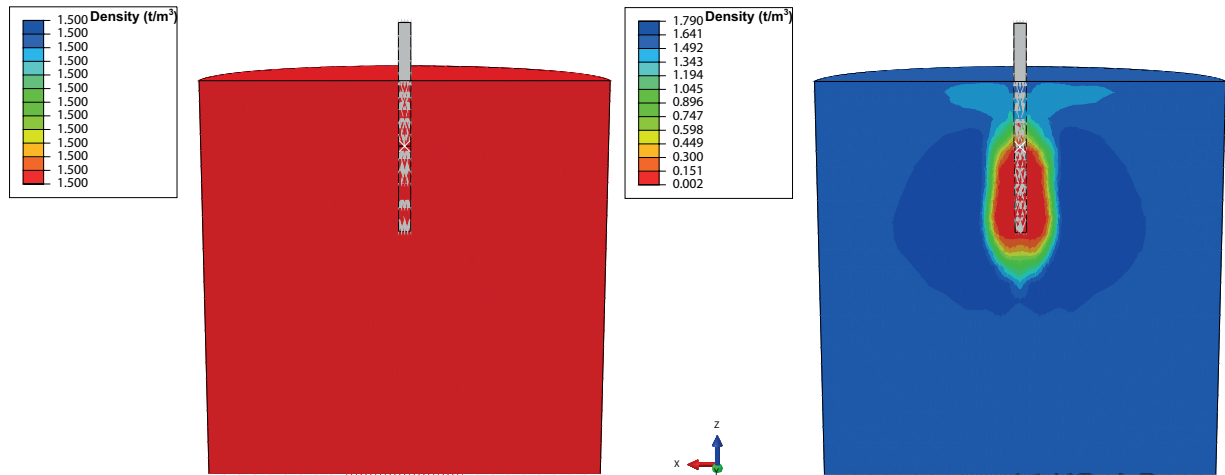


Figure 5.17: Contour of density around vibrator before (left) and after (right) compaction at compaction frequency of 45 Hz for Hamburger sand as obtained from simulation

5.3.1 Cottbus Field Measurements

Chapter 4 described in detail field measurements in Cottbus, Germany, where deep vibratory compaction was used to compact loose residual granular soil called as Kippen soil. CPT measurements before and after compaction and machine data of the vibrator during compaction was collected as part of these field trials. The succeeding sections would discuss the CPT and machine parameters data logged during the field trials, followed by comparison of the simulation results to field measurements. The section would try to analyse the accuracy of CEL framework to simulate on-field deep vibratory compaction process under realistic stress state conditions. This acts a primary step to validate CEL method as an appropriate medium to simulate this compaction process before it can be used to study factors influencing compaction.

5.3.1.1 CPT and Machine Parameters

Figure 5.18 depicts the CPT-u data in the form of tip resistance, sleeve friction and friction ratio before and after three months of compaction for AP16013 compaction point. It should be noted that the ground water level in the area is below the compaction depth; however, water was used to facilitate the penetration of the vibrator into the sand. CPT-u tests before compaction recorded no pore water pressure, as the ground water level was 33 m below surface. CPT-u tests after three months of compaction also recorded no pore pressure, suggesting complete dissipation of any potential pore water pressure caused by water used during compaction. Figure 5.19 describes the time log of power consumption and frequency of operation along depth for three steps of compaction between 21.5 m and 19 m depth. It is to be noted that power is hydraulic unit of the vibrator which includes reactive power and power loss (friction loss, pressure loss) of the vibrator and not the actual compaction power. The frequency remained constant at 30 Hz, and the

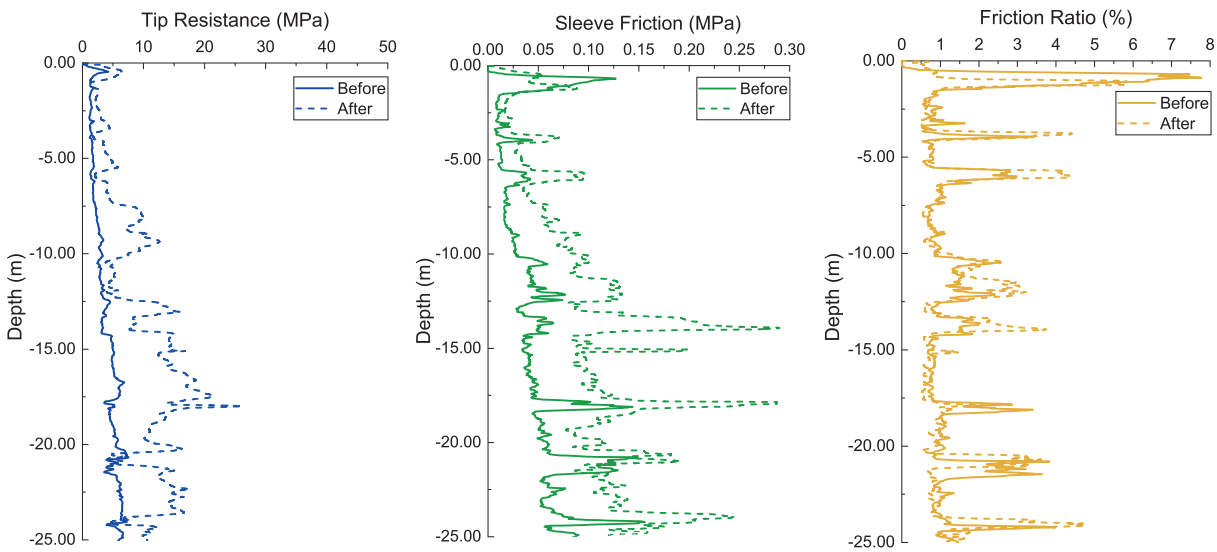


Figure 5.18: Tip resistance (left), Sleeve friction (centre) and Friction Ratio (right) measurement data from field before and after compaction for AP16013 compaction point

power consumption varied drastically only when the vibrator was either pushed down or pulled up. As shown in Figure 5.18 (left), the soil hardly underwent compaction at 20.5 m depth; however, at 20 m, higher CPT values were reached after compaction. An increase in power consumption was observed at 20 m (Figure 5.19), where effective compaction has been observed. The experience of practitioners suggests that an increase in power with compaction is observed as the soil gains stiffness. However, it should also be noted that the magnitude of power increase could vary depending on type of granular material under compaction and type of compaction process. The non-compaction at certain depths can be attributed to the presence of excessive silty layers, Figure 5.20 describes the ratio of CPT tip resistance after and before compaction with friction ratio and it can be observed that soil experiences less compaction for friction ratios beyond 4 %.

5.3.2 Cottbus Field Deep Vibratory Compaction Simulations

The following sections would describe the CEL model created to simulate deep vibratory compaction as carried out in field in Cottbus and would also compare the simulation results to field measurements.

5.3.2.1 CEL Model and Simulation Methodology for Field Deep Vibratory Compaction

Chapter 4 stated that simulation of the entire deep vibratory compaction process involves large-scale deformations and CEL framework was used to simulate the process. The model definition and simulation methodology to replicate the on-field compaction process has already been detailed in Chapter 4.

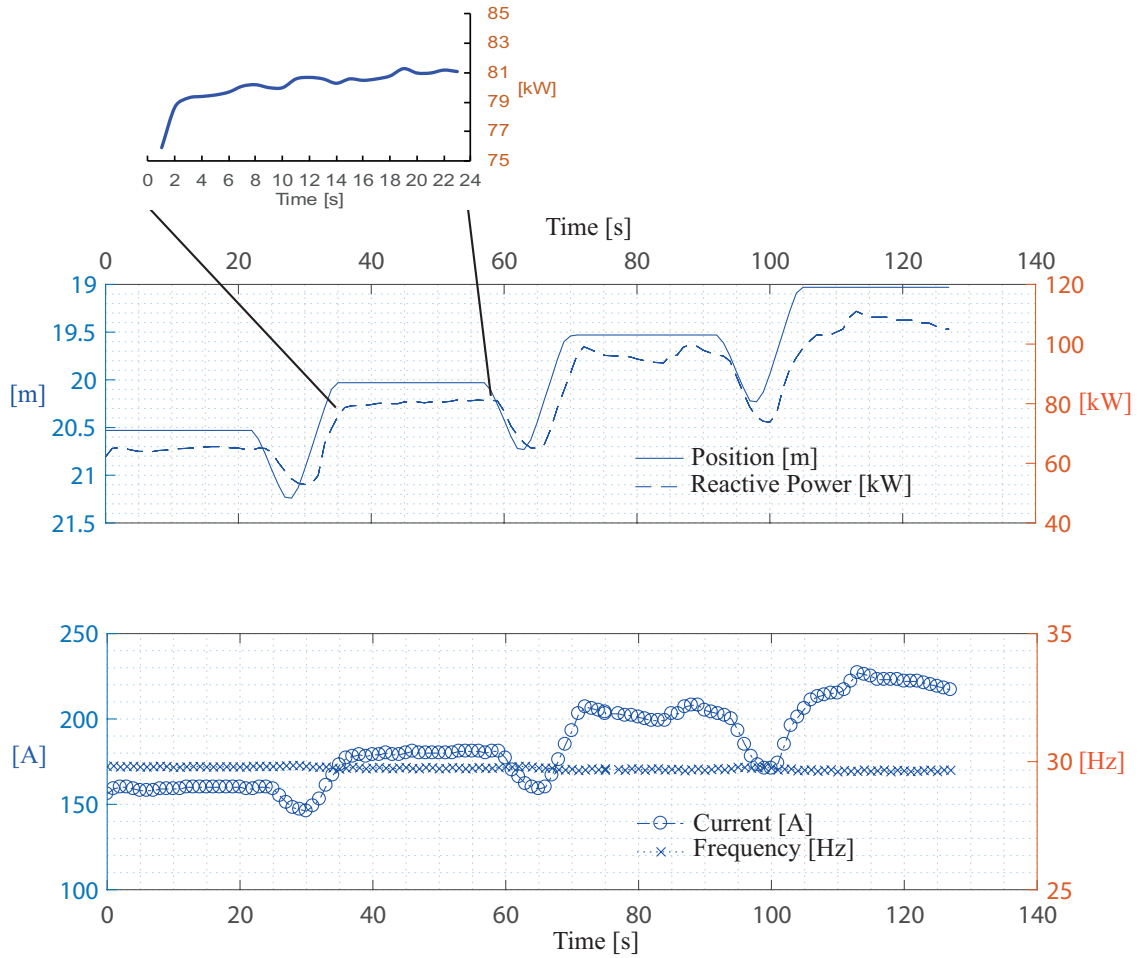


Figure 5.19: Frequency of operation, reactive power and current consumed during deep vibration compaction as recorded by sensors in vibrator during field measurements at Cottbus, Germany

5.3.2.2 CPT Correlation for Kippen Sand

Deep vibratory compaction simulation does not directly yield us the CPT tip resistance values and hence a CPT model was created to develop CPT correlation for Kippen sand as described in Chapter 4. Simulations were carried out for three different relative densities (I_D) and effective vertical stresses (σ'_v) according to stress levels expected in the field. Tip resistance values (q_c) obtained for the various initial conditions are depicted in Figure 5.21. Tip resistance is plotted against vertical stress in double logarithmic form (Figure 5.21 (left)) and against relative density in half logarithmic form (Figure 5.21 (right)). The CPT simulation results were used to find the constants of Equation 4.2 and the following Equation 5.2 was derived

$$q_c = 5.13 P_a \left[\frac{\sigma'_v}{P_a} \right]^{0.89} \exp^{2.18 I_D} \quad (5.2)$$

where, the terms follow those in Equation 5.2.

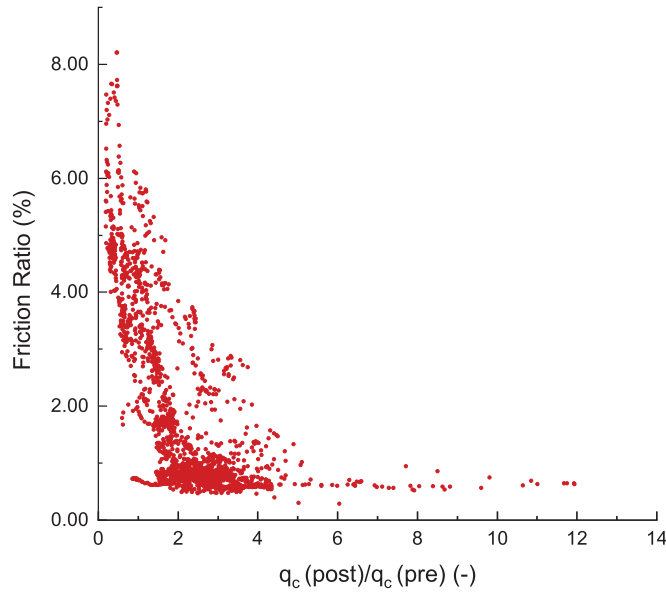


Figure 5.20: Tip resistance ratio v/s friction ratio as per field measurements for AP16013 compaction point

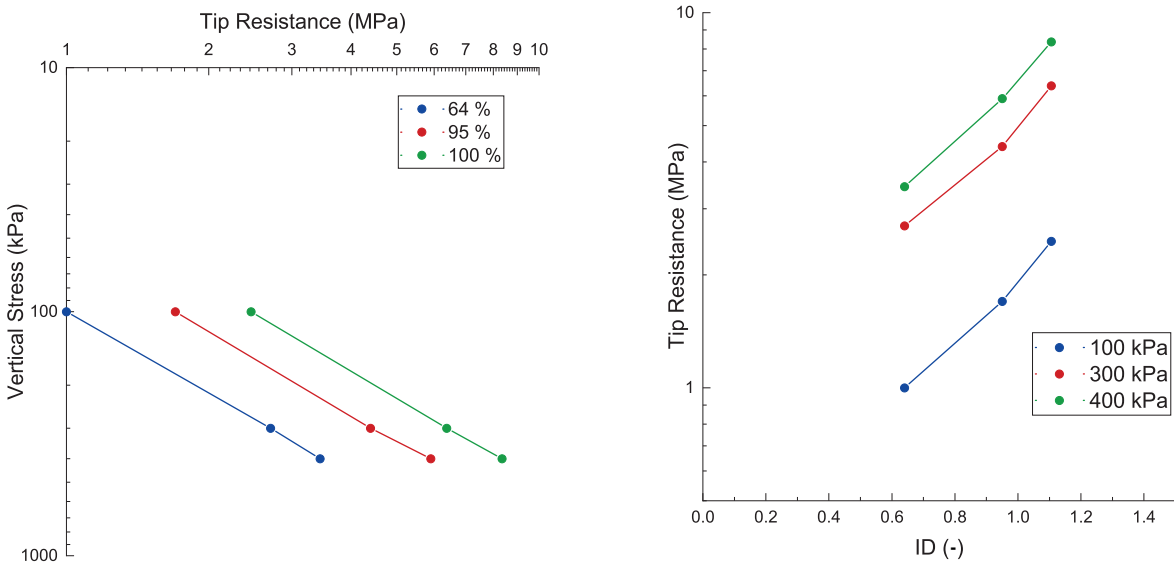


Figure 5.21: Tip resistance variation with vertical stress (left) and relative density (right) for Kippen sand as obtained from CPT simulations

5.3.2.3 Comparison of Cottbus Field Measurements and Simulations Results

Similar to in-field compaction, the entire simulation process was carried out at a frequency of 30 Hz with a centrifugal force of 520 kN. The compaction in the simulations were carried out as per the simulation methodology detailed in Chapter 4 and as per the Pilgrim Step method as described in Figure 4.11. Compaction process of two compaction points AP16015 and AP16013 (Figure 4.6) was simulated. The sand was considered dry in all simulations as the ground water was 33 m below ground level in field and compaction was

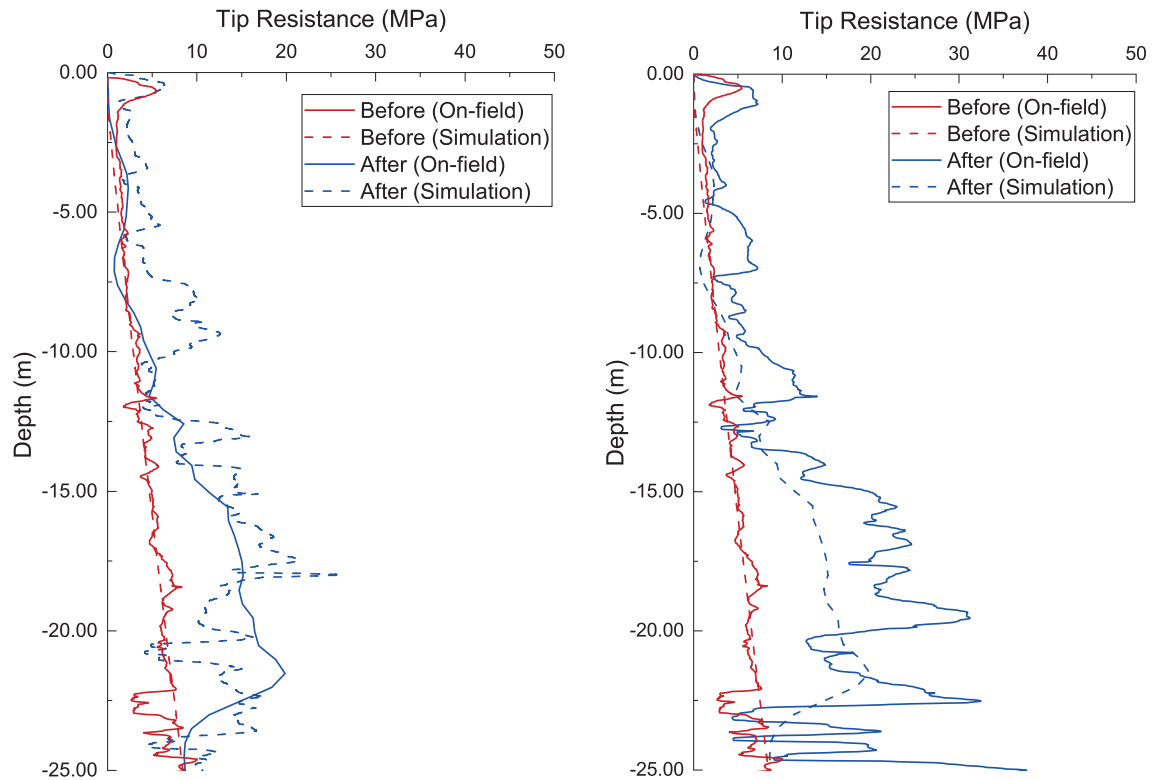


Figure 5.22: Comparison of simulation and field tip resistance values after deep vibration compaction for AP16013 (left) AP16015 (right) compaction point in Cottbus, Germany

carried out between 5 to 25 m depth. Vertical stress and void ratio values over depth at a radial distance of 0.5 m from the centre of the compaction point were extracted. The developed correlation (Equation 5.2) was used to derive the tip resistance values. The in-field CPT was conducted after three months of compaction in order to ensure that all water used to facilitate the penetration of the vibrator had dissipated. Figure 5.22 compares the tip resistance values for two compaction points (AP16015, AP16013). While the simulation results have qualitatively captured the in-field CPT tip resistance values, they show substantial quantitative deviation at some locations. This could be due to the numerical simulation's failure to capture the increase in horizontal stresses after compaction. It has been observed by Massarsch and Fellenius (2002) that an increase in sleeve friction is an indication of increase in horizontal stresses. This was also observed in the field CPT sleeve measurement data (Figure 5.18). However, this was not captured in the simulations, as pulling out the vibrator at the end of compaction to add new sand to compensate for the void created by compaction was not modelled. It should also be noted that the field CPT was conducted three months after compaction; until that time, the re-arrangement of soil particles due to dissipation of excess pore pressures would have occurred, leading to increase in horizontal stresses. In the simulations, the CPT data was evaluated at the end of compaction while the vibrator probe remained in the soil at 3 m depth. The extraction of the vibrator probe out of the soil was not modelled.

5.3.2.4 Comparison of Machine Data

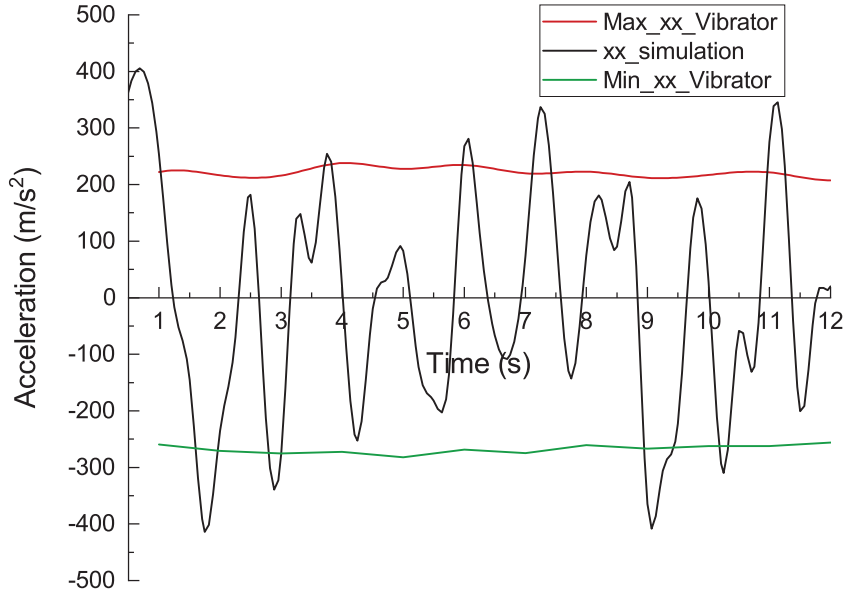


Figure 5.23: Comparison of simulation and vibrator acceleration data during deep vibration compaction for AP16013 compaction point in Cottbus, Germany

The vibrator was equipped with various sensors to log data during compaction as described in Chapter 4. Data loggers logged power consumed, operational frequency, temperature of vibrator, maximum and minimum acceleration of the vibrator, depth of operation and time log of the process during compaction. In addition to comparing CPT data with simulation results, acceleration data of the vibrator was also compared to acceleration results obtained from simulations. Acceleration data in the x -direction at the tip of the vibrator during compaction at a constant depth of 15 m below ground level was chosen. The field data consisted of minimum and maximum acceleration values in the x -direction. Figure 5.23 depicts the comparison of the measured and simulated values. The simulated acceleration time signal in the x -direction falls within the range of the in-field recorded data. This validation further concretizes the accuracy and precision of CEL framework to simulate deep vibratory compaction process.

5.3.2.5 Spatial and Temporal Insight into Field Deep Vibratory Compaction

Numerical simulations help visualize the spatial and temporal effects of compaction as stated earlier, which cannot be achieved in the field with existing measurement techniques. Numerical simulations help in visualizing change in various state parameters due to compaction which cannot be measured during field measurements. Figure 5.24 describes the void ratio contours around the compaction point before (Figure 5.24 (left)) and at the end of compaction between 25 and 5 m depth (Figure 5.24 (right)) at a frequency of 30 Hz with a centrifugal force of 520 kN in Kippen sand as described in Chapter 4 and Chapter 5. The compaction is not uniform, and the compacted area is in the form of a frustum not a cylinder as was intuitively expected. It is apparent that while the vibrator is compacting,

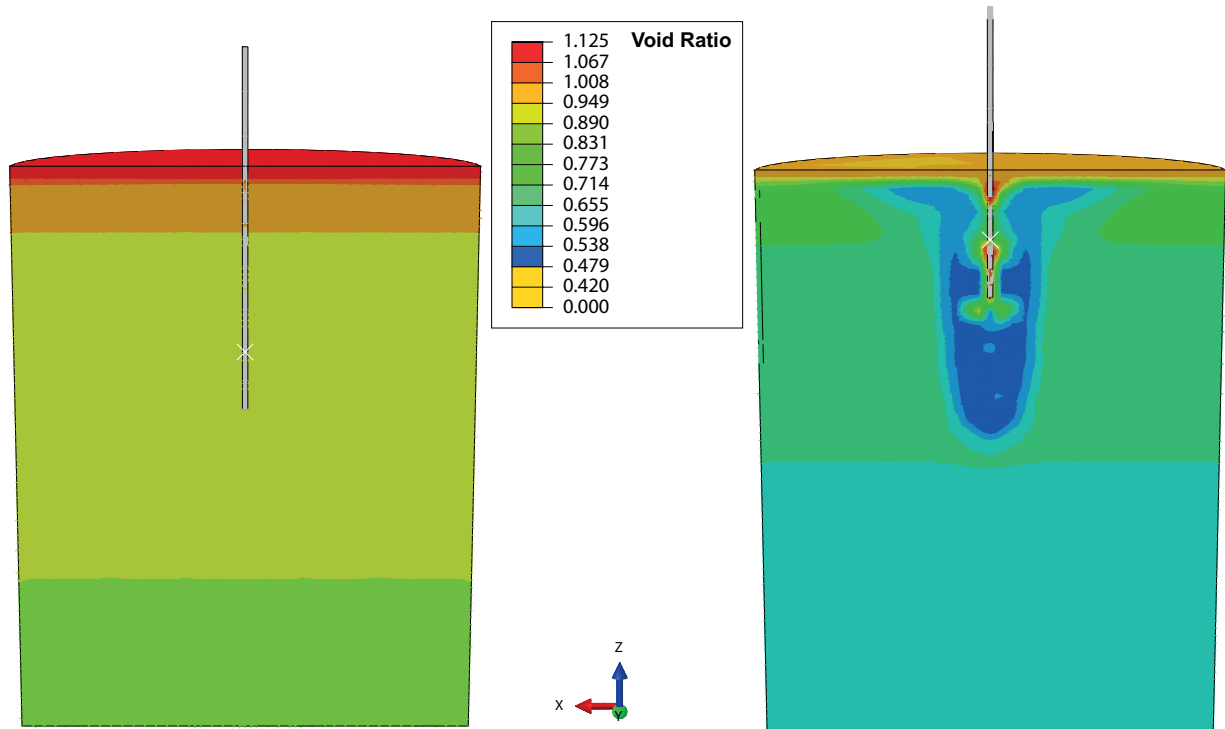


Figure 5.24: Contour of void ratio before (left) and after compaction (right) at compaction frequency of 30 Hz for Kippen sand as obtained from simulation

the area just around the vibrator undergoes no compaction (contraction) or even dilates. Kirsch and Kirsch (2017) suggest that this is due to the large acceleration amplitudes generated near the vibrator. As acceleration amplitude reduces with radial distance, the effect of compaction can be observed. This observation is in line with simulations at model test scale. When the vibrator moves up, the soil fills in the void and is compacted by the vibrations of the vibrator in the upper depths. Figures 5.25 and 5.26 depict the contours for vertical and horizontal stress before and after compaction for Kippen sand. Unlike model test results, a decrease in magnitude of compressive vertical stress was observed. An increase in compressive horizontal stress was observed but was not as predominant as in the model tests. The vibrator is still compacting at the last time step of simulation leading to the downward movement of soil in order to occupy the created void spaces hence, an evident increase in stress magnitudes is not observed. On the other hand in the model test simulations soil was compacted at a constant depth and also the model dimensions were limited ensuring equilibrium and complete rearrangement of soil at end of last simulation step.

In order to study the variation of compaction with time for Kippen sand, numerical simulation was carried out for a compaction time of 30 s at a constant compaction depth of 20 m at 30 Hz with a centrifugal force of 520 kN. Figure 5.27 describes the evolution of void ratio with time around the vibrator. It can be observed that the compaction radius gradually increased with time, eventually reaching stagnation near 25 s; only a negligible increase in compaction was observed thereafter. The average radial extent of compaction

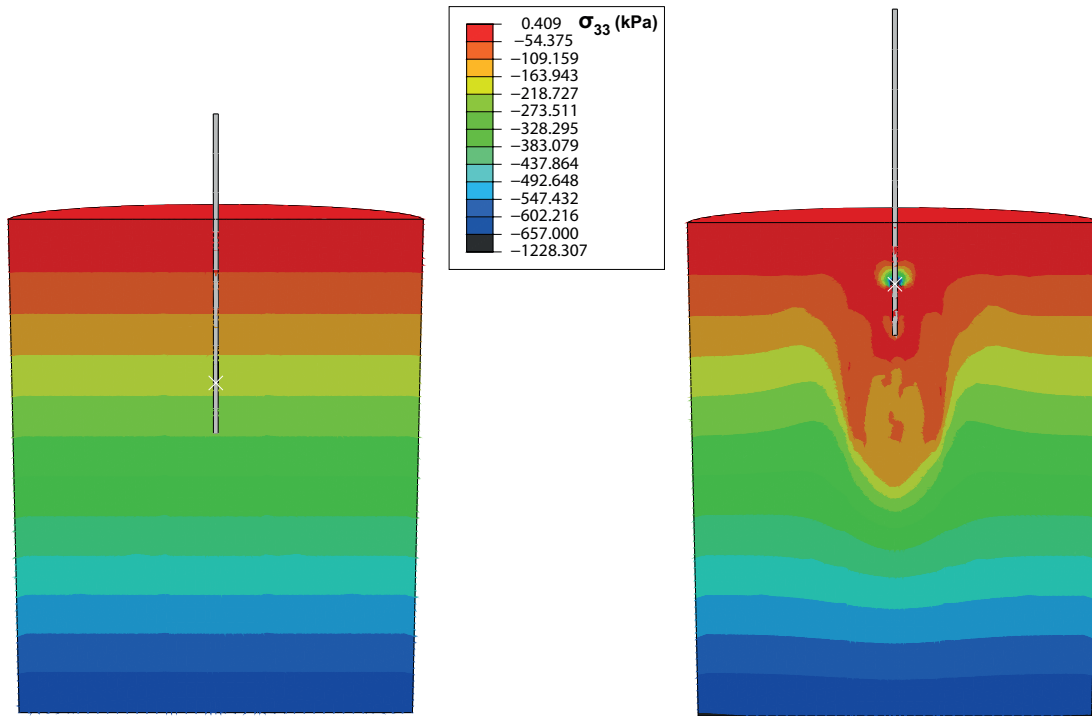


Figure 5.25: Contour of vertical stress (σ_{33}) around vibrator before (left) and after (right) compaction at compaction frequency of 30 Hz for Kippen sand as obtained from simulation

observed in this case was found to be approximately 2.5 m to 3 m, extending beyond the 0.6 m to 1.75 m range suggested by Fellin (2000) and Witt (2009).

Figure 5.28 describes the evolution of the volumetric strain versus deviatoric strain at 20 m depth at various radial distances alongside the variation of void ratio with time. It can be observed that the chosen constitutive model is able to capture evolution of volumetric strain no predominant ratcheting. These results further validate the efficacy of using the hypoplastic model with intergranular strain to model such a complex dynamic process. It can be observed on one hand that void ratio at 1 m radial distance reaches saturation beyond 10 s while void ratio at 3.5 m radial distance undergoes minor dilation leading to no reduction in void ratio. It can be observed that the compaction radius gradually increased with time, eventually reaching stagnation near 25 s; only a negligible increase in compaction was observed thereafter.

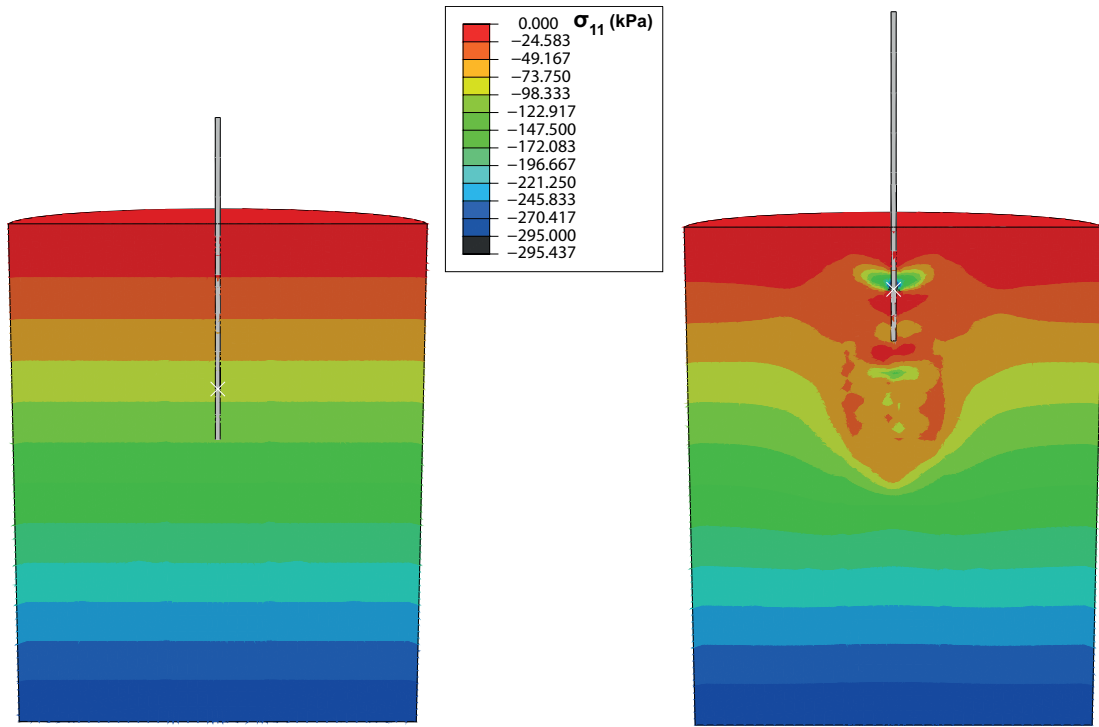


Figure 5.26: Contour of horizontal stress (σ_{11}) around vibrator before (left) and after (right) compaction at compaction frequency of 30 Hz for Kippen sand as obtained from simulation

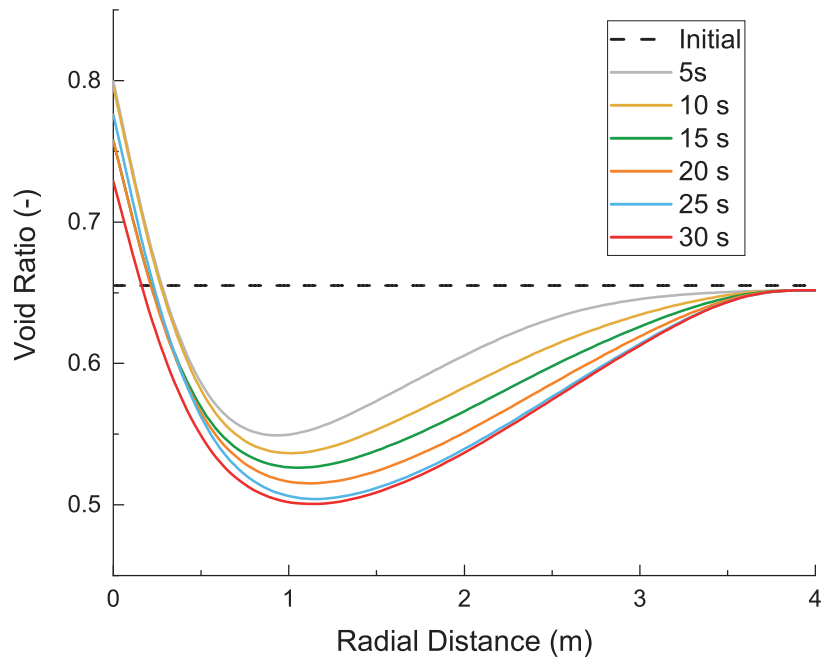


Figure 5.27: Variation of void ratio around vibrator with time at compaction frequency of 30 Hz for Kippen sand as obtained from simulation

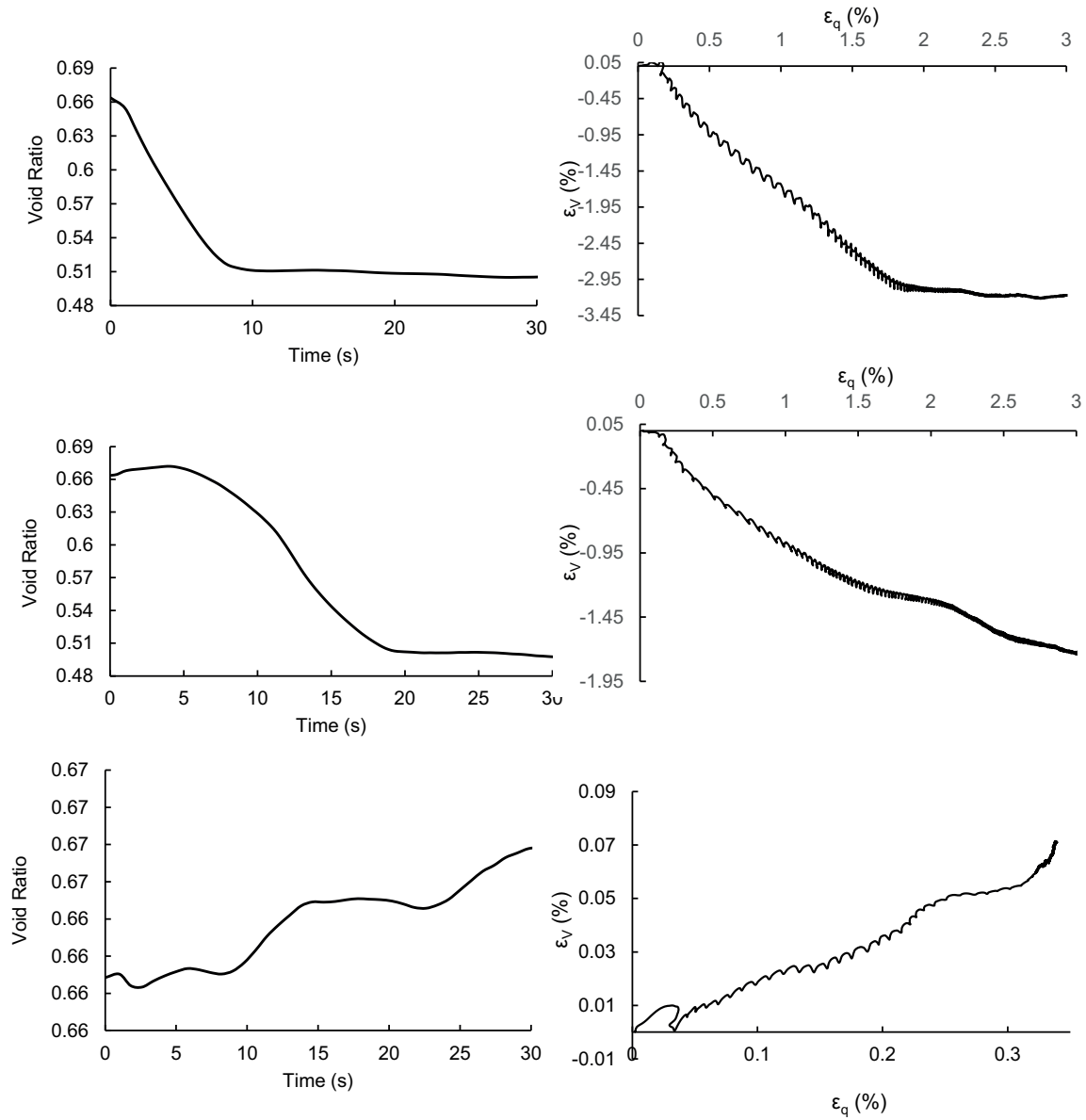


Figure 5.28: Variation of void ratio with time and evolution of the volumetric strain versus deviatoric strain as obtained from simulation at 1 m (top), 2 m (middle) and 3.5 m (bottom) radial distance at 20 depth

6 Understanding Factors Affecting Deep Vibratory Compaction

1g model tests and CEL framework was then used to study the effects of various parameters namely the frequency, relative density, type of granular material, shape of vibrator, compaction process, grid spacing and soil saturation on deep vibratory compaction. The advantages and shortcomings of model tests and numerical simulations to analyse deep vibratory compaction process would be discussed.

6.1 Frequency

Frequency of compaction plays an important role in determining the efficiency of deep vibratory compaction (Arnold and Herle, 2009). The centrifugal force applied by the vibrator depends on the eccentric mass, eccentricity and frequency. Equation 6.1 shows that for a vibrator with fixed mass and eccentricity, the centrifugal force increases with frequency. Compaction must be carried out at a frequency that neither consumes additional power nor causes excessive wear on the vibrator motor but leads to efficient compaction (Wersäll et al., 2013). It is to be noted that in reality power that can be applied by the vibrator is limited hence, as soil densifies compaction power raises and if this reaches the limiting power it would lead to reduction of frequency. In this work applied frequency is held constant as it was observed both in model tests and Cottbus field measurements indicating that the compaction power never reached limiting power of the vibrator.

$$F = m e_m \omega^2 \quad (6.1)$$

where, F = centrifugal force, m = mass of eccentric weights, e_m = eccentricity of masses and ω = angular frequency.

This section discusses the effect of frequency for a vibrator with fixed mass and eccentricity by means of both 1g model test results and numerical simulations. The 1g model test results discuss the effect of frequency at a reduced stress state for Hamburger sand whereas, numerical simulations account for effect of frequency at realistic stress state for Kippen sand.

6.1.1 1g Model Test Results for Frequency

In order to study the effect of frequency on extent of compaction for Hamburger sand, model tests were conducted at 4 frequencies of 15, 35, 40 and 60 Hz. The frequencies were chosen in order to evaluate the effect of frequency over a wide range. CPT tests were performed at centre and three radial distances namely 70, 140 and 250 mm from the

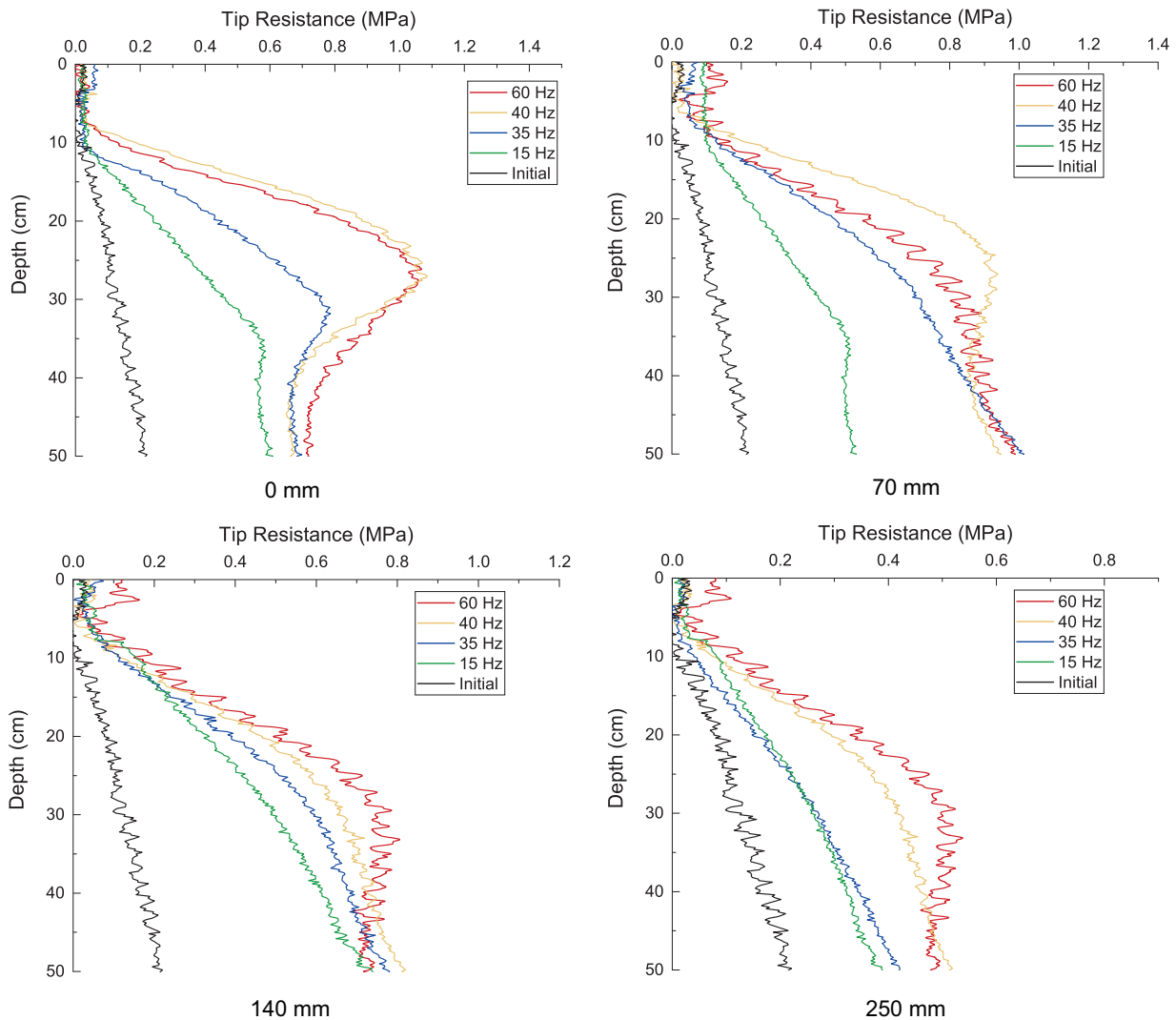


Figure 6.1: CPT tip resistance over depth at different radial distance from vibrator at various compaction frequencies of model vibrator as obtained from 1g model tests

centre of compaction point in order to evaluate compaction success with varying frequency. Figure 6.1 compares the variation of CPT tip resistance along the depth of the test tank at the aforementioned radial distances for different compaction frequencies. The centrifugal force applied by the vibrator depends on the eccentric mass, eccentricity and frequency of compaction as described before. It can be observed that the sand underwent negligible compaction at 15 Hz. At the centre of the compaction point, compaction at 40 and 60 Hz led to the best compaction. Higher CPT values were observed at 70 mm radial distance for compaction at 40 Hz. This observation can be supported by the findings of Fellin (2000), which suggested an existence of an optimal frequency around which the vibrator amplitude was highest. It can be observed that 60 Hz led to marginally better compaction than 40 Hz at 140 and 250 mm radial distance. 15 and 35 Hz led to similar degree of compaction

at a radial distance of 250 mm. The similar tip resistance values indicate that compaction at lower frequencies leads to a negligible compaction at larger radial distances. This phenomenon of variation of compaction efficiency with frequency is further explained in Chapter 7. Chapter 7 would discuss the variation of amplitude of vibrator with frequency and how this variation decides the effectiveness of compaction.

6.1.2 Numerical Simulations Results for Frequency

In the preceding section, influence of frequency on compaction via model tests. The following section would discuss the influence of frequency at realistic stress state condition as existing in practice via numerical simulations.

6.1.2.1 Deep Vibratory Compaction Simulations at Field Scale

40 x 50 m measuring 3D numerical model based on the CEL method (Figure 4.13) used to simulate field deep vibratory compaction. In order to study the influence of frequency on compaction for Kippen sand, simulations were carried out at 15, 20, 25 and 30 Hz. This range is in line with the frequencies used in practice on field. The corresponding centrifugal forces applied at the tip of vibrator were calculated using Equation 6.1. It should be noted that the simulations were carried out for one compaction step at a depth of 20 m and not for the entire depth. Compaction time of 30 s was considered in all simulations. The initial relative density was held constant at 46 % for all simulations. Figure 6.2 describes the evolution of void ratio around the vibrator at 20 m depth for various frequencies with a compaction time of 30 s. At 15 Hz, both the extent and degree of compaction was less than at other frequencies. The best compaction occurred at 20 and 25 Hz, while efficiency marginally reduced at 30 Hz. Figure 6.3 depicts the void

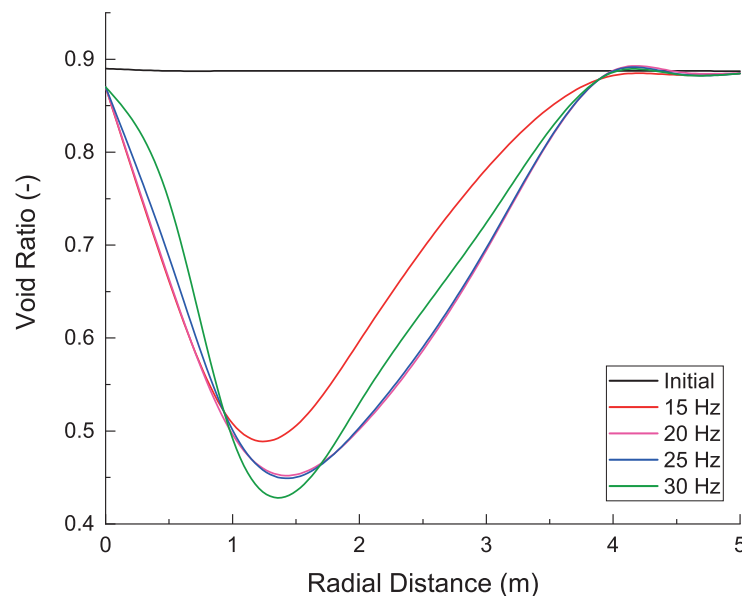


Figure 6.2: Radial variation of void ratio around tip of vibrator for Kippen sand at different compaction frequencies as obtained from simulations at field scale

ratio contours at different frequencies and it can be well observed that the compaction spread is maximised at 25 Hz frequency and reduces noticeably at 30 Hz. It was observed in-field that a lesser magnitude of centrifugal force around optimal frequency can lead to an increase in compaction efficiency (Kirsch and Kirsch, 2017). Compaction at lower frequency can lead to substantial reduction in motor wear, leading to financial benefit (Massarsch and Fellenius, 2002). Importantly, the choice of optimised frequency depends on both the nature and initial state of granular material. In order to demonstrate that optimised frequency varies with nature of sand, numerical simulations were carried out for three kinds of sands namely Hamburger, Kippen and A3 (refer Table 6.1 and Figure 4.17) sand between 15 to 60 Hz at intervals of 5 Hz. One compaction step at a depth of 20 m for compaction time of 30 s was simulated in each case. Frequency that lead to best compaction is enlisted in Table 6.2 and it can be deduced that Hamburger sand which is a poorly graded sand was best compacted at higher frequency whereas Kippen sand with more fines content was best compacted at a lower frequency.

Table 6.1: Physical properties of Hamburger, Kippen and A3 sands

Sand	Gradation	D10	e_{\max}	e_{\min}	C_u
Kippen	With fines	0.08 mm	1.116	0.672	2.25
Hamburger	Poor	0.51 mm	0.813	0.526	1.47
A3	Normal	0.3 mm	0.72	0.47	2.1

Table 6.2: Optimised frequency of compaction for Hamburger, Kippen and A3 sand

Sand	Optimised Frequency
Hamburger	40 Hz
Kippen	20-25 Hz
A3	30 Hz

6.2 Relative Density and Stress State

Initial density is one of the prime soil properties that affect the efficiency of deep vibratory compaction (Kirsch and Kirsch, 2017). Stress state varies with depth of compaction and it is important to understand the effectiveness of the compaction method in various stress conditions. Deep vibratory compaction is a technique used to compact loose granular soils but initial densities of soil before compaction that can maximise the effect of deep vibratory compaction have not been quantified. This section would try to identify by means of numerical simulations the impact of initial density and stress state of soil on the effectiveness of compaction.

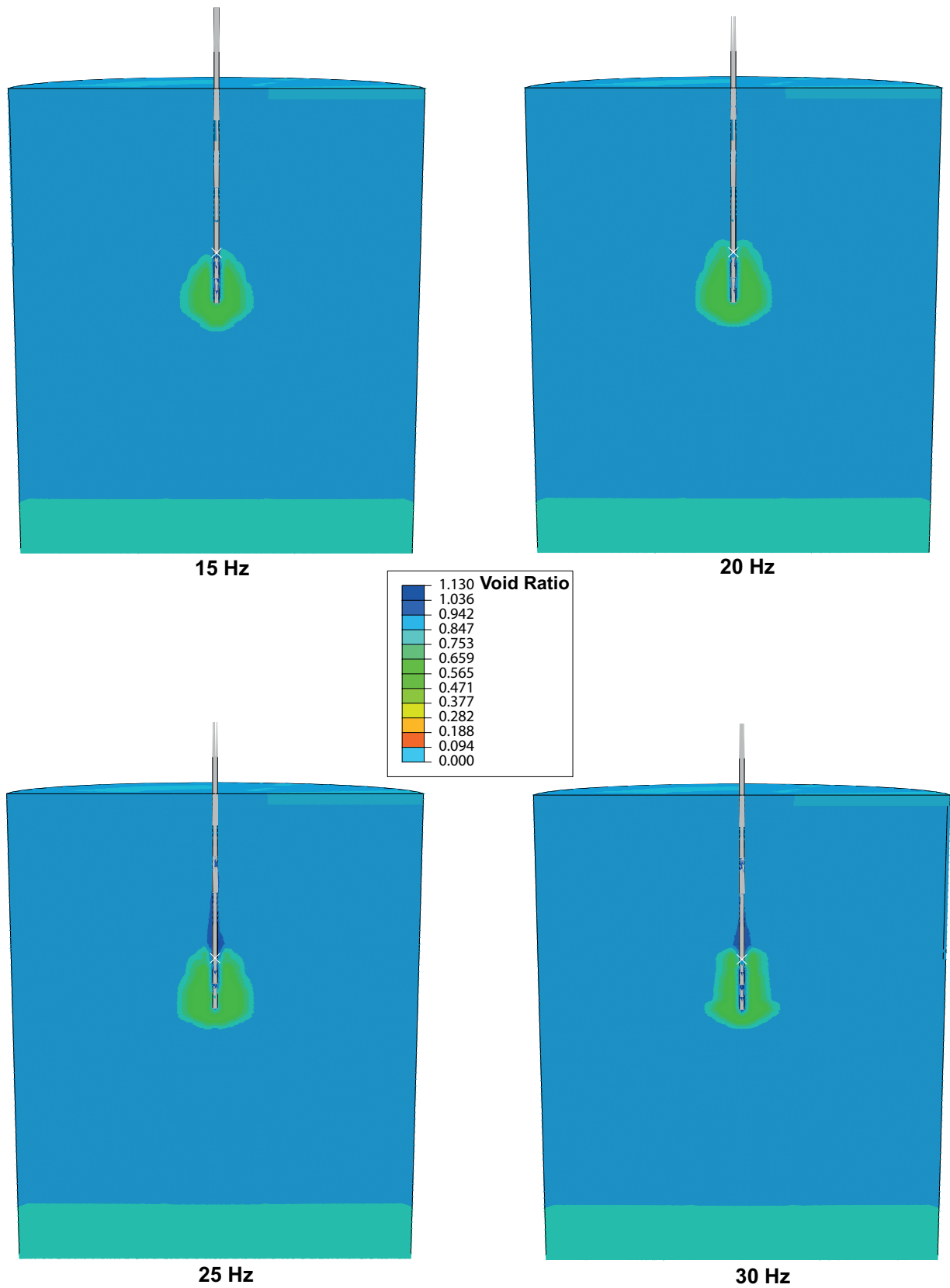


Figure 6.3: Void ratio contours for Kippen sand at different compaction frequencies as obtained from simulations at field scale

6.2.1 Numerical Simulations Results for Relative Density and Stress State

40 x 50 m measuring 3D numerical model based on the CEL method (Figure 4.13) used to simulate field deep vibratory compaction compaction as described in Chapter 4 was used for the below simulations.

6.2.1.1 Effect of Relative Density in Field Scale Simulations

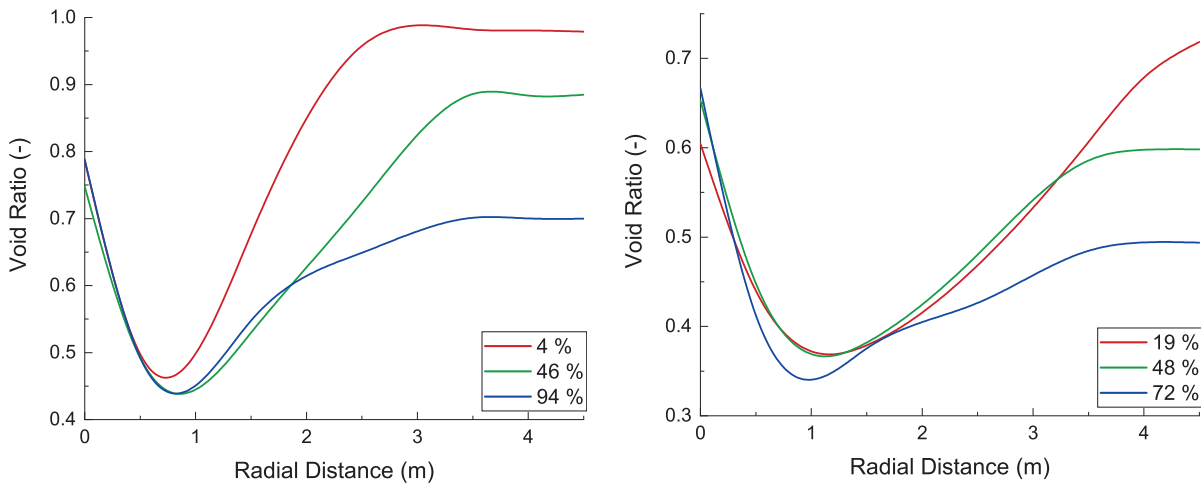


Figure 6.4: Influence of initial relative density on reduction of void ratio around vibrator for Kippen (left) and A1 (right) sand as obtained from simulations at field scale

In order to understand the effect of relative density on compaction efficiency, numerical simulations were carried out for Kippen and A1 sand (Figure 4.17). Simulations were carried out for one compaction step at a depth of 20 m for 30 s at 30 Hz frequency with a centrifugal force of 520 kN. Three initial relative densities 4, 46 and 94 % for Kippen sand and 19, 48 and 72 % for A1 sand were considered. Figure 6.4 describes the radial variation of void ratio around the tip of the vibrator at the end of compaction. The magnitude of void ratio reduction was similar for all densities; however, the radius of influence was maximised for relatively dense sand. Damping ratio for sand with fines has been observed to reduce with relative density (Cheng et al., 2019), leading to improved transmissibility of vibrations and extended radius of influence. This explains the predominant effect of increasing density in improving the efficiency of compaction for Kippen sand which has higher content of fines. Here it can be observed that A1 sand does not show much sensitivity to the initial relative density. In order to understand the spatial influence of relative density on compaction, Figures 6.5 and 6.6 depicting the void ratio contours for Kippen and A1 sand are plotted. It can clearly be observed with increasing initial relative density of the soil, there is a spatial increase of compaction radius. It can also be observed that compaction is more uniform at higher relative density. A1 sand which is a better graded sand shows improved and uniform compaction radius at higher relative density. Whereas for Kippen sand with more fines the degree of compaction is improves with increasing relative density.

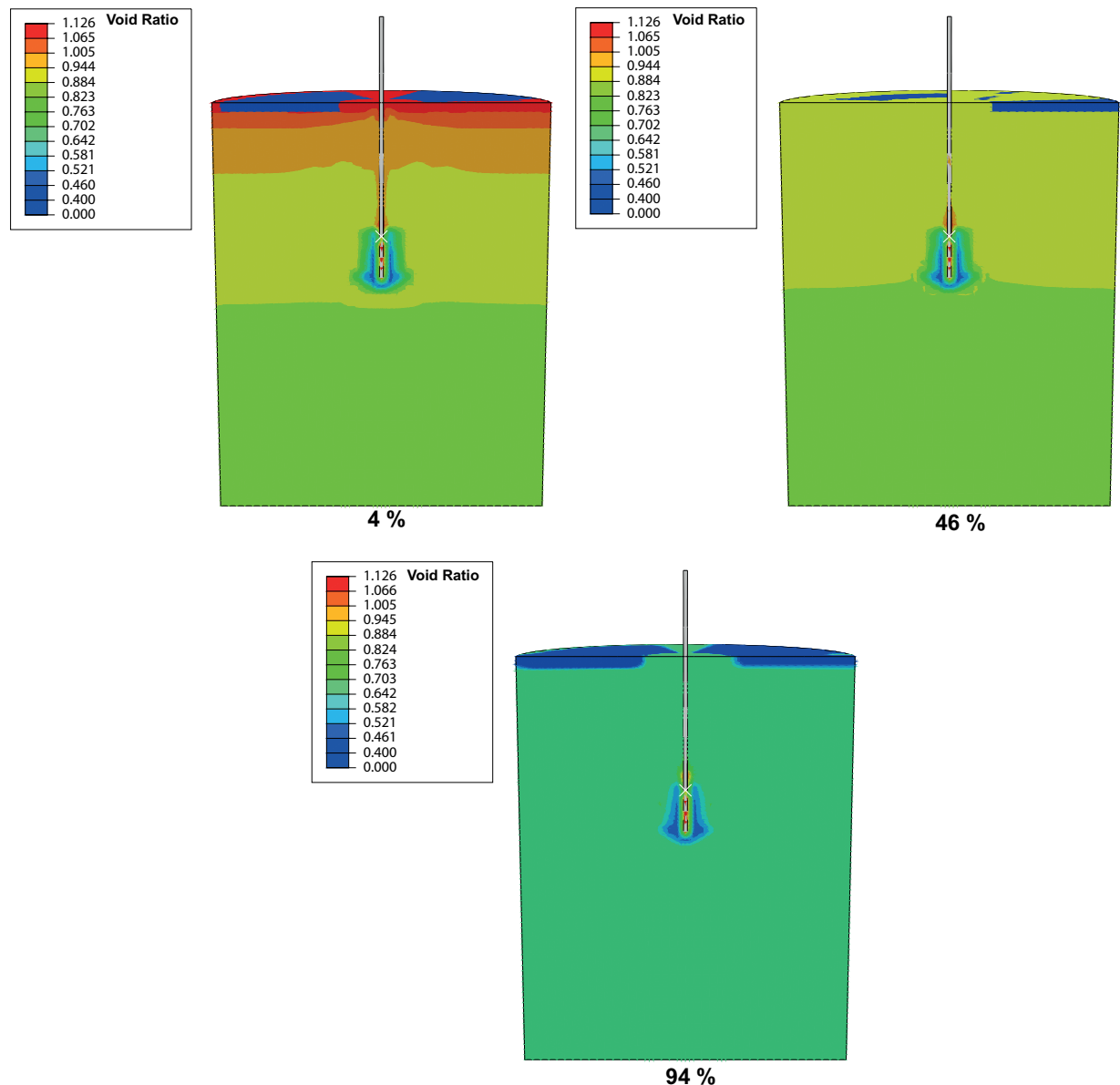


Figure 6.5: Void ratio contours of Kippen sand indicating the influence of initial relative density on compaction as obtained from simulations at field scale

6.2.1.2 Effect of Stress State in Field Scale Simulations

It is well known that stress state in soil varies with depth; the vertical and horizontal stresses increase with depth. Deep vibratory compaction in certain projects has been used to compact soil till depths of 45 m (Kirsch and Kirsch, 2017). The extent of soil depths until which the method would be effective is debatable hence, this section would try to analyse the effect of stress state on the effectiveness of deep vibratory compaction. Numerical simulations were carried out for Kippen soil at various depths namely 30, 25, 20, 15 and 10 m. One compaction step at each depth for 30 s at 30 Hz frequency with

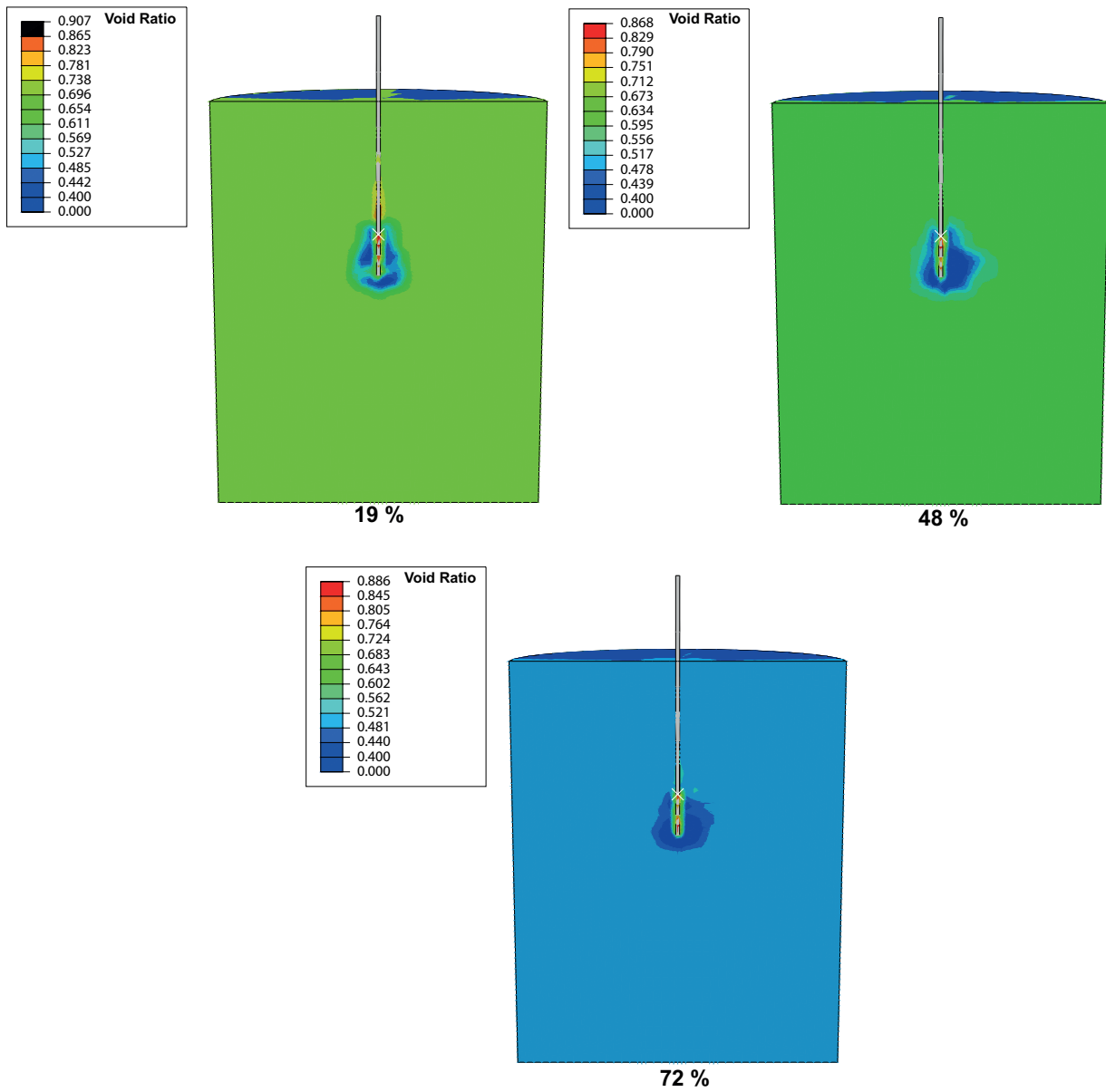


Figure 6.6: Void ratio contours of A1 sand indicating the influence of initial relative density on compaction as obtained from simulations at field scale

a centrifugal force of 520 kN was simulated. The initial relative density was set at 46 % at all depths. Figure 6.7 describes void ratio contours at various depths and it seems that compaction is nearly the same between 15 to 25 m depth and deviation is observed at 10 and 30 m depth. In order to closely analyse the variation, Figure 6.8 describes the radial variation of void ratio around the tip of the vibrator at each depth. Here it can be clearly observed that the radial extent and degree of compaction is reduced at 10 and 30 m depth and effectiveness of deep vibratory compaction is maximised between 15 to 25 m depth. At lower depths the soil is unable to provide the required horizontal support to the vibrator system leading to improper transmission of energy from vibrator to soil. At greater depths the stress state is high and restrains the movement of the vibrator leading to loss of efficiency of compaction. Numerical simulations can help identify depths until which deep vibratory compaction can be used to compact soil with marginal loss in compaction efficiency.

6.3 Granular Material

Kirsch and Kirsch (2017) identified various parameters that affect the efficiency of deep vibratory compaction method and one of them is nature of the granular material to be compacted. Mitchell (1982) discusses the suitability of deep vibratory compaction for various soil types based on their grain size distribution curves. The use of vibration compression is limited to non-cohesive, granular soils. In the case of cohesive soils, the existing cohesion prevents compaction due to the vibrations of the vibrator. The suitability of deep vibratory compaction is determined from the grain size distribution of the soil. The range of application is defined by limit curves as shown in Figure 6.9. In principle finer soils closer to red line are more difficult to compact. Literature suggests various maximum permissible fines content such as 15 % as per Kirsch (1979), 20 % as per Brown (1977) and 30 % as per Thorburn (1975). A uniformly graded coarse grained soil such as gravel/cobble make the penetration of vibrator difficult and hence reduce compaction efficiency. Soils with grain diameter greater than 100 mm can lead to difficulties in compaction via deep vibratory compaction. Grain shape also influences the compaction behaviour. It has been observed on field that soils with an angular shape (edge length > 50 mm) make usage of deep vibratory compaction considerably difficult. The suitable range of deep vibratory compaction depicted in Figure 6.9 is determined empirically and is partly dependent on type of vibrator used. In this section we would try to understand the effectiveness of deep vibratory compaction process to compact various kinds of granular materials via numerical simulations.

6.3.1 Numerical Simulations Results for Granular Material

Numerical simulations were carried out considering various kinds of granular materials and their response to compaction by deep vibratory compaction is commented upon. The simulations have been categorised into two sections namely 1g model test and field deep vibratory compaction simulations. Numerical simulations are carried out at stress level of the 1g model test and also at realistic field conditions. Numerical simulations at model

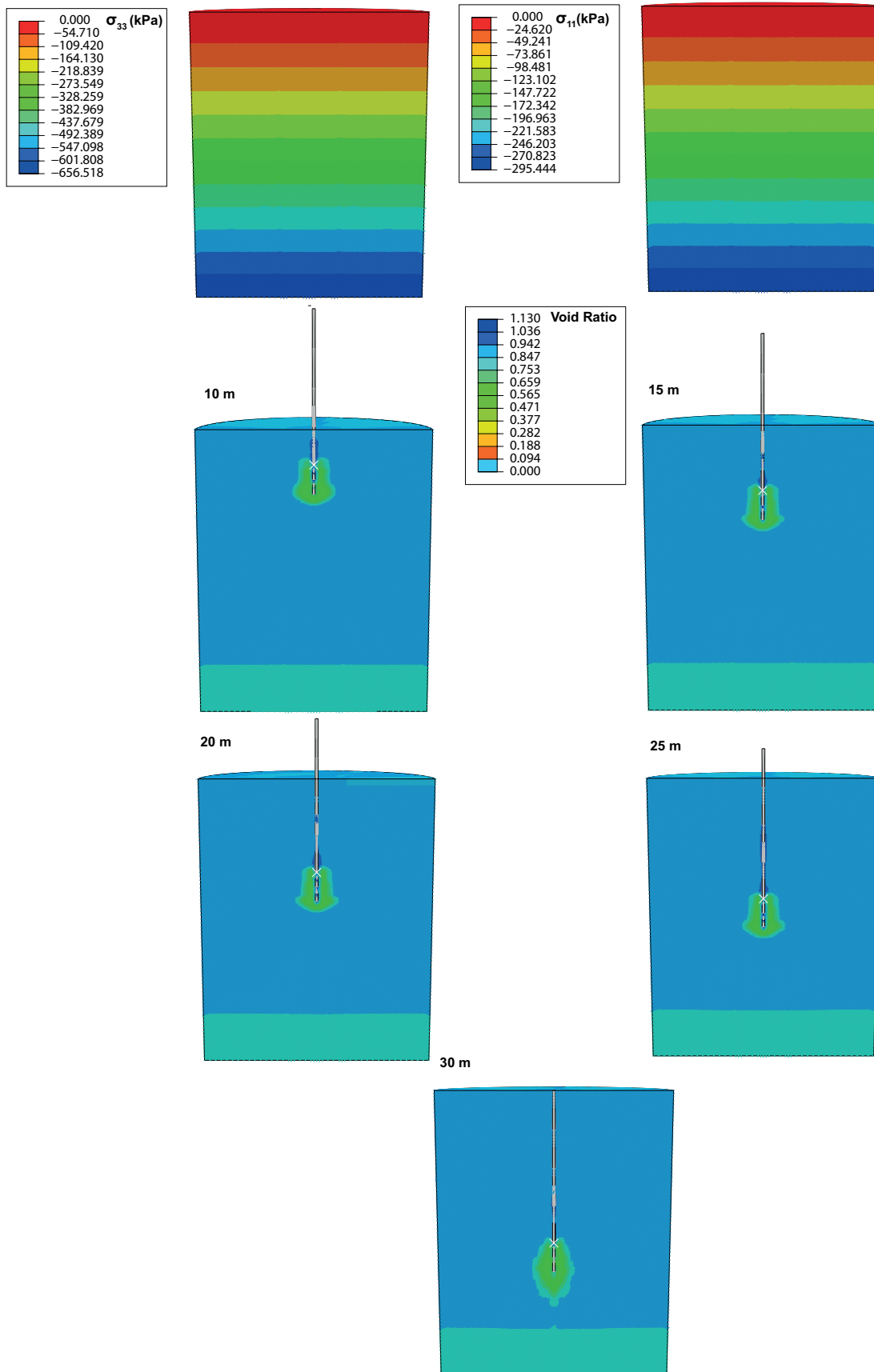


Figure 6.7: Void ratio contours of Kippen sand indicating the influence of stress state on compaction as obtained from simulations at field scale

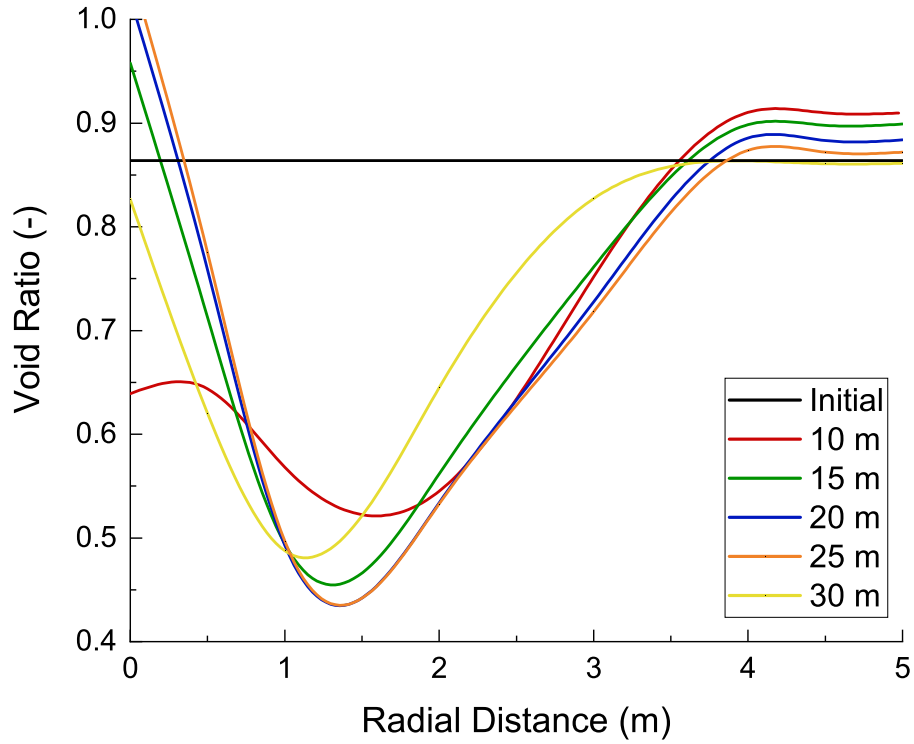


Figure 6.8: Influence of compaction depth on radial extent of compaction as obtained from simulations at field scale

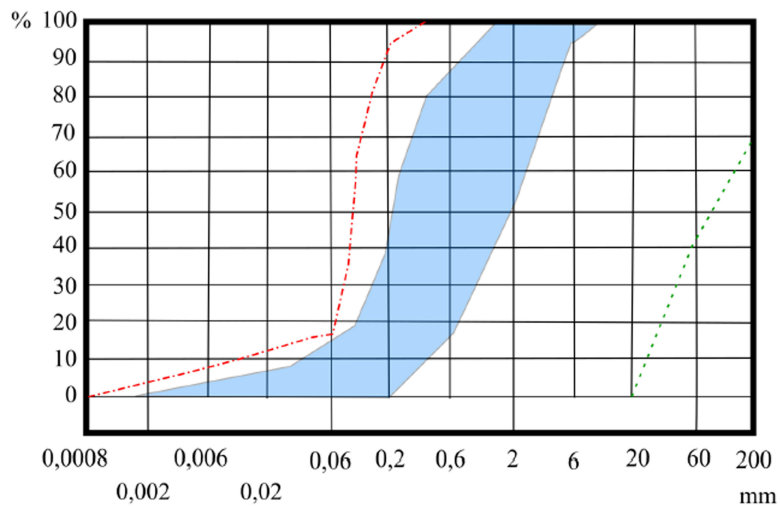


Figure 6.9: Limits on feasibility of deep vibratory compaction for soils based on their GSD (Witt, 2017a)

scale level highlight the advantages of performing numerical simulations in place of physical tests. The simulations not only helped circumvent performing 9 sets of laborious and time-consuming physical tests but also provided more detailed insight. In addition it also helps compare and analyse variations in key observations at two drastically different stress state conditions.

6.3.1.1 1g Model Test Simulation Results

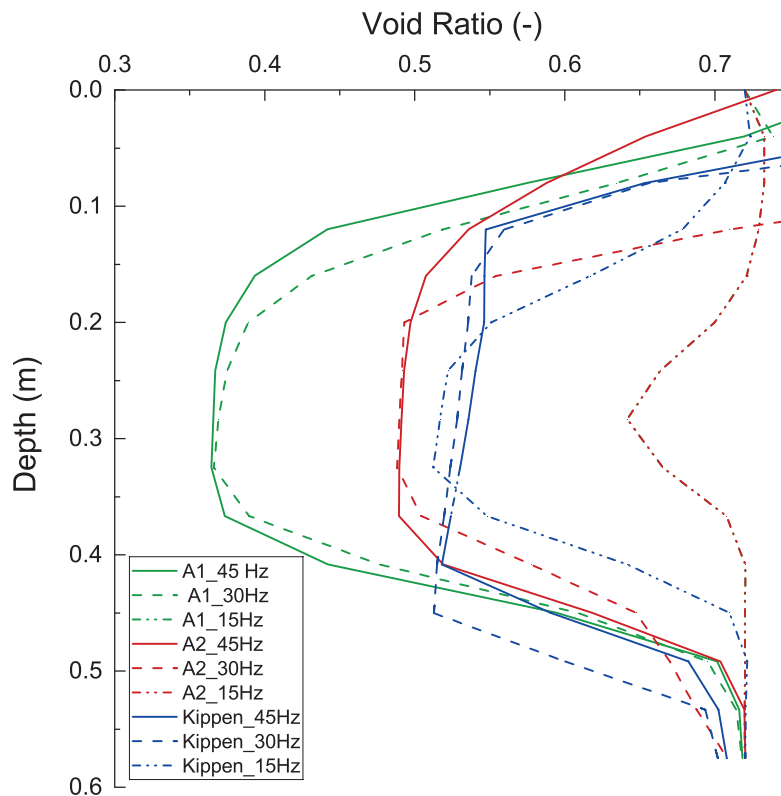


Figure 6.10: Variation of void ratio with depth at radial distance of 70 mm for different compaction frequencies for A1, A2 and Kippen sand as obtained from simulations at model scale

Details of the numerical model to simulate deep vibratory compaction in 1g model test has already been discussed in Chapter 5. The vibrator was wished in place at a depth of 0.35 m and centrifugal force was applied as per Equation 6.1 (mass and eccentricity of model vibrator were used) by the vibrator in x and y directions at three frequencies of 15, 30 and 45 Hz. Different frequencies were chosen to better understand the effect of frequency on the three kinds of sands. The hypoplastic material properties of chosen sands namely A1, A2 and Kippen are listed in Table 4.6, and the grain size distributions are depicted in Figure 4.17. The initial void ratio of 0.72 was considered for all three kinds of sands. Figure 6.10 depicts the variation in the void ratio with depth at a radial distance of 70 mm at a frequency of 15, 30 and 45 Hz for the three types of sand. It can be observed that the A1 sand responds best to compaction, as it is a better graded sand (Kirsch and

Kirsch, 2017) and, hence, leads to the densest packing. A2, which is a poorly graded sand, undergoes compaction to a lesser degree compared to that of A1. It should be noted that A1 and A2 undergo marginal compaction at 15 Hz and similar compaction at 30 and 45 Hz. Kippen sand contains nearly 8 % fines which leads to least compaction compared to other two types of sand. It has already been highlighted that the presence of fines hinders the efficiency of deep vibratory compaction (Kirsch and Kirsch, 2017). It is noteworthy that compaction of Kippen sand is found to be least sensitive to frequency.

6.3.1.2 Field Scale Simulation Results

The full scale 40 x 50 m measuring 3D model based on the CEL method (Figure 4.13) was used to carry out simulations to study the effect of nature of granular material on compaction effectiveness. The deep vibratory compaction method is suitable for granular materials ranging from gravel to sand that are approximately 8-30 % fines (Baumann and Bauer, 1974; Kirsch and Kirsch, 2017) as discussed earlier. In this section, an analysis of the efficiency of deep vibratory compaction for three classes of sands namely A1, A2 and A5 at realistic stress state conditions is attempted, the grain size distribution curves of which are depicted in Figure 4.17. A5 was chosen instead of Kippen sand as it contains 15 % of fines, higher than the 8 % fines of Kippen sand. The calibrated hypoplastic material properties of chosen sands are listed in Table 4.6. Entire compaction process was simulated between 25 to 5 m depth following the pilgrim step method as described in Figure 4.11. A vibrator nodal force of 520 kN at 30 Hz was applied in all the cases. The initial relative density was held constant at 46 % for all simulations.

Figure 6.11 depicts the variation of void ratio over depth after compaction at a radial distance of 0.5 m from the compaction point. A1, with a C_u (co-efficient of uniformity) of 3.45, displays the best compaction followed by A2, a poorly graded sand with a C_u of 1.43. A3 which has 13 % fines, shows the least compaction even though it has a higher C_u (3), hence reconfirming that the deep vibratory compaction method is less efficient for granular materials with higher fines content. Figure 6.12 describes the void ratio contours before and after compaction for the three sands. A1 undergoes an uniform compaction forming a compacted column of soil. In A2 sand the radial spread of compaction was seen to be lesser though it is uniform in nature. A5 sand undergoes uneven compaction with zones in-between experiencing very less compaction. This again reinstates the idea that efficiency of the compaction process reduces with increasing quantity of fines.

6.4 Shape of Vibrator Probe and Friction

The compaction probe is an important component of the vibratory compaction system. Probes have evolved over the years since their inception. The design is being improved in order to ensure better degree and extent of compaction. The design improvements are based on field experience and the concept of soil-vibrator system resonance in order to capitalise compaction with least consumption of energy (Massarsch and Fellenius, 2005). Conventional horizontal vibrators (vibroflot) feature a cylindrical shaft with wings and conical tip at the end. The wings on the side are believed to improve compaction through enhanced contact with soil. In this section the effect of shape of vibroflot on compaction

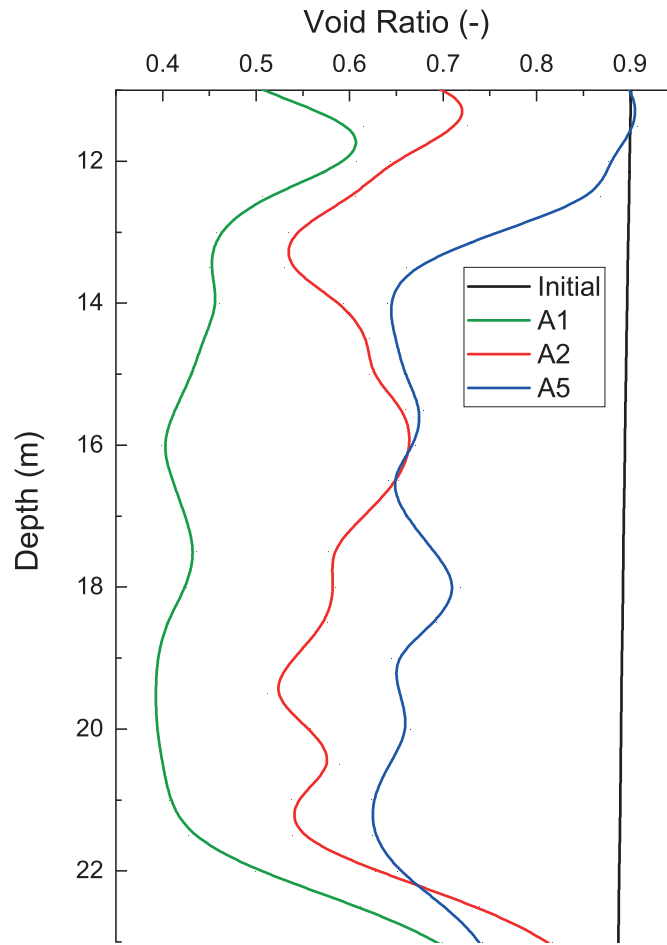


Figure 6.11: Reduction in void ratio with depth for A1, A2 and A5 sands as obtained from simulations at field scale

success would be studied by means of numerical simulations. As this work focusses on compaction by horizontal vibrations, two kinds of probe shapes have been considered namely the conventional cylindrical shaft with and without wings. Purpose is to identify if existence of wings improves compaction and till what extent.

6.4.1 Numerical Simulations Results for Vibrator Shape and Friction

The full scale 40 x 50 m 3D numerical model based on the CEL method (Figure 4.13) used to carry out the simulations at realistic stress state conditions. It is to be noted that in this case simulations at model scale level were not carried out. The calibrated hypoplastic material properties of Kippen sand as listed in Table 4.6. All the simulations were carried out for a single compaction step at a depth of 20 m for 30 s with a centrifugal force of 520 kN at 30 Hz frequency. The initial relative density was held constant at 46 % for all simulations.

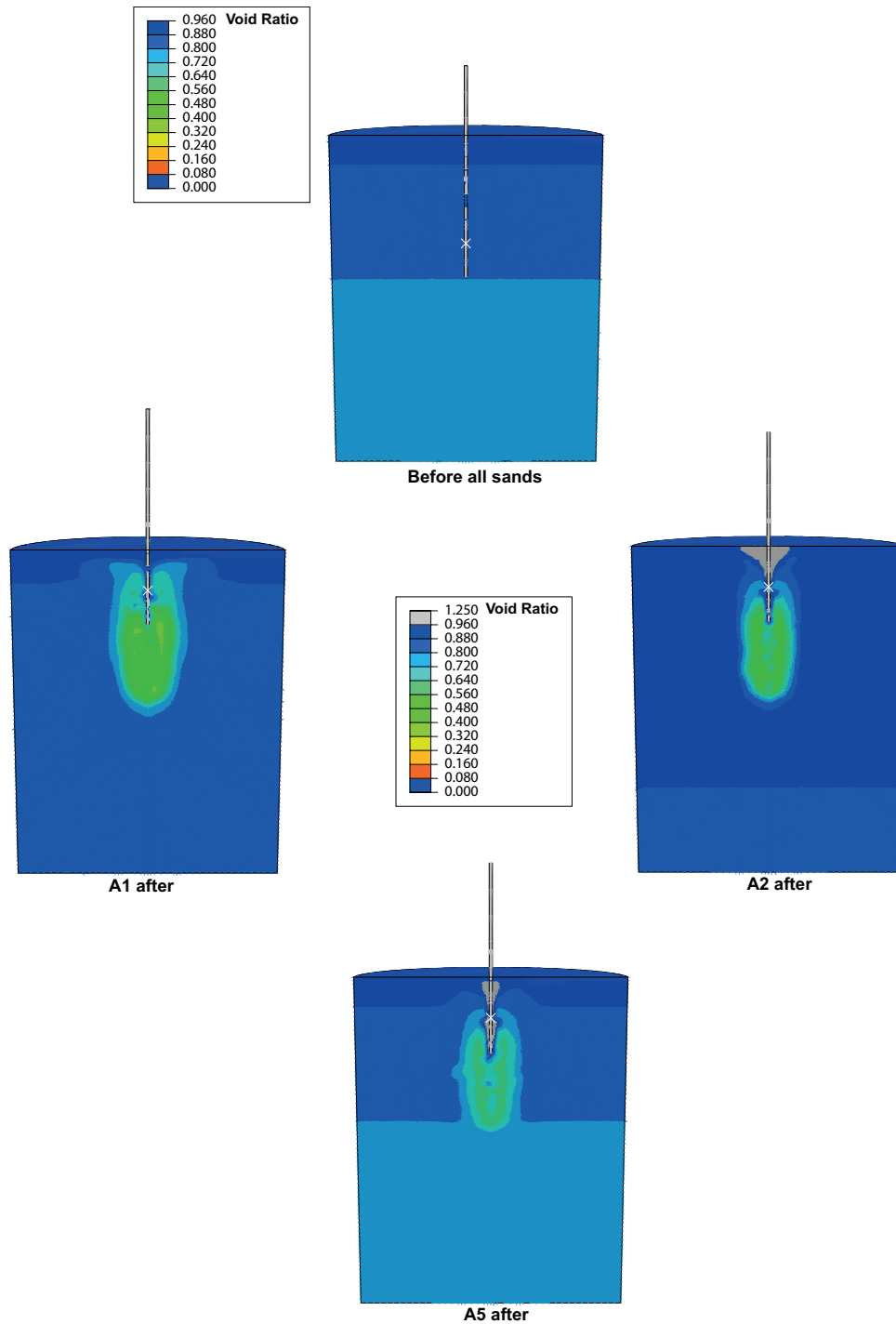


Figure 6.12: Void ratio contours before and after compaction for A1, A2 and A5 sands as obtained from simulations at field scale

6.4.1.1 Effect of Different Vibrator Probes in Field Scale Simulations

Simulations were carried out with two different forms of vibrators, one comprising a simple cylindrical solid tube, other replicating the exact shape of the vibrator with two wings on diametrically opposite sides similar to the V48 vibrator (Figure 4.7) used in Cottbus field deep vibratory compaction. The meshed model of the two types of vibrator is depicted in Figure 6.13. Special attention was paid to mesh both the vibrator probes plus stay tube system with nearly the same number of elements. The vibrator probe and stay tube were modelled as a linear elastic material with the properties of steel. Simulations in this scenario were carried out with friction using Coulomb's friction law with wall friction co-efficient $\mu = \tan(\phi_c)$. Where ϕ_c is considered equal to the effective friction angle of the soil under consideration ($\phi_c = 31$ for Kippen sand).

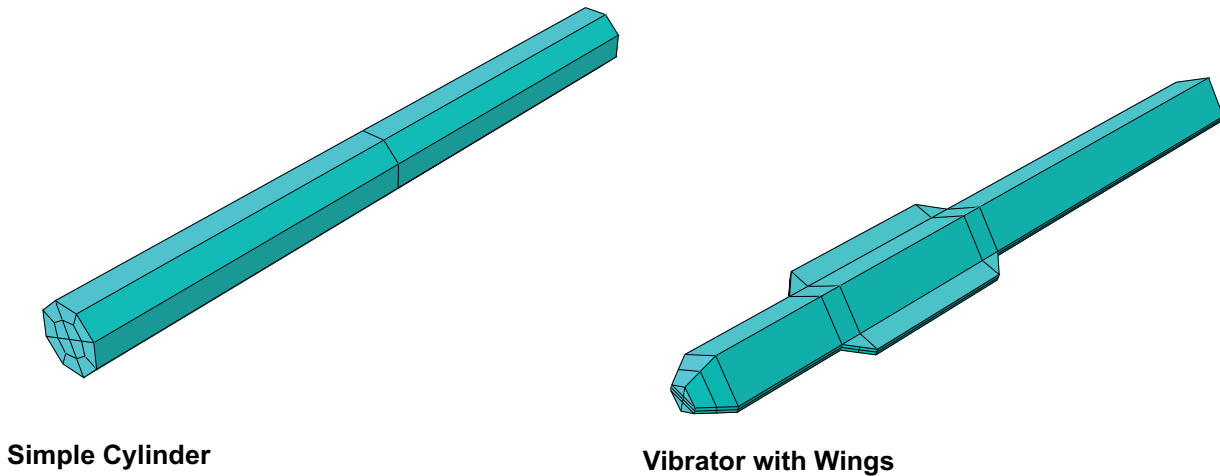


Figure 6.13: Numerical model of vibrator probe with and without wings

In Figure 6.14, it can be observed that a vibrator with wings leads to more uniform compaction even if the magnitude of void ratio reduction is marginally lesser. Figure 6.14 depicts that the compaction spread is higher in case of vibroflot with wings. This verifies that presence of wings ensures better contact between vibroflot and soil, eventually ensuring better transmission of energy between probe and surrounding soil. Wings ensure extra surface area for soil/vibrator interaction. Numerical simulations can act as a preliminary step to improvise and suggest modifications to existing vibroflot designs in order to ensure better extent and degree of compaction.

6.4.1.2 Influence of Friction in Field Scale Simulations

Numerical simulations with a probe with wings as described in the previous section were computationally expensive. It was concluded that in order to simulate the entire compaction process a simpler vibrator probe had to be chosen hence, the cylindrical probe was chosen to carry out all the simulations in this work. In order to further optimise the computational demand, effect of friction was studied. Two sets of simulations were

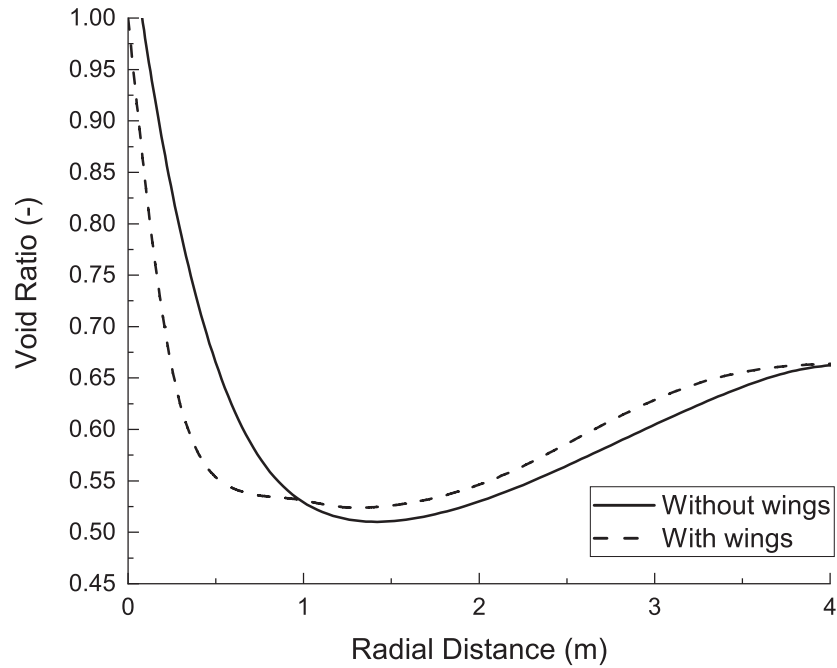


Figure 6.14: Variation of void ratio around vibrator with and without wings as obtained from simulations at field scale

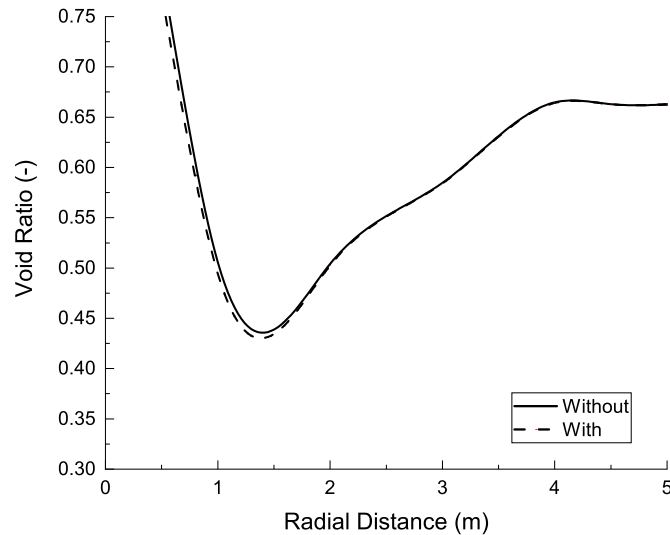


Figure 6.15: Comparison of void ratio around vibrator with and without friction for a cylindrical probe as obtained from simulations at field scale

carried out using the cylindrical probe one considering no friction (the tangential friction coefficient between vibrator and soil was assumed to be zero) and the other with friction (Coulomb's friction law with wall friction co-efficient $\mu = \tan(\phi_c)$ for Kippen sand). Figure 6.15 compares results from both the cases and it can be observed case I of zero

tangential friction co-efficient can be assumed to produce realistic behaviour with minimum compromise in results and lesser computational effort. In all, the cylindrical probe without friction was chosen to execute all the simulations in this work as it led to efficient capturing of the deep vibratory compaction process with optimised computational effort.

6.5 Compaction Process

Like any other compaction process, the sequence of execution plays key role in determining its success. Deep vibratory compaction process being a complex one involving a vibrator probe being pushed deep into the soil and being pulled up vibrating leading to a compacted soil column, heavily relies on the sequencing of the process. The technique used to withdraw the vibrator while vibrating to create a compacted soil column influences the degree and extent of compaction. Deep vibratory compaction is performed according to a variety of methods, the most popular being the pilgrim step method and back-step method. In the pilgrim step method, the vibrator was pushed down and pulled up after vibrating at constant depth (Figure 4.11). In the back-step method, the vibrator was penetrated to the required depth; next, compaction was performed by sequentially lifting the vibrator up by 1 m then pushing it down by 0.5 m (Nagy, 2019). The process unlike pilgrim step method, did not involve vibration at a constant depth. During the entire compaction process, the vibrator vibrated at a constant frequency. A third compaction method that has not been applied in practice so far, the continuous compaction method, was also simulated. In this method, the vibrator was pulled up at a slow constant rate while vibrating. The methods are described in detail in Table 6.3. All three cases were simulated to compact Kippen sand between 20 m and 15 m. It is to be noted that the pilgrim step method was carried out during field measurements in Cottbus, Germany; the other two methods were only studied via numerical simulation.

Table 6.3: Details regarding sequence of steps for various compaction processes

Type	Fixed Depth	Pull Up	Pull Down	Compaction time for 5 m
Pilgrim	23 s	1 m 6 s	0.5 m in 7 s	360 s
Back Step	2 s	1 m in 12 s	0.5 m in 27 s	410 s
Continuous	-	5 m in 384 s	-	384 s

6.5.1 Numerical Simulation Results for Compaction Process

The simulations were carried out using the full scale 40 x 50 m 3D numerical model (Figure 4.13). The calibrated hypoplastic material properties of Kippen sand were considered (Table 4.6). The initial relative density was held constant at 46 % for all simulations. It is to be noted that in this case simulations at model scale level were not carried out.

6.5.1.1 Effect of Compaction Process in Field Scale Simulations

All calculations simulated compaction process between 20 m and 15 m following the above described processes with a constant centrifugal force of 520 kN at 30 Hz frequency. Figure 6.16 describes the variation of void ratio with depth at a radial distance of 1 m. The continuous compaction method led to non-uniform compaction, whereas the other two methods led to lower void ratio. This is likely due to the repetitive pushing down and pulling up of the vibrator, leading to better compaction of Kippen sand which has around 8% of fines. This repetitive pushing down leads to a contractant behaviour and aids the sand to reach a denser packing. But, Figure 6.16 describes void ratio at a radial distance of 1 m from the centre of the vibrator and may not represent the entire zone of compaction. Figure 6.17 plots the void ratio contours after the various processes of compaction and it can be observed that Pilgrim step method leads to an uniform column of compacted soil. Unlike in Figure 6.16, back step method leads to a non uniform compaction zone. The continuous method only leads to pockets of compacted soil. Compared to the back-step method, the pilgrim step method also requires less compaction time and leads to better and uniform compaction. Spatial distribution of compaction effect is well captured by numerical simulations which is not possible in point-by-point measurement techniques on

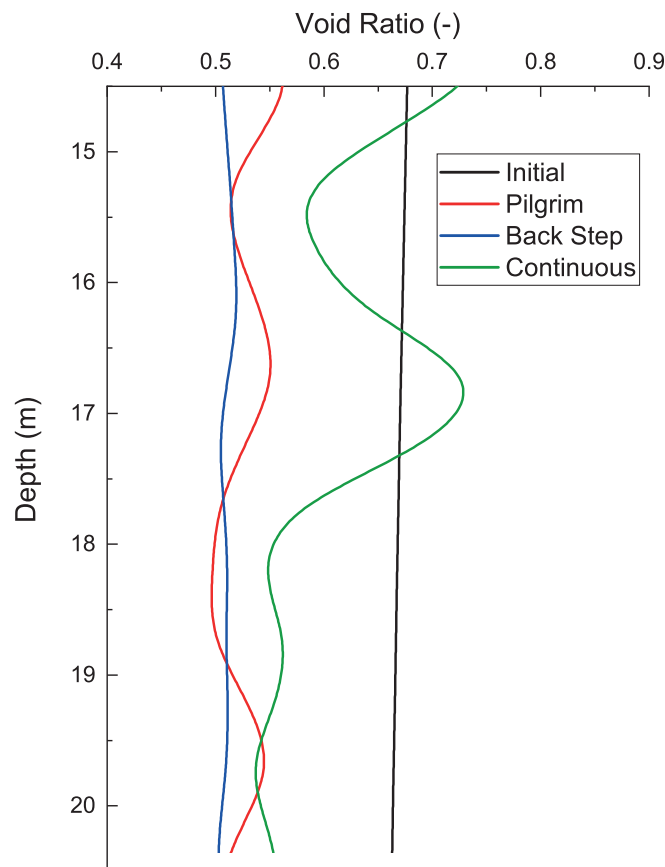


Figure 6.16: Comparison of void ratio with depth at 1 m radial distance for pilgrim step, back step and continuous method of compaction for Kippen sand as obtained from simulations at field scale

field such as the CPT. It should be noted that these results are only applicable to Kippen sand, which is a fine sand; these compaction processes require further analysis for other kinds of granular material. Numerical simulation can help identify best suited compaction process for granular material under consideration. Field trials using these compaction processes would further substantiate their efficiency but currently is out of scope of this work.

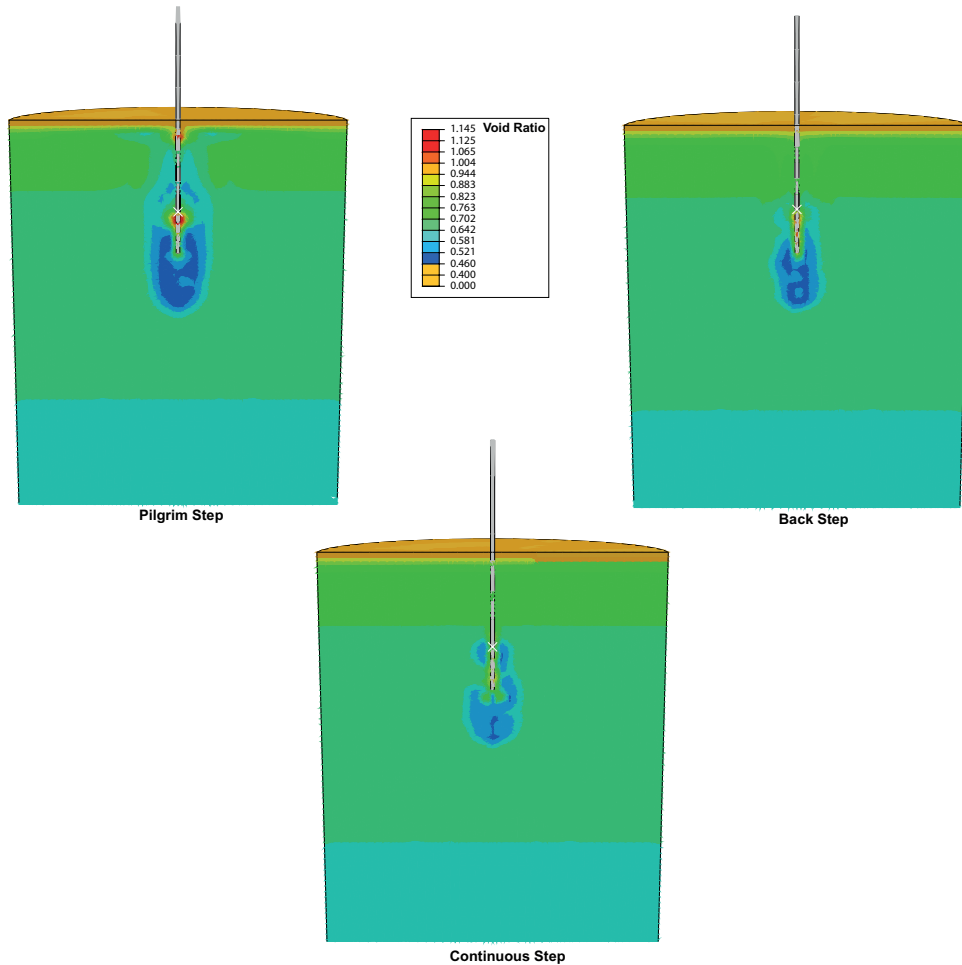


Figure 6.17: Void ratio contours for Kippen sand caused by pilgrim step, back step and continuous method of compaction as obtained from simulations at field scale

6.6 Spacing and Compaction Grid

The spacing of compaction points plays an important role in the success of compaction in a grid. The spacing is usually determined on the basis of field trials or past project experience (Fellin, 2000; Massarsch and Fellenius, 2002; Nagy, 2019). The sequencing of execution of compaction points in a grid can also effect compaction. In the following section two kinds of execution of compaction points in a grid is analysed. Numerical

simulations are carried out in order to visualise the effect of spacing and sequencing of compaction points, on the degree and extent of compaction.

6.6.1 Numerical Simulation Results for Spacing and Compaction Grid

The simulations were carried out using the full scale 40 x 50 m 3D numerical model (Figure 4.13). In order to comprehend the effect of spacing and compaction grid on compaction efficiency, simulations were run at various spacings with a centrifugal force of 520 kN at a frequency of 30 Hz in Kippen sand. The initial relative density was held constant at 46 % for all simulations. Pilgrim step method of compaction was simulated in all the cases (Figure 4.11). It is to be noted that in this case simulations at model scale level were not carried out.

6.6.1.1 Effect of Spacing in Field Scale Simulations

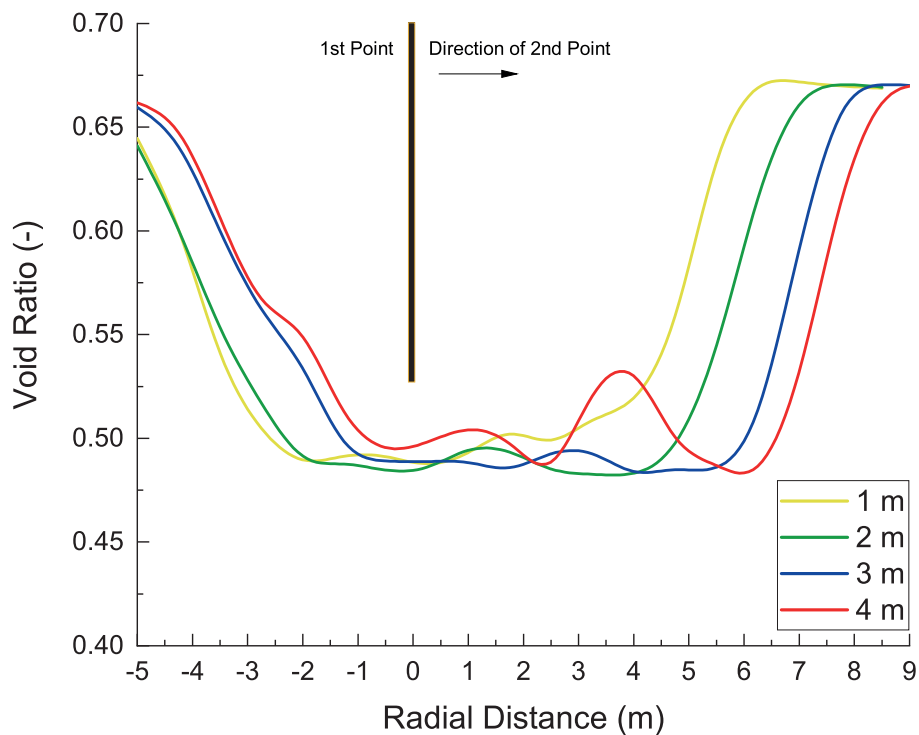


Figure 6.18: Radial variation of void ratio development around compaction points with different spacings at 16 m depth for Kippen sand as obtained from simulations at field scale

After the execution of one compaction point between 25 m and 10 m depth, the results were imported to a new model, and another set of simulations were run for an adjacent compaction point. Figure 6.18 describes the variation of void ratio radially around the compaction points at 16 m depth. Figure 6.18 demonstrates that close spacing of 1 m to 2 m does not maximise the compaction zone, even if a similar magnitude of void ratio was achieved. The compaction zone of the second point overlaps with the already compacted

first zone, leading to an expanded compaction zone. Maximum compaction zone was observed at 3 m spacing due to the positive interference of the two compaction zones with optimised overlapping. As the spacing was increased to 4 m, an interference point developed, which experienced a spike in void ratio. The two compaction zones failed to interfere positively, leading to a poorly compacted intersection zone. In order to better understand the effect of spacing spatially, void ratio contours after the execution of two compaction points at varying spacing were plotted (Figure 6.19). It can be observed that though 1 and 2 m spacing lead to a uniformly compacted soil column, 3 m spacing leads to a maximised compaction zone due to positive interference of the overlapping zones. On the other hand at 4 m spacing some pockets of less compacted soil can clearly be observed.

6.6.1.2 Effect of Compaction Grid in Field Scale Simulations

In all the numerically analysed cases discussed, only single or two compaction points were considered. In the field, on the other hand, a large area is typically compacted following a grid pattern. In order to study the influence of compaction in a realistic 3D space due to multiple compaction points, compaction process was numerically investigated for three compaction points in triangular grid. After the execution of one compaction point between 25 to 5 m depth following the pilgrim step method for Kippen sand, the results were imported to a new model and another set of simulation was run for an adjacent compaction point at 3 m spacing (as 3 m was found to be the optimum spacing). Results from the second model were imported to a third model, and compaction was subsequently executed for a third point to form a triangular grid of 3 m spacings as shown in Figure 6.20(top). In practice, compaction is executed one point after the other in a sequential manner in order to complete the compaction grid. A new parallel compaction technique is analysed in this work by means of numerical simulations in which three compaction points, part of a triangular grid at 3 m spacings are compacted parallelly. In the beginning of the simulation all the three compaction points at 3 m spacing are occupied by a wished in place vibrator system at 25 m depth. All the vibrators started vibrating parallelly with centrifugal force of 520 kN at 30 Hz and simultaneously compacted soil around them following the pilgrim step method. The compaction efficiency for the two methods of compaction, sequential and parallel is compared in Figure 6.20. Results from the two methods are difficult to compare as they are highly non-symmetric in 3D space hence, isosurface was plotted. Figure 6.20 describes the void ratio isosurface achieved following the two above described compaction technique. An interesting observation comes forth that, compacting all the three points parallelly leads to larger radius of spread. Thought, the degree of compaction in both the methods remains same. Trials in field need to be executed incorporating the parallel compaction method in order to ascertain its efficiency in practice. Unfortunately, this is out of scope of this work.

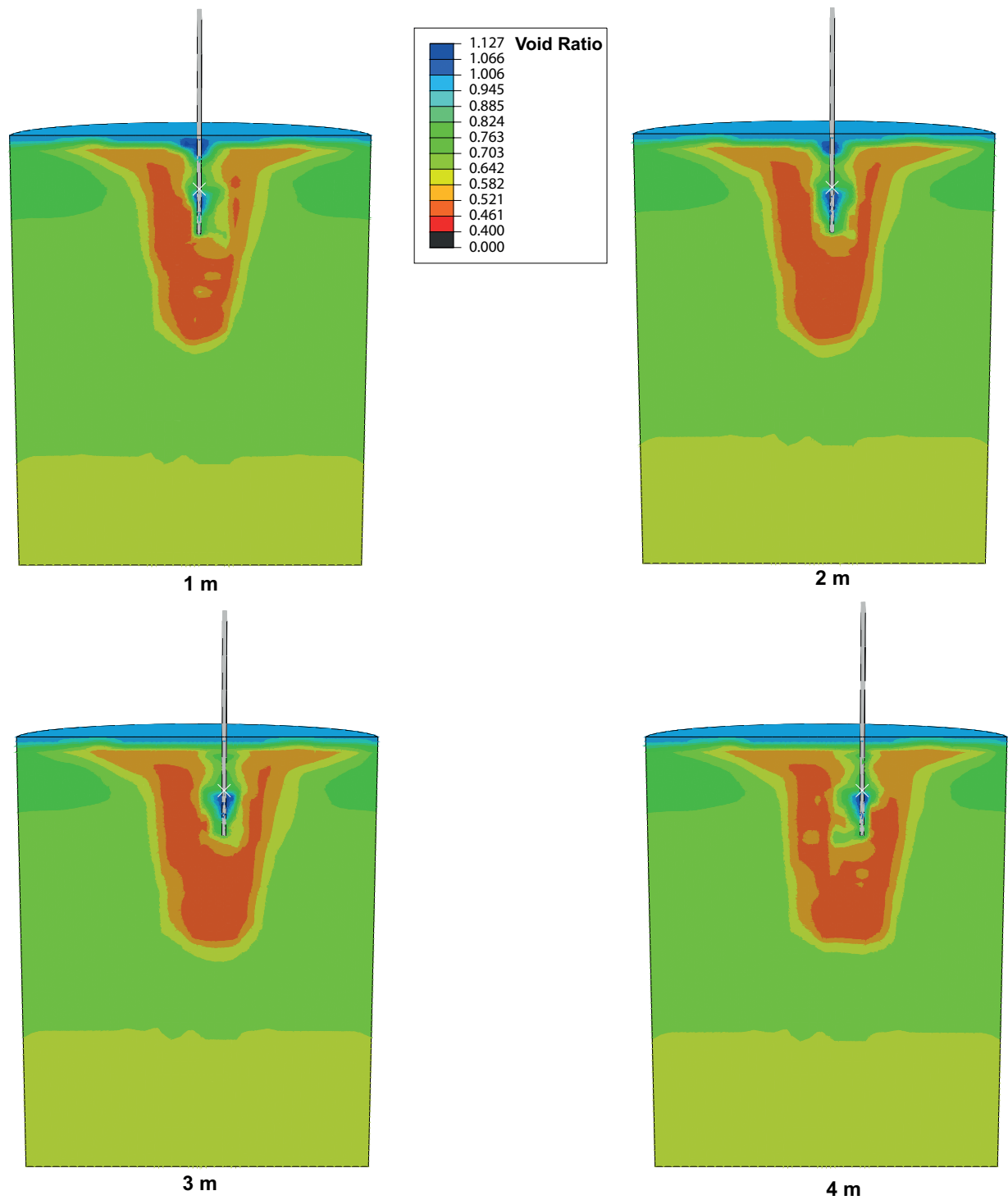


Figure 6.19: Void ratio contours for Kippen sand after compaction with different spacings as obtained from simulations at field scale

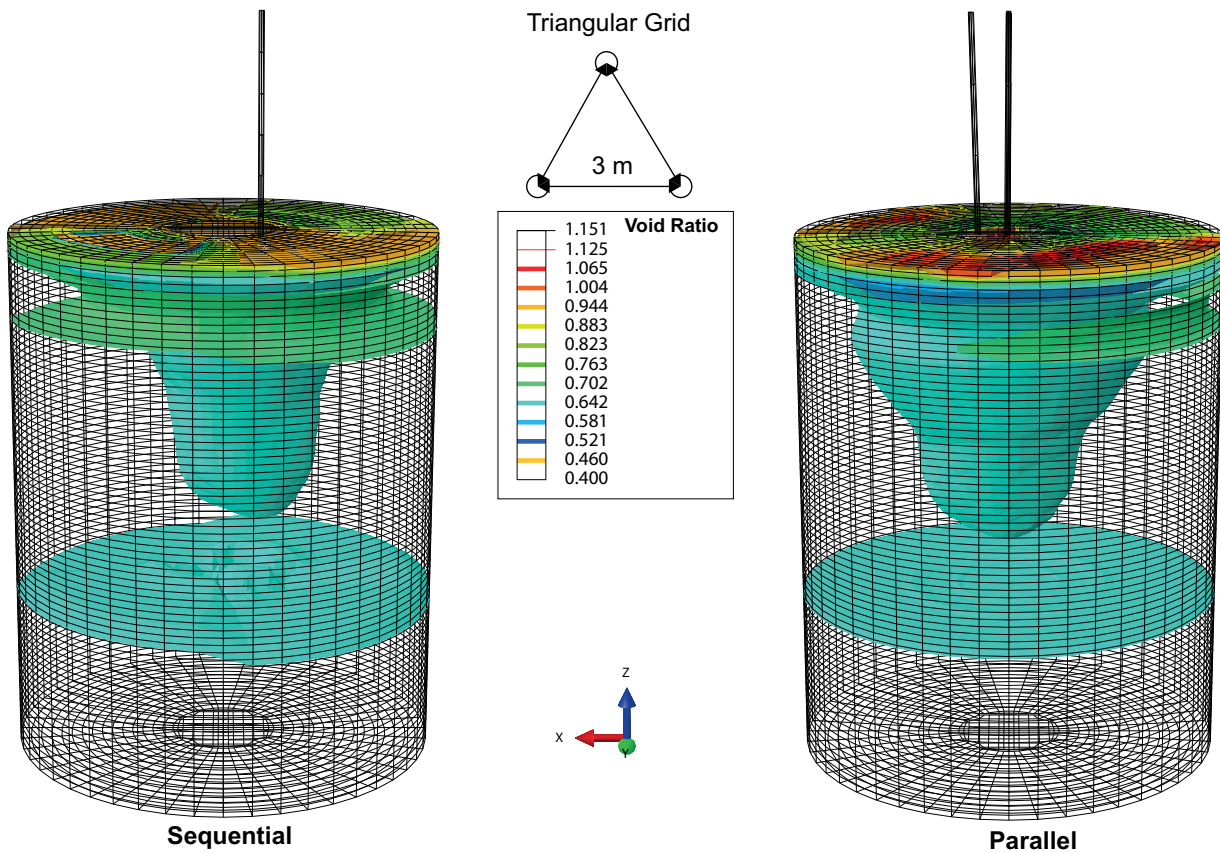


Figure 6.20: Void ratio isosurface for sequential (left) and parallel (right) compaction methods in a triangular grid of 3 m spacing for Kippen sand as obtained from simulations at field scale

6.7 Soil Saturation

Kirsch and Kirsch (2017) suggested that degree of saturation and permeability of soil being compacted influences deep vibratory compaction process. Bo et al. (2014) suggested, based on field observations that saturated sands after deep vibratory compaction exhibit time effects. Excessive pore pressures hinder the reduction in void ratio (Bo et al., 2015). Once the excessive pore pressures dissipate, a reduction in void ratio is observed, leading soil to a denser state (Bo et al., 2014). This reduction of void ratio with dissipation of excess pore pressure is termed as time effect in saturated granular soils (Bo et al., 2014). In addition, it has been observed in-field by Massarsch and Fellenius (2005) that a liquefaction zone develops around the compaction probe in water-saturated soils. Liquefaction occurs when the rate of pore water pressure increase exceeds the rate of dissipation. It may also occur in dry soils by the action of water jetting or when the upward-directed vertical component of acceleration exceeds gravity. As modern machines easily produce accelerations in excess of 10 g, liquefaction is induced in the vicinity of the vibrator due to the vibrator-induced oscillations depending on the permeability. Interpretations suggest that the fluidized zone,

which is characterized by minimum shear strength, is a measure of the soil's transmissibility of vibrations and thus is responsible for the radius of influence of the vibratory treatment. In the transitional or plastic zone, the dynamic forces are not sufficient to fluidize the soil but are still strong enough to shear the soil particles from each other at such a rate that they can find a closer packing. From the point of maximal achievable density (Figure 6.21), attenuation of vibration occurs until it reaches certain threshold shear strength in the ground where any further compaction is inhibited. Water saturation reduces the effective stresses and therefore increases the radius of compaction. As the acceleration transmitted from the vibrator decreases with increasing distance from its source, several annular density zones surrounding the vibrator can be defined as is shown in Figure 6.21. It is for this reason that in dry soils the use of flushing water and even flooding of the whole site extends the radius of compaction. In this section influence of saturation and permeability on deep vibratory compaction would be discussed by means of numerical simulations. Gradual void ratio reduction with dissipation of excess pore pressures would also be commented upon. In order to simulate saturated sand using the hypoplastic model, the constitutive law is modified to simulate two phase behaviour which is briefly described in the next section.



Figure 6.21: Idealized response of saturated granular soils to accelerations created by the vibrator (Rodger, 1979)

6.7.1 Performance of Coupled Hypoplastic Model to Model Saturated Kippen Sand

ABAQUS Explicit does not have any in-built features to model pore pressures (Dassault Systemes, 2014). The coupled two phase hypoplastic model based on the $u - p$ formulation was used in order to simulate the behaviour of saturated sand (Hamann and Grabe, 2011; Hamann et al., 2015). The $u - p$ formulation neglects the acceleration of water phase with respect to the solid phase unlike the $u - p - U$ formulation which includes it. The solid phase is considered to be compressible. Zienkiewicz et al. (1999) suggested that the $u - p$ formulation can work well for cases considering quasi static and low frequency dynamic forces. The formulation provides sufficient mathematical and physical accuracy for modelling of earthquake loads (Zienkiewicz et al., 1999). Implementation of the $u - p - U$ formulation where acceleration of fluid phase is also considered, would only lead to a marginal improvement (Zienkiewicz et al., 1999). The linear momentum balance equation of a mixture of the solid and water phase is given by the following Equation 6.2. The relative acceleration of the water phase with respect to the solid phase is neglected.

$$-\rho_r \mathbf{a}_s + \text{div}(\boldsymbol{\sigma}_{tot}) + \rho_r \mathbf{g}_s = 0 \quad (6.2)$$

with $\rho_r = (1 - n_p)\rho_s + n_p\rho_w$ where, ρ_r is the density of the mixture of the solid and the water phase, \mathbf{a}_s is the current acceleration of the solid phase, n_p is the porosity, ρ_w is the density of water, \mathbf{g}_s is an external applied acceleration and ρ_s is the density of the solid grains. The development of the total stress state $\boldsymbol{\sigma}_{tot}$ with time is obtained by the definition of a hypoplastic constitutive model in an incremental formulation for the mixture of the solid and the water phase with consideration of the concept of effective stress by Equation 6.3.

$$\left(\frac{\alpha - n}{K_s} + \frac{n}{K_w} \right) \frac{\partial p_w}{\partial t} + \alpha \text{div}(v_s) + \frac{1}{\rho_w} \text{div} \left\{ \rho_w \frac{k}{\mu_w} [-\text{grad}(p_w) + \rho_w (g_s - a_s)] \right\} = 0 \quad (6.3)$$

with the Biot's constant $\alpha = 1 - \frac{K_T}{K_S} = 1 - \frac{E}{3-6\nu}$ where, K_S is the bulk modulus of the solid grains, K_w is the bulk modulus of water, v_s is the current velocity of the solid phase, k is the permeability of the solid skeleton, μ_w is the viscosity of fluid, K_T is the bulk modulus of the solid skeleton, E_s is the Young's modulus of the solid skeleton and ν is the Poisson's ratio of the solid skeleton. The coupled hypoplastic model was developed as a single VUMAT capable of performing coupled pore fluid analysis, which is inherently not possible in ABAQUS Explicit. A non-linear dynamic analyses procedure with an explicit central-difference time integration rule was used to solve the governing equations described above.

Wichtmann et al. (2019) concluded that the intergranular strain anisotropy (ISA) model (Fuentes and Triantafyllidis, 2015) is best suited to capture the behaviour of saturated sands under cyclic loading. However, the stability of the ISA model in a finite element (FE) framework (as a VUMAT with $u - p$ formulation if modelling saturated sands in ABAQUS) and performance of the model to capture the densification-related boundary value problem has not been evaluated. Wichtmann et al. (2019) suggested that the hypoplastic model with intergranular strain can be used without major compromise on strain accumulation

Table 6.4: Physical properties of Kippen, A3 and A2 saturated sands

Property	Kippen	A3	A2
Gradation	With Fines	Normal	Poor
e_{\max}	1.116	0.715	1
e_{\min}	0.672	0.456	0.51
ϕ_c	31°	30°	30.3°
C_u	2.25	2.1	1.43
D_{10}	0.08 mm	0.3 mm	0.122 mm
k	2.52×10^{-5}	2×10^{-3}	2.3×10^{-4}

under undrained conditions for problems with strains below 5 %, which is sufficient for our case. The calibrated material parameters for Kippen sand are as tabulated in Table 4.6 along with properties of saturated Kippen sand as tabulated in Table 6.4. Figure 6.22 (top) compares predicted and measured $q - p'$ curve for an undrained cyclic triaxial test, with 30 axial loading cycles performed at 0.2 Hz. Figure 6.22 (middle) compares development of axial strain for the same. Figure 6.22 (bottom) compares the evolution of excess pore pressure with time eventually leading to liquefaction. It can be observed that the coupled hypoplastic model was able to capture very well the maximum stress ratios and accumulation of excess pore water pressures upon loading. As it has been discussed earlier the constitutive law has issues in capturing accumulation of strains under undrained conditions but can be used for strain below 5 %. It is to be noted that strains developed during the deep vibratory compaction simulation were analysed and found to lie between 3-8 %.

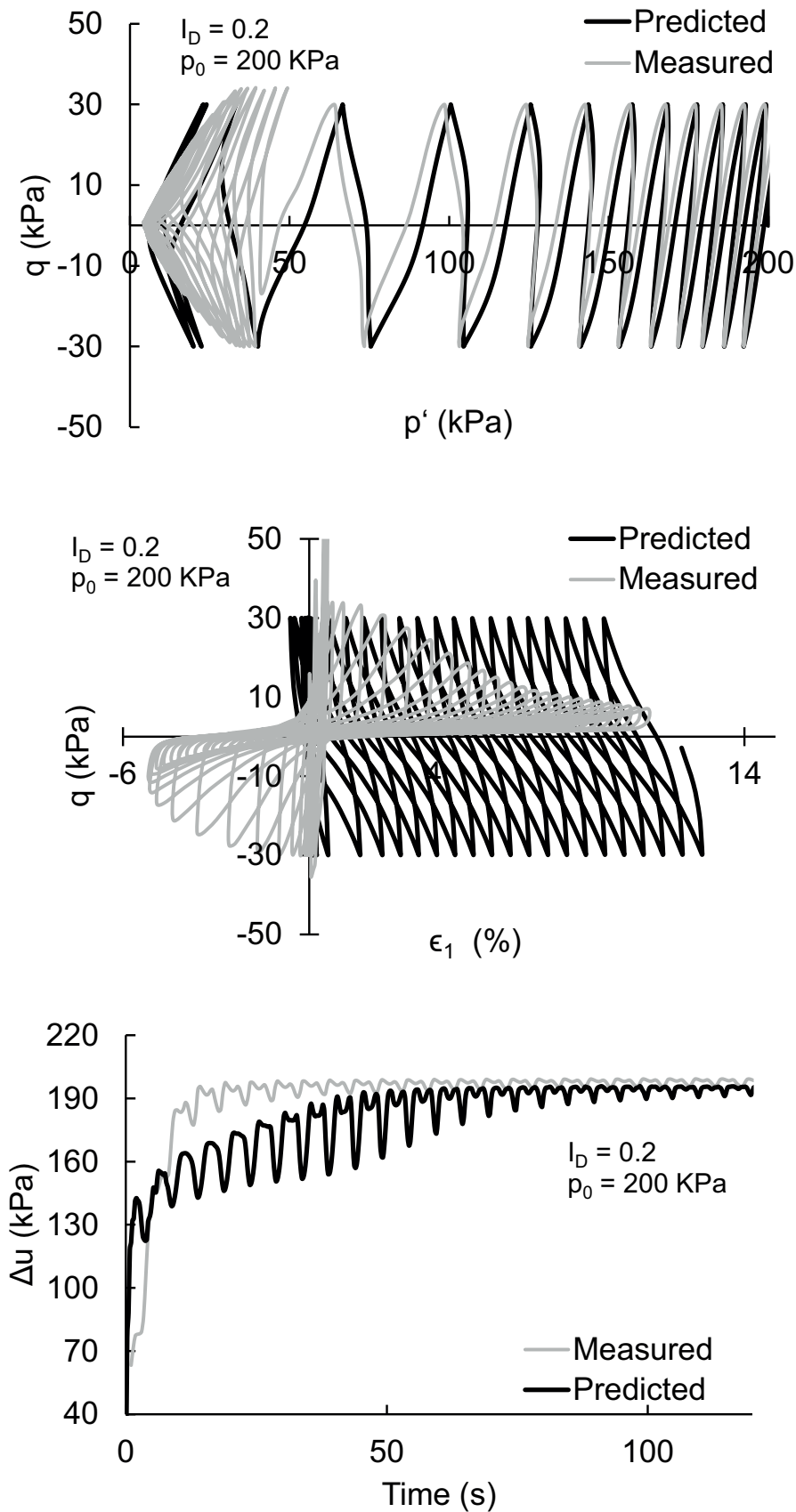


Figure 6.22: Measured and predicted values for $q - p'$ curve (top), development of axial strain with axial cyclic loading (middle) and evolution of excess pore pressure with time (bottom) for 30 cycles of loading at 0.2 Hz for Kippen sand in cyclic triaxial tests

6.7.2 Numerical Simulation Results with Saturated Soil

The compaction saturated sand was carried out using the pilgrim step method between 25 to 5 m depth as described earlier in the full scale 40 x 50 m 3D numerical model (Figure 4.13). The soil was assumed to be completely saturated, with an initial relative density of 46 %, similar to that of dry sand in previously described simulations. The lateral boundaries and top surface of the numerical model (Figure 4.13) were set to be permeable. The bottom surface was assumed to be impermeable. A centrifugal force of 520 kN at 30 Hz for considered in all simulations. The material properties of various sands used in the simulations was as per Table 6.4 and Table 4.6.

6.7.3 Development of Void Ratio and Pore Pressure in Field Scale Simulations

Figure 6.23(b) describes the development of void ratio around the vibrator right after compaction for saturated Kippen sand. The results indicate that the achieved level of compaction was less in saturated sand compared to a dry condition (Figure 6.23(a) and Figure 6.23(b)). Excessive pore pressures hinder the reduction in void ratio (Bo et al., 2015) (Figure 6.23 (c)). Once the excessive pore pressures dissipate, a reduction in void ratio is observed, leading soil to a denser state (Bo et al., 2014). This reduction of void ratio with dissipation of excess pore pressure is termed as time effect in saturated granular soils as discussed earlier (Bo et al., 2014). Modelling of the dissipation of excessive pore pressures is discussed in the following section. The resulting reduction in void ratio after dissipation of excess pore pressures should ideally be compared to dry sand. Massarsch and Fellenius (2002) observed in the field that a liquefaction zone develops around the compaction probe in saturated soils. This was also observed in the simulation results in the form of effective stresses tending to zero around the compaction zone (Figure 6.23(d)). It is noteworthy that the radius of influence is greater compared to dry sand [Figure 6.23(a)]. This can be attributed to the liquefied zone, which is characterised by a low shear strength and greater transmissibility of vibrations, leading to a larger radius of influence (Kirsch and Kirsch, 2017).

In order to understand how effect of saturation on deep vibratory compaction varies with nature of sand, simulations were carried out considering two more kinds of sand namely, A2 and A3 (Table 6.4). Figure 6.24 describes the variation of void ratio with depth at a radial distance of 1 m from the centre of compaction immediately after compaction for 3 kinds of sands. Sand A3 underwent maximum compaction and the Kippen sand the least. The variation could be attributed to the magnitude of excess pore pressures developed after compaction for each kind of sand (Figure 6.25). Sands A3 and A2 with greater permeability (Table 6.4) developed lower excess pore water pressures after compaction compared to Kippen sand. The Kippen sand on the other hand, developed greater excess pore water pressures owing to its lower permeability.

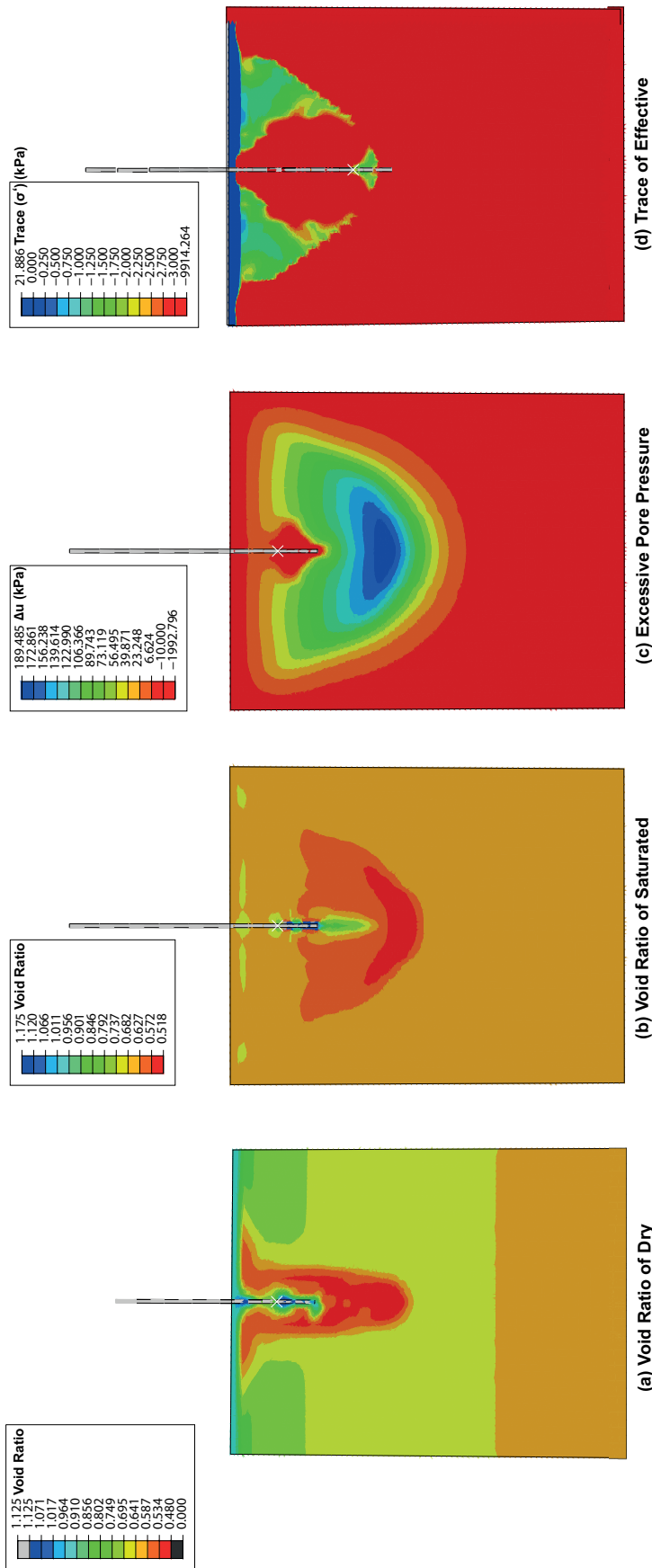


Figure 6.23: (a) Void ratio contour of dry Kippen sand (b) Void ratio contour of saturated Kippen sand (c) Excessive pore water pressures contour (d) Trace of effective stresses contour for Kippen sand as obtained from simulations at field scale

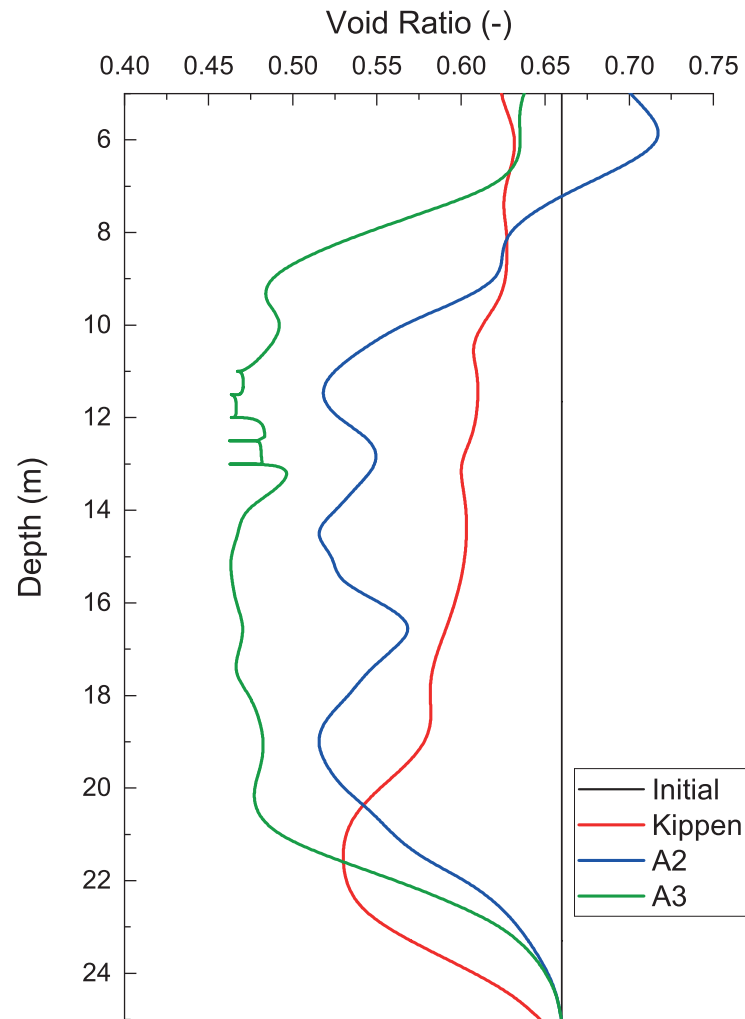


Figure 6.24: Variation of void ratio with depth at 1 m radial distance after compaction of Kippen A2 and A3 saturated sands as obtained from simulations at field scale

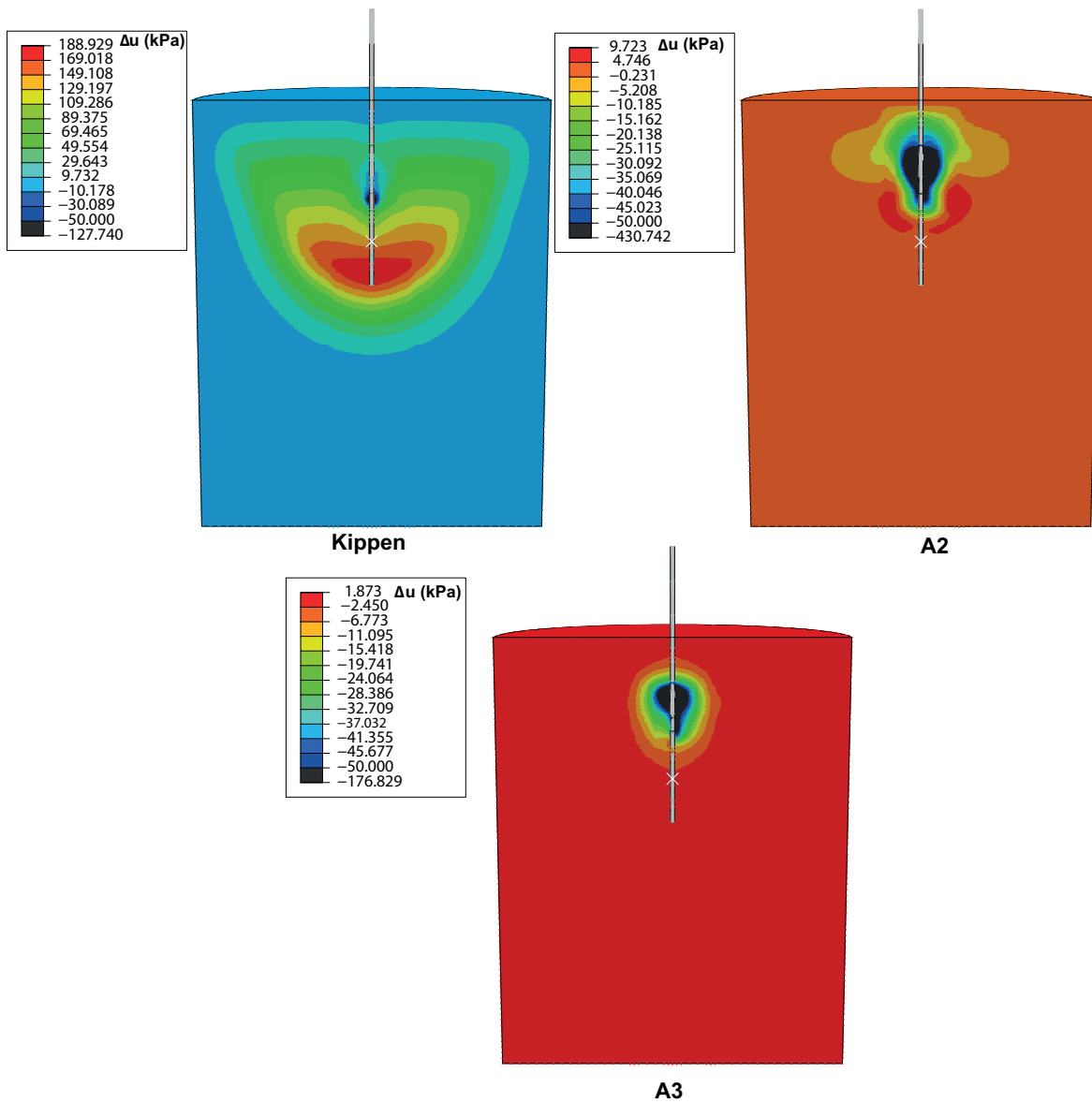


Figure 6.25: Excessive pore water pressure contours for Kippen, A2 and A3 sands as obtained from simulations at field scale

6.7.4 Influence of Permeability in Field Scale Simulations

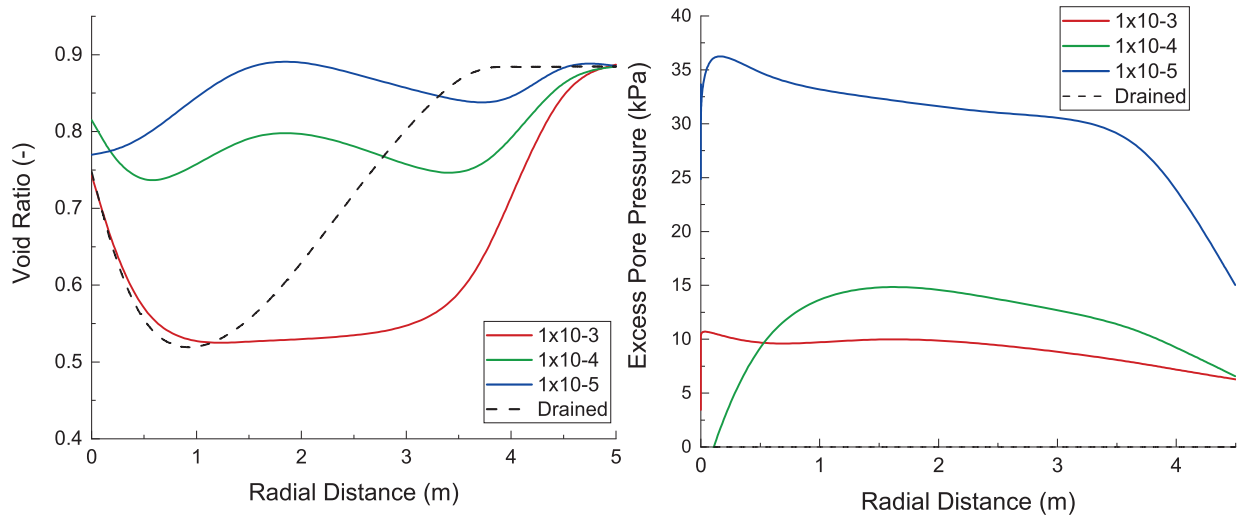


Figure 6.26: Radial development of void ratio (left) and excess pore pressure (right) for Kippen sand with varying permeability as obtained from simulations at field scale

It has been displayed in the preceding section that permeability of sand decides the magnitude of excess pore pressures and this in turn controls the reduction in void ratio. Permeability of sand plays a vital role in deciding the efficiency of compaction. In order to study its effect exclusively, Kippen and A3 sands with 3 permeabilities (all in m/s as mentioned in Figure 6.26) were subjected to compaction at a depth of 20 m for 30 s with a centrifugal force of 530 kN at 30 Hz. Figure 6.26 (left) compares the void ratio variation after compaction around the tip of the vibrator as a function of the radial distance. Deep vibratory compaction efficiency reduced with reducing permeability and increasing magnitudes of excess pore water pressure (Figure 6.26 (right)). Figure 6.26 (left) confirms that saturation of sand along with a greater permeability led to a greater radius of influence compared to dry sand. This observation can be explained by analysing the acceleration that developed in the soil as plotted in Figure 6.27 (left). It can be observed that sand with permeability of 1×10^{-3} experienced maximum acceleration (Figure 6.27(left)) and the acceleration was large enough to cause rearrangement of soil particles according to Figure 6.21. Other higher permeabilities also lead to higher accelerations but the lower dissipation of pore pressures due to lower permeability hindered reduction of void ratio. Figure 6.27 (right) describes the rate at which lowest void ratio was reached and it can be observed that sand with permeability of 1×10^{-3} densified faster due to higher acceleration and faster dissipation of excess pore pressures as explained before. Kippen sand contains 8 % fines on the other hand A3 is a normally graded sand with no fines (Figure 4.17). Figure 6.28 (top left) plots the void ratio reduction around the tip of the vibrator for A3 sand for different permeabilities. It can be observed that dry sand and sand with permeability of 1×10^{-3} led to similar degree and extent of compaction unlike for Kippen sand. This

can be explained by the fact that the sand develops very less excess pore pressures and experienced similar acceleration similar to that of dry sand at permeability of 1×10^{-3}) (Figure 6.28 (top left and bottom)). The void ratio reduction is less at permeability of 1×10^{-4}) and 1×10^{-5}) due to development of negative pore water pressure, leading to a dilative effect instead of compressive (Figure 6.28 (top left)). It can be concluded that deep vibratory compaction may not be suitable for compaction of sands with a low permeability, but saturation of sand for highly permeable sands with fines increases the radial extent of compaction. Sensitivity of permeability reduces as gradation of sand improves. Simons and Kahl (1987) acknowledged that deep vibratory compaction should be used for soils with the higher permeability. Low permeability led to higher magnitudes of excess pore water pressure. Grain rearrangement into a denser state occurs once the excess pore pressures dissipate. So, soils with higher permeability not only lead to reduced excess pore pressures but also aid in faster dissipation.

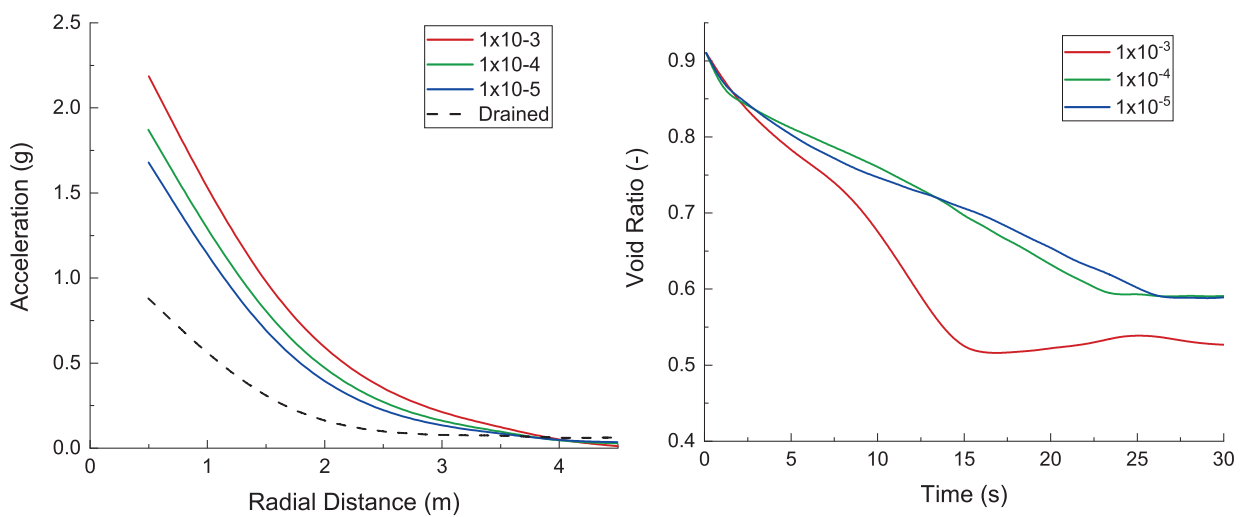


Figure 6.27: Radial development of acceleration (left) and void ratio with time for Kippen sand with varying permeability as obtained from simulations at field scale

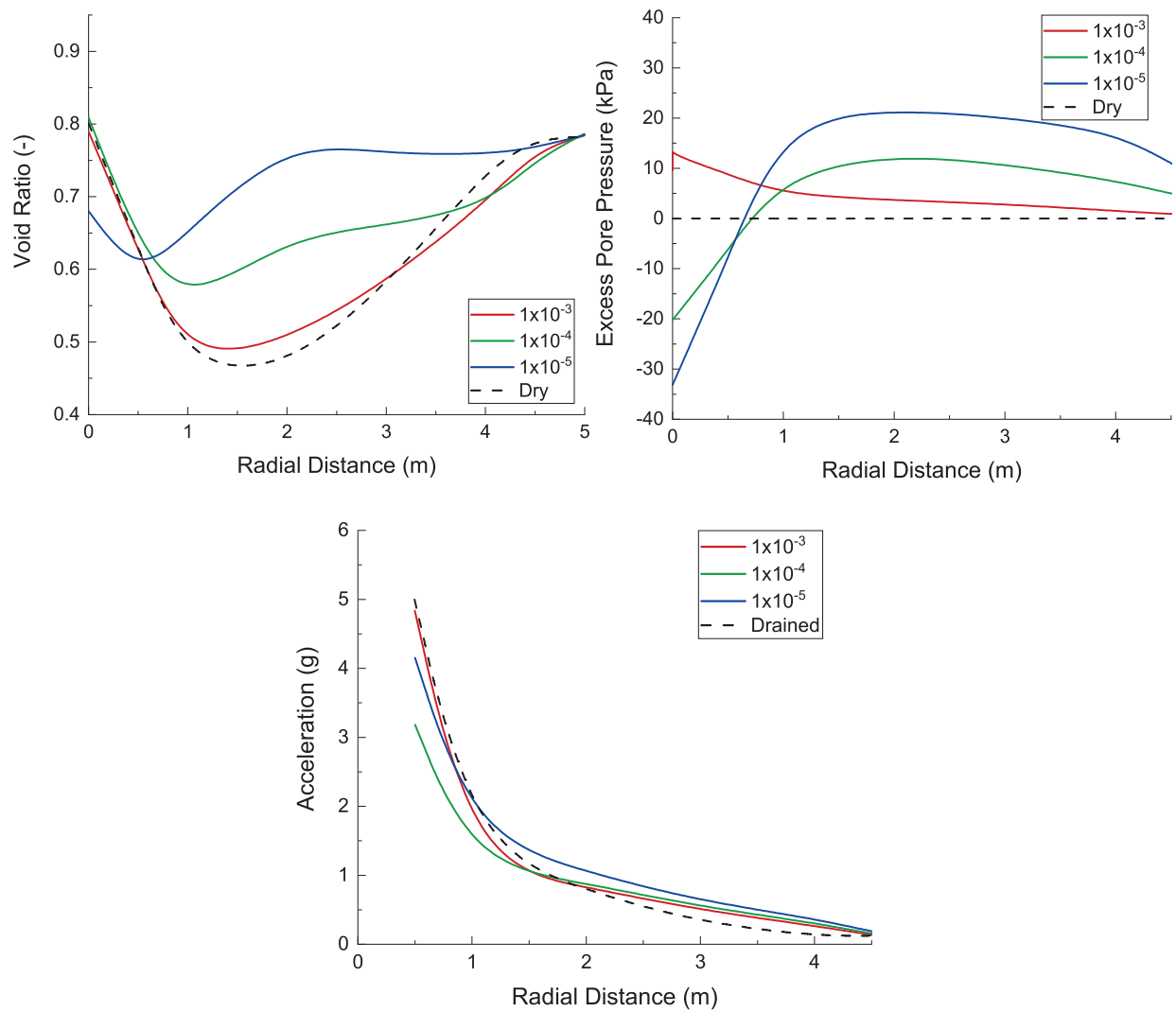


Figure 6.28: Radial development of void ratio (top left), excess pore pressure (top right) and acceleration (bottom) for A3 sand with varying permeability as obtained from simulations at field scale

6.7.5 Variation of Void Ratio with Consolidation in Field Scale Simulations

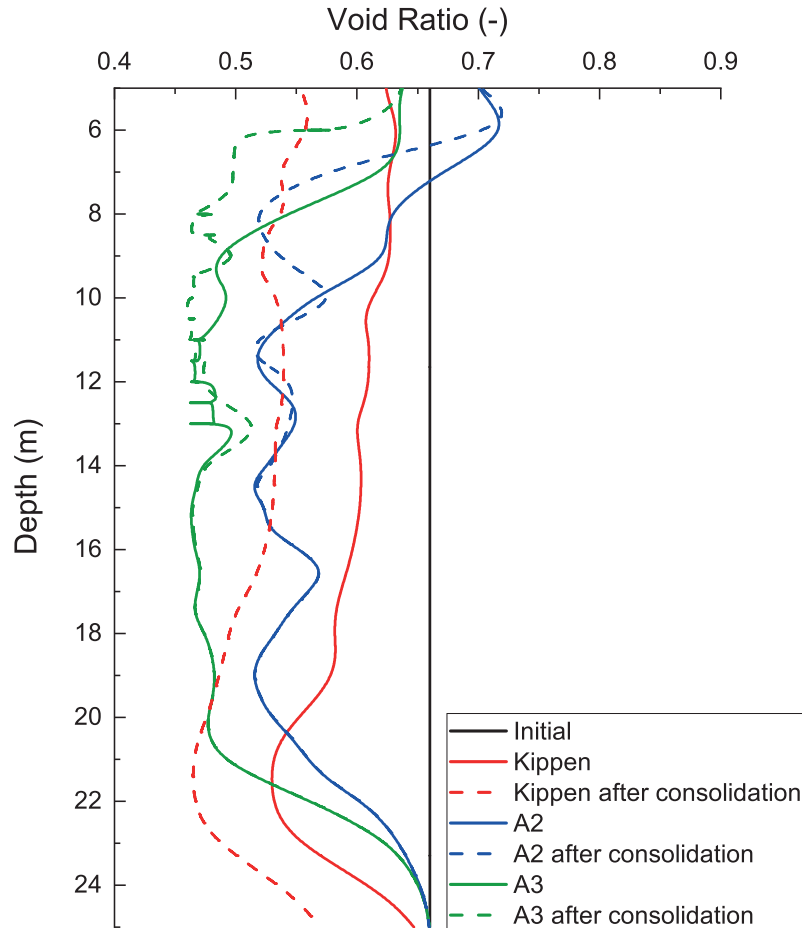


Figure 6.29: Variation of void ratio with depth for Kippen, A2 and A3 saturated sands after dissipation of excess pore water pressures as obtained from simulations at field scale

Bo et al. (2014) suggested, based on field observations that saturated sands after deep vibratory compaction exhibit time effects as discussed earlier. Modelling of the dissipation of excess pore water pressure in an Explicit framework is not possible due to higher computational efforts. The developed stress state in the 3 saturated sands after compaction was exported to an Implicit model in ABAQUS 6.14. The state variables were mapped from the 8-noded Eulerian elements to 8-noded brick elements in an Implicit framework using a Matlab routine. The new model with imported variables was subjected to consolidation steps, where the model was run until all the excess pore pressures dissipated. Figure 6.29 compares the void ratio after dissipation for the 3 sands. Kippen sand developed greater excess pore water pressures after compaction compared to A2 and A3 sands [Figure 6.25], which hindered the reduction in void ratio. Once the excess pore water pressures dissipated, a reduction in void ratio was observed confirming the existence of time effect. Sands A3 and A2 developed negligible excess pore water pressures due to a greater permeabil-

ity. Hence, they underwent major reductions in void ratio immediately after compaction, exhibiting no time effects. Figure 6.30 compares void ratio reached by each sand after consolidation to the void ratio reached by same sand in dry state. It can be observed that sand attains similar void ratio in each case suggesting that consolidated saturated sand reaches a densified state comparable to dry sands. In some scenarios presence of water increases the radial extent of compaction as discussed before.

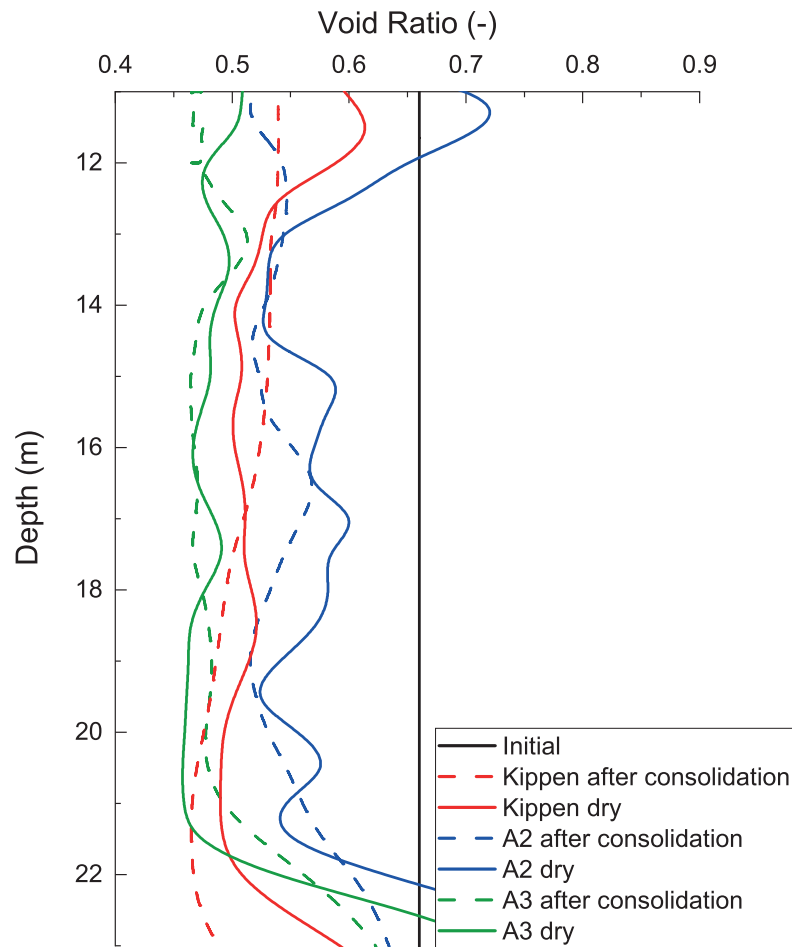


Figure 6.30: Comparison of void ratio after compaction for dry and Kippen, A2 and A3 saturated sands as obtained from simulations at field scale

7 Optimisation of Deep Vibratory Compaction: Compaction Control

The lack of analytical design methodology and dependence on field experience of past projects inhibits cost effective utilisation of deep vibratory compaction. Nagy (2019) and Nagy and Adam (2019) conducted deep vibratory compaction in gravel and found that the compression process was divided into a contracting behaviour indicating compaction followed by a dilate behaviour, indicating end of compaction. The dilative behaviour indicated an increased soil stiffness leading to reduction of amplitude and phase angle of the vibrator. Nendza (2006) conducted model tests with a simple model vibrator and concluded that amplitude and phase angle of vibrator reduced with compaction time. Fellin et al. (2000) and Fellin et al. (2003) and Nagy and Adam (2019) identified amplitude of the vibrator probe to be an effective on-line compaction control parameter. Currently used on-line compaction control parameters such as power, current consumed and quantity of additional granular material are imprecise and fallible (Fellin, 2000). The real-time increase in density of soil with progress of compaction cannot be realised and hence identification of an effective online control parameter for the optimisation of compaction process is necessary. It is also to be ascertained if such online control would lead to better compaction. In order to study the effectiveness of amplitude as on-line compaction control parameter, 1g tests with model vibrator were performed. The variation of amplitude and phase angle during compaction was studied. Compaction efficiency in model tests using amplitude as control parameters was compared to ones without it. Once the feasibility of using amplitude as control parameter was established at 1g model test level, the same was verified at realistic stress state conditions by means of numerical simulations in Coupled Eulerian Lagrangian (CEL) framework.

7.1 1g Model Tests

1g model tests were conducted using an in-house fabricated model vibrator under controlled conditions on a granular material. Details regarding the test set-up, mini vibrator, Hamburger sand and test conditions has already been discussed in Chapter 4. Tests were conducted at compaction frequencies of 15, 35, 40 and 60 Hz. The model vibrator penetrated into the sand layer at the centre of the test tank to a depth of 30 cm from the top of the sand layer. In certain tests compaction was carried out at two depths of 50 and 25 cm from the top of the tank. After reaching the required depth, the frequency of the vibrator was set to the required compaction frequency and was vibrated for a time period of 30 s. After compaction, the vibrator was withdrawn without vibration. CPTs were performed before and after compaction. Mini CPT with a diameter of 16 mm was mounted on the

test frame rig and driven into the sand at a rate of 20 mm/s. CPT with a with a cone area of 2 cm² was used to substantially reduce size and boundary effects. CPT results were recorded at the centre of the compaction point and at radial distances of 70 mm, 140 mm and 250 mm from the centre. It is to be noted that each test was conducted 3 times in order to ensure repeatability and the average of all test results are discussed.

7.1.1 Measurement of Amplitude and Phase Angle

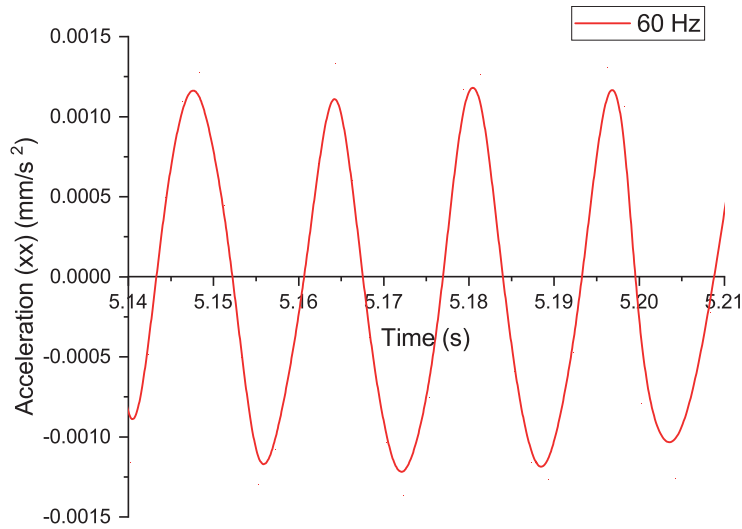


Figure 7.1: Acceleration variation with time of tip of the vibrator at compaction frequency of 60 Hz in 1g model test

Researchers in the past have recognised the variation of amplitude and phase angle of the vibrator while compacting and have suggested their suitability to study progress of compaction with time. In order to ascertain if these two can be used as control parameters for compaction, the 1g model test system has to be equipped to measure phase angle and amplitude of the vibrator in real-time. The amplitude of the vibrator tip was derived from the acceleration sensor signal. The acceleration signal was idealized as sinusoidal signal (see Figure 7.1) as described in Equation 7.1. This assumption is justified as the vibrator tip has been observed to follow a circular movement due to centrifugal force created by the rotating eccentric mass (Fellin, 2000).

$$a(t) = a_0 \sin(\omega t) \quad (7.1)$$

where, a_0 = acceleration amplitude, ω = angular frequency and t = time. The above expression was double integrated in real-time to arrive at the amplitude of the vibrator tip in the x and y direction using data from the orthogonal acceleration sensors installed in the model vibrator.

Acceleration signal from the accelerometers while the vibrator was compacting sand in test tank was integrated using the above expression to determine the vibrator tip amplitude. Figure 7.2 depicts the movement of the vibrator (displacement) during compaction at an operational frequency of 60 Hz. It can be observed that the movement of the vibrator was

nearly circular, hence confirming the assumption of acceleration signal to be sinusoidal, correct. The circular path traced by the vibrator tip is divided into four quadrants as shown in Figure 7.3. The expression in Table 7.1 was used to calculate position angle of the vibrator tip. The position of the eccentric mass was determined using the trigger. The trigger output a signal when the eccentric mass crossed the trigger. Since, the trigger was fixed, the position of the eccentric mass at that time instant was known. The position angle of the vibrator tip at the instant the trigger was triggered was obtained using the acceleration sensor data and Table 7.1. The difference between the position angle of the vibrator tip and position of the eccentric mass gave the phase angle. LabVIEW NXG 3.0 (Laboratory Virtual Instrument Engineering Workbench) a system-design platform and development environment with a visual background from National Instruments (National Instruments, 2018) was used to obtain signal from various sensors. Environment was build using equations previously described, to process these signals to evaluate amplitude and phase angle in real-time.

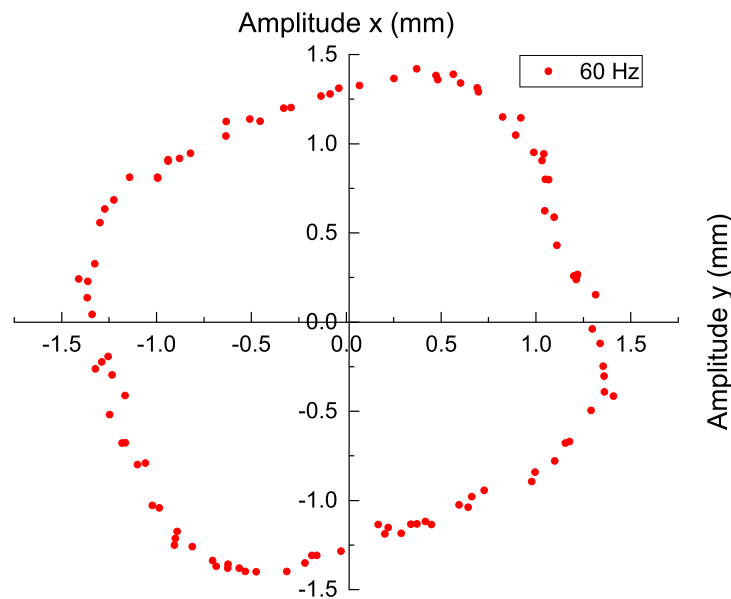


Figure 7.2: Movement of the tip of the vibrator at compaction frequency of 60 Hz in 1g model test

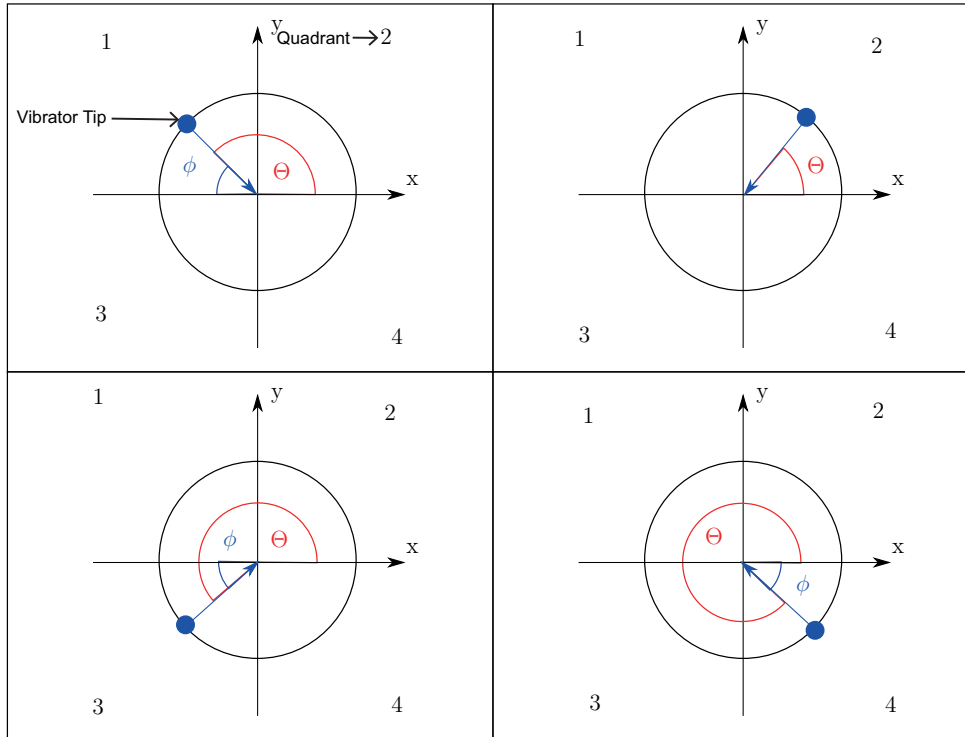


Figure 7.3: Position angle of vibrator tip in various quadrants

Table 7.1: Determination of position angle of vibrator tip

Quadrant	a_x	a_y	ϕ	θ
1	> 0	< 0	$-\text{Arctan}\left(\frac{a_{yy}}{a_{xx}}\right)$	$\pi - \phi$
2	< 0	< 0	$\text{Arctan}\left(\frac{a_{yy}}{a_{xx}}\right)$	ϕ
3	> 0	> 0	$\text{Arctan}\left(\frac{a_{yy}}{a_{xx}}\right)$	$\pi + \phi$
4	< 0	> 0	$-\text{Arctan}\left(\frac{a_{yy}}{a_{xx}}\right)$	$2\pi - \phi$

7.1.2 Identification of Control Parameter: Variation of Amplitude and Phase Angle with Compaction

Model tests were conducted at 15, 35, 40 and 60 Hz. The installed sensors and set-up measured the amplitude of the vibrator tip and phase angle in real-time while the vibrator was compacting Hamburger sand at different frequencies. Figure 7.4(a) describes the variation of amplitude of the tip of the vibrator with time for different frequencies. Vibrator amplitude at 15 Hz is the least and remains constant throughout the compaction process. Vibrator amplitude peaks between 1 to 4 s for 35 Hz frequency and later on remains constant at around 0.2 mm. The power provided by the vibrator is not enough to displace the sand around. The vibrator experiences maximum displacement of around 2.5 mm at 40 Hz which remains constant until 7 s and gradually reduces to 0.2 mm after 12 s of compaction. The maximum displacement amplitude at 60 Hz reduces and theoretically this reduction of amplitude with frequency is well known. The maximum

amplitude plateau of 1.5 mm at 60 Hz, remains constant for 12 s before it collapses to 0.2 mm. Majority of compaction occurs during this constant amplitude plateau regime, as observed in 40 and 60 Hz amplitude curves (Nendza, 2006). As the soil rearranges into a denser state an increase in the soil stiffness is expected leading to a decrease in the vibrator amplitude. Hence, the drop-in amplitude marks the end of compaction which has also been observed by Nagy (2019). 40 Hz with maximum amplitude led to highest degree of compaction at 70 mm radial distance but marginally better compaction was observed for 60 Hz at 140 and 250 mm radial distance (Figure 6.1). This observation can be studied in tandem with amplitude curve of 40 and 60 Hz (Figure 7.4(b)). The higher magnitude of amplitude at 40 Hz explains better compaction by it at 70 mm radial distance whereas the longer duration of constant amplitude curve at 60 Hz explains the increased radial spread of compaction. Once soil densified at 70 mm radial distance for 40 Hz, the power exerted by the vibrator was not sufficient to maintain the amplitude of the vibrator and hence the radial spread of compaction also reduced. Whereas at 60 Hz higher power ensured a prolonged amplitude plateau leading to higher radial spread of compaction. So it can be observed that extent and degree of compaction is an interplay of frequency and amplitude (acceleration) of vibrator and both need to be monitored in order to arrive at optimised compaction regime (Kirsch and Kirsch, 2017). Figure 7.4(b) describes the variation of phase angle with time for different frequencies. The phase angle at 15 Hz remains constant throughout, similar to the amplitude. Rise in phase angle increases with frequency unlike amplitude. The rise and drop in phase angle at 35, 40 and 60 Hz coincide with the amplitude curve trend but it is to be noted that the drop is not as evidently demarcated as in the case of amplitude.

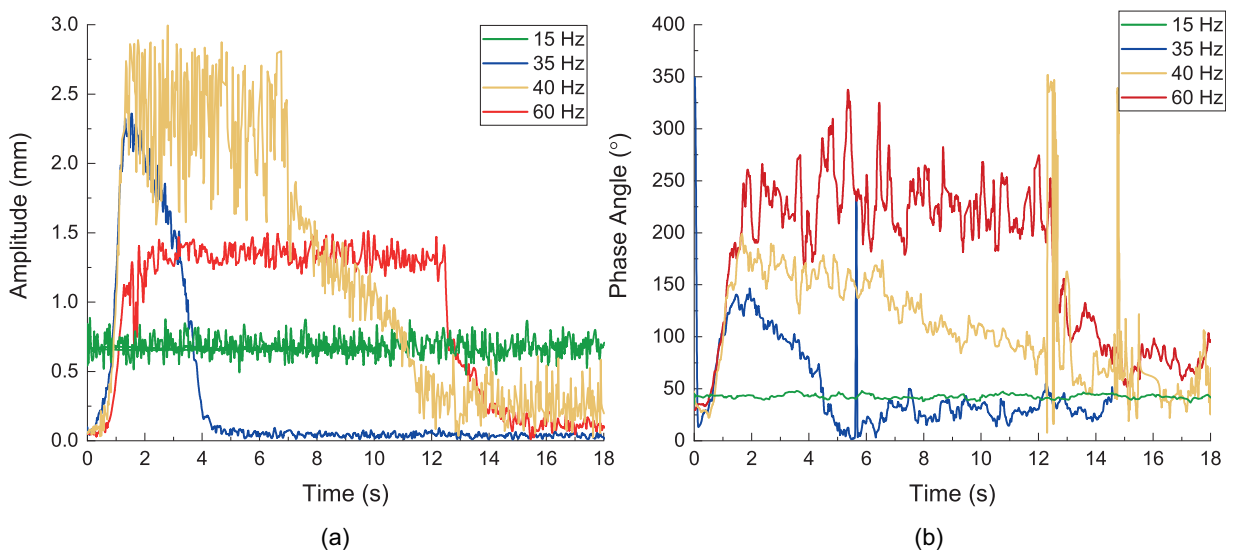


Figure 7.4: Variation of a) amplitude of vibrator b) phase angle of eccentric mass with time for different compaction frequencies in 1g model tests

7.1.3 Calculation of the reaction stiffness according to Nagy (2019)

It has been discussed earlier that Nagy (2019) conducted deep vibratory compaction in gravel and concluded that the process could be divided into a contracting behaviour, indicating compaction followed by a dilate behaviour, indicating end of compaction. The dilative behaviour indicated an increased soil stiffness leading to reduction of amplitude and phase angle of the vibrator. Increase in soil stiffness is often considered as a measure of soil improvement. In this section, soil stiffness variation during compaction in the 1g model test would be evaluated in order to study its variation along the course of compaction and to verify if it would demarcate the end of contractive behaviour.

Mass spring-dashpot system was used as the analytical model for the dynamic soil vibrator system (Nagy, 2019). The soil-machine interaction consisted of two orthogonal arranged Kelvin-Voigt elements, represented by an elastic spring k^* and a viscous damper c^* connected in parallel. The spring stiffness in the analytical model was considered as an indicator for actual soil stiffness. The reaction stiffness k^* was calculated according to Nagy (2019). The product of the mass of the vibrator (M_R) and the amplitude in air at infinitely large frequency ratio ($A_{\beta=\infty,air}$) corresponds to the product of sum of mass of vibrator (M_R) plus mass of vibrating soil (M_B) and amplitude in soil at infinitely large frequency ratio ($A_{\beta=\infty,soil}$) (Nagy, 2019) as described in Equation 7.2:

$$A_{\beta=\infty, soil} (M_R + M_B) = M_R A_{\beta=\infty, air} \quad (7.2)$$

where, all terms are as described before.

The amplitude in air and soil at 60 Hz frequency (high frequency ratio) in the quasi static phase (when amplitude was constant) were evaluated from the results of the 1g model test and found to be $A_{\beta=\infty,air} = 1.3$ mm and $A_{\beta=\infty,soil} = 1.4$ mm. As the mass of the vibrator (M_R) is known, Equation 7.2 was used to evaluate mass of vibrating soil (M_B). Once M_B is known, reaction stiffness k^* as per Nagy (2019) was as per Equation 7.3:

$$k^* = (M_R + M_B) \omega_0^2 \quad (7.3)$$

where, ω_0 = natural frequency and all other terms are as described before.

The natural frequency (ω_0) of the vibrator-soil system was derived from the following Equation 7.4:

$$\omega_0 = \frac{\omega}{\beta_\omega} \quad (7.4)$$

where, β_ω = frequency ratio and ω = actual frequency.

According to Nagy (2019), frequency ratio (β_ω) can be determined as per Equation 7.5 described below:

$$\beta_\omega = \frac{1}{\sqrt{1 \pm \sqrt{\frac{\left(\frac{A_{\beta=\infty,soil}}{A}\right)^2}{1+\tan^2 \Theta}}}} \quad (7.5)$$

where, Θ = phase angle, A = amplitude in particular case and $A_{\beta=\infty,soil}$ = magnitude of the amplitude at infinitely high frequency ratio from model test measurements.

The value of β_ω determined as per Equation 7.5 was used to determine value of ω_0 . This was followed by determination of k^* as per Equation 7.3. The above equations were used

to determine value of soil stiffness k^* and as depicted in Figure 7.5 along with variation of amplitude and phase angle with time for compaction at 60 Hz. The transition from contractancy to dilatancy as per Nagy (2019) is point at which the gradient of the reaction stiffness increases sharply (marked with black dotted line in Figure 7.5). It can be observed that this point coincides with sharp decrease and achieved saturation in magnitudes of amplitude and phase angle. This further validates the usage of amplitude as compaction control parameter indicating the end of contractant behaviour of soil marking the end of compaction.

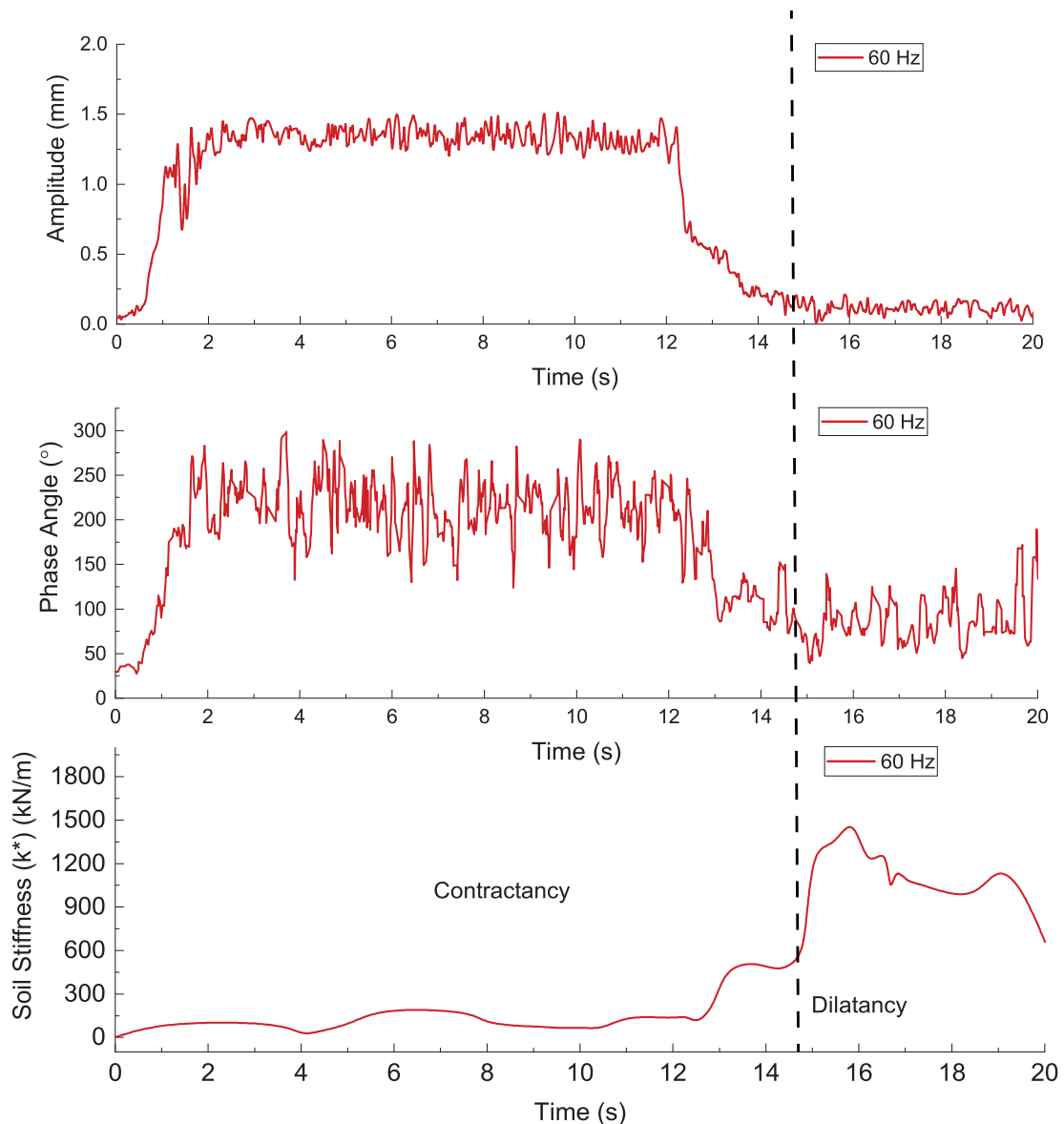


Figure 7.5: Variation of amplitude (top), phase angle (middle) of vibrator and soil stiffness k^* as per Nagy (2019) (bottom) at compaction frequency of 60 Hz as obtained from 1g model test results

7.1.4 Compaction with and without Control

It was observed that fall in amplitude with progress of compaction was more evident than the drop in phase angle. It is also to be noted that measuring amplitude variation in real-time needs only the installation of acceleration sensors and integrating acceleration values leads to obtain amplitude values. On the other hand evaluation of phase angle in real-time needs advanced data loggers and analysis system. Hence, in this work amplitude was chosen as an appropriate control parameter and two sets of tests were carried out at two frequencies of 40 and 60 Hz using amplitude as a control parameter. Two sets of experiments were performed at a frequency of 40 Hz and 60 Hz with and without amplitude as control parameter. In one set, the vibrator was pushed to a depth of 45 cm without vibration and compaction was carried out at concerned frequency for 30 s and then the vibrator was pulled up to 25 cm depth without vibration and at this depth again compaction was carried out at concerned frequency for 30 s. In another set, the compaction at each depth was stopped after a drastic drop followed by constant plateau in amplitude curve was observed. CPT measurements were made after compaction for both the sets of tests at radial distances of 0, 70, 140 and 250 mm from centre of compaction point. These CPT measurements were compared in order to analyse if the amplitude controlled compaction led to similar compaction to that achieved by constant 30 s compaction.

Figure 7.6 and Figure 7.7 compares the variation of amplitude with time at two depths for the four sets of experiments with and without amplitude control at 40 and 60 Hz. It can be observed in Figures 7.6 and 7.7 that the amplitude-controlled tests were terminated at around 6-16 s after a drastic drop followed by plateauing in amplitude curve was observed at both frequencies. It is to be observed that drop in amplitude occurred earlier at 40 Hz than 60 Hz. Figure 7.8 and Figure 7.9 compares the CPT tip resistance values before and after compaction for the four sets of experiments at various radial distances. It depicts that compaction with amplitude control led to similar compaction as observed in uncontrolled case, in lesser amount of time at 40 Hz frequency. At 60 Hz the controlled simulation led to lesser CPT values compared to the non-controlled test. This can be explained by comparing Figures 7.6 and 7.7, in case of 60 Hz vibrator was stopped right after drop in amplitude was observed whereas at 40 Hz there was a delay. This extra compaction time could have led to marginally higher densification in amplitude controlled compaction at 40 Hz.

7.2 Numerical Simulations

1g model tests demonstrated the efficiency of amplitude control compaction at reduced stress level. Once the said was verified at 1g model test level, the same was verified at realistic stress state conditions by means of numerical simulations in Coupled Eulerian Lagrangian (CEL) framework. A 3D CEL based model with 66304 hexahedral elements (Figure 4.13) as described in previous chapters was used to simulate amplitude controlled compaction. The soil body was modelled as an Eulerian domain with a diameter of 40 m and height of 50 m. A V48 type vibrator probe was modelled as depicted in Figure 4.7. The vibrator was modelled as a Lagrangian body, wished-in-place at required depth. To replicate the vibrations of the vibrator, centrifugal force applied by the vibrator in x and

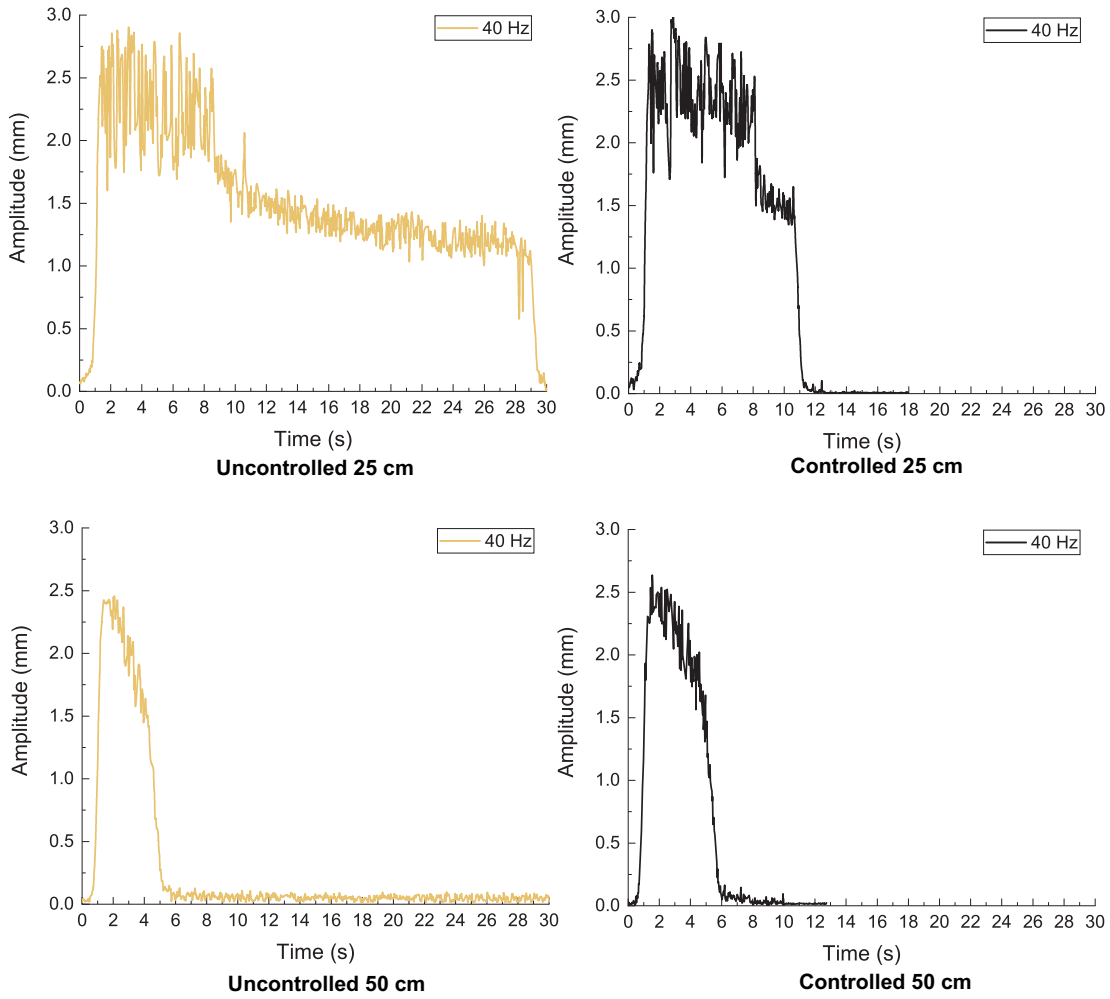


Figure 7.6: Comparison of amplitude of vibrator with and without amplitude control at compaction frequency of 40 Hz in 1g model tests

y directions (horizontal plane) was calculated based on the variables in Equation 7.6, and was idealized to act at the tip of the vibrator.

$$F = m e_m \omega^2 \quad (7.6)$$

where, F = centrifugal force, m = mass of eccentric weights, e_m = eccentricity of masses and ω = angular frequency.

A sinusoidal amplitude for the corresponding operational frequency was applied to the central node at the tip of the vibrator in x and y directions to simulate circular horizontal vibration. Contact between the vibrator and soil was modelled according to Coulomb's friction law. Coulomb's friction law with wall friction co-efficient $\mu = \tan(\phi_c)$ was considered (Chmelnizkij et al., 2017). Hard contact was assumed in the normal direction. The numerical calculation steps considered a linear bulk viscosity of 0.42 and quadratic bulk viscosity of 1.2 as per the work of Kelm (2004) and Hamann et al. (2015) which successfully modelled 1D wave propagation in sand. A time scaling factor (which determines the number of time steps in ABAQUS) of 0.2 was chosen after multiple iterations.

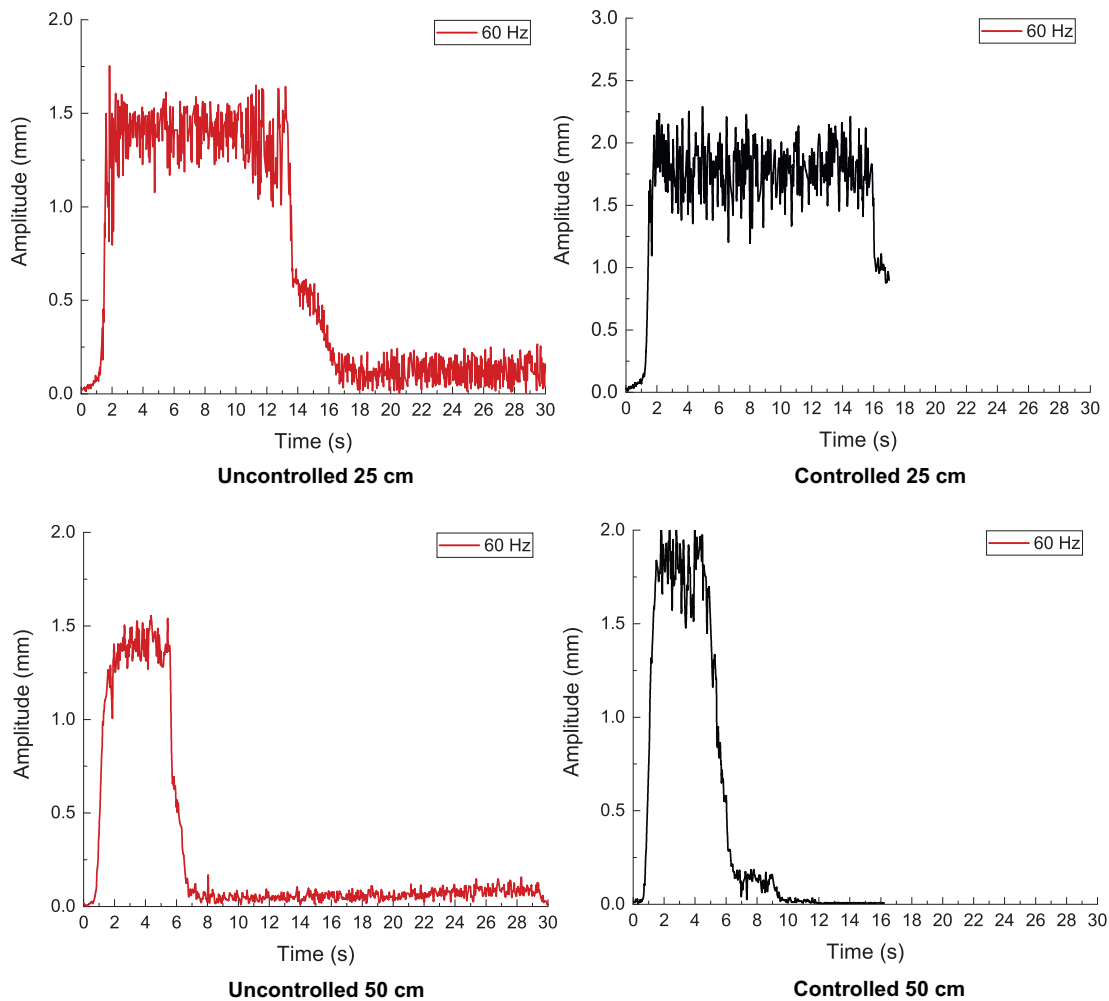


Figure 7.7: Comparison of amplitude of vibrator with and without amplitude control at compaction frequency of 60 Hz in 1g model tests

7.2.1 Code to Control Simulations

The material behaviour of the sand was modelled by the hypoplastic model developed by Kolymbas (1985) and Kolymbas (1991) and Wolffersdorff (1996) and further extended for intergranular strain by Niemunis and Herle (1997). The advantages of using the model for densification problems has already been discussed in detail in Chapter 4. The hypoplastic model was developed as a VUMAT (user subroutine to define material behaviour) to be used in the explicit numerical framework of ABAQUS to model material behaviour of both dry sand. In this case the VUMAT was modified into a VUAMP (User defined amplitude control) subroutine for ABAQUS 6.14 (Dassault Systemes, 2014), in order to simulate the amplitude controlled compaction. Other than being integrated with the hypoplastic VUMAT, the subroutine allowed sensor to be defined at the vibrator tip which automatically evaluated the amplitude of vibrator at each time step. The magnitude of amplitude together with the elapsed compaction time was used to either terminate or continue compaction after each time step. The amplitude control part of the VUAMP is

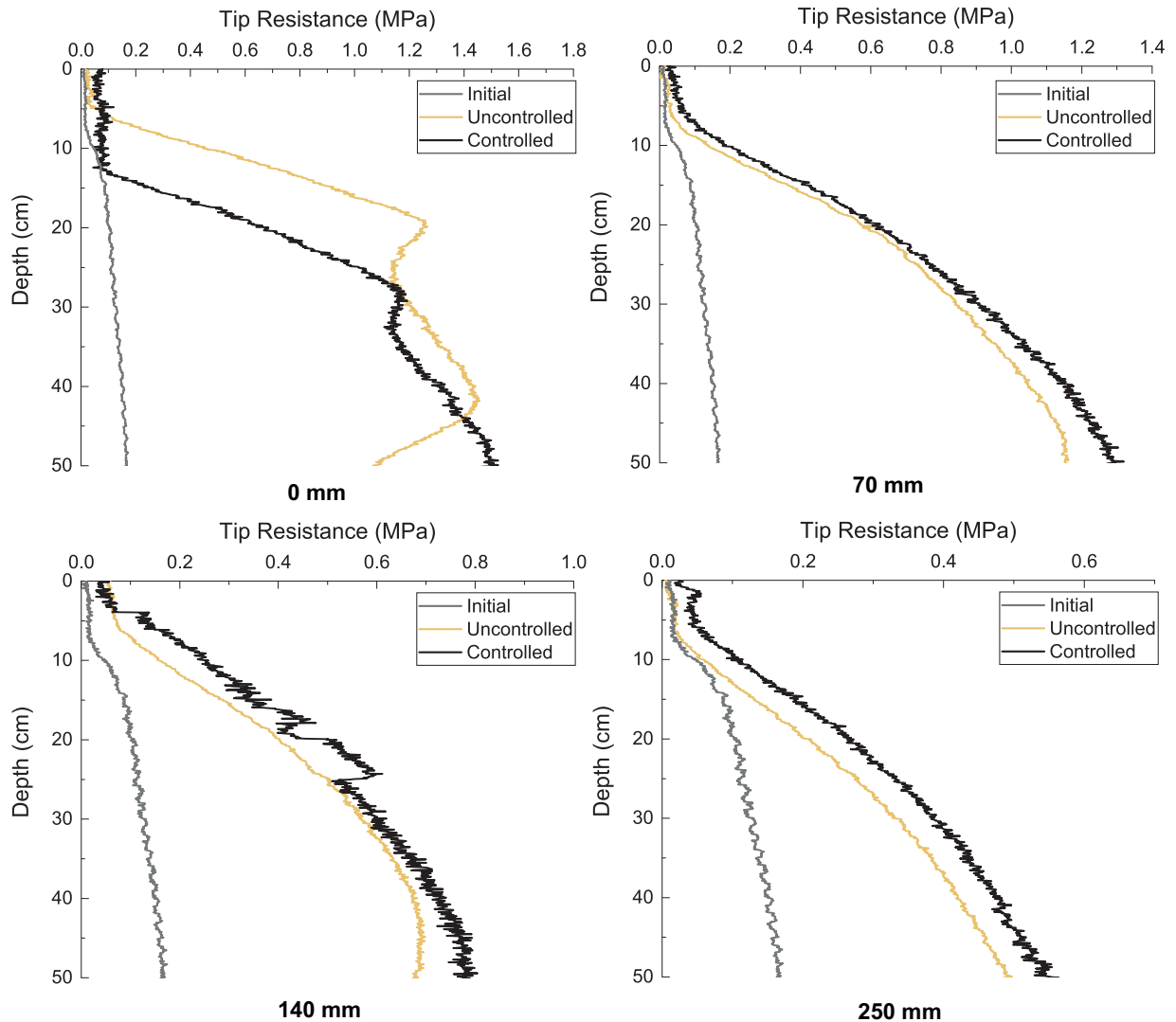


Figure 7.8: Comparison of CPT tip resistance with and without amplitude control at compaction frequency of 40 Hz in 1g model tests

described in Appendix D. The typical calibrated material parameters for Hamburger sand were used in these simulations as tabulated in Table 4.6. Hamburger sand was modelled in order to maintain similarity between the simulations at realistic stress levels and 1g model tests. The vibrator and stay tube were modelled as a linear elastic material with the properties of steel as described before.

7.2.1.1 Simulation Steps

The simulations were carried out using the developed VUAMP which enabled the simulation progress to be controlled based on the amplitude of the vibrator. Two sets of simulations were carried out with VUAMP and without VUAMP where, compaction was carried out for a fixed time. The deep vibratory compaction simulations were carried out

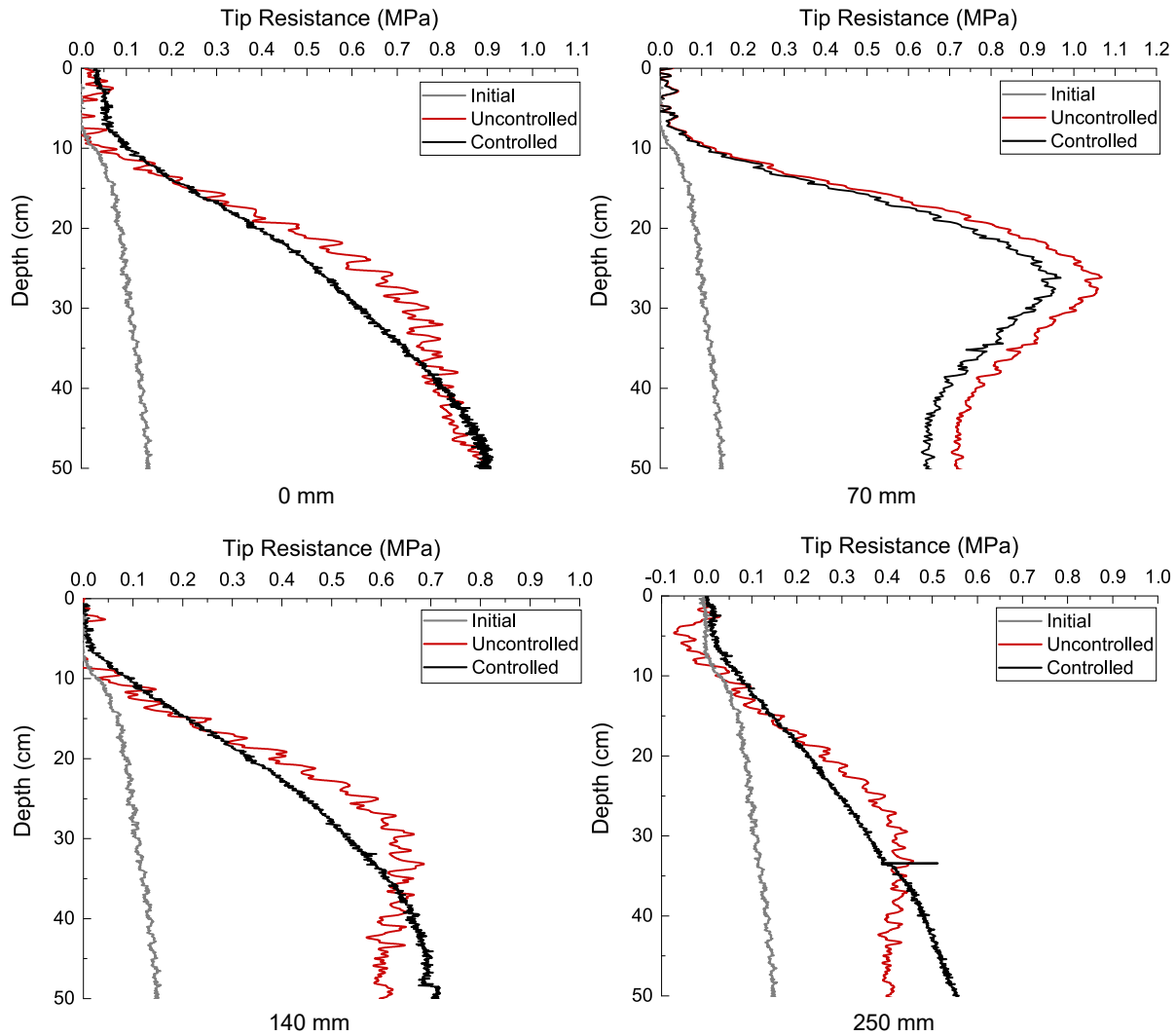


Figure 7.9: Comparison of CPT tip resistance with and without amplitude control at compaction frequency of 60 Hz in 1g model tests

as per the following simulation steps:

1. Initial Phase: Initial state parameters were calculated based on the K0-stress state (Hamburger sand). It should be noted that the penetration effect of the vibrator into the soil was not considered due to computational limitations.

2. Compaction Phase: The vibrator was wished-in-place at a depth of 25 m. In order to replicate the vibrations of the vibrator, nodal forces in x and y directions (horizontal plane) were calculated based on eccentric mass, eccentricity of vibrator and frequency. The force was evaluated to be 520 kN for the V48 vibrator for an operational frequency of 30 Hz as per Equation 7.6. The centrifugal force was idealised to act at the tip of the vibrator.

Two sets of simulations were carried out, one for a fixed compaction time of 30 s and the

other with VUAMP enabled amplitude control routine.

7.2.2 Validation of Numerical Framework based on Amplitude Controlled Model Tests

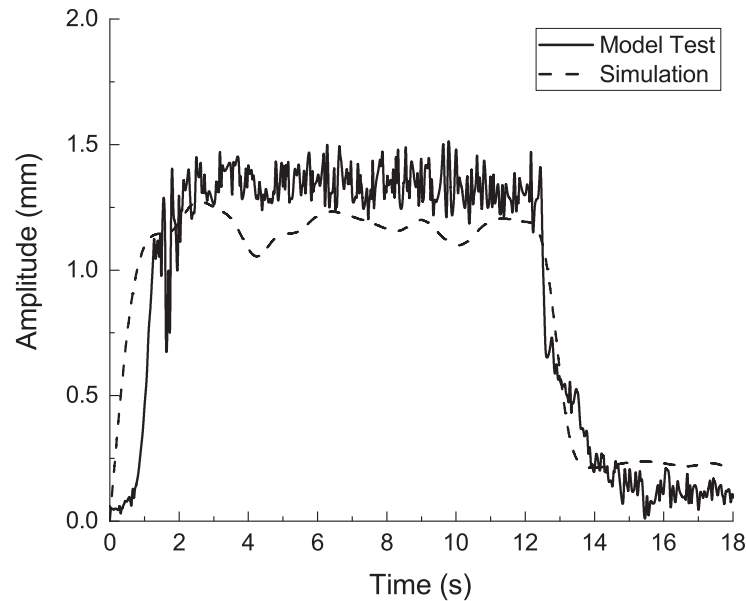


Figure 7.10: Comparison of CEL simulation and 1g model test results for variation of vibrator amplitude with time at compaction frequency of 60 Hz

Prior to using the CEL model to analyse the feasibility of using amplitude as an on-line compaction control measure at realistic stress conditions, one needs to verify if the chosen CEL framework can capture vibrator movement in soil accurately. The CEL framework was used to simulate model tests with model vibrator by Nagula and Grabe (2020) and CPT results at various frequencies were compared to simulation results. The simulation results were found to be in good agreement. CEL model similar to Nagula and Grabe (2020) was created to simulate model test. Simulation was carried out for compaction time of 30 s at 60 Hz frequency. Centrifugal force to be applied was calculated as per Equation 7.6 according to the eccentric mass and eccentricity of model vibrator. Figure 7.10 compares vibrator amplitude as obtained from simulations with model test measurements for 60 Hz compaction. It is evident from the comparison that the CEL framework was able to accurately capture vibrator-soil interaction at model stress state. Following validation, the CEL framework was used to simulate amplitude controlled compaction whose results are discussed in the following paragraphs.

7.2.3 Compaction Simulation with and without Control

In order to verify if model scale results could be extrapolated to prototype scale, two sets of simulations at realistic stress state were carried out. One without amplitude control and other with amplitude control routine (VUAMP). In the first simulation the deep vibratory

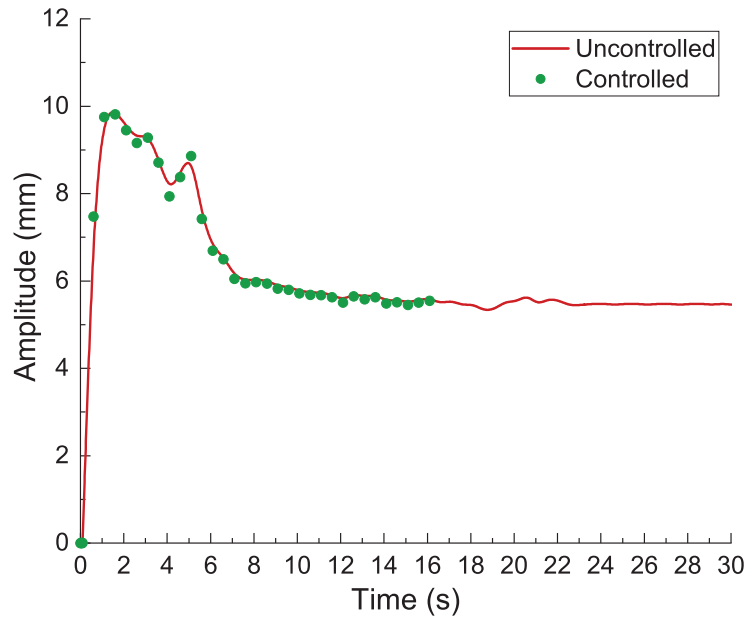


Figure 7.11: Comparison of amplitude of vibrator with and without amplitude control at compaction frequency of 30 Hz as obtained from simulation at field scale

compaction process was simulated at a depth of 25 m for a fixed compaction time of 30s. The amplitude variation with time for fixed compaction time is as depicted in Figure 7.11. The magnitude of amplitude observed in the simulation was found to be in amplitude range of a V48 vibrator. It can be observed that the amplitude initially increased to reach a value of 10 mm and gradually reduced to reach saturation value of 5.5 mm beyond 15 s. The rise and fall followed by saturation of amplitude, should mark the end of compaction as per the observations made in the model tests. Figure 7.12 describes the void ratio around the vibrator after 30 s of compaction. This observation was used to define the criteria for VUAMP for controlled simulation. In the second set of simulation, VUAMP was used, which defined a sensor on the vibrator and evaluated the the amplitude of the vibrator at each time step. The routine was coded to continue compaction for a minimum of 5 s and beyond it was customised to compare the amplitude value from current step with amplitude value of previous step for each time step. The difference between the two was evaluated and the simulation was stopped once the difference reached 0.05 mm. Figure 7.11 depicts the evolution of amplitude with time and how the simulation was terminated by the VUAMP at 16.16 s when the required criteria of difference in amplitude was reached. This ensured rise and fall followed by stagnant amplitude value indicating end of possible compaction. Figure 7.12 compares the void ratio reached around the tip of the vibrator and it can be observed that the amplitude controlled compaction reached void ratio similar to the uncontrolled compaction, with a marginal variation of -1.2 %. The amplitude controlled compaction ensured a gain in compaction of around 14 s which would not only lead to huge financial benefit but would also reduce wear of the vibrator motor.

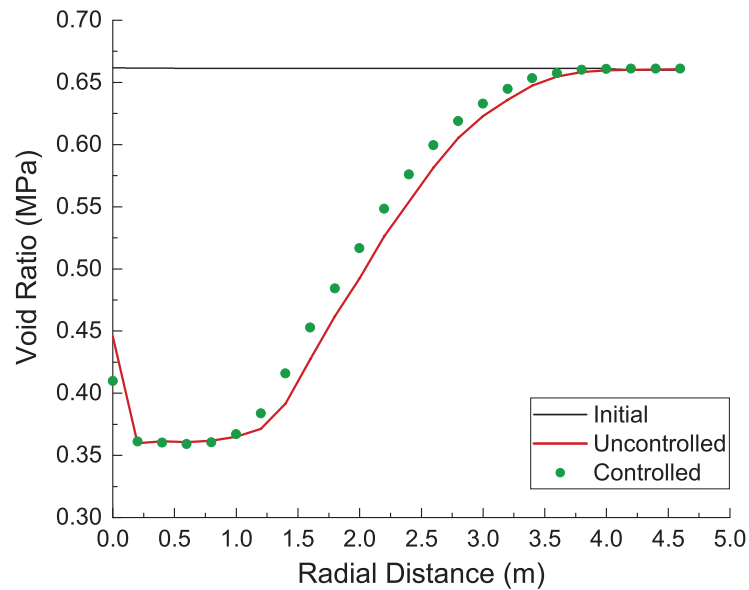


Figure 7.12: Comparison of radial void ratio with and without amplitude control at compaction frequency of 30 Hz as obtained from simulation at field scale

7.3 Extension to Field: Conceptualization

The phenomenon observed in 1g model test and numerical results displayed that compaction achieved by using amplitude as control parameter could not only lead to efficient compaction but also substantial reduction in compaction time. The concept is envisaged to put under field trial in future so as to further substantiate the usage of vibrator amplitude for compaction control. The measurement of vibrator amplitude during compaction process can be easily realised in-field, as vibrators currently in use can be upgraded with acceleration sensors. The data from acceleration sensors can be logged via data loggers and LabVIEW can be used to process the data to evaluate amplitude of vibrator. The data can be evaluated in real-time hence, the operator can use this real-time data to stop compaction at particular depth when drop in amplitude is witnessed. Trials on field with and without amplitude compaction control would verify its applicability in practice. If successful, compaction control can not only reduce compaction time leading to huge financial gain but would also aid in reducing wear of equipment.

8 Liquefaction Mitigation of Deep Vibratory Compaction

Deep vibratory compaction is one of the ground improvement techniques used for liquefaction mitigation in saturated sand. In order to study the feasibility of deep vibratory compaction for liquefaction mitigation, numerical seismic site response of saturated sand before and after deep vibratory compaction was analysed. The non-linear, coupled, hypoplastic u-p formulation as described in Chapter 6 was used to simulate the behaviour of saturated sand. In order to validate the numerical framework used to carry out the seismic simulations, results were validated against centrifuge test simulating seismic site response of saturated sand. The validated framework was used to analyse the efficiency of deep vibratory compaction for liquefaction mitigation for different sands.

8.1 Plane Strain Lagrangian framework

The section describes in brief the numerical framework used to carry out seismic simulations and the centrifuge test carried out to validate the numerical framework.

8.1.1 Numerical Model and Methodology

A plane strain model of 50 m height and 40 m width was created in the Lagrangian domain (Figure 4.15) to simulate seismic analysis of saturated sand before and after compaction by deep vibratory compaction. Additional details about the numerical model have already been discussed in Chapter 4. The coupled two phase hypoplastic model based on the $u - p$ formulation was developed to simulate the behaviour of saturated sand. The formulation provides sufficient mathematical accuracy for modelling of earthquake loads (Zienkiewicz et al., 1999). The coupled hypoplastic model was developed as a single VUMAT capable of performing coupled pore fluid analysis, which is inherently not possible in ABAQUS Explicit, which has already been discussed in detail in Chapter 6. Three kinds of sand namely Kippen, A2 and A3 were used for the seismic analysis and Ottawa sand was used in the centrifuge test. The physical properties of these saturated sands is as tabulated in Table 8.1. The grain size distribution curves and calibrated hypoplastic material parameters of the sands are as described in Figure 4.17 and Table 4.6. It is to be noted that in the absence of experimental tests for determination of the intergranular strain parameters for Ottawa sand, Hochstetten sand parameters were adopted as per Niemunis and Herle (1997). The parameters have been seen to work reasonably well for finite element simulations simulating other similar sands without much variation in results (Niemunis and Herle, 1997). The hypoplastic material parameters of Ottawa sand were calibrated

Table 8.1: Physical properties of Kippen, A3, A2 and Ottawa saturated sands for seismic analysis

Property	Kippen	A3	A2	Ottawa
Gradation	With Fines	Normal	Poor	Fine
e_{\max}	1.116	0.715	1	0.82
e_{\min}	0.672	0.456	0.51	0.53
ϕ_c	31°	30°	30.3°	32°
C_u	2.25	2.1	1.43	1.45
D_{10}	0.08 mm	0.3 mm	0.122 mm	0.13 mm
k	2.52×10^{-5}	2×10^{-3}	2.3×10^{-4}	1.41×10^{-4}

against triaxial experimental results. Figure 8.1 compares the laboratory and hypoplastic model predicted results for Ottawa sand for both dense and loose conditions. Seismic load was applied as horizontal (xx) acceleration time history input to the base of the numerical model. The north-south fault horizontal component of the 1940 Imperial Valley Earthquake in California, USA recoded at El Centro station (Hough, 2004) (Figure 8.2) was used to study liquefaction mitigation effects. The sequence of seismic analysis simulations to model the behaviour of saturated sand before and after compaction has been detailed in Chapter 4. The seismic loading was applied in the form of horizontal (xx) acceleration time histories.

8.1.2 Validation of Plane Strain Model

Centrifuge tests were performed at the University of Colorado Boulder, USA on layered saturated sand deposits subjected to 1D seismic loading and results of same were used to validate the plane strain numerical framework to simulate seismicity led liquefaction scenarios. The centrifuge test consisted of a three-layered saturated sand system subjected to one-dimensional seismic shaking at the base. The test set-up was equipped with accelerometers, pore pressure transducers, and LVDTs at various levels. The comparison of results was used to assess the performance of the hypoplastic model for predicting the liquefaction phenomenon in terms of accelerations, pore pressures, and importantly, settlements. A numerical model based on the finite element framework was developed to simulate and predict the seismic response of saturated sand under free-field conditions in a centrifuge test.

8.1.2.1 Seismic Centrifuge Test

A series of centrifuge experiments were conducted using the 5.5 m radius, 400g ton centrifuge facility at the University of Colorado Boulder (in the U.S.) to evaluate seismic site response and soil-structure interaction in a layered liquefiable soil deposits in the free-field as well as in presence of one or multiple structures (Ramirez et al., 2018; Kirkwood and Dashti, 2018b; Kirkwood and Dashti, 2018a; Kirkwood and Dashti, 2019). In this work,

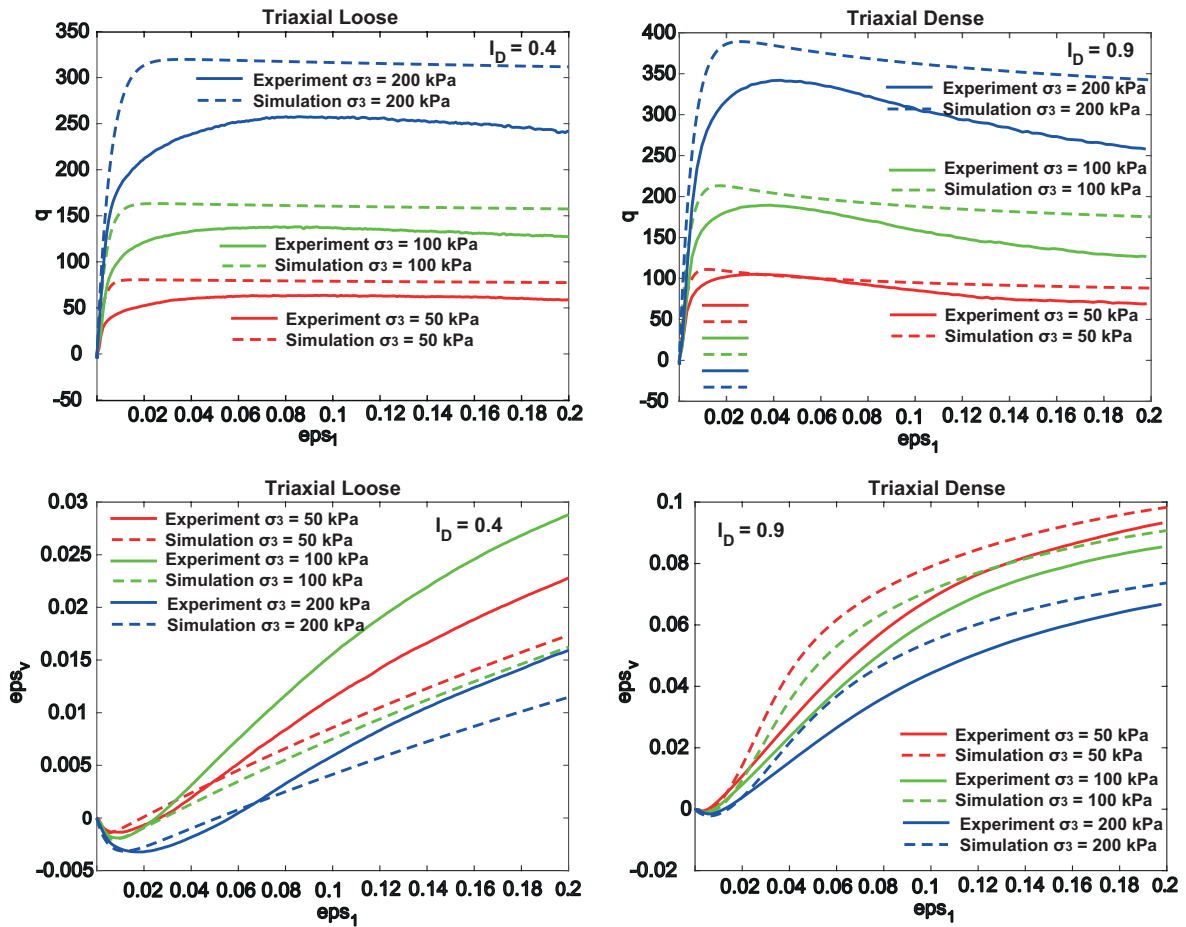


Figure 8.1: Measured and predicted values for monotonic triaxial tests on Ottawa sand

the focus is on one centrifuge experiment that modelled free-field conditions, without any superstructures present. The total thickness of the soil deposit was 18 m in prototype scale, which composed of a 10 m-thick dense Ottawa sand layer with an initial relative density (I_D) of 90 % at bottom, overlaid by a 6 m thick loose Ottawa sand layer with an initial I_D of 40 %. Finally, a 2 m thick coarse Monterey 0/30 sand crust with an initial I_D of 90 % was placed at the top. To enhance the uniformity of the soil properties across the layer, an automated sand pluviator (Kirkwood and Dashti, 2018a) was used to prepare the soil deposit inside a flexible-shear-beam container (Olarate et al., 2017). The initial soil properties for each layer are summarized in Table 8.2, and the soil profile with the layout of instruments is shown in Figure 8.3. The three instrumented arrays were placed to measure the settlement, acceleration, and pore water pressure at the base of the container, middle of each layer, and interface between various layers. Following the preparation of the model, a solution of hydroxy propyl methyl cellulose (HPMC) with a viscosity 70 times greater than water was used to saturate the soil deposit under the centrifuge scaling laws (Olarate et al., 2017; Kirkwood and Dashti, 2018a). The model was then spun to a nominal centrifugal acceleration of 70g estimated at the centre of loose Ottawa sand layer

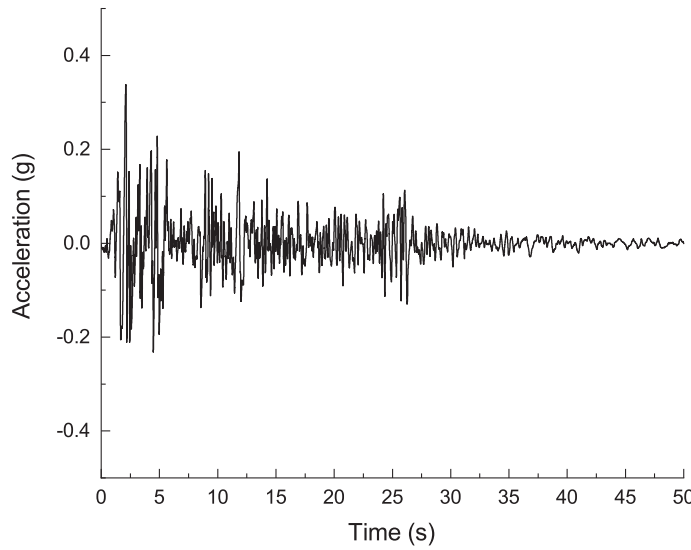


Figure 8.2: Acceleration time history of El Centro earthquake used for seismic analysis

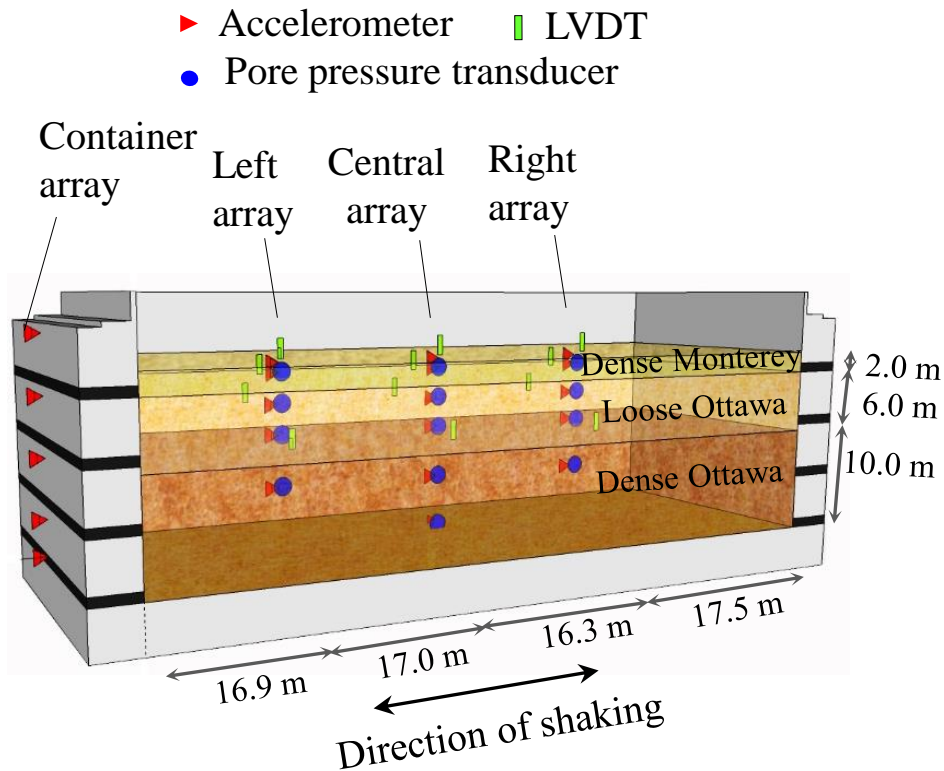


Figure 8.3: The soil profile and instrument layout in seismic centrifuge test (adapted from Ramirez et al. 2018)

prior to the application of one-dimensional shaking. A scaled version of the north-south fault normal horizontal component of the 1995 Kobe, Japan earthquake recorded at the Takatori station was applied at the base of the container, which was referred to as Kobe-L

Table 8.2: Initial properties of saturated sands used in centrifuge test

I_D /Layer	Thickness (m)	e	γ_{sat} (kN/m ³)	k (m/s)
90 %/Monterey 0/30 sand	2	0.57	19.8	5.3×10^{-4}
40 %/Ottawa sand	6	0.698	19.1	1.41×10^{-4}
90 %/Ottawa sand	10	0.56	19.9	1.19×10^{-4}

motion in this paper. Figure 8.4 shows the acceleration, Arias Intensity time histories, and 5 % damped response spectra of the motion recorded at the base of the container.

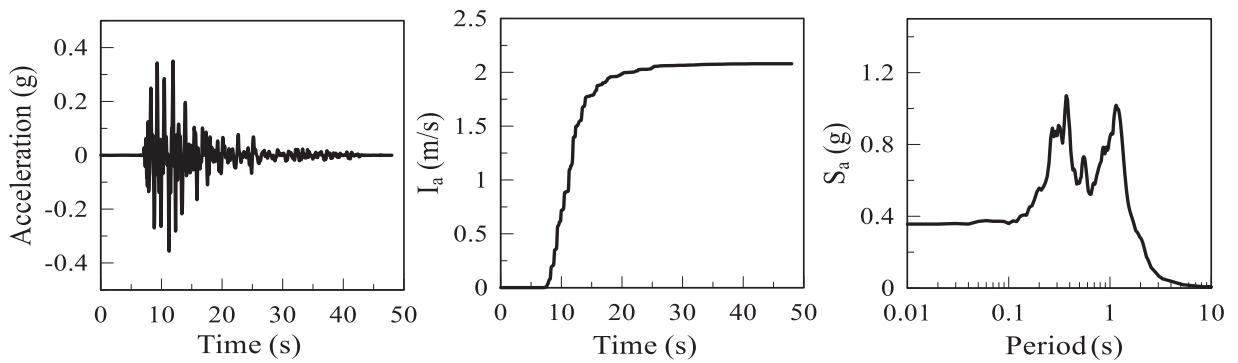


Figure 8.4: The acceleration (left) and Arias Intensity time histories (middle) and 5 % damped response spectrum of the Kobe-L motion (right)

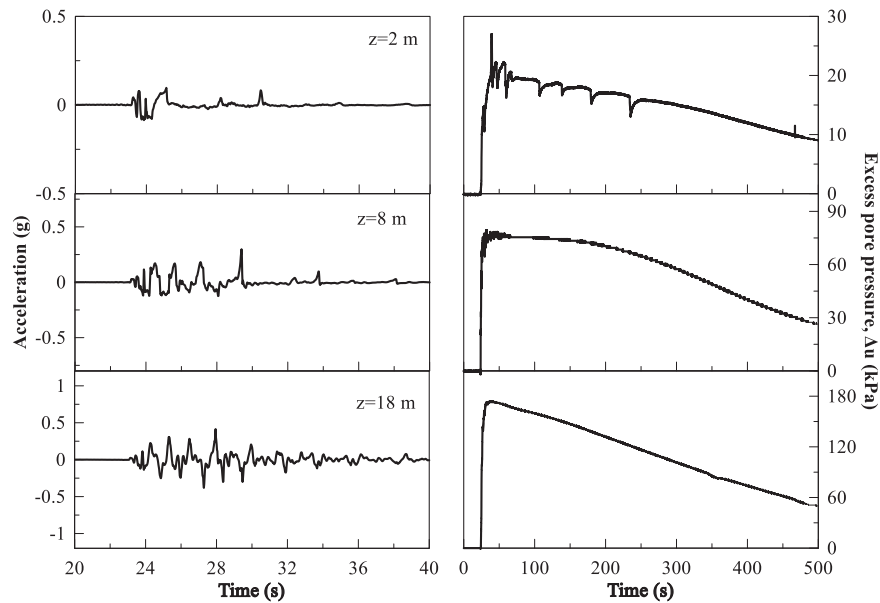


Figure 8.5: The acceleration and excess pore pressure time histories at different depths during the Kobe-L motion in centrifuge test

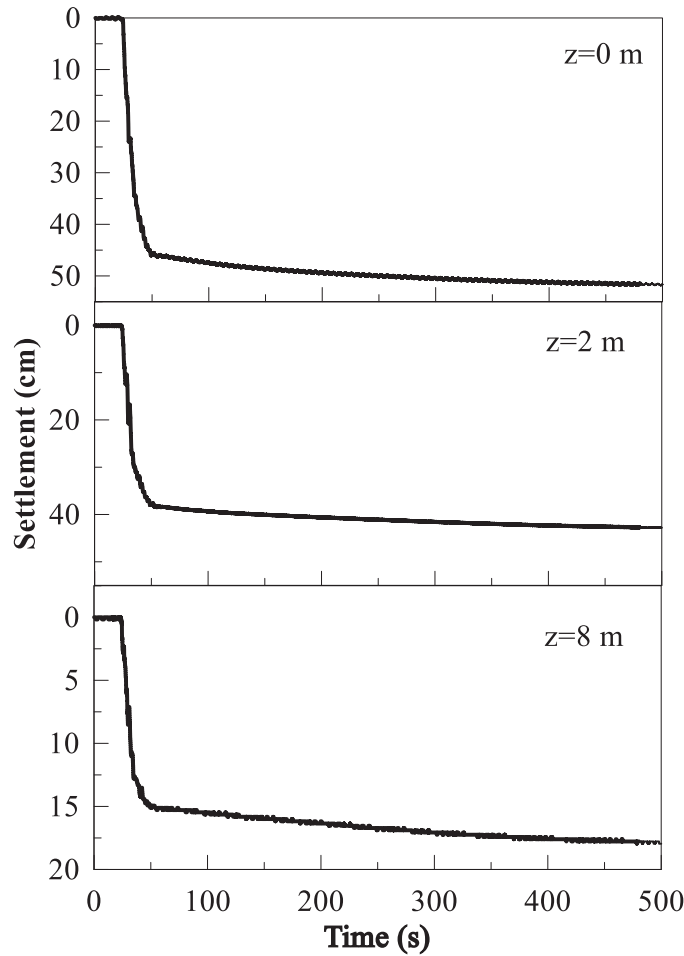


Figure 8.6: The measured settlement histories at different depths during the Kobe-L motion in centrifuge test

The response in free-field at the central instrumentation array during the Kobe-L motion is presented to show the overall dynamic behaviour of the liquefiable deposit. The transverse acceleration and excess pore pressure time histories measured at top, bottom of liquefiable layer, and the bottom of container are shown in Figure 8.5. The time window of the acceleration records is restricted to the period of strong shaking to show the details of seismic response in a porous medium. During the Kobe-L motion, the acceleration time histories displayed a de-amplification of shear waves from the bottom up, particularly at higher frequencies as excess pore pressures increased within the soil column. Initial liquefaction (defined as $r_u = \Delta u / \sigma'_{z_0} = 1.0$ where, Δu = excess pore pressure and σ'_{z_0} = initial vertical effective stress) was observed in all layers during the motion, but at a slightly slower rate in the lower dense layer of Ottawa sand. The dilation of soil under large shear strains and low confining stresses resulted in the large amplitude spikes in acceleration response, which were visible particularly at $z = 2$ m and 8 m. As shown in Figure 8.6, the settlement time histories are presented at different depths within the liquefiable layer. The volumetric deformation was most significant at the ground surface and accumulated during 0-50 sec as excess pore pressures built up shown in Figure 8.5.

8.1.2.2 Comparison of Centrifuge and Numerical Results

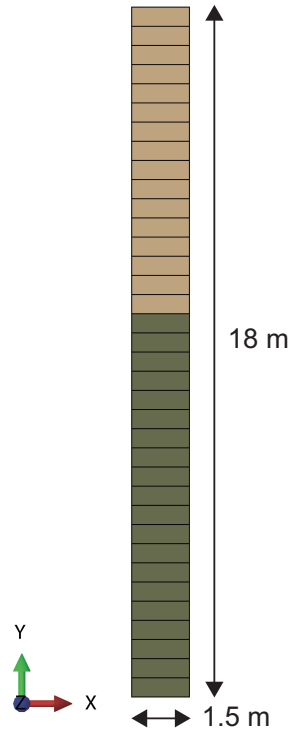


Figure 8.7: Plane strain numerical model to simulate free-field conditions as in the seismic centrifuge test

A plane strain model of 18 m height and 1.5 m width with 25 Lagrangian elements was created in ABAQUS 6.14 (Dassault Systemes, 2014), as shown in Figure 8.7 to simulate the centrifuge test and validate the plane strain framework. The dimensions of the model were to represent free-field conditions as in the centrifuge prototype scale model. The maximum element size at each depth was determined as per Ramirez et al. (2018). The bottom of the model was completely fixed in the vertical direction, and a lateral periodic boundary condition was imposed by constraining the opposite side nodes on the lateral boundaries to undergo the same displacement. This boundary condition is reasonable for strong earthquakes since the energy dissipation in the soil due to hysteretic damping supersedes the energy radiation from the boundaries. It is to be noted that the periodic boundary condition provides exact results in the case of level ground with free surface subjected to base shaking without any structure (Gudehus et al., 2004). The assigned fixities or boundary conditions forced the soil column to follow a shear beam mechanism and roughly reproduce the conditions in a flexible-shear-beam container. The recorded base acceleration in the centrifuge was applied as input to the base of the numerical model hence, assuming a rigid rock condition at base (Figure 8.8). The long rest period was chosen in order to be also able to capture the dissipation of developed excess pore pressures with time and compare the same to as observed in the centrifuge test. The total thickness of the soil model was composed of a 10 m dense Ottawa sand layer (initial $I_D = 90\%$)

at bottom, overlaid by 8 m thick loose Ottawa sand layer ($I_D = 40\%$). The 2 m thick Monterey 0/30 sand layer as used in the centrifuge tests was not modelled due to lack of triaxial data to calibrate the constitutive material parameters. Instead it was modelled as 2 m thick dense Ottawa sand layer. The numerical calculation steps considered a linear bulk viscosity of 0.42 and quadratic bulk viscosity of 1.2 as per the work of Kelm (2004) and Hamann et al. (2015) which successfully modelled 1D wave propagation in saturated sand. A time scaling factor (which determines the number of time steps in ABAQUS) of 0.4 was chosen after multiple iterations in order to ensure convergence.

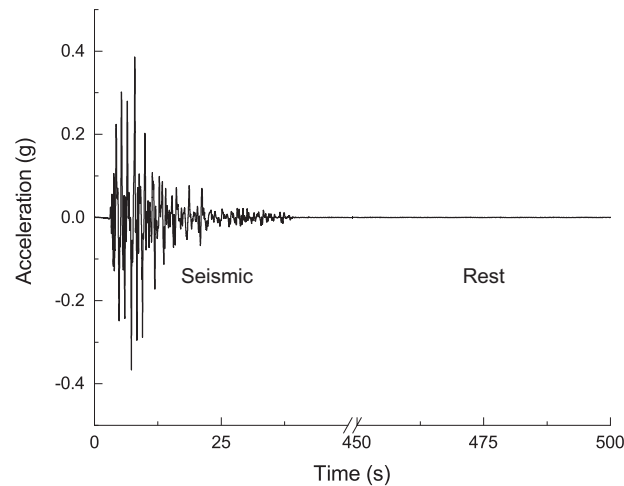


Figure 8.8: Acceleration time history with rest period applied in numerical simulation replicating seismic centrifuge test

Acceleration time history

The acceleration was compared at the bottom of the soil column (base) and top of the

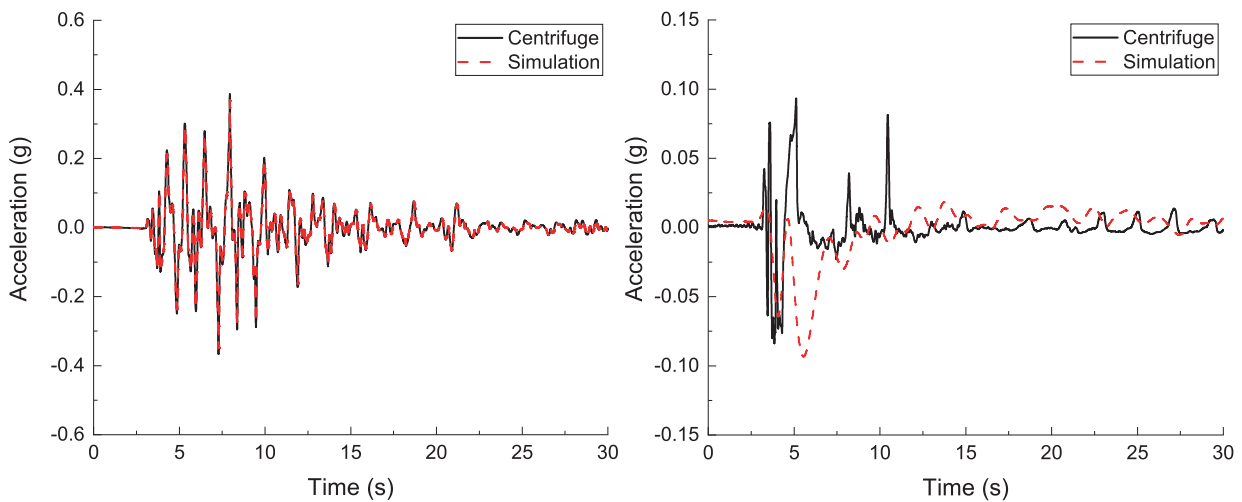


Figure 8.9: Comparison of centrifuge and simulation results for acceleration at base of model (left) and at -2 m from top (right)

liquefiable layer (2 m below top of model) between the numerical model and the centrifuge measurements (Figure 8.9). The numerical acceleration data matched the experimental data at the bottom of the model which verifies that acceleration input given to the numerical model was accurate. At the top of the liquefiable layer (Figure 8.9), accelerations showed similarity for the first few cycles, but with progression of time and building up of pore pressures, the numerical model started to over predict accelerations. This over prediction could be due partly to the underestimation of damping and overestimation of soil's dilative behaviour. The numerical model considers no additional damping other than the inherently occurring material damping in the constitutive model and damping due to a pre-defined linear bulk viscosity (value = 0.42) of the explicit numerical model in ABAQUS. It is also noteworthy that the constitutive material parameters of Ottawa sand have been calibrated according to drained monotonic triaxial tests (Figure 8.1). The calibrated material parameters under an element test conditions seem to overestimate stiffness and accelerations in a fully-coupled boundary value problem.

Excess pore pressures

Figure 8.10 compares the development of excess pore pressures at 2 m below the surface

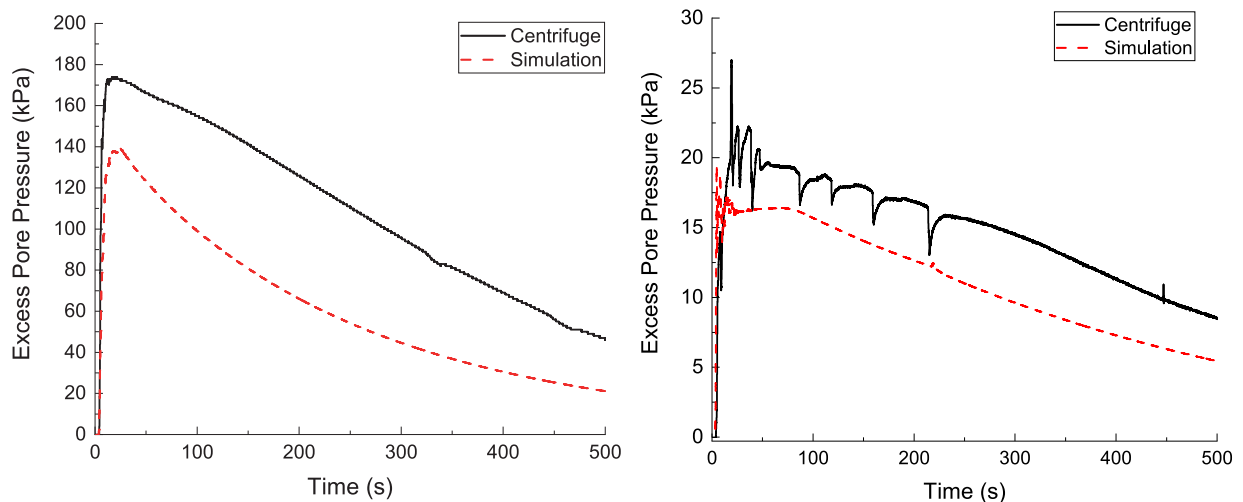


Figure 8.10: Comparison of centrifuge and simulation results for excess pore water pressure at base of model (left) and at -2 m from top (right)

and at the base of model. The numerical and experimental maximum value and dissipation of excess pore pressures over time matched well for the loose Ottawa sand layer (-2 m below). The numerical model slightly underestimated the magnitude and over predicted pore pressure dissipation for the dense Ottawa sand layer. The dense sand layer showed highly dilative behaviour in triaxial tests at lower stress levels (Figure 8.1), against which the material parameters were calibrated. This can lead to an under prediction of excess pore pressures. Whereas the numerical model was able to capture excess pore pressures comparatively well in the looser sand layer. The calibrated material parameters also predicted less dilatancy for looser sand at the element (triaxial) level, likely aiding the centrifuge predictions.

Total Settlements

Figure 8.11 describes the settlement on surface of the soil model over time. The numerical simulations captured the volumetric strain behaviour of Ottawa sand in the free-field. Ramirez et al. (2018) and Wichtmann et al. (2019) discussed that the PDMY02 and SANISAND models underestimated volumetric settlements governed by consolidation and sedimentation mechanisms as well as those due to partial drainage. The better performance of the coupled $u - p$ hypoplastic model can be attributed to its ability to better capture changes in soil properties during shaking such as void ratio. The implementation of the $u - p$ formulation by the user also assures the proper functioning of the multiphase formulation, which may not be the case when one uses built-in features in the available commercial software. Though the numerical predictions of volumetric strain was better compared to other constitutive models, it predicted a much higher settlement compared to centrifuge test result during initial 0-10 sec. This was because the peak excess pore pressure was underestimated but the dissipation rate was overestimated in the dense Ottawa layer (Figure 8.10) that caused a greater acceleration response which is evident in the acceleration history on the surface (Figure 8.9 (right)). This observation can be related to material parameter calibration. The Ottawa sand in dense state was seen to exhibit higher dilative tendencies at triaxial level (Figure 8.1) and this dilatancy behaviour led to under prediction of excess pore pressures and over prediction of dissipation leading to quicker settlements. On the whole, plane strain numerical simulations could capture the seismic behaviour of Ottawa sand in an acceptable range.

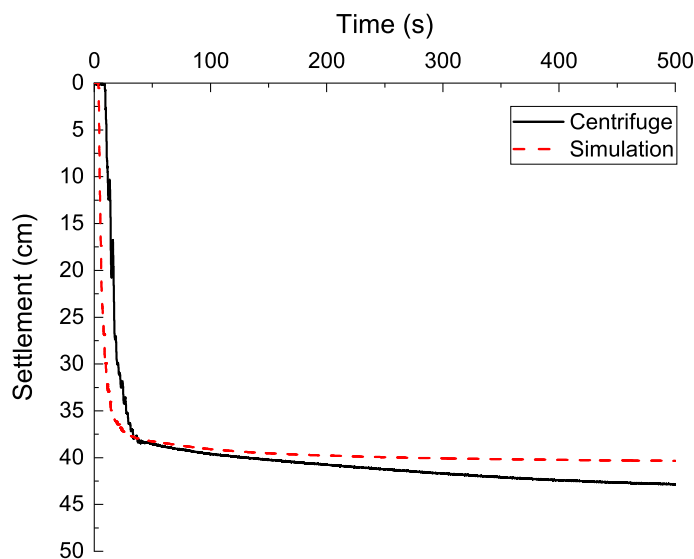


Figure 8.11: Comparison of centrifuge and simulation results for settlement time history of soil surface

8.2 Mitigation Potential of Deep Vibratory Compaction

The liquefaction mitigation potential of the deep vibratory compaction method would be discussed; Kippen, A2 and A3 sands would be subjected to seismic loading before and after compaction. The response of sands to compaction in terms of developed effective stresses would be discussed. As first step sands in their loose saturated state were subjected to seismic loading and observed liquefaction was studied, followed by seismic loading on a compacted saturated soil layer. In Chapter 6 the influence of compaction in a realistic, 3D space due to multiple compaction points was numerically investigated for three compaction points in triangular grid with 3 m spacing (Figure 6.20). Similar simulations were carried out for Kippen, A2 and A3 sand but in this case they were considered saturated unlike simulations described in Chapter 6 where, they were considered dry. After the execution of three compaction points, results from the model were mapped from the 8-noded Eulerian elements to 8-noded brick elements in an Implicit framework and subjected to consolidation step. The developed stress state in the $y-z$ plane was sliced from the centre of the 3D model and mapped using a Matlab code (by the method of extrapolation) to the entire plane strain model (Figure 4.15), mimicking compaction of the entire area as would be expected in the field. The plane strain model with the updated stress state set as initial conditions was then subjected to seismic loading.

8.2.1 Before Deep Vibratory Compaction

Kippen, A2 and A3 saturated sands described previously were subjected to seismic loading. In this case, the acceleration time history of the El Centro Earthquake was applied at the base of the model to mimic seismic loading. Shahir et al. (2012b) recognised variations of permeability with liquefaction. But in these simulations the permeability of sand was kept constant at values described in Table 8.1. The development of effective stress over time was studied, and effective stress approaching zero, was considered as an indicator for onset of liquefaction (Rascol, 2009). Figure 8.12, Figure 8.13 and Figure 8.14 depicts the normalized effective stress (complement to excess pore pressure ratio) with depth at different times for the different kinds of sand.

The reduction in effective stress was due to the build-up of excess pore pressures in saturated sand during seismic loading (Figures 8.15, 8.16 and 8.17). The excess pore water pressure led to the reduction of effective stresses. The sand is said to have undergone liquefaction in this case, as the normalized effective stress approached zero. The Kippen sand underwent loss of effective stress nearly over the entire depth, whereas sand A3 experienced lesser excessive pore water pressure and softening. In Kippen sand liquefaction was triggered between 2-5 s whereas, in A2 sand between 5-10 s and for A3 sand between 15-20 s. Figures 8.18, 8.19 and 8.20 depict the contour of trace of effective stresses for the three sands. The depth of the liquefied layer of sand can be visualised in terms of vanished effective stresses. It can be observed that more than 2/3rd of the Kippen soil layer has liquefied with trace of effective stresses above -5 kPa (compressive). The liquefaction depth was much reduced in sand A2 compared to the Kippen sand. Sand A3 underwent the lowest degree of pore pressure generation and softening compared to others hence, was observed to have lowest liquefaction depth. It can be observed from Table 8.1 and Figure

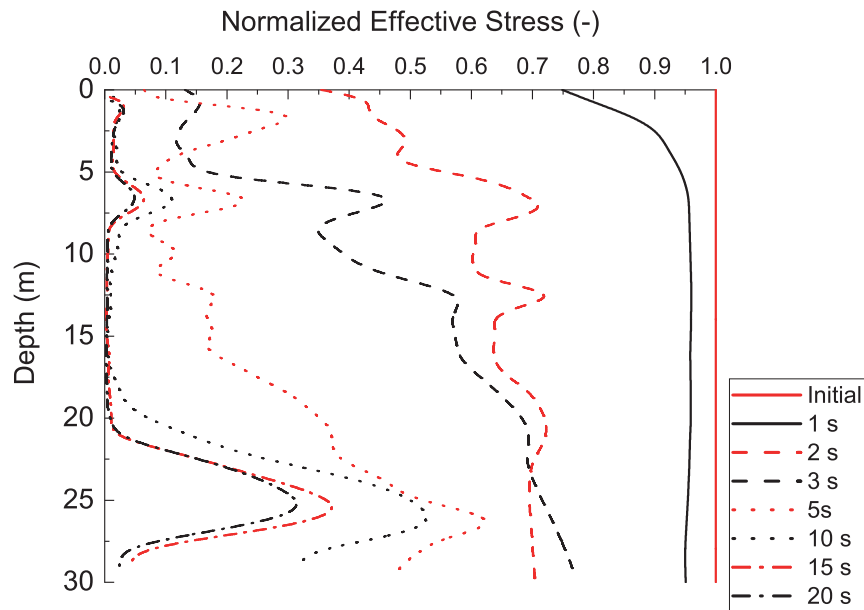


Figure 8.12: Normalized effective stress with depth before compaction for Kippen sand as obtained from simulation at field scale

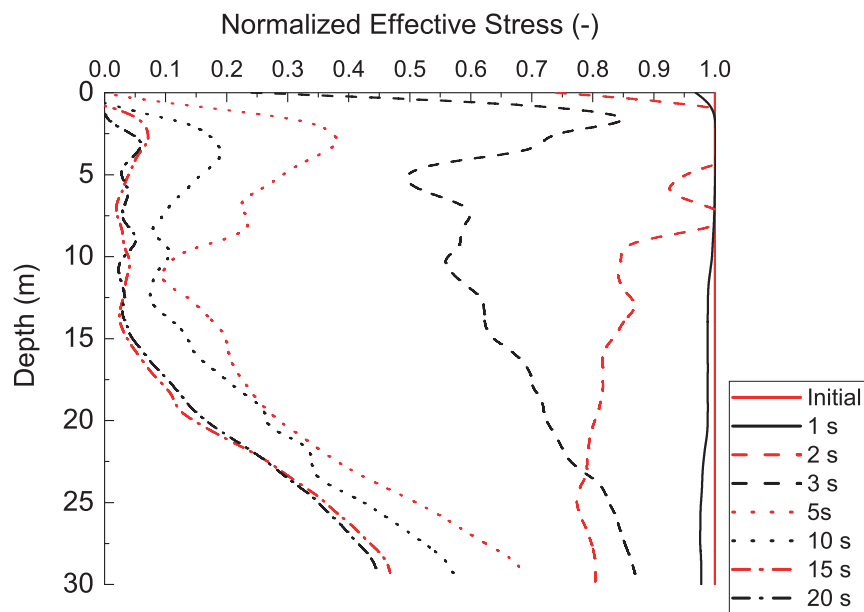


Figure 8.13: Normalized effective stress with depth before compaction for A2 sand as obtained from simulation at field scale

4.17 that A3 sand was better graded compared to other two sands and also contained no fines. Hence, A3 sand under saturated conditions experienced least liquefaction under seismic loading.

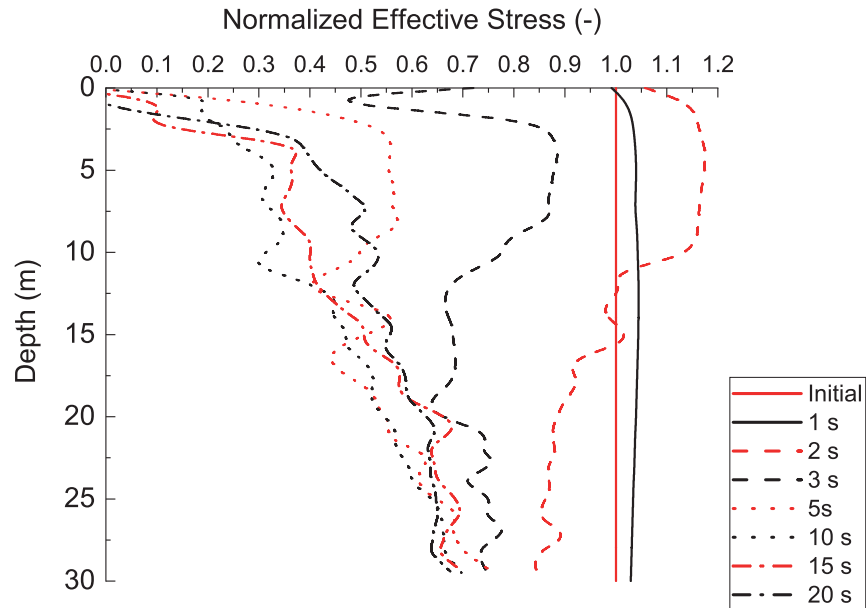


Figure 8.14: Normalized effective stress with depth before compaction for A3 sand as obtained from simulation at field scale

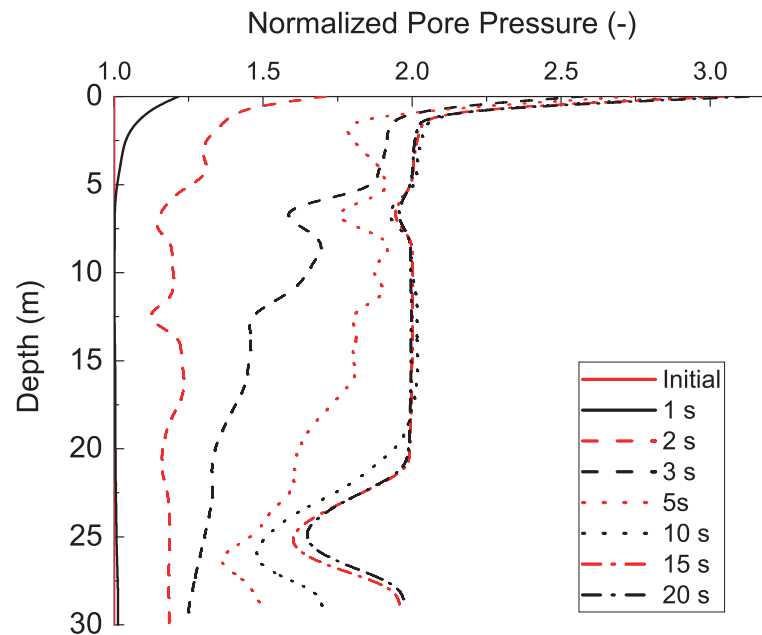


Figure 8.15: Normalized pore water pressure with depth before compaction for Kippen sand as obtained from simulation at field scale

8.2.2 After Deep Vibratory Compaction

The corresponding stress state in saturated sand after deep vibratory compaction was imported to the plane strain model in the form of updated initial conditions as described before. The plane strain model with updated initial conditions was subjected to seismic loading and the observed variation in liquefaction is discussed in this section. Figures

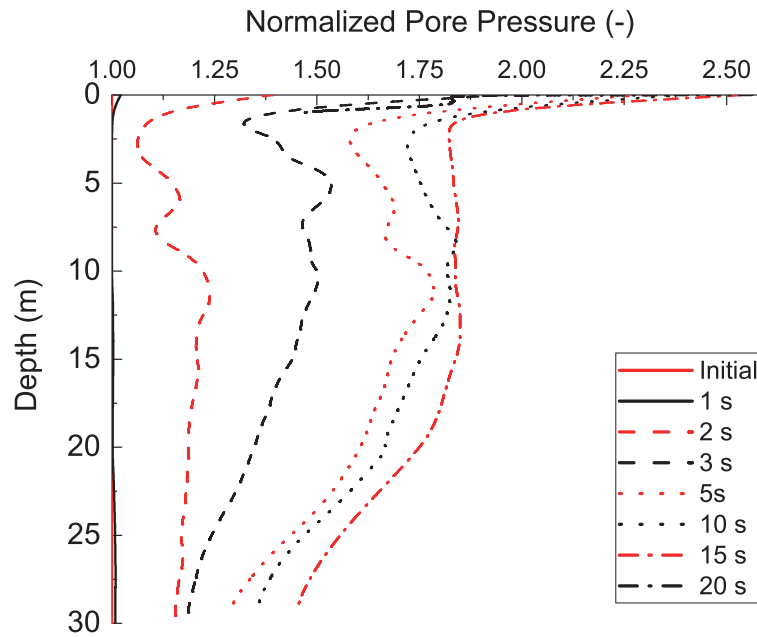


Figure 8.16: Normalized pore water pressure with depth before compaction for A2 sand as obtained from simulation at field scale

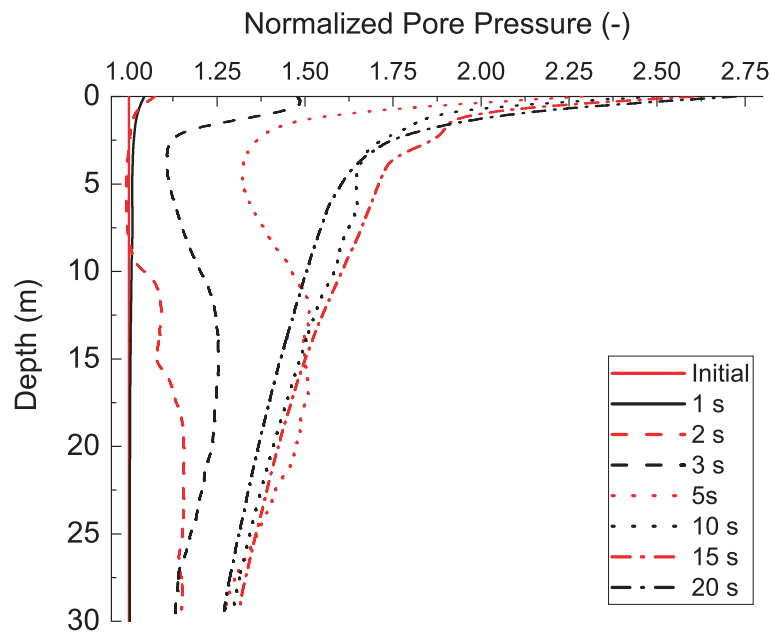


Figure 8.17: Normalized pore water pressure with depth before compaction for A3 sand as obtained from simulation at field scale

8.21, 8.22 and 8.23 describe the normalized effective stress over depth for the 3 sands. It can be observed for Kippen sand that the depth over which effective stress tended to zero, reduced to less than 2 m below the ground surface (Figure 8.21). Additionally, late onset of loss of effective stress beyond 20 s was observed (Figure 8.21). In the case of sands A2 and A3, no liquefaction was observed, which is evident from the non zero tending values

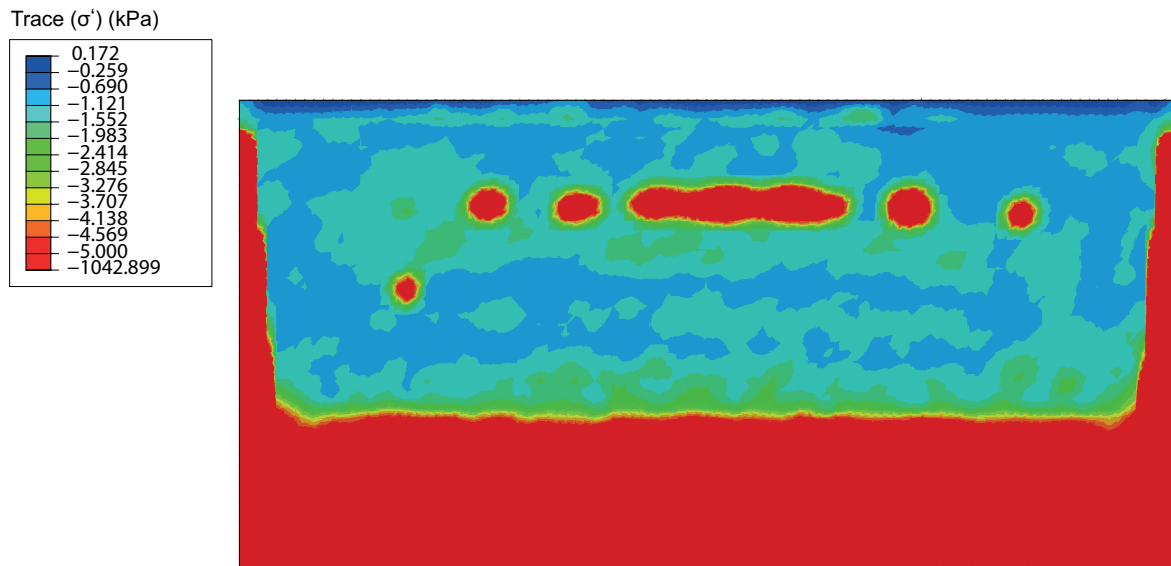


Figure 8.18: Contour of trace of effective stresses for Kippen sand before compaction as obtained from simulation at field scale

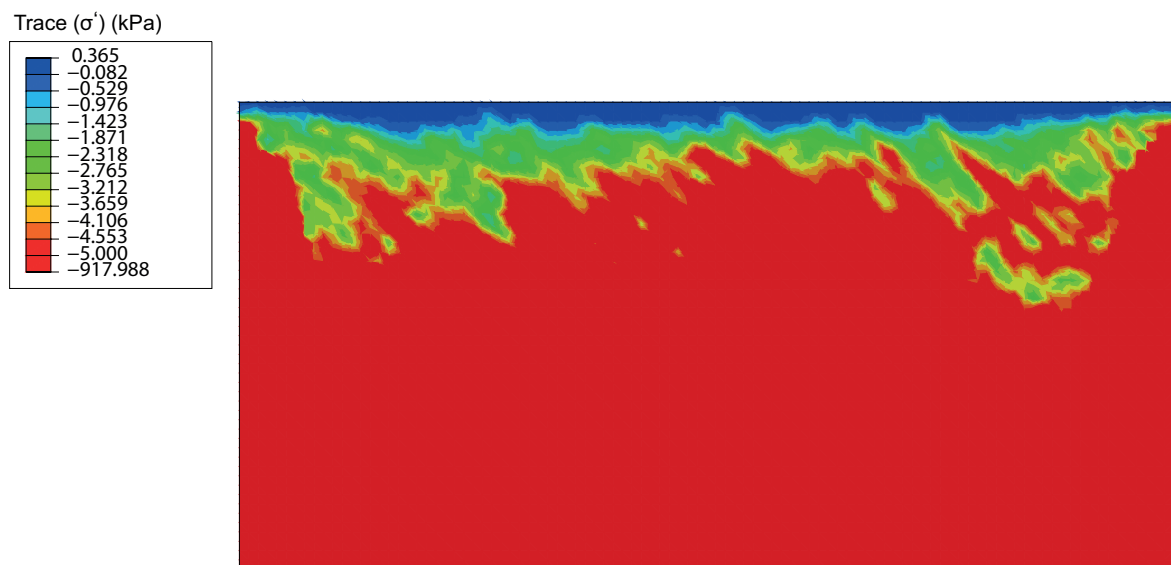


Figure 8.19: Contour of trace of effective stresses for A2 sand before compaction as obtained from simulation at field scale

of normalized effective stress (Figures 8.22 and 8.23).

Figures 8.24, 8.23 and 8.26 depict the normalised pore water pressures and it can be observed that only Kippen sand experienced build up of excess pore water pressures at

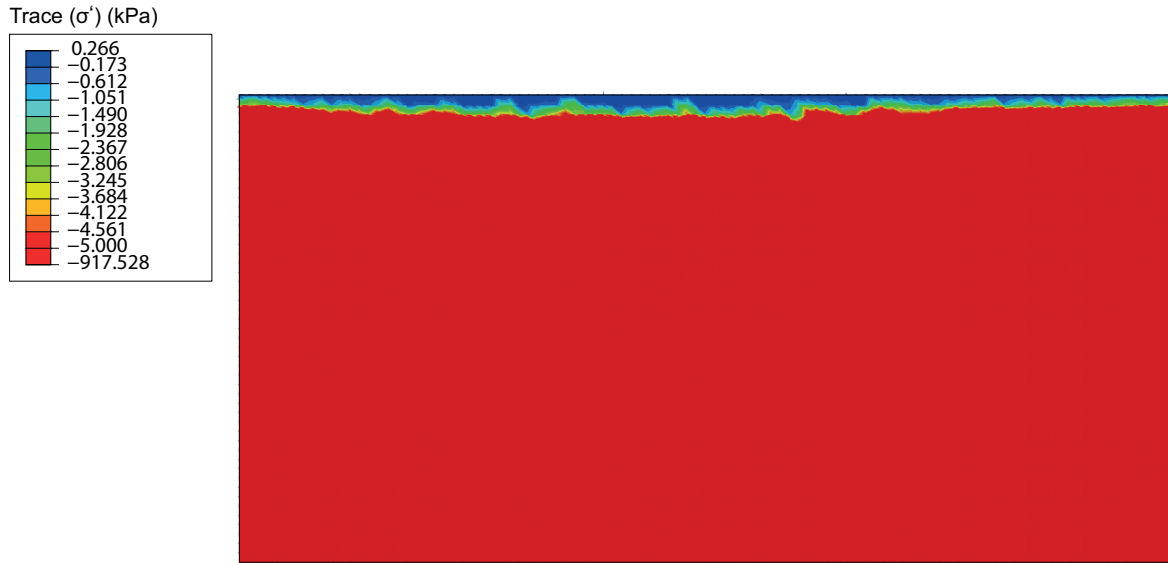


Figure 8.20: Contour of trace of effective stresses for A3 sand before compaction as obtained from simulation at field scale

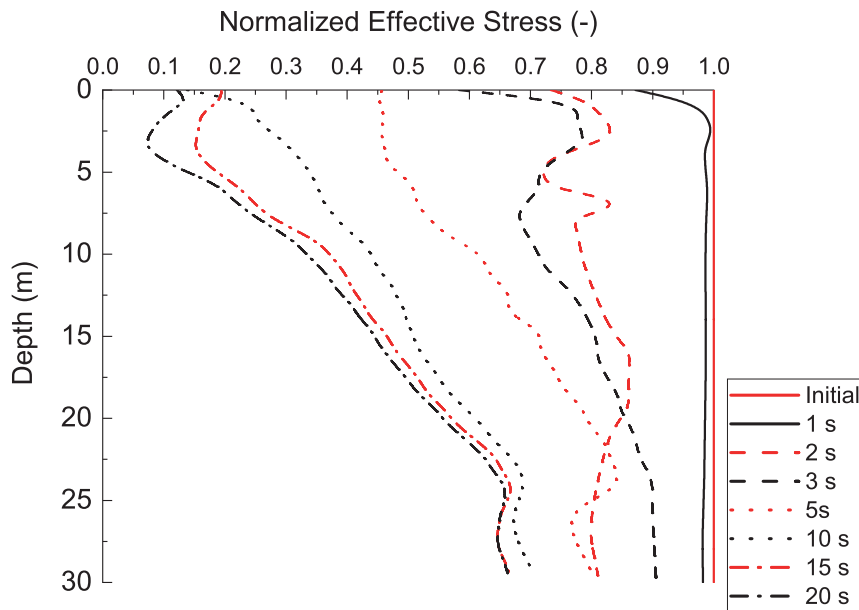


Figure 8.21: Normalized effective stress with depth after compaction for Kippen sand as obtained from simulation at field scale

shallower depths (1-2 m) eventually leading to loss of strength and liquefaction. Figure 8.27 depicts the contour of trace of effective stress and it can be well observed that Kippen sand even after being subjected to compaction, undergoes liquefaction at shallower depths where as A2 and A3 sands experience no loss of effective stresses. The Kippen sand

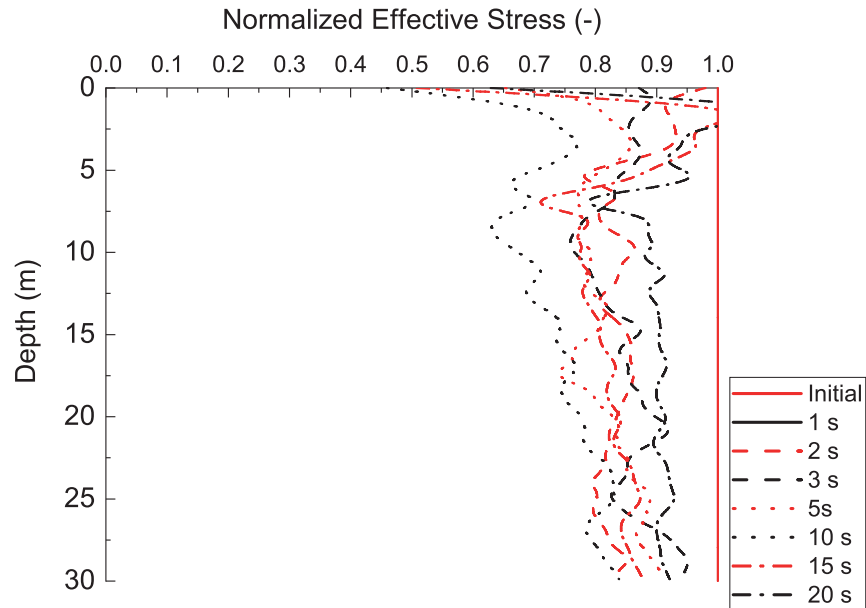


Figure 8.22: Normalized effective stress with depth after compaction for A2 sand as obtained from simulation at field scale

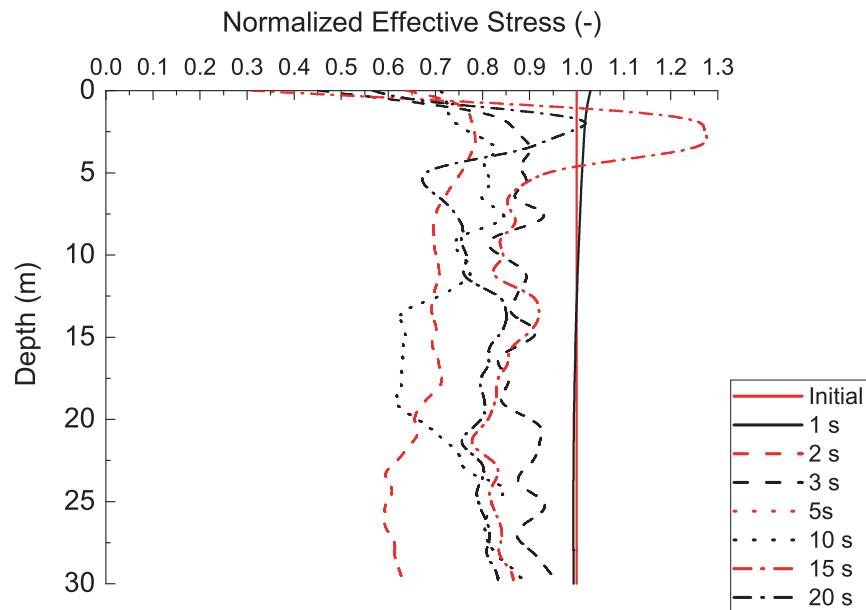


Figure 8.23: Normalized effective stress with depth after compaction for A3 sand as obtained from simulation at field scale

underwent more effective compaction compared to A2 sand (Figure 6.29), but underwent greater excess pore pressure generation (Figure 8.24) even after compaction due to the presence of fine eventually leading to liquefaction. This explains that deep vibratory compaction alone may not be an effective measure to completely eradicate liquefaction in sands with fines. A low permeability could be one of the probable factors influencing the behaviour of sandy soils with fines.

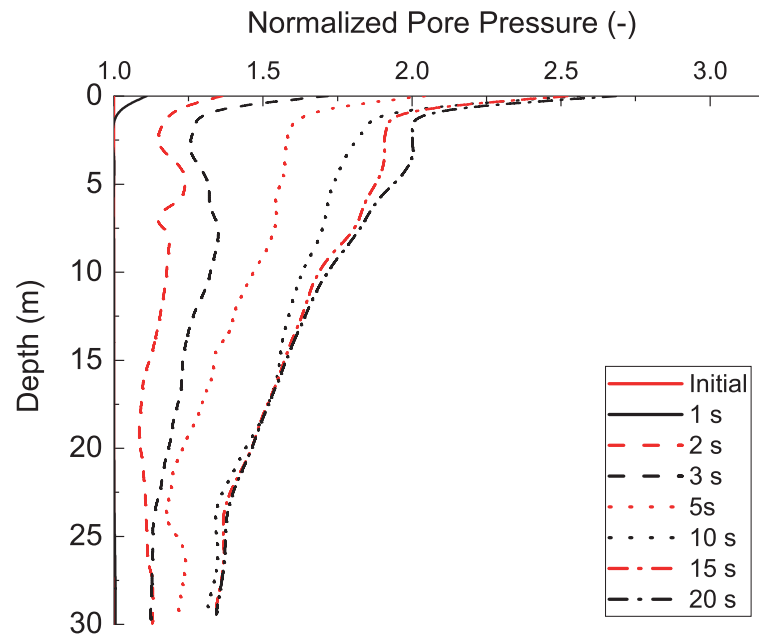


Figure 8.24: Normalized pore water pressure with depth after compaction for Kippen sand as obtained from simulation at field scale

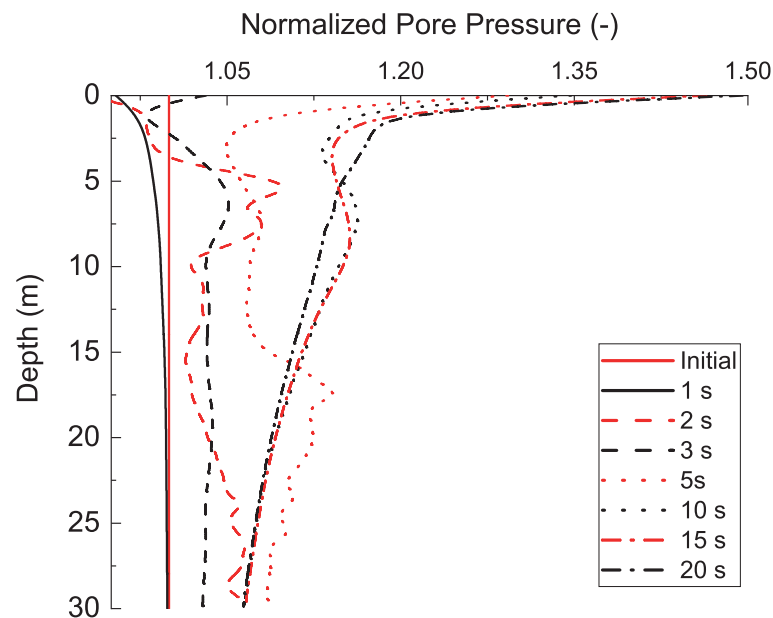


Figure 8.25: Normalized pore water pressure with depth after compaction for A2 sand as obtained from simulation at field scale

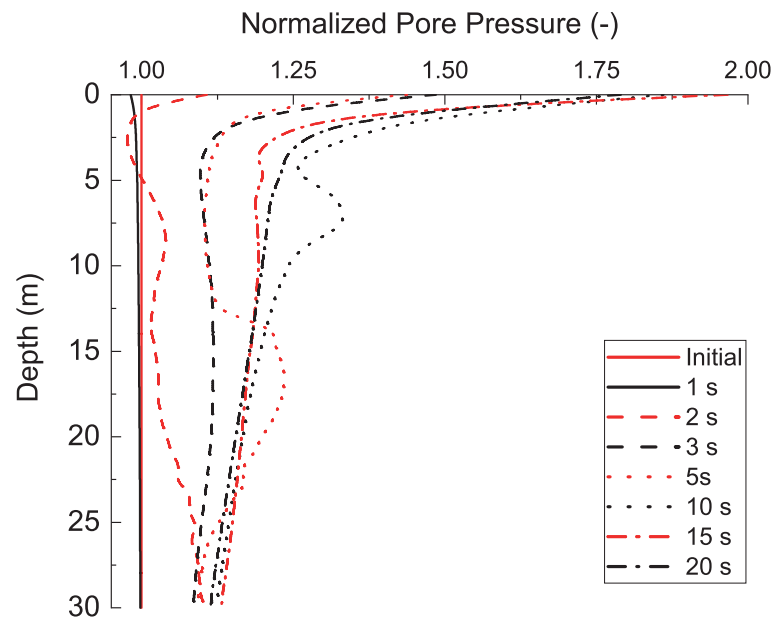


Figure 8.26: Normalized pore water pressure with depth after compaction for A3 sand as obtained from simulation at field scale



Figure 8.27: Contour of trace of effective stresses for Kippen sand after compaction as obtained from simulation at field scale

9 Inference and Perspective

The last chapter of the thesis would make an effort to link the research questions outlined in Chapter 3 to the answers achieved in the chapters following it. The conclusions are categorised as per the flow of thesis and would outline the major take away from each of the chapters and also demonstrate which research question was answered. At end of the chapter, perspective for the future is laid out and key avenues are enlisted which need to be looked at in the future, in order to better consolidate the ideas presented in this work and also inch steps closer to bettering the deep vibratory compaction process for the industry and also precisely outline the limitations of the method to serve as a liquefaction mitigation technique.

9.1 Key Research Answers

It has been highlighted throughout the thesis that lack of analytical design methodology, dependence on field trials and past experience, inhibits the efficient use of deep vibratory compaction. Numerical simulations of the process can help one understand the various physical processes, the soil undergoes during the compaction process and help optimize it. Numerical models till date, have not been able to realistically model soil-vibrator interaction using an elastic-plastic constitutive model and suffer from excessive deformations beyond certain vibration cycles in most cases. The coupled Eulerian-Lagrangian based numerical model with hypoplastic with intergranular strain routine was chosen to simulate deep vibratory compaction. The choice and determination of material parameters for the constitutive model was of utmost importance in order to be rightly capture deep vibratory compaction process via simulations. The suitability of constitutive model to capture compaction phenomenon was discussed. The hypoplastic parameters were found to be closely associated with the granulometric properties of sands. The hypoplastic parameters along with the intergranular strain parameters were not only material dependent but also varied as per the stress state and initial density. The intergranular strain parameters are often assumed similar to the standard values as quoted by Niemunis and Herle (1997) due to lack of knowledge and difficulty level associated with the determination of these parameters. In this work, an innovative method involving the stress path controlled tri-axial test was described and utilised to determine intergranular strain parameters. On the whole hypoplastic material parameters were found to be stress state and density dependent hence, were calibrated according to the expected test or in field conditions to better capture material behaviour.

The prediction accuracy of numerical models developed till date to capture deep vibratory compaction have not been validated. Hence, in this work CEL framework was validated against 1g model test results and field deep vibratory compaction measurements. A mini

model vibrator was fabricated to conduct 1g deep vibratory compaction model tests in sand. CPT was performed before and after compaction to determine the degree of compaction. The tip resistance values from the 1g model tests and numerical simulation results were found to be in good agreement, hence validating the numerical model. Deep vibratory compaction was used to compact an open-cast mine deposit using a V48 vibrator. Field measurements including CPT and accelerometer data from the vibrator were used to validate the developed numerical framework. Shortcomings such as not modelling the penetration of vibrator probe into the soil and requirement for furthering our simulation methodology was discussed in order to improve the predictive capability of the numerical model. Simulation results provided temporal and spatial data to better understand deep vibratory compaction process, that could not be captured during field or 1g test measurements. Numerical simulations not only helped circumvent performing laborious and time-consuming physical 1g tests or field trials but also provided more detailed insight. The verified numerical framework coupled with 1g model tests was used to study and analyse the effects of various parameters affecting deep vibratory compaction; namely the frequency, relative density, type of granular material, shape of vibrator, compaction process, grid spacing and soil saturation.

Frequency: The individual 1g model tests at various frequencies in Hamburger sand indicated the existence of an optimal frequency at around 35-40 Hz with marginal compromise in compaction at larger radial distance. On similar lines, numerical simulations found that compaction efficiency increased with frequencies from 15 to 20/25 Hz but reduced at 30 Hz for Kippen sand. Hence, simulations can help optimise frequency, balancing compaction efficacy with cost of operation as suggested by (Wersäll et al., 2013). Execution of compaction at optimised frequency can lead to efficient power utilisation and lesser wear of the vibrator motor. Numerical simulations at 1g model tests scale and field deep vibratory compaction scale were also effective in identifying an optimised compaction time. It was found that both Hamburger sand at 1g model scale and Kippen sand at field scale attained maximum compaction at a certain depth between 20-25 s. A combination of 1g model tests and numerical simulations can be carried out to identify optimised compaction frequency and time for any granular material under consideration.

Relative Density and Stress State: The effect of initial density and depth of compaction on deep vibratory compaction efficiency for Kippen sand was studied at field scale via simulations. Radial extent of compaction was found to increase with increasing initial relative density. Sand with medium dense packing was found to experience increase radial extent of compaction compared to loosely packed sand. It was found that compaction efficiency reduced at 10 and 30 m depth and was maximised between 15 to 25 m depth for Kippen sand. Numerical simulations can help identify depths until which deep vibratory compaction can be used to compact soil with marginal loss in compaction efficiency.

Type of Granular Material: Numerical simulations were carried out at both 1g model scale and field scale and results from both concluded that gradation and fines content of the sand played a vital role in determining compaction efficiency. Results confirmed that well-graded sands were well-suited for deep vibratory compaction, and as the fines content increased, the efficiency of the method decreased. Compaction efficiency was found to increase with increasing C_u values for clean sands without fines. Well graded sands were also found to experience more uniform compaction compared to sands with fines. It can

be suggested that efficiency of deep vibratory compaction technique for sands with fine above 15 % is drastically reduced.

Shape of Vibrator and Friction: Massarsch and Fellenius (2005) suggested that optimised vibrator shape can lead to efficient compaction. Numerical simulations indicated improvement in compaction due to the presence of wings on the shaft of the vibrator. It was also found that tangential friction could be neglected with minimum compromise in results enabling lesser computational effort. On the whole, numerical simulations can serve as an effective tool to develop and test the efficiency of new vibroflot designs before they are physically designed.

Compaction process: Three kinds of compaction processes were simulated at field scale and out of the three Pilgrim step method was found to most efficient in creating a uniform and well densified column of Kippen soil in least amount of compaction time. Instead of using a standard compaction process for all granular soils, aid of numerical simulations can be sought in order to identify the most efficient scheme of compaction for soil under consideration.

Spacing and Compaction Grid: Kirsch and Kirsch (2017) explained that the choice of spacing between compaction points, which determines the overall quality of the compacted grid, is based on experience or field trials due to lack analytical design. Numerical analysis at field scale for Kippen sand demonstrated that lesser spacing may not lead to better compaction and can cause ineffective overlapping of compaction zones. On the other hand 3 m spacing lead to positive interference and maximised compaction. Simulation results indicated presence of an optimised spacing for each kind of sand which can be identified by means of numerical simulations. Compaction in a grid was executed by both sequential and parallel modes for three compaction points in a triangular grid and it was found that parallel compaction of three compaction points led to an enhanced and larger compaction zone. Parallel compaction technique would also reduce time required to compact target area hence, aiding financial cost of any project.

Soil Saturation: Saturated sand showed lesser reduction in void ratio immediately following deep vibratory compaction due to the development of excessive pore water pressure, explaining the time effect observed by Bo et al. (2014). Whereas, deep vibratory compaction in dry sands led to the reduction in void ratio immediately after compaction. Saturated sands with greater permeability underwent reduction in void ratio right after compaction unlike sands with higher fines content. Gradation and fines content of the sand played a vital role in determining compaction efficiency in saturated sands. Saturation of sand with high permeability and some fines increases the radial extent of compaction. Sensitivity of permeability reduces as gradation of sand improves. Saturation and initial relative density of sand affects the transmissibility of vibrations, in turn affecting the radius of compaction. This suggests that the radius of influence suggested by Fellin (2000) and Witt (2017a) may not apply to all scenarios. Saturated sands with fines after compaction exhibited time effect and gradually reached a denser state once the excess pore pressures dissipated. Well graded sands developed negligible excess pore water pressure due to greater permeability. Hence, they underwent major reductions in void ratio immediately after compaction, exhibiting no time effects. The results concluded that saturated sand after consolidation reached a densified state comparable to dry sands. In some scenarios presence of water for some sands increased the radial extent of compaction.

The real-time increase in density of soil with progress of compaction cannot be realised and hence identification of an effective online control parameter for the optimisation of compaction process was necessary. In order to determine parameter which can serve as on-line compaction control parameter, 1g tests with model vibrator and CEL simulations were performed. Amplitude and phase angle were observed to reduce with progressing compaction. Due to ease of data acquisition and required sensors, amplitude was suggested to serve as an on-line compaction control criterion. Compaction efficiency in model tests using amplitude as control parameter was compared to ones without it. Once the feasibility of using amplitude as control parameter was established at 1g model test level, the same was verified at realistic stress state conditions by means of numerical simulations.

Research to date has noted that the choice of the constitutive model and calibration of parameters play a critical role in capturing the soil response under seismic loading (Jeremić et al., 2008). The efficiency of chosen constitutive model to capture changes in soil porosity during seismic shaking holds the key. Hypoplastic model with intergranular strains used in this work, incorporates void ratio as a state variable. Hence, a coupled hypoplastic model based on the u-p formulation was used in the ABAQUS 6.14 explicit to predict soil response of layered saturated sand under seismic excitation. Centrifuge tests were performed at the University of Colorado Boulder on layered saturated sand deposits subjected to 1D seismic loading. The results of centrifuge tests in terms of accelerations, pore pressures, and importantly, settlements were used to assess the performance of hypoplastic model for predicting the liquefaction phenomenon. The coupled formulation was successfully able to capture the seismic behaviour of saturated loose and dense Ottawa sand based on single set of calibrated parameters from monotonic triaxial tests. The chosen hypoplastic model was able to capture the volumetric changes during seismic shaking, unlike many other constitutive models used to date.

In order to analyse the efficiency of deep vibratory compaction for liquefaction mitigation, seismic numerical simulation of saturated sand before and after compaction was performed. The Kippen sand, with more fines and smaller permeability, underwent substantial softening and liquefaction under seismic loading before compaction. The resulting state after compaction ensured improved resistance against liquefaction in terms of reduced liquefaction depth and delayed onset of liquefaction for sands with higher fines content. Well graded sands with lesser fines such as A2 and A3 sands responded well to deep vibratory compaction and experienced a complete eradication of liquefaction. It was concluded that deep vibratory compaction can be used as an effective complete liquefaction mitigation measure in clean and well graded sands with no fines and can lead to reduced liquefaction depth in sands with higher fines content. Hence, deep vibratory compaction may not be an effective liquefaction mitigation measure for all kinds of granular soils.

In a nut shell, numerical simulation coupled with 1g model test can help identify the suitability of deep vibratory compaction for compacting a granular material under consideration. Once, the suitability is established, factors affecting compaction can be designed such as time, grid spacing, frequency and nature of compaction. As per requirement liquefaction mitigation capability of deep vibratory compaction for the sand under consideration can also be commented upon. This can be seen as a major step in better understanding and designing a compaction method which lacks a design analogy and majorly works on field experience. Deeper understanding of the method would not only lead to efficient util-

isation but would also lead to identifying its usability in liquefaction mitigation scenarios.

9.2 Future Scope

The work enlisted various factors that affect deep vibratory compaction and also suggests variations which can help improvise compaction in Kippen soil. Field trials need to be carried out in field for Kippen soil to verify if suggested changes such as compaction frequency of 25 Hz, compaction time of 25 s at each depth and grid spacing of 3 m would lead to most efficient scheme of compaction. On similar lines the numerical framework needs to be used to design a new deep vibratory compaction site and field trials needs to be carried as per the compaction scheme designed numerically. The outcome of the design should be evaluated both financial and efficiency wise.

It has already been emphasised that currently used on-line compaction control parameters such as power, current consumed and quantity of additional granular material are imprecise and fallible (Fellin, 2000). Amplitude has been suggested as an effective on-line compaction control parameter in this work. One needs to further substantiate the idea by carrying out deep vibratory compaction field trials with modified vibrator probe, that can log real-time vibrator amplitude. The operator needs to be trained to control and stop compaction at a particular depth when sudden drop in amplitude magnitude is observed. In-field compaction data with and without amplitude control needs to be compared to verify the suggested concept.

Deep vibratory compaction as a liquefaction mitigation measure has been a debatable concept across the globe. In order to project numerical simulations as one of the platforms to analyse suitability of deep vibratory compaction for mitigate liquefaction in any granular material, needs to be backed by further seismic centrifuge tests. Seismic centrifuge tests need to be carried out for various sands before and after subjected them to deep vibratory compaction and their effectiveness to reduce liquefaction potential needs to be observed. Parallely numerical simulations should be carried out to verify if they too lead to similar observations as the centrifuge tests.

Once the effectiveness of numerical simulations to design deep vibratory compaction is established, improvements in the numerical framework and constitutive model can be made, in order to further capture nuances of the compaction method. Material Point Method (MPM) and Smooth Particle Hydrodynamics (SPH) both capable of simulating boundary value problems involving large scale deformations are promising contenders to simulate deep vibratory compaction. The particle in cell concept of both the frameworks can probably lead to better mimicking of the vibrator-soil interaction. Wichtmann et al. (2019) concluded that the intergranular strain anisotropy (ISA) model (Fuentes and Triantafyllidis, 2015) was best suited to capture the behaviour of sands under cyclic loading. Once the stability of the ISA model in a finite element (FE) framework is established, the framework developed in this work can be expanded to compare simulation results across various constitutive models.

References

- Adam, D. (1996). “Flächendeckende dynamische Verdichtungskontrolle (FDVK) mit Vibrationswalzen”. PhD. Thesis. Vienna, Austria: TU Wien, Fakultät für Bauingenieurwesen.
- Affi, S. S. and Woods, R. D. (1971). “Long-Term Pressure Effects on Shear Modulus of Soils”. In: *Journal of Soil Mechanics & Foundations Div*, pp. 1445–1460.
- Arnold, M. and Herle, I. (2009). “Comparison of Vibrocompaction Methods by Numerical Simulations”. In: *International Journal for Numerical and Analytical Methods in Geomechanics* 33.16, pp. 1823–1838. DOI: 10.1002/nag.798.
- Arulanandan, K. and Scott, R. F. (1993). “Verification of Numerical Procedures for the Analysis of Soil Liquefaction Problems”. In: *International Conference on the Verification of Numerical Procedures for the Analysis of Soil Liquefaction Problems (1993: Davis, Calif.)* AA Balkema.
- Balachowski, L. and Kurek, N. (2016). “Vibroflotation Control of Sandy Soils Using DMT and CPTU”. In: *The 3rd International Conference on the Flat Dilatometer*. Rome, pp. 185–190.
- Bauer, E. (1996). “Calibration of a Comprehensive Hypoplastic Model for Granular Materials”. In: *Soils and Foundations* 36.1, pp. 13–26. DOI: 10.3208/sandf.36.13.
- Baumann, V. and Bauer, G. E. A. (1974). “The Performance of Foundations on Various Soils Stabilized by the Vibro-Compaction Method”. In: *Canadian Geotechnical Journal* 11.4, pp. 509–530.
- Berg, J. and Köcher, J. (2003). “Verfahren zur Steuerung eines Tiefenrüttlers”. DE 199 30 885 C 2.
- Berg, J. and Köcher, J. (2009). “Verfahren und Vorrichtung zur Tiefenverdichtung mit gestreuter Frequenz- und Umwuchtänderung eines Tiefenrüttlers”. DE 199 30 884 B4.
- Bernatzik, W. (1947). “Baugrund Und Physik”. In.
- Bilfinger and Berger Bauktiengesellschaft (1982). “Schlagwerk für einen Tiefenrüttler zum Verdichten von Erdreich”. G 81 34 822.3U1.
- Biryaltseva, T., Kreiter, S., and Dyvik, R. (2016). “The Influence of Grain Size Distribution and Grain Shape on the Small Strain Shear Modulus of North Sea Sand”. In: *Proceedings of the 17th Nordic Geotechnical Meeting Challenges in Nordic Geotechnic*. Reykjavik.
- Bo, M. W., Chu, J., and Choa, V. (2005). “The Changi East Reclamation Project in Singapore”. In: *Elsevier Geo-Engineering Book Series*. Vol. 3. Elsevier, pp. 247–276.
- Bo, M. W. et al. (2014). “Densification of Land Reclamation Sands by Deep Vibratory Compaction Techniques”. In: *Journal of Materials in Civil Engineering* 26.8, p. 06014016.
- Bo, M. W. et al. (2015). “Deep Compaction of Granular Fills in a Land Reclamation Project by Dynamic and Vibratory Compaction Techniques”. In: *Ground Improvement Case Histories: Compaction, Grouting and Geosynthetics*, pp. 263–274.

- Brown, K. H., Burns, S. P., and Christon, M. A. (2002). "Coupled Eulerian-Lagrangian Methods for Earth Penetrating Weapon Applications". In: *Computational Physics R&D Department Sandia National Laboratories*.
- Brown, R. E. (1977). "Vibroflotation Compaction of Cohesionless Soils". In: *Journal of Geotechnical and Geoenvironmental Engineering* 103.ASCE 13415 Proceeding.
- Chen, J. et al. (2015). "DEM Simulation of Laboratory Compaction of Asphalt Mixtures Using an Open Source Code". In: *Journal of Materials in Civil Engineering* 27.3, p. 04014130. DOI: 10.1061/(ASCE)MT.1943-5533.0001069.
- Cheng, K. et al. (2019). "The effect of plastic fines on the shear modulus and damping ratio of silty sands". In: *Bulletin of Engineering Geology and the Environment* 78, pp. 5865–5876. DOI: <https://doi.org/10.1007/s10064-019-01522-1>.
- Chmelnizkij, A., Nagula, S., and Grabe, J. (2017). "Numerical Simulation of Deep Vibration Compaction in Abaqus/CEL and MPM". In: *Procedia engineering* 175, pp. 302–309. DOI: 10.1016/j.proeng.2017.01.031.
- Cornforth, D. H. (1973). "Prediction of Drained Strength of Sands from Relative Density Measurements: Evaluation of Relative Density and Its Role in Geotechnical Projects Involving Cohesionless Soils". In: *Evaluation of Relative Density and Its Role in Geotechnical Projects Involving Cohesionless Soils*. Ed. by E. T. Selig and R. S. Ladd. 100 Barr Harbor Drive, PO Box C700, West Conshohocken, PA 19428-2959: ASTM International, pp. 281-281–23. DOI: 10.1520/STP37878S.
- Cudmani, R., Meier, T., and Osinov, V. (2006). "Development of a Numerical Model for the Prediction of Densification of Cohesionless Soils during Deep Vibratory Compaction". In: *TRANSVIB 2006, International Symposium on Vibratory Pile Driving and Deep Soil Vibratory Compaction. Editions Du LCPC, Paris*, pp. 131–140.
- Cudmani, R. O. (2001). *Statische, Alternierende Und Dynamische Penetration in Nichtbindigen Boden*. Institutes für Bodenmechanik und Felsmechanik der Universität Friedericiana \textbackslash ldots.
- d'Appolonia, E., ed. (1954). *Loose Sands\textemdash Their Compaction by Vibroflotation*. ASTM International.
- Dassault Systemes (2014). *ABAQUS, Version 6.14 Documentation*. Documentation.
- DIN 18123 (1996). "Baugrund, Untersuchung von Bodenproben: Bestimmung Der Korngrö\ss enverteilung". In: nov.
- DIN 18126 (1996). "Baugrund, Untersuchung von Bodenproben: Bestimmung Der Dichte Nichtbindiger Böden Bei Lockerster Und Dichtester Lagerung : DIN 18126". In: nov.
- DIN EN ISO 17892-4 (2017). "Geotechnische Erkundung Und Untersuchung- Laborversuche an Bodenproben - Teil : Bestimmung Der Korngrö\ss ernverteilung". In: apr.
- DIN EN ISO 22476-1 (2013). "Drucksondierungen Mit Elektrischen Messwertaufnehmern Und Messeinrichtungen Für Den Porenwasserdruck". In: oct.
- Elnashai, A. S. and Di Sarno, L. (2008). *Fundamentals of Earthquake Engineering*. Wiley Online Library.
- Fellin, W. (2000). "Rütteldurckverdichtung Als Plastodynamisches Problem [Deep Vibration Compaction as a Plastic Dynamic Problem]". In: In Advances in Geotechnical Engineering and Tunneling, Insitute of Geotechnics and Tunneling.
- Fellin, W., Hochenwarter, G., and Geiß, A. (2000). "On-Line Verdichtungskontrolle Bei Der Rütteldruckverdichtung". In: *Bauingenieur* 75.9.

- Fellin, W., Hochenwarter, G., and Geiss, A. (2003). "GroEntwicklung Eines Qualitätssicherungssystems Für Die Rütteldruckverdichtung". In: *Bauingenieur* 78.9, pp. 433–439.
- Fuentes, W. and Triantafyllidis, T. (2015). "ISA model: A constitutive model for soils with yield surface in the intergranular strain space". In: *International Journal for Numerical and Analytical Methods in Geomechanics* 39.11, pp. 1235–1254. DOI: <https://doi.org/10.1002/nag.2370>. URL: <https://onlinelibrary.wiley.com/doi/abs/10.1002/nag.2370>.
- Geß, S. (2009). "Bauen Auf Tagebaukippen Eine Herausforderung an Die Geotechnische Sicherheit". In: Zittau.
- GMB GmbH, H. (2017b). "Rütteldruckverdichtung in Lausitzer Kippen". In.
- Grabe, J., Heins, E., and Hamann, T. (2015). "Simulation of Ground Improvement Using Deep Vibration Compaction". In: *Proc. 6th Int. Geotech. Symposium on Disaster Mitigation in Special Geoenvironmental Conditions*. Chennai, India.
- Grabe, J. and Milatz, M. (2014). "The Change of Matric Suction Due to Heavy Vehicle Crossing". In: *Proc. of 6th International Conference on Unsaturated Soils (UNSAT 2014)*. Vol. 2. Sydney, Australia, pp. 1431–1437.
- Grabe, J. (1992). "Experimentelle und theoretische Untersuchungen zur flächendeckenden dynamischen Verdichtungskontrolle". PhD. Thesis. Karlsruhe, Germany: Institut für Geotechnik und Baubetrieb, University of Karlsruhe.
- Grabe, J. and König, F. (2004). "Zur Aushubbedingten Reduktion Des Drucksondierwiderstandes [Excavation Induced Reduction in Cone Penetration Resistance]". In: *Bautechnik* 81.7, pp. 569–577. DOI: 10.1002/bate.200490130.
- Gudehus, G. (1996). "A Comprehensive Constitutive Equation for Granular Materials". In: *Soil and Foundations* 36.1, pp. 1–12. DOI: 10.3208/sandf.36.1.
- Gudehus, G. et al. (2004). "In-Plane and Anti-Plane Strong Shaking of Soil Systems and Structures". In: *Soil Dynamics and Earthquake Engineering* 24.4, pp. 319–342. DOI: 10.1016/j.soildyn.2003.12.007.
- Hamann, T. and Grabe, J. (2011). "A Simple Dynamic Approach for the Numerical Modelling of Soil as a Two-Phase Material". In: *geotechnik* 36.3, pp. 180–191.
- Hamann, T., Qiu, G., and Grabe, J. (2015). "Application of a Coupled EulerianLagrangian Approach on Pile Installation Problems under Partially Drained Conditions". In: *Computers and Geotechnics* 63, pp. 279–290. DOI: 10.1016/j.compgeo.2014.10.006.
- Heins, E., Grabe, J., and Hamann, T. (2015). "Numerische Simulation Einer Bodenverbesserungsmarütteldruckverdichtung". In: *Numerische Methoden in der Geotechnik* 98, pp. 59–68.
- Henke, S., Hamann, T., and Grabe, J. (2012). "Numerische Untersuchungen Zur Bodenverdichtung Mittels Rütteldruckverfahren". In: *Proceedings des 2. Symposiums Baugrundverbesserung in der Geotechnik 2012*, pp. 209–228.
- Herle, I. (1998). "A Relation between Parameters of a Hypoplastic Constitutive Model and Grain Properties". In: *Localisation and Bifurcation Theory for Soils and Rocks*, pp. 91–99.
- Herle, I. and Gudehus, G. (1999). "Determination of Parameters of a Hypoplastic Constitutive Model from Properties of Grain Assemblies". In: *Mechanics of Cohesive-frictional Materials* 4.5, pp. 461–486. DOI: 10.1002/(SICI)1099-1484(199909)4:5<461::AID-CFM71>3.0.CO;2-P.

- Holubec, I. and D'Appolonia, E. (1973). "Effect of Particle Shape on the Engineering Properties of Granular Soils". In: *Evaluation of Relative Density and Its Role in Geotechnical Projects Involving Cohesionless Soils*. Ed. by E. T. Selig and R. S. Ladd. Jan, 100 Barr Harbor Drive, PO Box C700, West Conshohocken, PA 19428-2959: ASTM International, pp. 304–318.
- Hough, S. E. (2004). *Finding Fault in California: An Earthquake Tourist's Guide*. Mountain Press Publishing Company.
- Iai, S. et al. (1994). "Effects of Remedial Measures against Liquefaction at 1993 Kushiro-Oki Earthquake". en. In: *Proceedings from the Fifth U.S.-Japan Workshop on Earthquake Resistant Design of Lifeline Facilities and Countermeasures against Soil Liquefaction*. State University of New York, Buffalo: National Center for Earthquake Engineering Research, pp. 135–152.
- Idriss, I. M. and Boulanger, R. W. (2008). *Soil Liquefaction during Earthquakes*. Earthquake Engineering Research Institute.
- Jaky, J. (1944). "The Coefficient of Earth Pressure at Rest" *Journal for Society of Hungarian Architects and Engineers* October". In.
- Jeremić, B. et al. (2008). "Numerical Simulation of Fully Saturated Porous Materials". In: *International Journal for Numerical and Analytical Methods in Geomechanics* 32.13, pp. 1635–1660.
- Karcher, C. (2003). "Tagebaubedingte Deformationen Im Lockergestein". PhD Thesis. Karlsruhe: University of Karlsruhe.
- Karray, M. et al. (2010). "Assessment of Deep Compaction of the Péribonka Dam Foundation Using "Modal Analysis of Surface Waves" (MASW)". en. In: *Canadian Geotechnical Journal*. DOI: 10.1139/T09-108.
- Kaya, H. and Grabe, J. (2015). "Numerische Untersuchungen Zur Bodenverschleppung Und Spaltbildung Infolge Spundwandeinbringung in Dichtungsschichten". In: *Numerische Methoden in der Geotechnik* 98, pp. 47–58.
- Kelm, M. (2004). "Numerische Simulation Der Verdichtung Rolliger Böden Mittels Vibrationswalzen". PhD. Thesis. Hamburg, Germany: Institut für Geotechnik und Baubetrieb, Technische Universität Hamburg.
- Kenneally, B. et al. (2015). "Finite Element Analysis of Vibratory Roller Response on Layered Soil Systems". In: *Computers and Geotechnics* 67, pp. 73–82. DOI: 10.1016/j.compgeo.2015.02.015.
- Kessler, S., Heibrock, G., and Triantafyllidis, T. (2006). "On Prediction of Vibrocompaction Performance Using Numerical Models". In: *In Symposium Int. Sur Le Vibrofoncage et La Vibrocompaction (H. Gonin, Holeyman A., F. Rocher-Lacoste Eds.)* Paris, France, pp. 233–242.
- Kirkwood, P. and Dashti, S. (2018a). "A Centrifuge Study of Seismic Structure-Soil-Structure Interaction on Liquefiable Ground and Implications for Design in Dense Urban Areas". In: *Earthquake Spectra* 34.3, pp. 1113–1134. DOI: 10.1193/052417EQS095M. URL: <https://doi.org/10.1193/052417EQS095M>.
- Kirkwood, P. and Dashti, S. (2018b). "Considerations for the Mitigation of Earthquake-Induced Soil Liquefaction in Urban Environments". In: *Journal of Geotechnical and Geoenvironmental Engineering* 144.10, p. 04018069. DOI: 10.1061/(ASCE)GT.1943-

- 5606.0001936. URL: <https://ascelibrary.org/doi/abs/10.1061/%28ASCE%29GT.1943-5606.0001936>.
- Kirkwood, P. and Dashti, S. (2019). “Influence of prefabricated vertical drains on the seismic performance of similar neighbouring structures founded on liquefiable deposits”. In: *Géotechnique* 69.11, pp. 971–985. DOI: 10.1680/jgeot.17.P.077. URL: <https://doi.org/10.1680/jgeot.17.P.077>.
- Kirsch, K. (1979). “Erfahrungen Mit Der Baugrundverbesserung Durch Tiefenrüttler”. In: 1.79, p. 21.
- Kirsch, K. and Kirsch, F. (2017). *Ground Improvement by Deep Vibratory Methods*. en. Second edition. Boca Raton: CRC Press, Taylor & Francis Group.
- Köcher, J. (2000). “Verfahren und Vorrichtung zur Verbesserung eines Baugrundes unter Ermittlung des Verdichtungsgrades”. EP 1 016 759 A1.
- Köcher, J. (2001). “Verfahren und Vorrichtung zur Verbesserung eines Baugrundes unter Ermittlung des Verdichtungsgrades”. DE 198 59 962 C 2.
- Koerner, R. M. (1970). “Effect of Particle Characteristics on Soil Strength”. In: *Journal of Soil Mechanics & Foundations Div*, pp. 1221–1234.
- Kolymbas, D. (1985). “A generalized hypoelastic constitutive law”. In: *Proceedings of 11th International Conference on Soil Mechanics and Foundation Engineering*. Vol. 5. Rotterdam: Netherlands, p. 2626.
- Kolymbas, D. (1988). “Generalized Hypoelastic Constitutive Equation”. In: *Constitutive Equations for Granular Non-Cohesive Soils*. Ed. by A. S. Saada and G. Bianchini. Rotterdam: Balkema, pp. 349–366.
- Kolymbas, D. (1991). “An Outline of Hypoplasticity”. In: *Archive of Applied Mechanics* 61(3), pp. 143–151. DOI: 10.1007/BF00788048.
- Kramer, S. L. (1996). *Geotechnical Earthquake Engineering*. Pearson Education India.
- Kumar, S., Holcomb, T., and Pezeshk, S. (2010). “Ground Improvement to Reduce Liquefaction Potential Using Vibrocompaction and Stone Columns”. en. In: p. 8.
- Kutter, B. L. et al. (2015). “LEAP Databases for Verification, Validation, and Calibration of Codes for Simulation of Liquefaction”. In: *Sixth International Conference on Earthquake Geotechnical Engineering, Christchurch, New Zealand*.
- Kutzner, C. (1962). *Über Die Vorgänge in Körnigen Schüttungen Bei Der Rüttelverdichtung*. Vol. 9. Institut f. Bodenmechanik u. Grundbau d. Techn. Hochschule Fridericiana.
- Mahutka, K.-P., Grabe, J., and Hoffmann, N. (2007). *Zur Verdichtung von Rolligen Böden Infolge Dynamischer Pfahleinbringung Und Durch Oberflächenrüttler: Zugl.: Hamburg-Harburg, Techn. Univ., Inst. Für Geotechnik Und Baubetrieb, Diss., 2007*. Erstaussg. Vol. 15. Veröffentlichungen Des Instituts Für Geotechnik Und Baubetrieb. Hamburg-Harburg: Techn. Univ. Inst. für Geotechnik und Baubetrieb.
- Makris, N. and Gazetas, G. (1993). “Displacement Phase Differences in a Harmonically Oscillating Pile”. In: *Géotechnique* 43.1, pp. 135–150.
- Manual, P. M. M. (2007). *Calibration of Hypoplastic Parameters*. Plaxis bv.
- Mašín, D. (Mar. 2014). “Clay hypoplasticity model including stiffness anisotropy”. In: *Géotechnique* 64, pp. 232–238. DOI: 10.1680/geot.13.P.065.
- Massarsch, K. R. (2016). “Grundlagen Der Rüttelverdichtung”. In: *Beiträge Zum 31. Christian Veder Kolloquium. (Graz). Mitteilungshefte Gruppe Geotechnik Graz*, pp. 109–126.

- Massarsch, K. R. and Fellenius, B. H. (2002). “Vibratory Compaction of Coarse-Grained Soils”. In: *Canadian Geotechnical Journal* 39.3. jun, pp. 695–709. DOI: 10.1139/t02-006.
- Massarsch, K. R. and Fellenius, B. H. (2005). “Deep Vibratory Compaction of Granular Soils”. In: *Ground Improvement Case Histories*. Ed. by B. Indraratna and J. Chu. Vol. 3. Elsevier Geo-Engineering Book Series. Elsevier, pp. 633–658. DOI: 10.1016/S1571-9960(05)80022-9.
- Massarsch, K. (1991). “Deep Soil Compaction Using Vibratory Probes”. In: *Deep Foundation Improvements: Design, Construction, and Testing*. Ed. by M. I. Esrig and R. C. Bachus. jan, West Conshohocken, PA: ASTM International, pp. 297–319. DOI: 10.1520/STP25067S.
- Massarsch, K. (1999). “Deep Compaction of Granular Soils”. In: *A look back for future geotechnics, Oxford & IBH Publishing*, pp. 181–223.
- Menq, F.-Y. (2003). “Dynamic Properties of Sandy and Gravelly Soils”. PhD Thesis. USA: University of Texas at Austin.
- Mitchell, J. K. (1982). “Soil Improvement-State-of-the-Art”. In: *Proc 10th Int. Conf. on Soil Mech. Found. Eng.* Vol. 4. Stockholm, Sweden, pp. 509–565.
- Mogami, T. and Yoshikoshi, H. (1968). “On the Angle of Internal Friction of Coarse Materials”. In: *3rd Budapest Conference on Soil Mechanics and Foundation Engineering*. Budapest, pp. 190–196.
- Morgan, J. G. D. and Thomson, G. . (1983). “Instrumentation Methods for Control of Ground Density in Deep Vibrocompaction”. In: *Proceedings of the 8th European Conference on Soil Mechanics and Foundation Engineering*. Vol. 1, pp. 59–72.
- Nagula, S. S. and Grabe, J. (2020). “Coupled Eulerian Lagrangian Based Numerical Modelling of Vibro-Compaction with Model Vibrator”. In: *Computers and Geotechnics* 123, p. 103545.
- Nagy, P. (2019). “Deep Vibration Compaction: Dynamic Compaction Control Based on the Vibrator Movement”. en. PhD Thesis. Vienna, Austria: Technische Universität Wien.
- Nagy, P. and Adam, D. (2019). “Arbeitsintegrierte Verdichtungskontrolle während der Rütteldruckverdichtung”. In: *geotechnik* 42.3, pp. 124–133. DOI: <https://doi.org/10.1002/gete.201900004>. URL: <https://onlinelibrary.wiley.com/doi/abs/10.1002/gete.201900004>.
- National Instruments (2018). *LabVIEW: User Manual*.
- Nendza, M. (2006). “Untersuchungen Zu Den Mechanismen Der Dynamischen Bodenverdichtung Bei Anwendung Des Rütteldruckverfahrens”. PhD. Thesis. Braunschweig, Germany: Mitteilung Des Instituts Für Grundbau Und Bodenmechanik, Braunschweig Technical University.
- Nendza, M., Stahlmann, J., and Wehr, W. (2008). “Untersuchungen Zur Optimierung Der Dynamischen Bodenverdichtung Bei Anwendung Des Ruetteldruckverfahrens”. In: *30. Baugrundtagung 2008 mit Fachausstellung Geotechnik in Dortmund*, pp. 559–561.
- Nielsen, A. H. (2006). “Absorbing Boundary Conditions for Seismic Analysis in ABAQUS”. en. In: p. 18.
- Niemunis, A. and Herle, I. (1997). “Hypoplastic Model for Cohesionless Soils with Elastic Strain Range”. In: *Mechanics of Cohesive-frictional Materials* 2.4. oct, pp. 279–299. DOI: 10.1002/(SICI)1099-1484(199710)2:4<279::AID-CFM29>3.0.CO;2-8.

- Olarte, J. et al. (2017). “Centrifuge modeling of mitigation-soil-foundation-structure interaction on liquefiable ground”. In: *Soil Dynamics and Earthquake Engineering* 97, pp. 304–323. DOI: <https://doi.org/10.1016/j.soildyn.2017.03.014>. URL: <https://www.sciencedirect.com/science/article/pii/S0267726116301385>.
- Qiu, G. (2012). “Coupled Eulerian Lagrangian Simulations of Selected Soil-Structure Interaction Problems”. In: *Veröffentlichungen des Instituts für Geotechnik und Baubetrieb der TU Hamburg-Harburg* Heft 24.
- Qiu, G., Henke, S., and Grabe, J. (2011). “Application of a Coupled EulerianLagrangian Approach on Geomechanical Problems Involving Large Deformations”. In: *Computers and Geotechnics* 38.1. jan, pp. 30–39. DOI: [10.1016/j.compgeo.2010.09.002](https://doi.org/10.1016/j.compgeo.2010.09.002).
- Ramirez, J. et al. (2018). “Site Response in a Layered Liquefiable Deposit: Evaluation of Different Numerical Tools and Methodologies with Centrifuge Experimental Results”. In: *Journal of Geotechnical and Geoenvironmental Engineering* 144.10, p. 04018073.
- Rascol, E. (2009). “Cyclic Properties of Sand: Dynamic Behaviour for Seismic Applications”. PhD Thesis. Lausanne, The Switzerland: Ecole Polytechnique Federale de Lausanne.
- Robertson, P. K. (2016). “Suggested QC Criteria for Deep Compaction Using the CPT”. In: *Proceedings of the 5th International Conference on Geotechnical and Geophysical Site Characterisation*. Sydney, Australia: Australian Geomechanics Society.
- Rodger, A. A. (1979). *Vibrompaction of Cohesionless Soils*.
- Schmitter, M. and Adam, C. (2017). “Simplified Numerical Modelling Strategies of Deep Vibratory Compaction”. In: *Proc. 6th Int. Conf. on Comput. Methods in Struct. Dyn and Earthquake Eng.* Rhodes Island, Greece: Ecomas Proceedia, pp. 4607–4622.
- Schultze, E. and Moussa, A. (1961). “Schultze, E. and Moussa, A. (1961) "Factors Affecting the Compressibility of Sand". Proceedings of 5th ICSMFE, Paris, 1, Pp 335-340”. In: *Proceedings of 5th ICSMFE*. Vol. 1. Paris, pp. 335–340.
- Seed, H. B. and Idriss, I. M. (1967). “Analysis of Soil Liquefaction: Niigata Earthquake”. In: *Journal of the Soil Mechanics and Foundations Division* 93.3, pp. 83–108.
- Shahir, H. et al. (2012a). “Evaluation of Variation of Permeability in Liquefiable Soil under Earthquake Loading”. In: *Computers and Geotechnics* 40, pp. 74–88.
- Shahir, H. et al. (2012b). “Evaluation of variation of permeability in liquefiable soil under earthquake loading”. In: *Computers and Geotechnics* 40, pp. 74–88. DOI: <https://doi.org/10.1016/j.compgeo.2011.10.003>. URL: <https://www.sciencedirect.com/science/article/pii/S0266352X11001662>.
- Simons, H. and Kahl, M. (1987). *Experimentelle Untersuchungen Zur Verdichtung Norddeutscher Sande Mit Tiefenrüttlern: Abschluforschungsvorhaben; Forschungsbericht*. IRB-Verlag.
- Sondermann, W. and Kirsch, K. (2017). “Baugrundverbesserung”. In: *Grundbau-Taschenbuch: Teil 2: Geotechnische Verfahren, 7. Auflage*, pp. 101–158.
- Taiebat, M., Jeremić, B., and Kaynia, A. M. (2009). “Propagation of Seismic Waves through Liquefied Soils”. EN. In: *Geotechnical Special Publication No. 186: Contemporary Topics in In Situ Testing, Analysis, and Reliability of Foundations*, pp. 198–205. DOI: [10.1061/41022\(336\)26](https://doi.org/10.1061/41022(336)26).

- Taiebat, M., Shahir, H., and Pak, A. (2007). “Study of Pore Pressure Variation during Liquefaction Using Two Constitutive Models for Sand”. In: *Soil Dynamics and Earthquake Engineering* 27.1, pp. 60–72.
- Tasiopoulou, P. et al. (2015). “On Validation of Fully Coupled Behavior of Porous Media Using Centrifuge Test Results”. In: *Coupled systems mechanics* 4.1, pp. 67–98.
- Thorburn, S. (1975). “Building Structures Supported by Stabilized Ground”. In: *Géotechnique* 25.1, pp. 83–94. DOI: 10.1680/geot.1975.25.1.83.
- Triantafyllidis, T. and Kimmig, I. (2019). “A Simplified Model for Vibro Compaction of Granular Soils”. In: *Soil Dynamics and Earthquake Engineering* 122, pp. 261–273.
- Vranckx, A. (2017). “Effect of Heterogeneous Densification Due to Vibroflotation on Liquefaction Resistance”. Master’s Thesis. Kungliga Tekniska Högskolan (KTH) Sweden: School of architecture and built environment.
- Wang, L. et al. (2007). “Fundamental Mechanics of Asphalt Compaction through FEM and DEM Modeling”. In: *Geotechnical Special Publication. Analysis of Asphalt Pavement Materials and Systems: Emerging Methods*. Vol. 176, pp. 45–63.
- Wegener, D. and Herle, I. (2012). “Zur Steifigkeit Bei Kleinen Dehnungen Im Rahmen Der Hypoplastizität”. In: *geotechnik* 35.4, pp. 229–235. DOI: 10.1002/gete.201200006.
- Wehr, W. (2005). “Variation Der Frequenz von Tiefenrüttlern Zur Optimierung Der Rütteldruckverdichtung”. In: *Hans-Lorenz Symposium, TU Berlin*, pp. 67–77.
- Wersäll, C., Larsson, S., and L. David Suits, William J. Likos (2013). “Small-Scale Testing of Frequency-Dependent Compaction of Sand Using a Vertically Vibrating Plate”. In: *Geotechnical Testing Journal* 36.3, pp. 394–403. DOI: 10.1520/GTJ20120183.
- Wersäll, C., Nordfelt, I., and Larsson, S. (2017). “Soil Compaction by Vibratory Roller with Variable Frequency”. In: *Géotechnique* 67.3, pp. 272–278. DOI: 10.1680/jgeot.16.P.051.
- Wersäll, C. et al. (2015). “Frequency Variable Surface Compaction of Sand Using Rotating Mass Oscillators”. In: *Geotechnical Testing Journal* 38.2, pp. 198–207. DOI: 10.1520/GTJ20130193.
- Wichtmann, T., Fuentes, W., and Triantafyllidis, T. (2019). “Inspection of three sophisticated constitutive models based on monotonic and cyclic tests on fine sand: Hypoplasticity vs. Sanisand vs. ISA”. In: *Soil Dynamics and Earthquake Engineering* 124, pp. 172–183. DOI: <https://doi.org/10.1016/j.soildyn.2019.05.001>. URL: <https://www.sciencedirect.com/science/article/pii/S0267726118303865>.
- Wichtmann, T. and Triantafyllidis, T. (2005). “Dynamische Steifigkeit Und Dämpfung von Sand Bei Kleinen Dehnungen”. In: *Bautechnik* 82.4, pp. 236–246.
- Witt, K. J. (2009). *Grundbau-Taschenbuch: Teil 2: Geotechnische Verfahren*. Grundbau-Taschenbuch. Ernst & Sohn, Berlin.
- Witt, K. J. (2017a). *Grundbau-Taschenbuch: Teil 1: Geotechnische Grundlagen*. Ernst, Wilhelm & Sohn.
- Wolffersdorff, P.-A. von (1996). “A Hypoplastic Relation for Granular Materials with a Predefined Limit State Surface”. In: *Mechanics of Cohesive-frictional Materials* 1.3. jul, pp. 251–271. DOI: 10.1002/(SICI)1099-1484(199607)1:3<251::AID-CFM13>3.0.CO;2-3.
- Wood, D. M. (2004). *Geotechnical Modelling*. Vol. 1. London: CRC press.

-
- Wu, W., Bauer, E., and Kolymbas, D. (1996). “Hypoplastic Constitutive Model with Critical State for Granular Materials”. In: *Mechanics of Materials* 23.1, pp. 45–69. DOI: 10.1016/0167-6636(96)00006-3.
- Yasuda, S. et al. (2006). “Effect of Soil Improvement on Ground Subsidence Due to Liquefaction”. In: *Soils and Foundations Special Issue on Geotechnical Aspects of the January 17*. Japanese Geotechnical Society, pp. 99–107.
- Youd, T. (1972). “Compaction of Sands by Repeated Shear Straining”. In: *ASCE* 98, pp. 709–725.
- Youd, T. L. and Hoose, S. N. (1976). “Liquefaction during 1906 San Francisco Earthquake”. In: *Journal of the Geotechnical Engineering Division* 102.5, pp. 425–439.
- Zienkiewicz, O. C. et al. (1999). *Computational Geomechanics*. Citeseer.

List of Symbols

Greek Symbols

α	Exponent
β	Exponent
β_χ	Exponent
β_ω	Frequency ratio
σ_{tot}	Total stress
χ	Exponent
Δu	Excess pore pressure
δ	Intergranular strain tensor
$\dot{\sigma}$	Strain rate
ϵ_{SOM}	Deformation to reach saturation
γ_{sat}	Saturated density
λ	Scale factor
μ	friction coefficient
μ_w	Viscosity of fluid
ν	Poisson's ratio
ω	Angular frequency
ω_0	Natural frequency
ϕ_c	Friction angle
ϕ_p	Peak Friction angle
ρ_r	Density of the mixture of the solid and the water phase
ρ_s	Density of the solid grains
ρ_w	density of water

σ	Effective Cauchy stress
σ'_v	Effective vertical stress
σ_{11}	Difference in pore water pressure
σ_{11}	Horizontal stress
σ_{33}	Vertical stress
σ'_{z_0}	Initial vertical effective stress
Θ	Phase angle
ϑ_p	Dilatancy angle

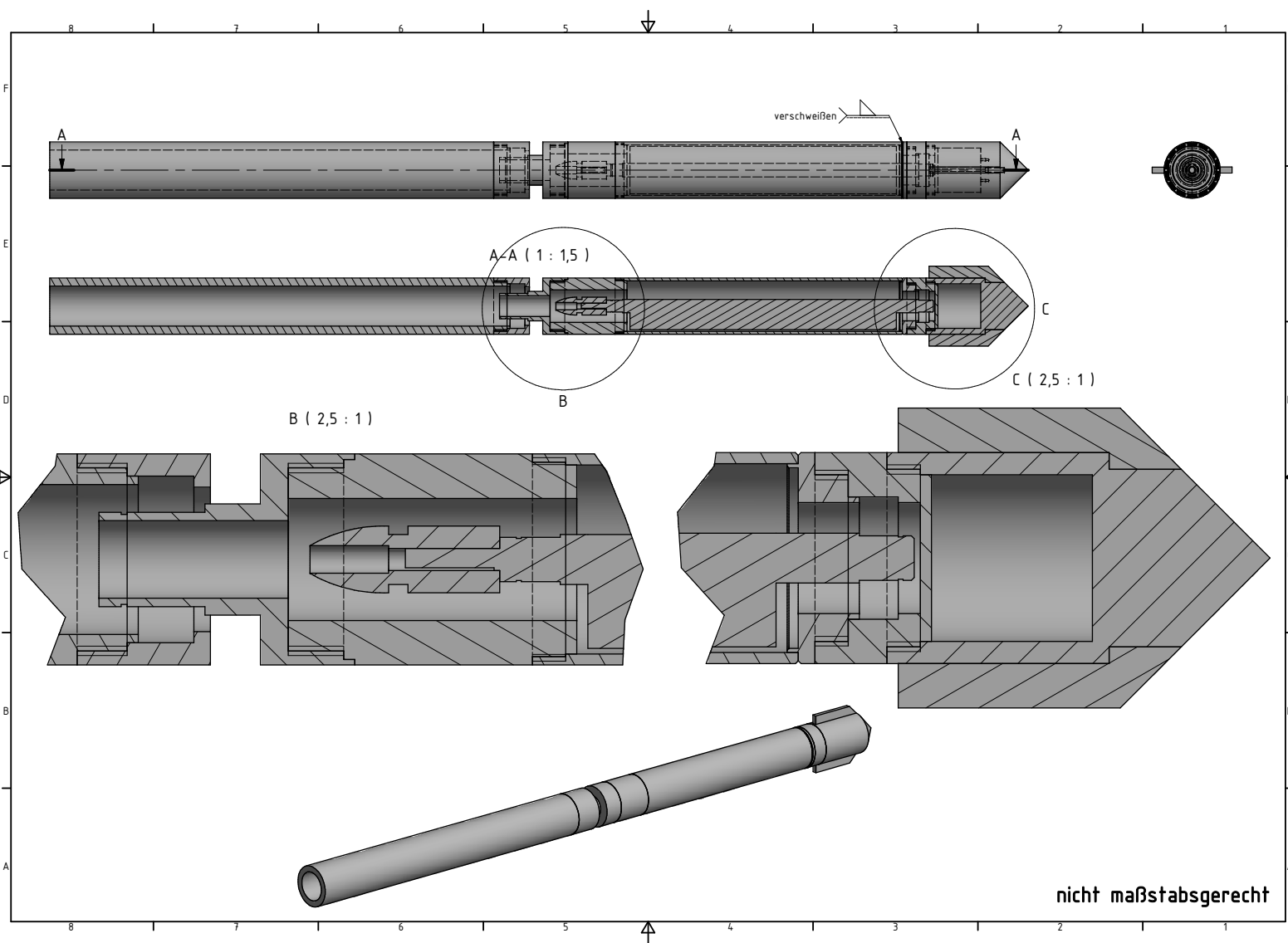
Latin Symbols

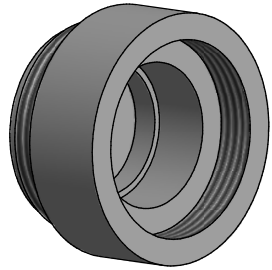
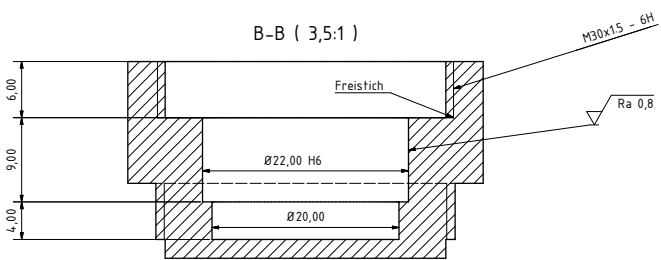
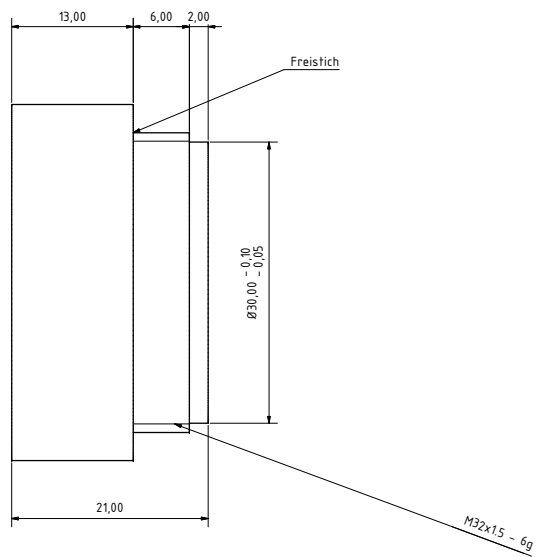
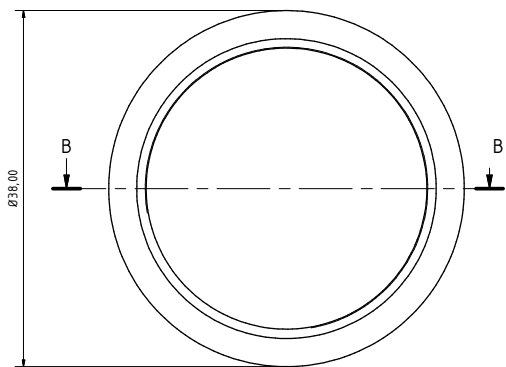
\dot{e}	Rate of change of void ratio
\dot{p}'	Rate of change of mean pressure
A	Amplitude
a	Constant
a_0	Acceleration amplitude
a_s	Current acceleration of the solid phase
$A_{\beta=\infty,air}$	Amplitude in air at infinitely large frequency ratio
$A_{\beta=\infty,soil}$	Amplitude in soil at infinitely large frequency ratio
a_{xx}	Acceleration in X direction
a_{yy}	Acceleration in Y direction
b	Constant
b	Grid spacing
c	Constant
c^*	Viscous damper
C_u	Co-efficient of uniformity
C_c	Compression Index
D	Deformation rate
d_{10}	10% finer diameter

d_{20}	20% finer diameter
d_{50}	50% finer diameter
D_{cone}	Diameter of CPT cone
E	Incremental stiffness
e	Void ratio
E_0	Asymptotic stiffness
e_c	Max void ratio
e_d	Min void ratio
e_i	Max void ratio
e_m	Eccentricity of masses
E_R	Stiffness at 180° change of direction
E_s	Young's modulus of the solid skeleton
E_T	Stiffness at 90° change of direction
e_{c0}	Critical void ratio at zero pressure
e_{d0}	Min void ratio at zero pressure
e_{i0}	Maximum void ratio at zero pressure
F	Centrifugal force
g	Acceleration due to gravity
g_s	External applied acceleration
h	Function
h_s	Granulate hardness
I_D	Relative density
K	Bulk modulus
k	Permeability
k^*	Elastic spring
k^*	Soil reaction stiffness as per Nagy (2019)
K_0	Earth pressure co-efficient at rest

K_P	Peak friction angle ratio
K_s	Bulk modulus of the solid grains
K_T	Bulk modulus of the solid skeleton
K_w	Bulk modulus of water
m	Mass of eccentric weights
M_B	Mass of vibrating soil
M_R	Mass of the vibrator
m_R	Stiffness ratio at 180° change of direction
m_T	Stiffness ratio at 90° change of direction
n	Exponent
n_p	Porosity
p	Mean pressure
p'	Effective mean pressure
P_a	Reference pressure (1 kPa)
q	Deviatoric stress
q_c	CPT tip resistance
R	Maximum value of intergranular strain
r	Distance between point of vibration and centre point
r_u	Pore pressure ratio
SN	Suitability Number
t	Time
v_s	Current velocity of the solid phase
z	Vertical coordinate

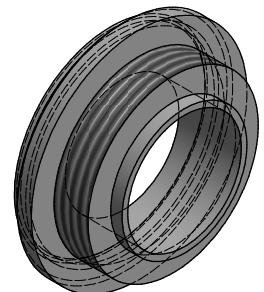
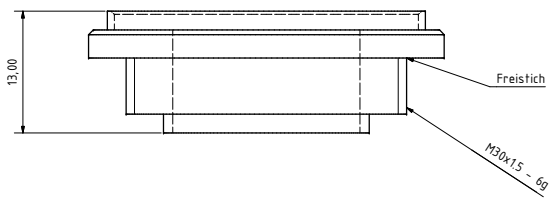
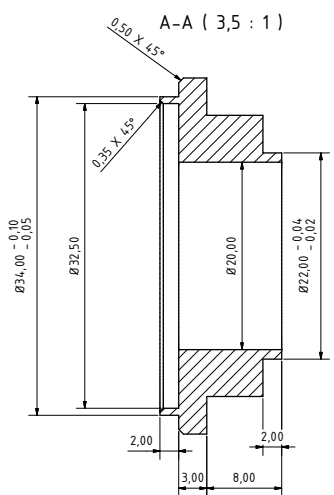
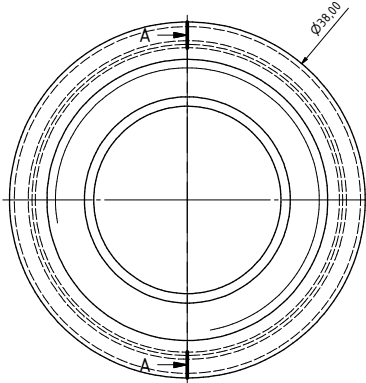
Appendix A Design of Model Vibrator





nicht maßstabgerecht

Datum		Name	
Gezeichnet	Gelesen	Prüf	
Gezeichnet			
Prüf			
Lagersitz		1	
		2	
Blatt	Blätter	Datum	Name



nicht maßstabsgerecht

Datum		Name	
Gezeichnet	Gelesen	Prüf	
Gezeichnet			
Schweiß_Flansch			
			1
			22

Appendix B Results of Experimental Tests

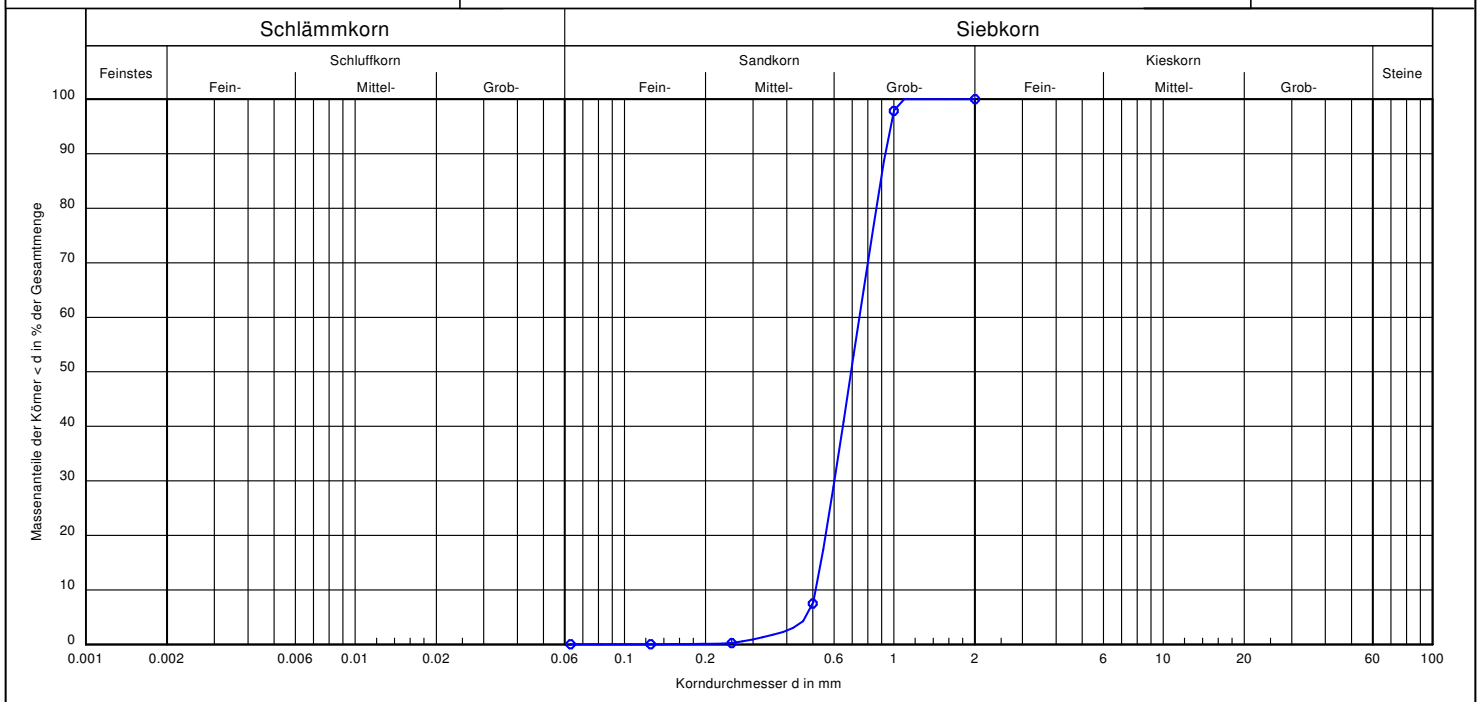
B.1 Grain size distribution of Hamburger sand

Korngrößenverteilung

DIN 18123


Anlage

Februar 2013



Signatur:		Projekt Nr.: Modellboden
Entnahmestelle	HH-01 Sand (k4)	
Tiefe		
Bodenart:	gS, ms	
U/Cc	1.5/0.9	Bearbeiter:

B.2 Grain density of Hamburger sand

Projektnr.:		Datei:		Prüfprotokoll BESTIMMUNG DER KORNDICHTE MIT DEM KAPILLARPYKNOMETER nach DIN 18 124 - KP (Juli 1997)		
Projektkurztitel:						
Entnahmestelle:		GP / UP / RK				
Entnahmetiefe:		Bodenart: Sand				
Ausgeführt von: mb		Beginn: 18.11.2013				
Geprüft von:				Datum:		
				Schale Nr.:		
Pyknometer Nr.				61	43	64
Pyknometer + Probe $m_1 = m_p + m_d$ [g]				77,480	73,464	74,995
Pyknometer + Probe + Wasser $m_2 = m_p + m_d + m_{wT}$ [g]				164,364	161,755	162,738
Wasser $m_{wT} = m_2 - m_1$ [g]				86,884	88,291	87,743
Temperatur des Wassers T [°C]				17,8	17,7	17,9
Dichte des Wassers bei T °C ρ_{wT} [g/cm³]				0,99866	0,99868	0,99864
Volumen des Wassers V_{wT} [cm³]				87,001	88,408	87,862
Volumen des Pyknometers bei T °C V_{pT} [cm³]				99,808	99,883	99,849
Volumen der Körner $V_k = V_{pT} - V_{wT}$ [cm³]				12,808	11,475	11,987
Masse des Pyknometers m_p [g]				43,681	43,184	43,366
Trockenmasse der Körner $m_d = m_1 - m_p$ [g]				33,799	30,280	31,629
Korndichte $\rho_s = m_d / V_k$ [g/cm³]				2,639	2,639	2,639
Mittelwert: [g/cm³]				2,639		
Ermittlung des Kapillarpyknometervolumens						
Masse des leeren Pyknometers mit Stopfen (auf 0,001 g) m_p [g]				43,681	43,184	43,366
Masse des mit entlüftetem, dest. Wasser gefülltem Pyknometers $m_p + m_{wT}$ [g]				143,361	142,931	143,083
Masse des Wassers m_{wT} [g]				99,680	99,747	99,717
Temperatur des Wassers T [°C]				17,5	17,9	17,7
Dichte des Wassers bei T °C ρ_{wT} [g/cm³]				0,99871	0,99864	0,99868
Volumen des Pyknometers V_{pT} [cm³]				99,81	99,88	99,85
 Technische Universität Hamburg-Harburg		Geotechnik und Baubetrieb Univ.-Prof. Dr.-Ing. Jürgen Grabe		Harburger Schloßstr. 20 21079 Hamburg		Tel.: +49 (0)40 / 428 78-3782 Fax: +49 (0)40 / 428 78-4020

B.3 Maximum and minimum void ratio of Hamburger sand as per DIN 18126

Bestimmung der Dichte nichtbindiger Böden bei lockerster und dichtester Lagerung DIN 18126

Projekt Nr.: Modellboden
 HH-01 Sand

Entnahmestelle:
 Entnahmetiefe:
 Entnahmearart : GP
 Bodenart: gS, ms

Korndichte $\rho_s = 2.639 \text{ g/cm}^3$
 Porenanteil in natürlicher Lagerung $n = \text{-----} \%$
 Porenanzahl in natürlicher Lagerung $e = \text{-----}$
 Ungleichförmigkeitszahl $U = \text{-----}$
 Größtkorn $maxd = \text{-----} \text{ mm}$

Bestimmung der Dichte in lockerster Lagerung

Versuchszylinder $V_Z = 438.45 \text{ cm}^3$ $m_Z = 913.91$

Probenmasse	min $m_{d1} =$	643.87	g
	min $m_{d2} =$	644.13	g
	min $m_{d3} =$	641.48	g
	min $m_{d4} =$	643.37	g
	min $m_{d5} =$	643.99	g
	Mittelwert :	643.37	g

min Trockendichte $min \rho_d = min m_d / V_Z = 1.467 \text{ g/cm}^3$
 max Porenvolumen $max n = 1 - (min \rho_d / \rho_s) = 0.444$
 max Porenzahl $max e = (\rho_s / min \rho_d) - 1 = 0.798$

Bestimmung der Dichte in dichtester Lagerung

Versuchszylinder $h = 11.15 \text{ cm}$ $A = 39.2 \text{ cm}^2$ Platte $h_p = 1.50 \text{ cm}$

Probenmasse	$m_d =$	643.99	g
Setzung	$s_1 =$	2.45	mm
	$s_2 =$	1.60	mm
	$s_3 =$	0.40	mm
	Mittelwert $s_m =$	1.48	mm
Volumen	$minV = A \cdot (h - h_p - s_m) =$	372.17	cm^3
Trockendichte	$\rho_d =$	1.730	g/cm^3

max Trockendichte $max \rho_d = m_d / minV = 1.730 \text{ g/cm}^3$
 min Porenvolumen $min n = 1 - (max \rho_d / \rho_s) = 0.344$
 min Porenzahl $min e = (\rho_s / max \rho_d) - 1 = 0.525$

Abgeleitete Größen

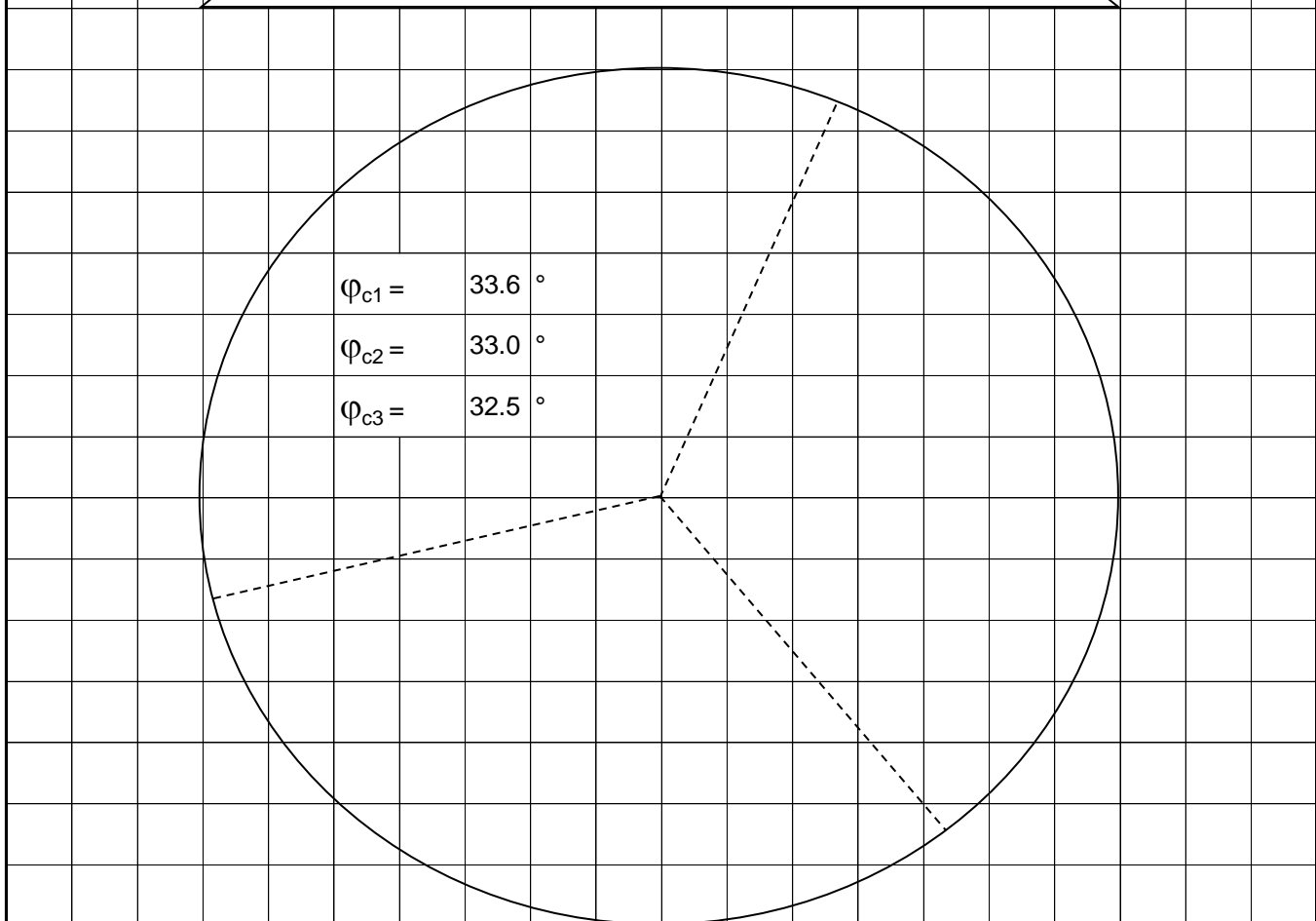
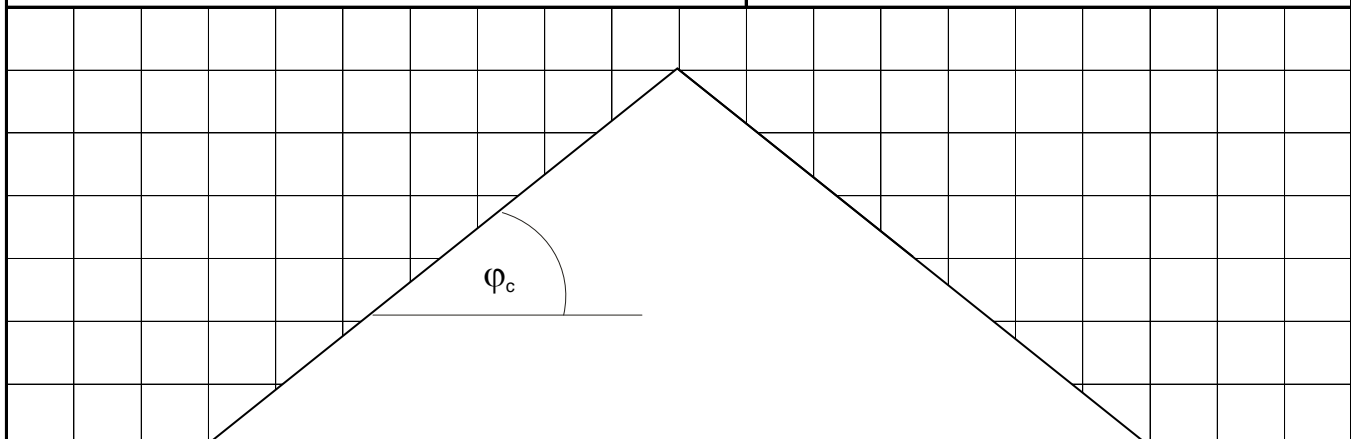
Lagerungsdichte $D = (max n - n) / (max n - min n) =$
 Bezogene Lagerungsdichte $I_D = (max e - e) / (max e - min e) =$
 Verdichtungsfähigkeit $I_f = (max e - min e) / min e = 0.52$

B.4 Critical friction angle of Hamburger sand

Projektnr.: i0106	Datei:	
Projektkurztitel: HAMBURGER		
Entnahmestelle:		
Entnahmetiefe:	Bodenart: Sand	
Ausgeföhrt von:	Beginn:	Ende:
Geprüft von:	Datum:	

Prüfprotokoll

**BESTIMMUNG DES
KRITISCHEN
REIBUNGSWINKELS
SCHÜTTKEGELVERSUCH**



Mittelwert $\varphi_c = 33.0^\circ$

B.5 CRS oedometer test of loose Hamburger sand



Technische Universität Hamburg-Harburg

Geotechnik und Baubetrieb
Univ.-Prof. Dr.-Ing. Jürgen Grabe

Harburger Schloßstr. 20
21079 Hamburg

Tel.: +49 (0)40 / 428 78-3782

Fax: +49 (0)40 / 428 78-4020

www.tu-harburg.de/gbt

Anlage

Juni 2013

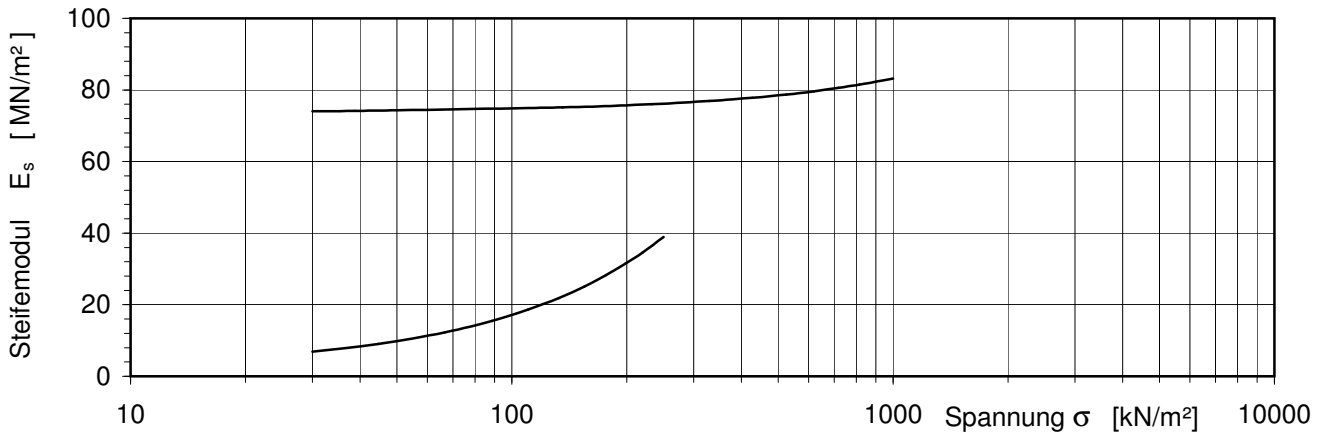
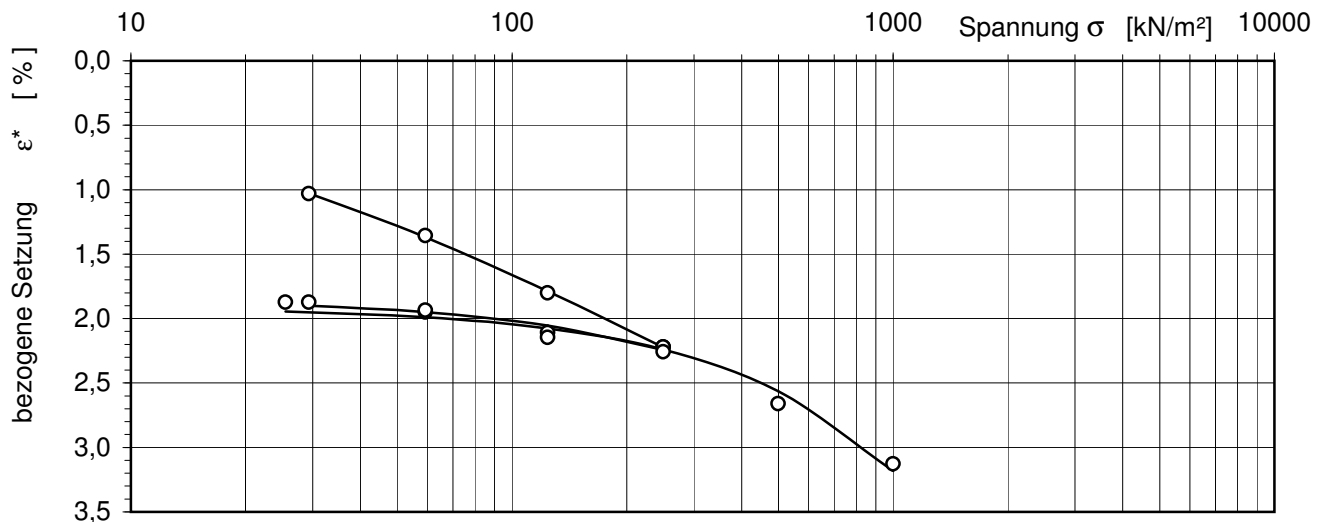
EINDIMENSIONALER KOMPRESSIONSVERSUCH

DIN 18 135 - K 7020 RF

Projekt Nr.: Modellboden
HH-01 Sand

Entnahmestelle: HH-01 Sand
Entnahmetiefe: hypoplastisch
Bodenart: gS, ms
Bemerkung: trocken, docking 0,02 kN

Prüfkörper h/d 29 / 100 mm
Laststeigerung 30 Min.
Wasserzugabe nach Aufbringen der Minimallast
Anfangswassergehalt 0,00 %
Endwassergehalt 0,00 %
Anfangsdichte 1,624 g/cm³
Anfangsporenzahl 0,631 lockere Lagerung



Spannung [kN/m ²]	Steifemodul E_s^*	
	1. Belastung [MN/m ²]	2. Belastung [MN/m ²]
30	6,9	74,1
60	11,3	74,4
125	20,7	75,0
250	38,9	76,2
500		78,5
1000		83,2

Kompressionsbeiwert $C_c = 0,025$

Schwellbeiwert $C_s = 0,011$

*: Tangentenmodul

Bearbeiter:

Geprüft von:

B.6 CRS oedometer test of dense Hamburger sand



Technische Universität Hamburg-Harburg

Geotechnik und Baubetrieb
Univ.-Prof. Dr.-Ing. Jürgen Grabe

Harburger Schloßstr. 20
21079 Hamburg

Tel.: +49 (0)40 / 428 78-3782

Fax: +49 (0)40 / 428 78-4020

www.tu-harburg.de/gbt

Anlage

Juni 2013

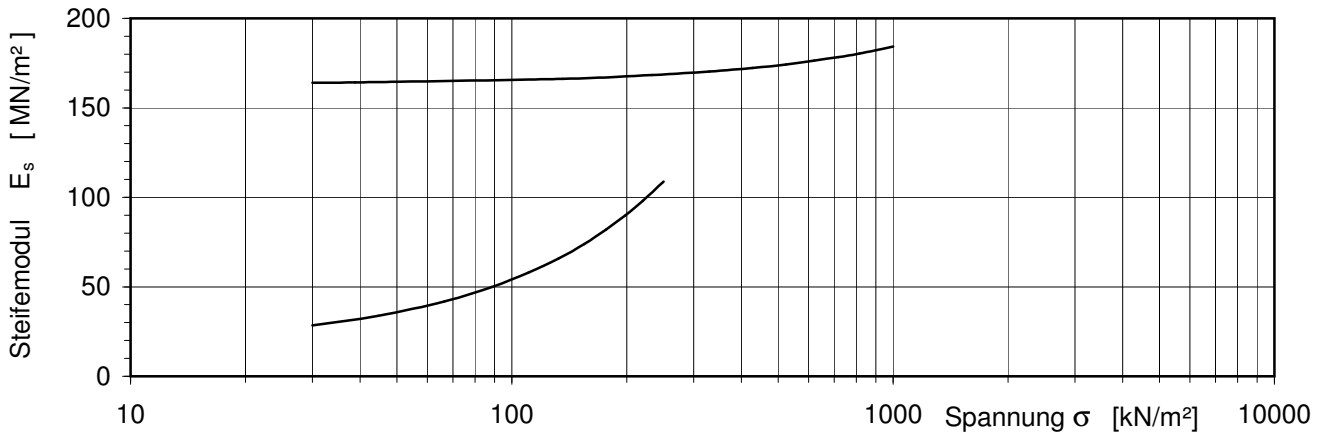
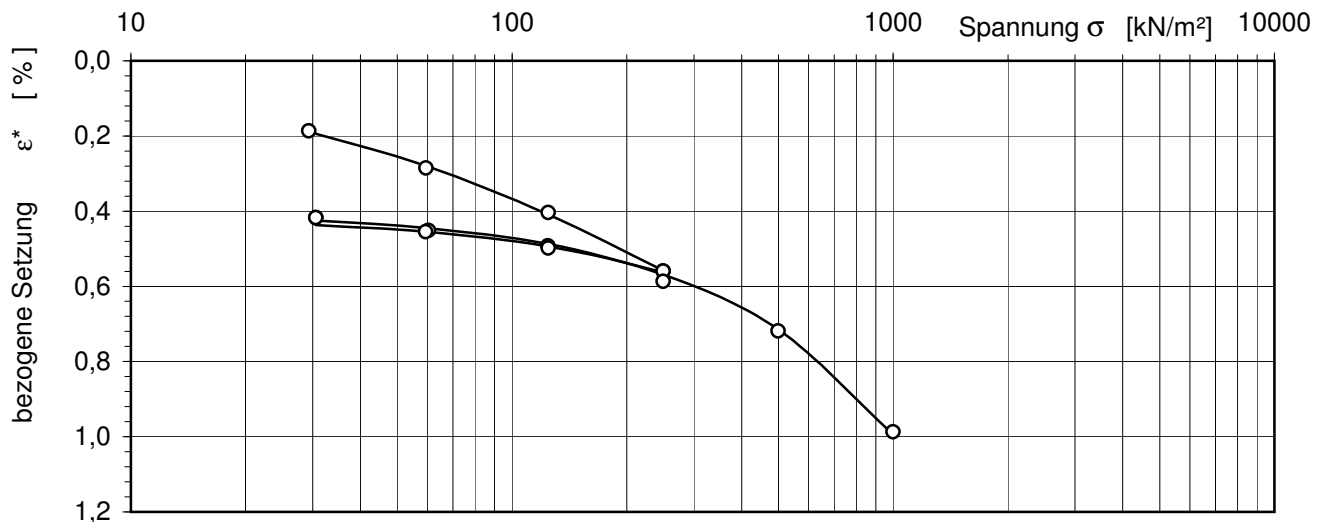
EINDIMENSIONALER KOMPRESSIONSVERSUCH

DIN 18 135 - K 7020 RF

Projekt Nr.: Modellboden
HH-01 Sand

Entnahmestelle: HH-01 Sand
Entnahmetiefe: hypoplastisch
Bodenart: gS, ms
Bemerkung: trocken, docking 0,02 kN

Prüfkörper h/d 29 / 100 mm
Laststeigerung 30 Min.
Wasserzugabe nach Aufbringen der Minimallast
Anfangswassergehalt 0,00 %
Endwassergehalt 0,00 %
Anfangsdichte 1,728 g/cm³
Anfangsporenzahl 0,534 dichte Lagerung



Spannung [kN/m ²]	Steifemodul E _S *	
	1. Belastung [MN/m ²]	2. Belastung [MN/m ²]
30	28,4	164,1
60	39,4	164,7
125	63,1	166,0
250	108,8	168,6
500		173,8
1000		184,2

Kompressionsbeiwert C_C = 0,019

Schwellbeiwert C_S = 0,004

*: Tangentenmodul

Bearbeiter:

Geprüft von:

B.7 Static triaxial test of loose Hamburger sand

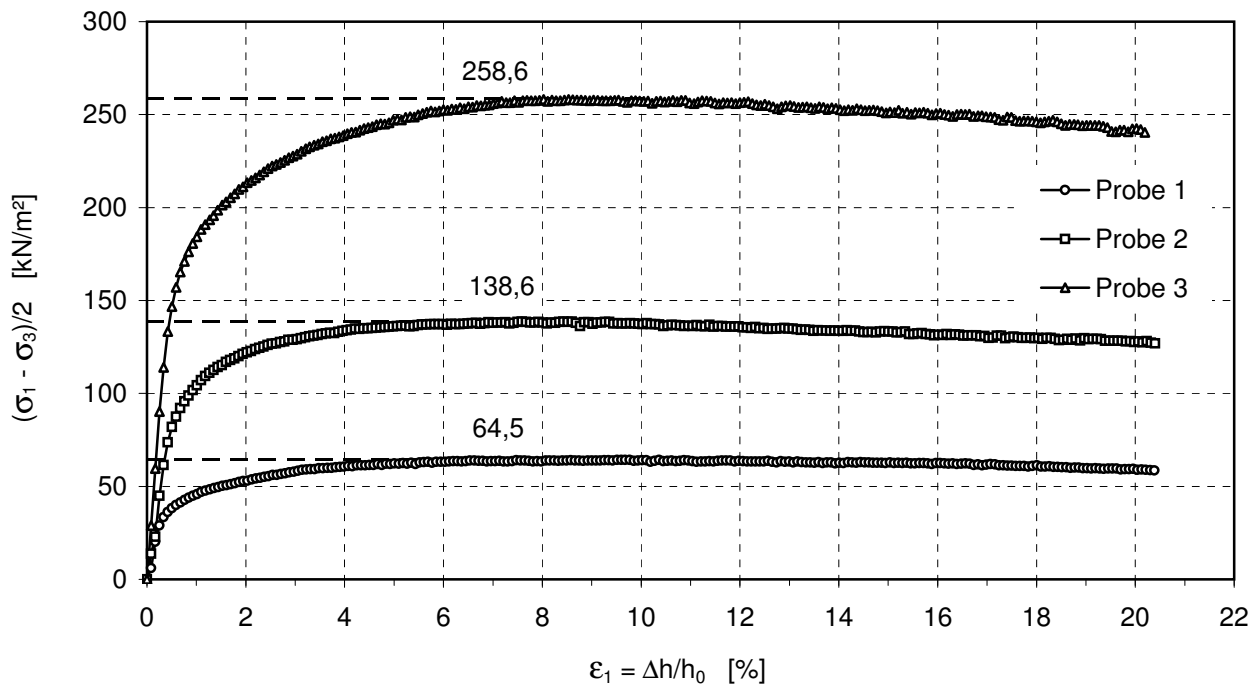
TRIAXIALVERSUCH

DIN 18 137 - D

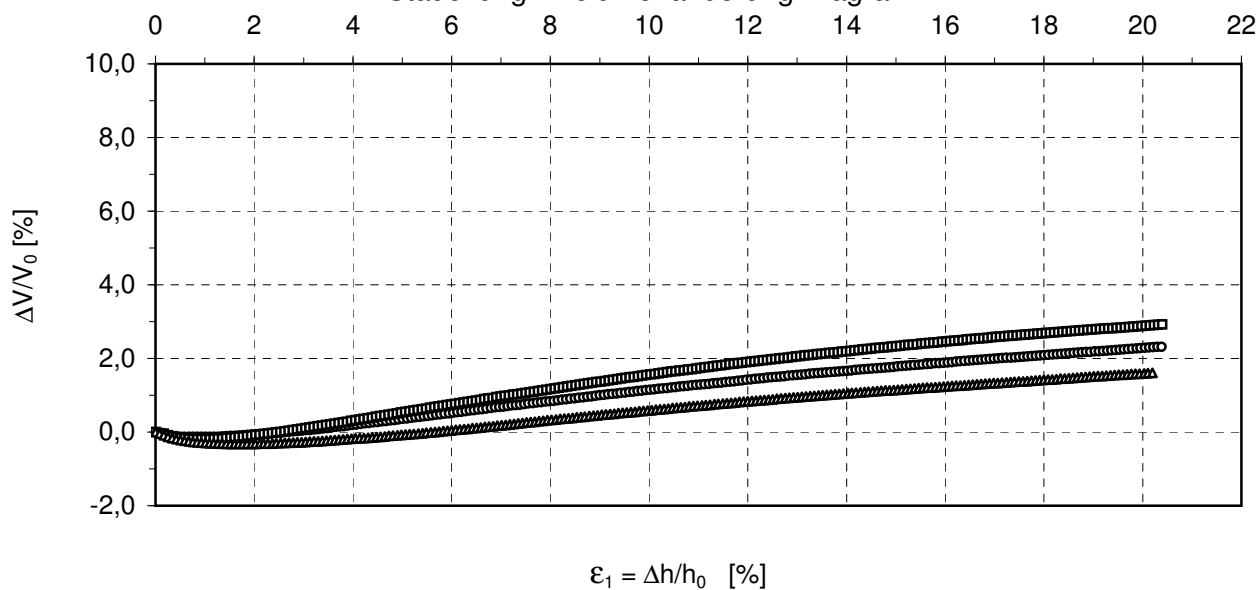
Projekt Nr.: i0912
HH-01-Sand
Stoffparameter

Entnahmestelle: -
Entnahmetiefe: -
Bodenart: HH-01-Sand

Stauchung - Spannung Diagramm



Stauchung - Volumenänderung Diagramm



Bearbeiter:

Geprüft von:

B.8 Static triaxial test of dense Hamburger sand

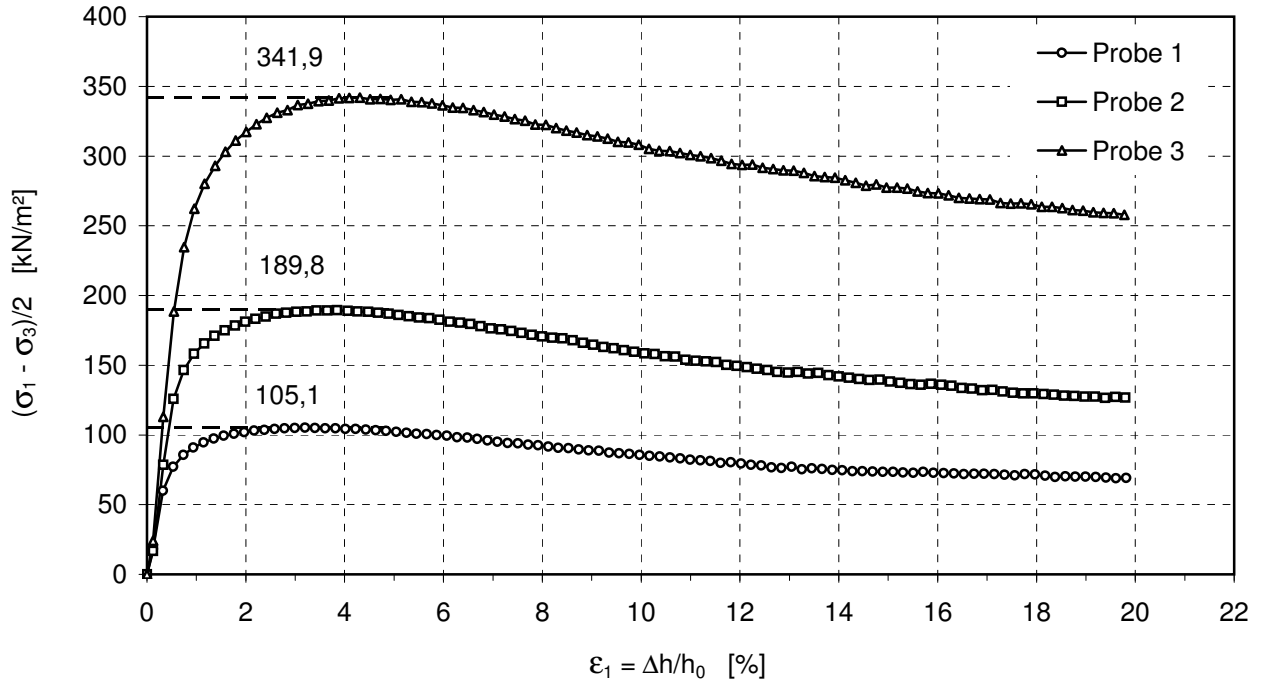
TRIAXIALVERSUCH

DIN 18 137 - D

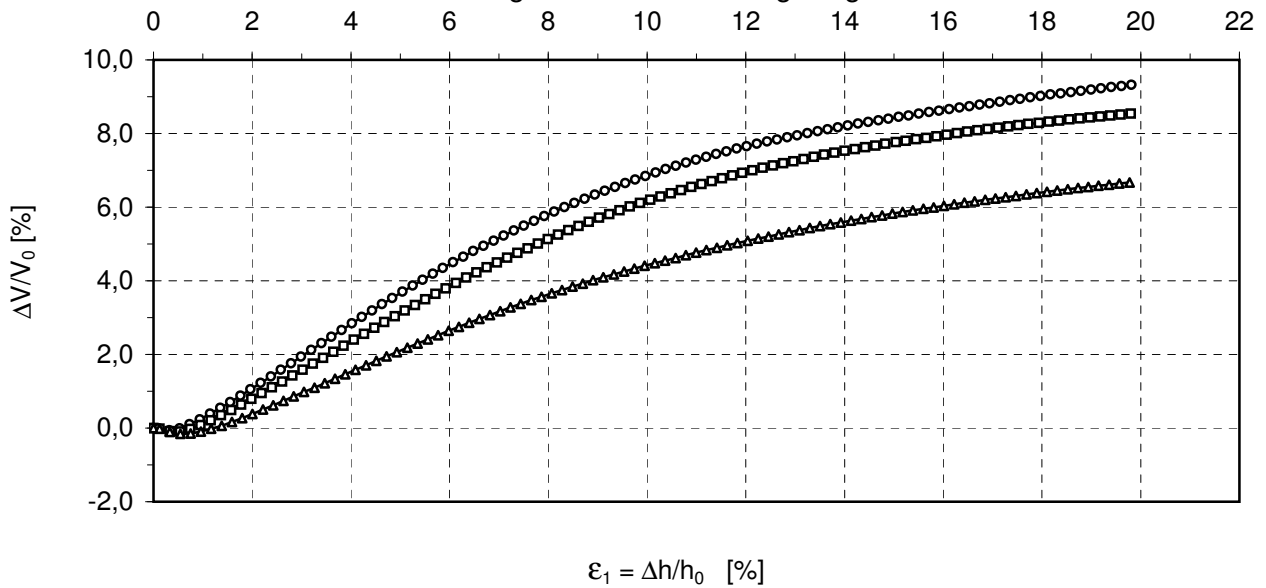
Projekt Nr.: i0912
HH-01-Sand
Stoffparameter

Entnahmestelle: -
Entnahmetiefe: -
Bodenart: HH-01-Sand

Stauchung - Spannung Diagramm



Stauchung - Volumenänderung Diagramm



Bearbeiter:

Geprüft von:

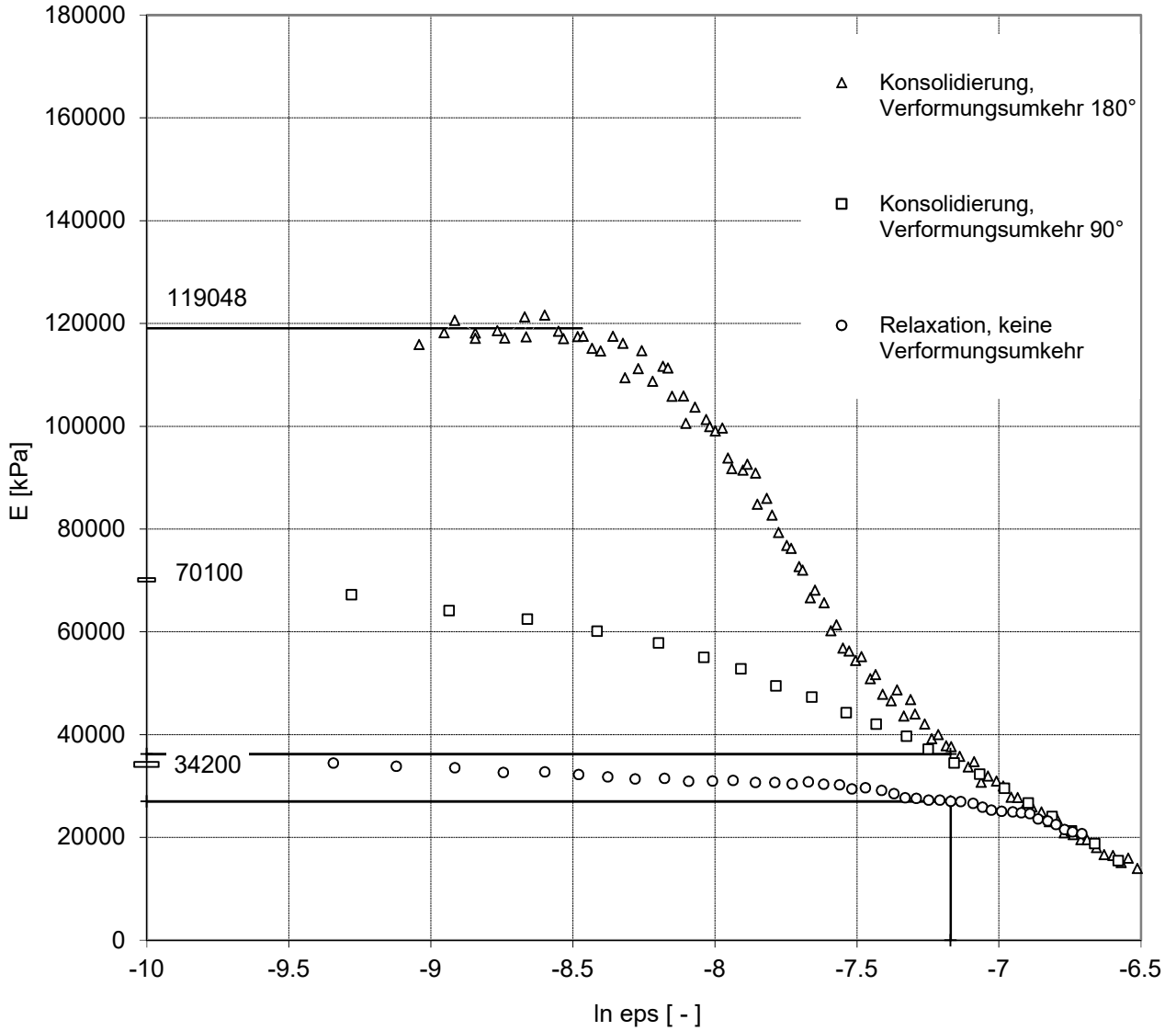
B.9 Stress path controlled triaxial test of Hamburger sand for intergranular strain parameters

TRIAxIALVERSUCH

DIN 18 137 - D

Projekt Nr.: i0417
TOP

Entnahmestelle: MP III
Entnahmetiefe: -
Bodenart: gS, ms, fg, mg'



R = 0.000210
 ϵ_{SOM} = 0.000769
 E_R = 119048 kPa
 E_T = 70100 kPa
 E_0 = 34200 kPa
 $m_R = E_R / E_0 = 3.48$
 $m_T = E_T / E_0 = 2.05$

$\epsilon_{SOM} / R = 3.7$
 $\chi = 1$
 $\beta_r = 0.7$

Bearbeiter:

Geprüft von:

B.10 Grain size distribution of Kippen sand



Technische Universität Hamburg-Harburg

Geotechnik und Baubetrieb

Univ.-Prof. Dr.-Ing. Jürgen Grabe

Harburger Schloßstr. 20
21079 Hamburg

Tel.: +49 (0)40 / 428 78-3782

Fax: +49 (0)40 / 428 78-4020

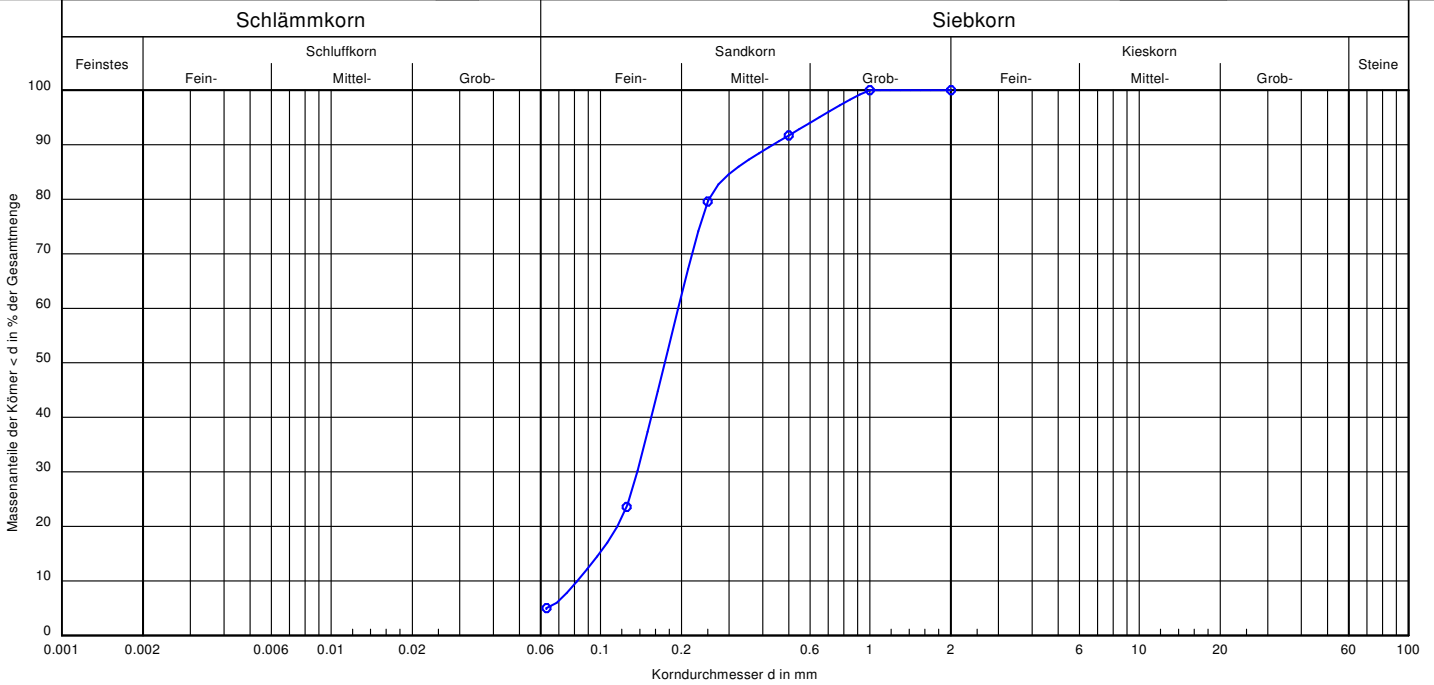
www.tu-harburg.de/gbt

Korngrößenverteilung

DIN 18123

Anlage


November 2017




Signatur:	
Entnahmestelle	HV 23
Tiefe	Aus der Trockensiebung
Bodenart:	fS, mS, u', gs'
U/Cc	2,4/1,2


Projekt Nr.:	Kippenböden, Lausitz
Bearbeiter:	Nguyen, Michael


B.11 Water content of Kippen sand

Projektnr.: 4117		Labornr.:		Prüfprotokoll <h1 style="margin: 0;">WASSERGEHALT</h1> <p style="margin: 0;">BESTIMMUNG DURCH OFENTROCKNUNG</p> <p style="margin: 0;">nach DIN 18 121-1</p>			
Projektkurztitel: Numerical modelling and validation of deep Vibration Compaction in granular soil							
Entnahmestelle & -tiefe: MP LEAG							
Probengütekategorie nach DIN 4021:		Bodenart: fS, ms, u', gs'					
Ausgeführt von: Ng		Beginn: Ende:					
Geprüft von:		Datum: 20.11.2017					
Bemerkungen: übliche Probemenge: Ton, Schluff (10-50); Sand (50-200)							
Behälter Nr.		1998		180		113	
Feuchte Probe + Behälter		A	[g]	197,95	173,67	167,00	
Trockene Probe + Behälter		B	[g]	182,24	161,25	154,70	
Behälter		C	[g]	81,67	80,34	74,65	
Wassergehalt		$w = (A-B)/(B-C)*100$ [%]		15,62	15,35	15,37	
Mittelwert		[%]		15,45			
Größtkorn		[mm]					
Meßunsicherheit der Wägung Δm		[g]					
 Technische Universität Hamburg		Geotechnik und Baubetrieb Univ.-Prof. Dr.-Ing. Jürgen Grabe		Harburger Schloßstr. 20 21079 Hamburg		Tel.: +49 (0)40 / 428 78-3782 Fax: +49 (0)40 / 428 78-4020	

Projektnr.: 4117		Labornr.:		Prüfprotokoll <h1 style="margin: 0;">WASSERGEHALT</h1> <p style="margin: 0;">BESTIMMUNG DURCH OFENTROCKNUNG</p> <p style="margin: 0;">nach DIN 18 121-1</p>			
Projektkurztitel: Numerical modelling and validation of deep Vibration Compaction in granular soil							
Entnahmestelle & -tiefe: MP LEAG							
Probengütekategorie nach DIN 4021:		Bodenart: fS, ms, u', gs'					
Ausgeführt von: Ng		Beginn: Ende:					
Geprüft von:		Datum: 20.11.2017					
Bemerkungen: übliche Probemenge: Ton, Schluff (10-50); Sand (50-200)							
Behälter Nr.		181		101		116	
Feuchte Probe + Behälter		A	[g]	174,77	171,22	192,91	
Trockene Probe + Behälter		B	[g]	163,05	159,77	179,42	
Behälter		C	[g]	79,04	78,68	81,04	
Wassergehalt		$w = (A-B)/(B-C)*100$ [%]		13,95	14,12	13,71	
Mittelwert		[%]		13,93			
Größtkorn		[mm]					
Meßunsicherheit der Wägung Δm		[g]					
 Technische Universität Hamburg		Geotechnik und Baubetrieb Univ.-Prof. Dr.-Ing. Jürgen Grabe		Harburger Schloßstr. 20 21079 Hamburg		Tel.: +49 (0)40 / 428 78-3782 Fax: +49 (0)40 / 428 78-4020	

B.12 Organic content of Kippen sand

ProjektNr.: 4117		LaborNr.:		Prüfprotokoll <h1>GLÜHVERLUST</h1> BESTIMMUNG nach DIN 18 128					
Projektkurztitel: Numerical modelling and validation of deep Vibration Compaction in granular soil									
Entnahmestelle & -tiefe:									
Probengüteklasse nach DIN 4021:		Bodenart: fS, ms, u', gs'							
Ausgeführt von: Ng		Beginn: Ende:							
Geprüft von:		Datum: 20.11.2017							
Bemerkungen:									
Tiegel Nr.				7		28		10	
Trockene Probe + Tiegel		A [g]		83,96		94,84		92,9	
Geglühte Probe + Tiegel		B [g]		81,876		92,677		91,038	
Tiegel		C [g]		47,62		44,51		47,6	
Glühverlust		$V_{gl} = (A-B)/(A-C)*100$ [%]		5,734727573		4,297635605		4,110375276	
Mittelwert		[%]		4,71					
GlühzeitStd.									
 Technische Universität Hamburg		Geotechnik und Baubetrieb Univ.-Prof. Dr.-Ing. Jürgen Grabe		Harburger Schloßstr. 20 21079 Hamburg		Tel.: +49 (0)40 / 428 78-3782 Fax: +49 (0)40 / 428 78-4020			

ProjektNr.: 4117		LaborNr.:		Prüfprotokoll <h1>GLÜHVERLUST</h1> BESTIMMUNG nach DIN 18 128					
Projektkurztitel: Numerical modelling and validation of deep Vibration Compaction in granular soil									
Entnahmestelle & -tiefe:									
Probengüteklasse nach DIN 4021:		Bodenart: fS, ms, u', gs'							
Ausgeführt von: Ng		Beginn: Ende:							
Geprüft von:		Datum: 20.11.2017							
Bemerkungen:									
Tiegel Nr.				14		23		8	
Trockene Probe + Tiegel		A [g]		106,94		87,2		98,26	
Geglühte Probe + Tiegel		B [g]		103,76		85,934		96,184	
Tiegel		C [g]		46,65		45,46		48,61	
Glühverlust		$V_{gl} = (A-B)/(A-C)*100$ [%]		5,274506552		3,033061811		4,181268882	
Mittelwert		[%]		4,16					
GlühzeitStd.									
 Technische Universität Hamburg		Geotechnik und Baubetrieb Univ.-Prof. Dr.-Ing. Jürgen Grabe		Harburger Schloßstr. 20 21079 Hamburg		Tel.: +49 (0)40 / 428 78-3782 Fax: +49 (0)40 / 428 78-4020			

B.13 Maximum and minimum void ratio of Kippen sand as per DIN 18126

Bestimmung der Dichte nichtbindiger Böden bei lockerster und dichtester Lagerung DIN 18126

Projekt Nr.: 4117 Lausitz

Entnahmestelle:

Entnahmetiefe:

Entnahmearart : GP

Bodenart: fS,ms* u*,gs',

Korndichte $\rho_s = 2.65 \text{ g/cm}^3$

Porenanteil in natürlicher Lagerung

$n =$ ----- %

Porenanzahl in natürlicher Lagerung

$e =$ -----

Ungleichförmigkeitszahl

$U =$ -----

Größtkorn

$max d =$ 1.00 mm

Bestimmung der Dichte in lockerster Lagerung

		1	2	3	4
Versuchszylinder $V_Z = 942.48 \text{ cm}^3$		1183.94	1181.74	1175.64	1181.06
		5	6	7	8
Probenmasse		1179.11	1178.14	1185.79	1179.01
	Mittelwert :	1180.55			g

min Trockendichte

$min \rho_d = min m_d / V_Z =$ **1.253** g/cm³

max Porenanteil

$max n = 1 - (min \rho_d / \rho_s) =$ **0.527**

max Porenzahl

$max e = (\rho_s / min \rho_d) - 1 =$ **1.116**

Bestimmung der Dichte in dichtester Lagerung

Versuchszylinder $h = 12.0 \text{ cm}$ $A = 78.5 \text{ cm}^2$ Platte $h_p = 4.0 \text{ cm}$

		1	2	
Setzung	$x_1 =$	14.8	14.90	mm
	$x_2 =$	14.7	14.70	mm
	$x_3 =$	14.9	15.00	mm
	Mittelwert $s_m =$	14.80	14.87	mm
Volumen	$min V = A \cdot (h - h_p + s_m) =$	744.6	745.1	cm ³

max Trockendichte

$max \rho_d = m_d / min V =$ **1.585** g/cm³

min Porenanteil

$min n = 1 - (max \rho_d / \rho_s) =$ **0.402**

min Porenzahl

$min e = (\rho_s / max \rho_d) - 1 =$ **0.672**

Abgeleitete Größen

Lagerungsdichte

$D = (max n - n) / (max n - min n) =$

Bezogene Lagerungsdichte

$I_D = (max e - e) / (max e - min e) =$

Verdichtungsfähigkeit

$I_f = (max e - min e) / min e =$ 0.66

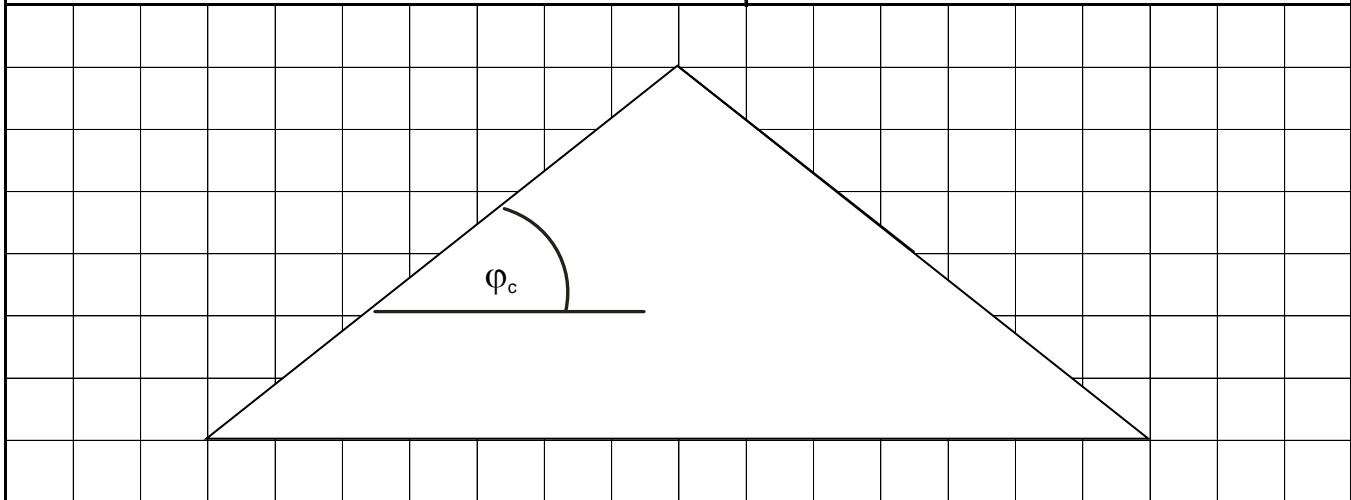
B.14 Critical friction angle of Kippen sand

Projektnr.: 4117	Datei:	
Projektkurztitel: Numerical modelling and validation of deep Vibration Compaction in granular soil		
Entnahmestelle: MP LEAG		
Entnahmetiefe:	Bodenart: fS, ms, u', as'	
Ausgeföhrt von: NG	Beginn:	Ende:
Geprüft von:		Datum: 01.11.2017

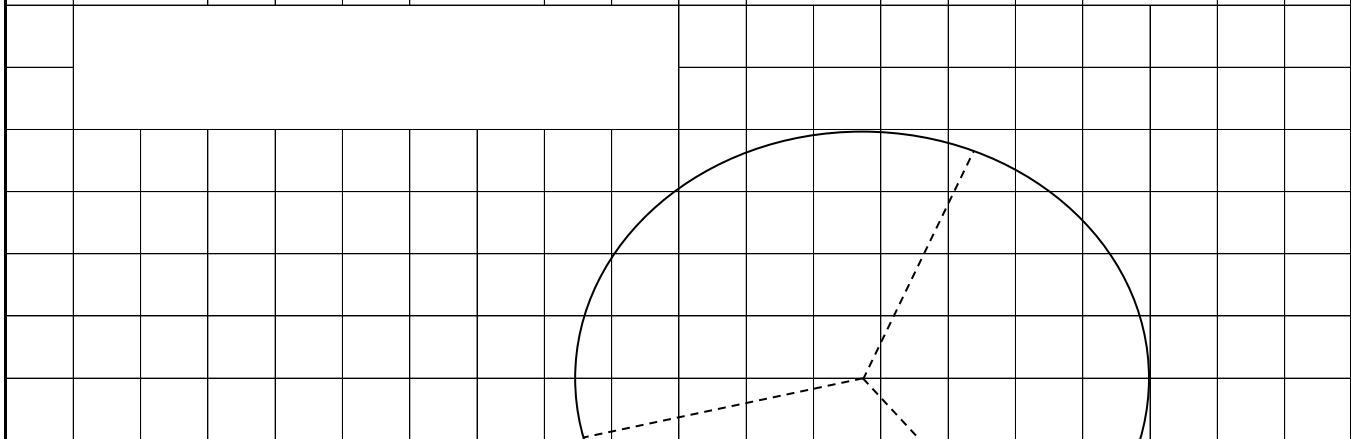
Prüfprotokoll

BESTIMMUNG DES KRITISCHEN REIBUNGSWINKELS

SCHÜTTKEGELVERSUCH



1. Messung		2. Messung		3. Messung		4. Messung	
$\varphi_{c1} =$	35,4 °	$\varphi_{c1} =$	34,6 °	$\varphi_{c1} =$	32,1 °	$\varphi_{c1} =$	33,5 °
$\varphi_{c2} =$	29,5 °	$\varphi_{c2} =$	33,8 °	$\varphi_{c2} =$	30,8 °	$\varphi_{c2} =$	31,7 °
$\varphi_{c3} =$	33,8 °	$\varphi_{c3} =$	32,7 °	$\varphi_{c3} =$	31,8 °	$\varphi_{c3} =$	31,1 °



1. Mittelwert	$\varphi_c =$	32,9	°
2. Mittelwert	$\varphi_c =$	33,7	°
3. Mittelwert	$\varphi_c =$	31,6	°
4. Mittelwert	$\varphi_c =$	33,7	°
Gesamtmittelwert	$\varphi_c =$	32,97	°

B.15 CRS oedometer test of Kippen sand

Ödometrische Kompression bis min. 400 kPa

Projekt Nr.: 4117 Lausitz

Entnahmestelle : MP LEAG
Entnahmetiefe:

Bodenart: fS, ms, u', gs'
Art der Entnahme : MP

Prüfdatum: 21.11.2017/22.11.2017

Aufnehmernummer 367

Anfangsdurchmesser d_a 70 mm

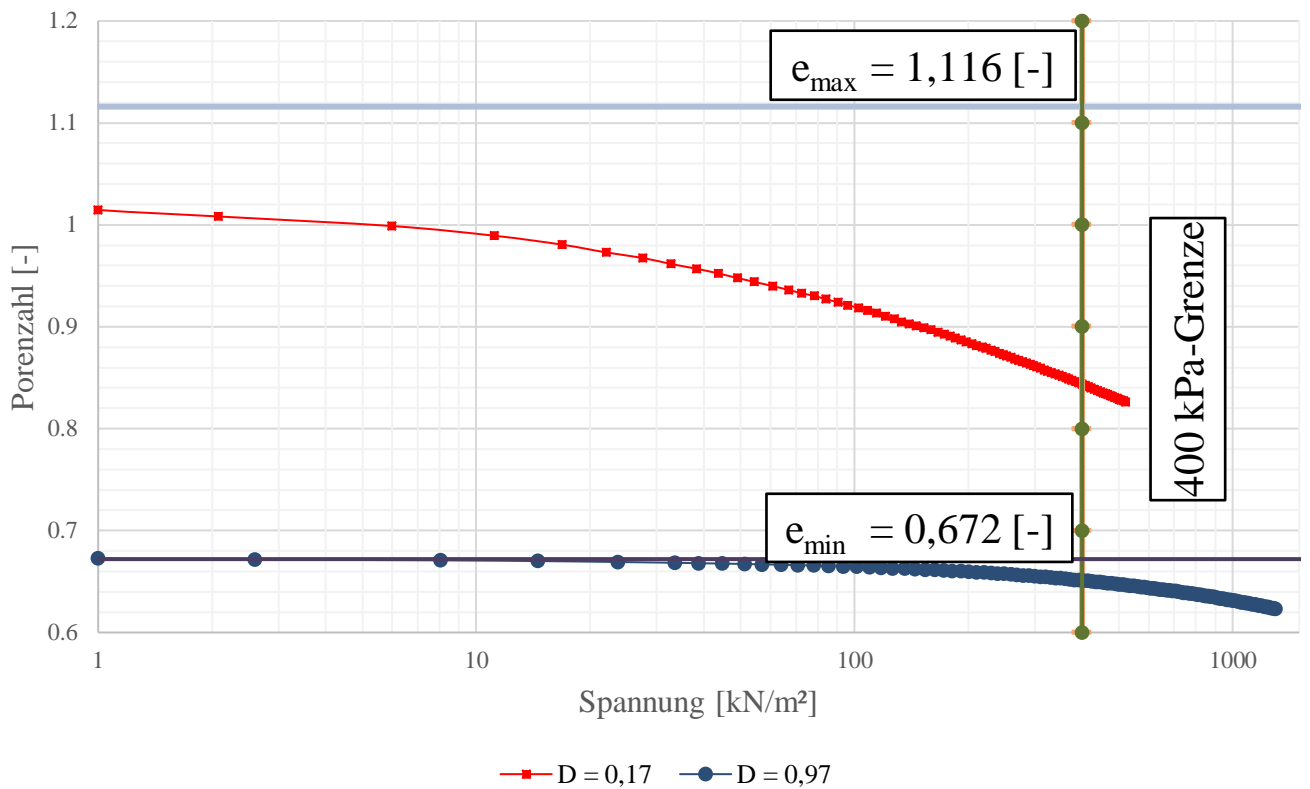
Schergeschwindigkeit 0.25 mm/min

Wassergehalt <0,5 %

Maximale Porenzahl e_{max} 1.116 [-]

Minimale Porenzahl e_{min} 0.672 [-]

Porenzahl- Spannungs-Diagramm



Probandaten	Probenbezeichnung	D = 0,17 (locker)		D = 0,97 (dicht)	
	Probenmasse m_0	110.02	g	119.88	g
	Probenhöhe h_0	21.83	mm	19.76	mm
	Lagerungsdichte D	0.17	[-]	0.97	[-]
	Dateiname	4117_Kippe_locker_3.eax		4117_Kippe_dicht_2.eax	

Bearbeiter: Ng

Geprüft von:

B.16 Static triaxial test of loose Kippen sand



Technische Universität Hamburg-Harburg

Geotechnik und Baubetrieb
Univ.-Prof. Dr.-Ing. Jürgen Grabe

Harburger Schloßstr. 20
21079 Hamburg

Tel.: +49 (0)40 / 428 78-3782

Fax: +49 (0)40 / 428 78-4020

www.tu-harburg.de/gbt

Anlage :

A.7b

Blatt :

3/6

Datum :

Dez 17

TRIAXIALVERSUCH

DIN 18 137 - D

Projekt Nr.: 4117 Lausitz

Masterarbeit Michael Nguyen

- locker -

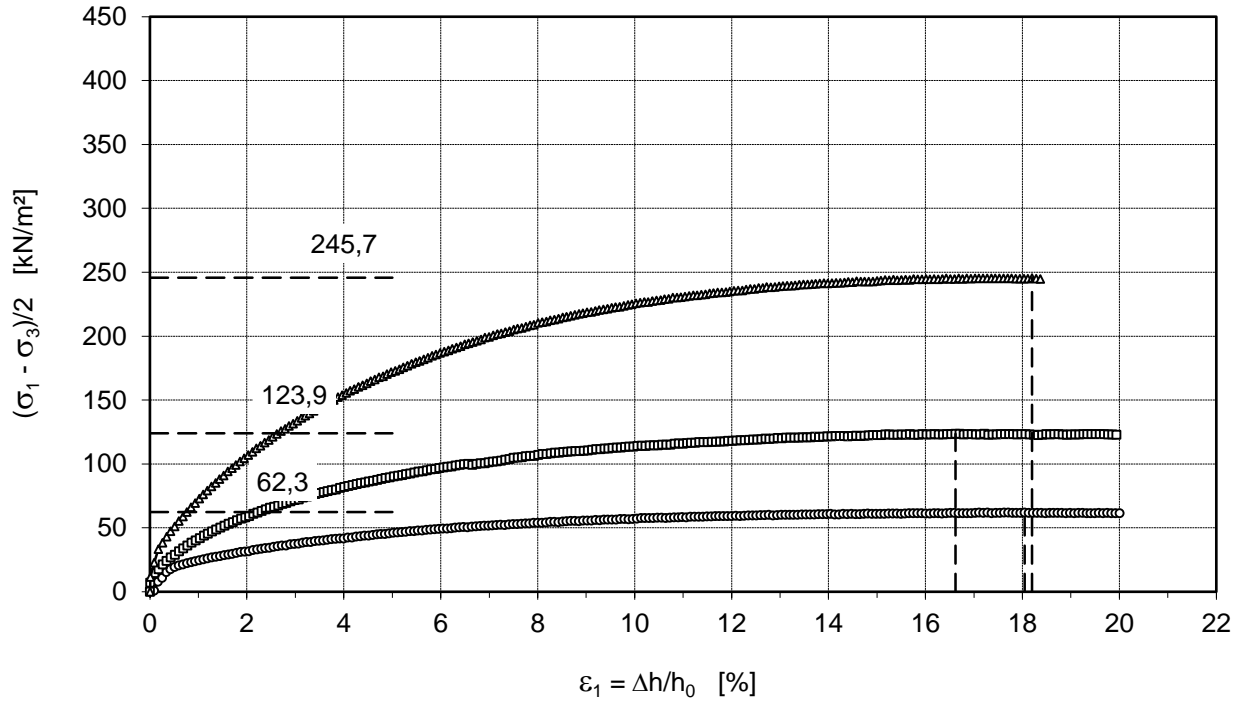
Entnahmestelle: MP LEAG

Entnahmetiefe: -

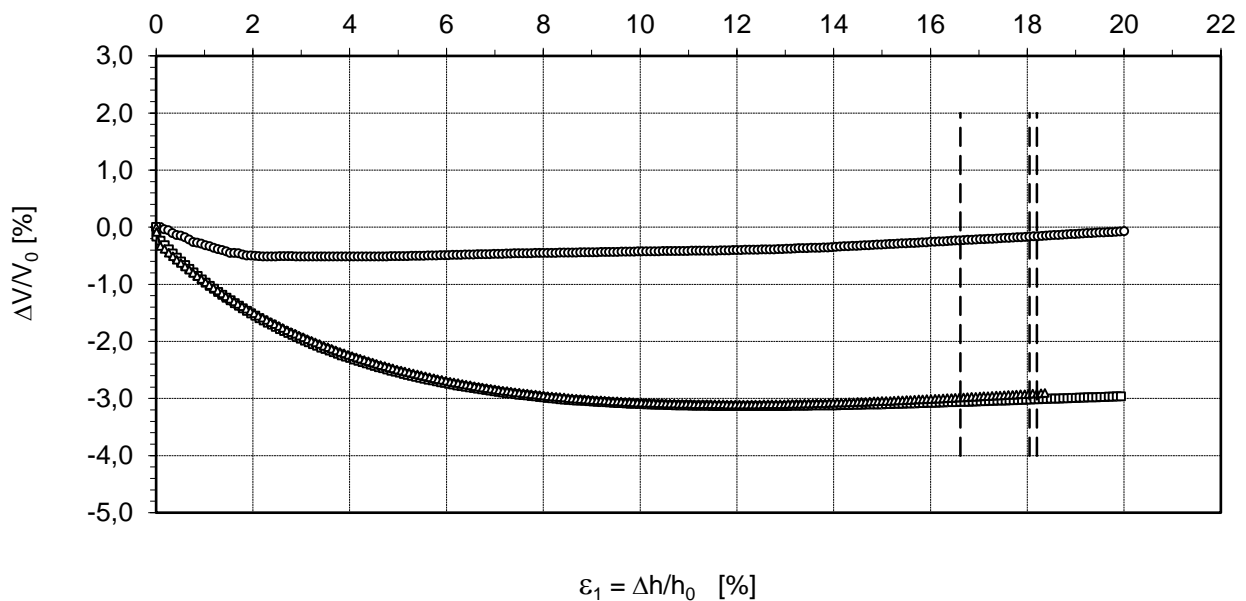
Bodenart: fS, ms, u

ΔV/V₀ [%]

Stauchung - Spannung Diagramm



Stauchung - Volumenänderung Diagramm



Dilatanzwinkel $v_p = -$

Bearbeiter: Ng

Geprüft von:

B.17 Static triaxial test of dense Kippen sand



Technische Universität Hamburg-Harburg

Geotechnik und Baubetrieb
Univ.-Prof. Dr.-Ing. Jürgen Grabe

Harburger Schloßstr. 20
21079 Hamburg

Tel.: +49 (0)40 / 428 78-3782

Fax: +49 (0)40 / 428 78-4020

www.tu-harburg.de/gbt

Anlage :

A.7b

Blatt :

3/6

Datum :

Dez 17

TRIAXIALVERSUCH

DIN 18 137 - D

Projekt Nr.: 4117 Lausitz

Masterarbeit Michael Nguyen

- locker -

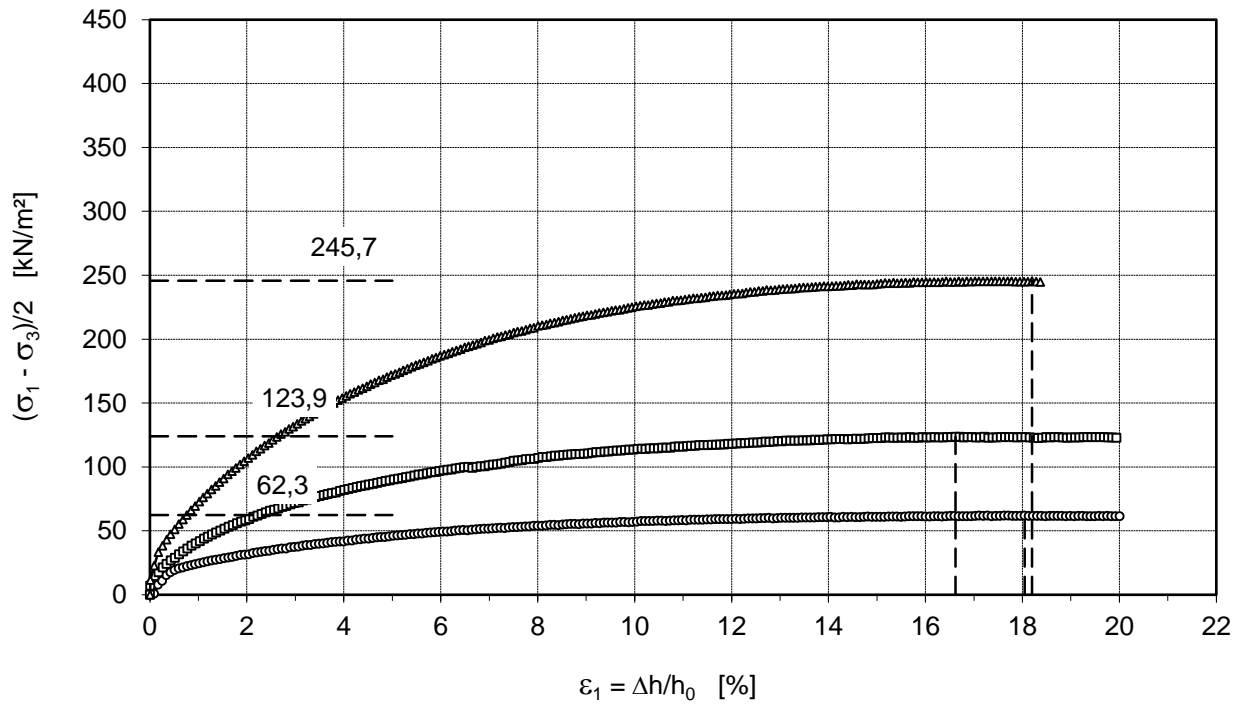
Entnahmestelle: MP LEAG

Entnahmetiefe: -

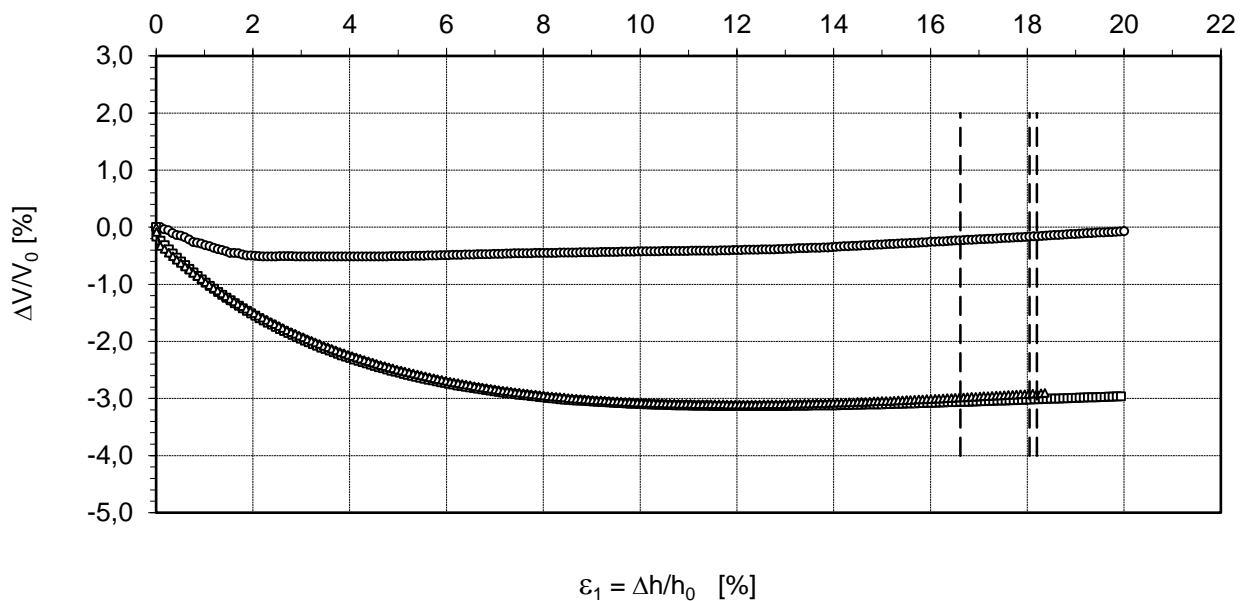
Bodenart: fS, ms, u

ΔV/V₀ [%]

Stauchung - Spannung Diagramm



Stauchung - Volumenänderung Diagramm



Dilatanzwinkel $v_p = -$

Bearbeiter: Ng

Geprüft von:

B.18 Stress path controlled triaxial test of Kippen sand for intergranular strain parameters

TRIAXIALVERSUCH

DIN 18 137 - D

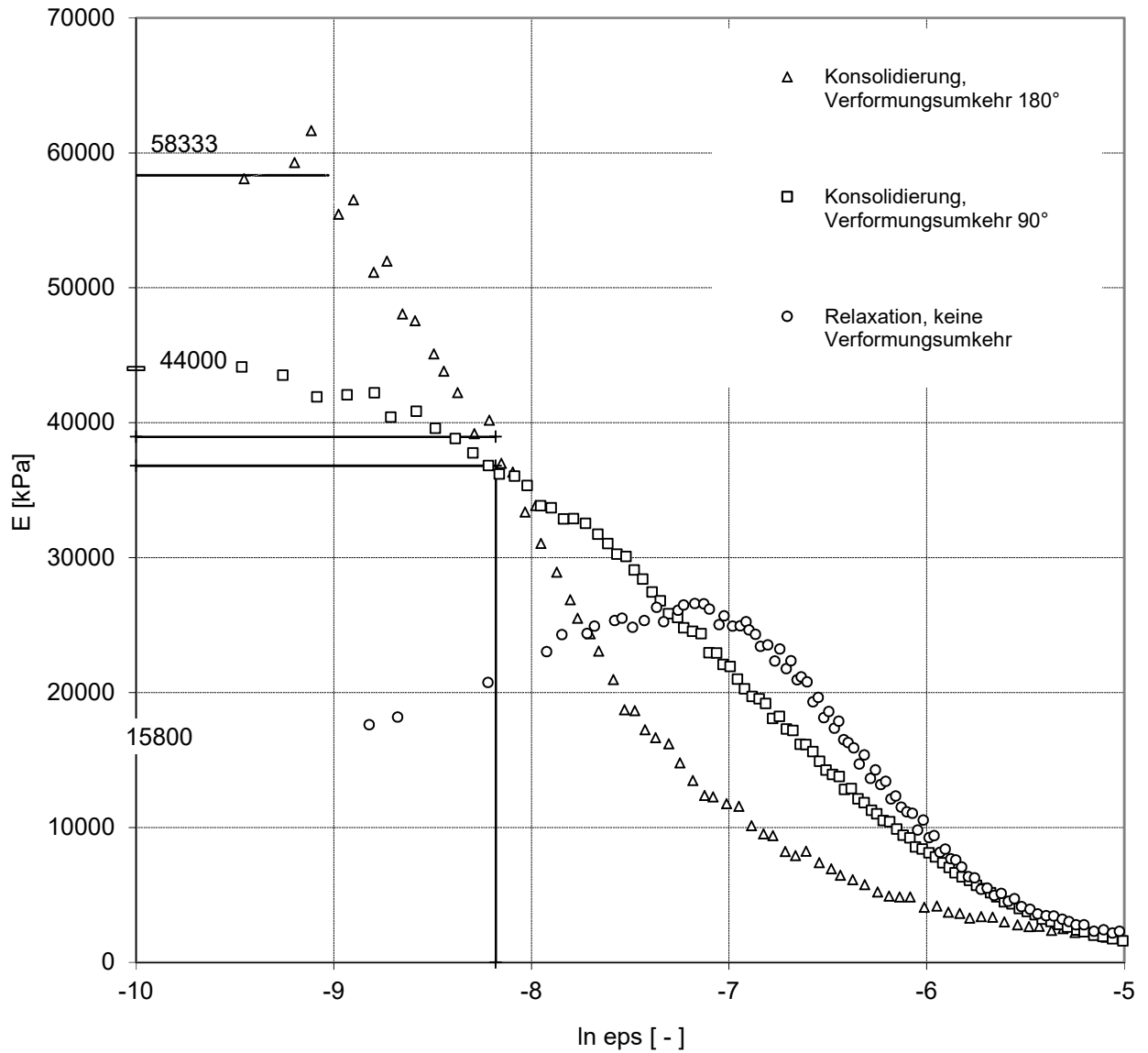
Projekt Nr.: 4117 Lausitz

Masterarbeit Michael Nguyen

Entnahmestelle: MP LEAG

Entnahmetiefe: -

Bodenart: fS, ms, u



R =	0,00012 [-]
$\epsilon_{SOM} =$	0,000280202 [-]
$E_R =$	58333 kPa
$E_T =$	44000 kPa
$E_0 =$	15800 kPa
$m_R = E_R / E_0 =$	3,69 [-]
$m_T = E_T / E_0 =$	2,78 [-]

Bearbeiter: Ng

Geprüft von:

Appendix C Details of field V48 vibrator

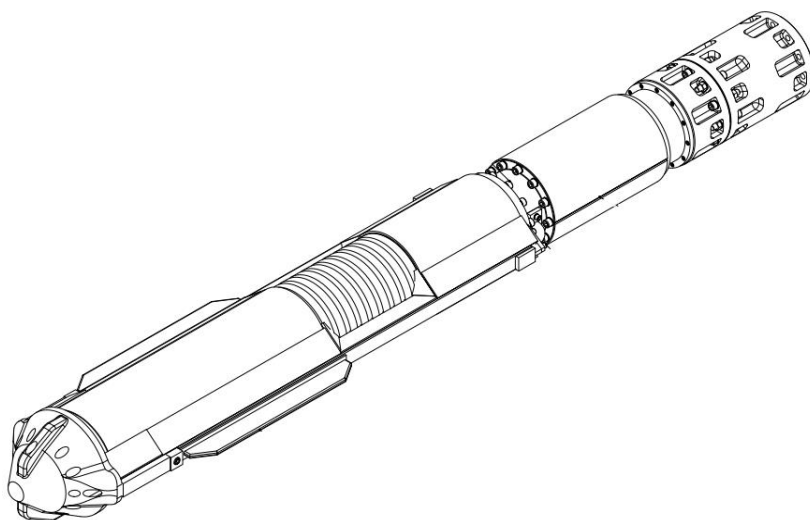


NO ORDINARY ENGINEERING
 Fördertechnik, Anlagenbau, Siebmaschinen
 Großgerätetechnik, Sondermaschinen
 Porenbetonanlagen und Kalksteintechnik
 Automatisierung, ISO 9001:2008, EN 1090-2

SKM GmbH, OT Kringelsdorf, Schadendorfer Str. 51, 02943 Boxberg / O.L.

GMB GmbH
 Knappenstraße 1
 01968 Senftenberg

Datenblatt Rütteldruckverdichter V48



Stand: 21.09.2015

Geräteeigenschaften:

Benennung	Einheit	Wert
Länge	mm	5000 mit Steckerteil
Durchmesser	mm	470 ohne Schwerter
Gewicht RDV V48	kg	4325 mit Steckerteil
Gewicht Exzenter	kg	240 inkl. 3 Schwerstäbe
Aufsatzrohr	mm	406
Spannung	V	400
Stromstärke (Leerlauf)	A	120
Stromstärke (Last)	A	max. 380 bei 212 KW
Leistung (Last)	kW	212
Drehzahl*	rpm	750 - 1800
Frequenzbereich*	Hz	25-60
Amplitude +/-	mm	17
Schlagkraft	kN	500 bei 60 Hz
max. Temperatur Motor	°C	140
Leistungsfaktor des Motors		0,86
Wirkungsgrad des Motors	%	93,1

*Die angegebenen Werte sind ideale Werte ohne angenommenen Schlupf des Motors

SKM GmbH OT Kringelsdorf
 Schadendorfer Straße 51, 02943 Boxberg/ O.L.

Geschäftsführer:
 Dipl.-Ing. Steffen Söll MBA, Kristin Söll

Telefon: +49 (35774) 356-0
 Telefax: +49 (35774) 356-12
 E-Mail: info@skm-boxberg.de
 Internet: www.skm-boxberg.de

HRB 20910 Dresden, USt-ID-Nr.: DE 813 468 608

Bankverbindungen:
Commerzbank AG
 IBAN DE79 1804 0000 0159 1619 00 BIC COBA DE FFXXX

Commerzbank AG
 IBAN DE39 8508 0000 0275 1720 00 BIC DRES DE FF 850

Deutsche Bank AG
 IBAN DE03 1207 0024 0509 8983 00 BIC DEUT DE DB160



Appendix D VUAMP: Amplitude controlled CEL simulations

```
      subroutine vuamp(  
C Variables passed in for information and state variables  
      & ampName,time,ampValueOld,dt,nprops,props,nSvars,  
        svars,  
      & lFlagsInfo,nSensor,sensorValues,sensorNames,  
      & jSensorLookUpTable,  
C Variables to be defined  
      & ampValueNew,  
c Variables that can be defined  
      & lFlagsDefine,AmpDerivative,AmpSecDerivative,  
      & AmpIncIntegral)  
  
c -----  
c Abaqus/Explicit user subroutine to define an amplitude  
c as a function of time. It can be used to model control  
c engineering aspects of your system when sensors are  
c used (sensor values are from the beginning of the  
c increment);  
c can use a predefined number of state variables in its  
c definition; and can optionally compute the derivatives  
c and integrals of the amplitude function.  
c  
c Note, that this subroutine is written in Fortran  
c format free form, i.e. you have to activate the  
c Fortran compiler option -free in the Abaqus  
c configuration file 'abaqus_v6.env'.  
c If you use more user subroutines ensure you use  
c the format free form also.  
c  
c Programmed by Sparsha Nagula (3/2020)  
c -----  
      include 'vaba_param.inc'  
C svars - additional state variables, similar to (V)UEL  
      dimension sensorValues(nSensor), svars(nSvars)
```

```

    dimension props(nprops)
    character(len=80) sensorNames(nSensor),ampName
C Two time indices
    parameter (
&   iStepTime=1,
&   iTotTime=2,
&   nTime=2)
C Three Flags passed in for information
    parameter(
&   iInitialization=1,
&   iRegularInc=2,
&   ikStep=3,
&   nFlagsInfo=3)
C Five optional flags to be defined
    parameter (iComputeDeriv=1,
&   iComputeSecDeriv=2,
&   iComputeInteg=3,
&   iStopAnalysis=4,
&   iConcludeStep=5,
&   nFlagsDefine=5)
    dimension time(nTime),lFlagsInfo(nFlagsInfo),
&   lFlagsDefine(nFlagsDefine),jSensorLookUpTable(*)
c Variables required for Abaqus utility subroutines
    dimension intv(1),realv(1)
    character(len=8) charv(1)
c Local variables
    parameter(pi=4.d0*atan(1.0d0))
    double precision f,omega,F_amp,u_1,u_2,u_mag,u_lim

c Compute 1st and 2nd derivative of amplitude automatically
    lFlagsDefine(iComputeDeriv) = 1
    lFlagsDefine(iComputeSecDeriv) = 1
c Get sensor values
    u_1 = vGetSensorValue('TRANS_X', jSensorLookUpTable,
        sensorValues)
    u_2 = vGetSensorValue('TRANS_Y', jSensorLookUpTable,
        sensorValues)
    u_mag = sqrt(u_1*u_1+u_2*u_2)
c Compute force F(t) = F_amp*sin(omega*t) or F(t)
    = F_amp*cos(omega*t)
    if (lFlagsInfo(iInitialization) == 1) then
        ampValueNew = ampValueOld
        call xplb_abqerr(1,'VUAMP□Message:□initialising□function',
&   intv,realv,charv)
    u_lim = 0.006d0

```

```

else
  tim = time(iStepTime)
  total =time(iTotalTime)
  ! Compute force F(t)
  F_1 = 520.0d0 ! force amplitude
  f = 30.0d0 ! frequency
  omega = 2.0d0*pi*f ! angular frequency
  u_lim = 0.006d0 ! limit sensor value
  if (lFlagsInfo(ikStep) == 2) then
    if (u_mag <= 0.006d0 .and. time(iStepTime) > 5.1d0
      .and.
&      abs(u_lim-u_mag) <= 0.01) then
      lFlagsDefine(iConcludeStep) = 1
      call xplb_abqerr
        (1,'VUAMP_Message: end of compaction'//
&      'reached',intv,realv,charv)
    else
      lFlagsDefine(iConcludeStep) = 0
    end if
  end if
  if (lFlagsInfo(ikStep) == 2) then
    select case(ampName(1:18))
    case('AMPLITUDE_TEST_SIN')
      ampValueNew = F_amp*sin(omega*time(iStepTime))
    case('AMPLITUDE_TEST_COS')
      ampValueNew = F_amp*cos(omega*time(iStepTime))
    case default
      call xplb_abqerr
        (-3,'VUAMP_Error: amplitude name not'//
&      'supported',intv,realv,charv)
    end select
    u_lim = u_mag
  end if
end if
end subroutine vuamp

```


Curriculum Vitae

Personal Details

Surname	Nagula
Name	Sparsha Sinduri
Nationality	Indian
Birthday	02.05.1989
Birth Place	Madanapalle, India

Schooling

03/1994 – 05/2003	Assembly of God Church School, Asansol, India
06/2003 – 06/2008	Bhartiya Vidya Bhavan, Nagpur, India

University

07/2008 – 06/2012	Visvesvaraya National Institute of Technology, Nagpur, India Civil Engineering Degree: Bachelor of Technology
07/2012 – 12/2015	Indian Institute of Technology Madras, Chennai, India Geotechnical Engineering Degree: Master of Science
01/2016 – 10/2021	Institute of Geotechnical Engineering and Construction Management, TUHH, Hamburg, Germany Degree: Doctor of Philosophy

Professional Experience

01/2016 – 03/2021	Research Associate Institute of Geotechnical Engineering and Construction Management Hamburg University of Technology, Hamburg, Germany
08/2021 – Present	Post Doctoral Research Associate Norwegian Geotechnical Institute Oslo, Norway

List of Publications

The list below highlights the most important peer reviewed research contributions made as part of the research work stated in this thesis.

Peer Reviewed Journal Papers

- Nagula, S. and Grabe, J. (2020) Coupled Eulerian Lagrangian based numerical modelling of vibro-compaction with model vibrator. *Computers and Geotechnics.*, Volume 123, 103545. <https://doi.org/10.1016/j.compgeo.2020.103545>.
- Nagula, S., Nguyen, M., Grabe, J., Kardel, J. and Bahl, T. (2021) Field Measurements and Numerical Analysis of Vibrocompaction of Sand. *Géotechnique*. <http://doi.org/10.1680/jgeot.20.P.195>
- Nagula, S.S., Hwang, .YW., Dashti, S. and Grabe, J. (2021) Numerical investigation of liquefaction mitigation potential with vibroflotation. *Soil Dynamics and Earthquake Engineering*, Volume 146, 106736. <https://doi.org/10.1016/j.soildyn.2021.106736>.
- Nagula, S., Katt, J. and Grabe, J. (2021) Optimisation of vibroflotation based on amplitude and phase angle using model vibrator in 1g tests. *International journal of physical modelling in geotechnics*. <https://doi.org/10.1680/jphmg.20.00083>
- Nagula S. and J. Grabe (2020): Hypoplastic model with intergranular strain: dependence on grain properties and initial state. In: *Geotechnical Engineering Journal of the SEAGS & AGSSEA* 51(4):122-129. <http://seags.ait.asia/journals/seags-agssea-journal-december-2020>
- Nagula, S., Hwang, Y., Dashti, S. and Grabe, J. (2021) Seismic site response of layered saturated sand: comparison of finite element simulations with centrifuge test results. *International journal of Geo-Engineering*, 12, 26. <https://doi.org/10.1186/s40703-021-00155-2>.

Peer reviewed Conference Proceedings

- Nagula, S., Grabe, J. and Bahl, T. (2019) Numerical simulation of vibrocompaction based on CEL approach. In *17th European conference on Soil Mechanics and Geotechnical Engineering*, Reykjavik, Iceland.
- Nagula, S., and Grabe, J. (2018) Effectiveness of ground improvement in sands upon seismic loading using non-linear soil model. In: *5th Geotechnical Earthquake Engineering and Soil Dynamics conference, ASCE-Geotechnical Special Publication Number 292*, 133-141, Austin, USA. <https://doi.org/10.1061/9780784481479.014>
- Nagula, S., and Grabe, J. (2018) Deep vibration compaction of sand using mini vibrator. In: *Physical Modelling in Geotechnics* (McNamara et al. (eds)), 1229-1233, Taylor and Francis, London, UK.

- Nagula, S., and Grabe, J., (2017) 2-Phase dynamic simulation of deep sand compaction to reduce liquefaction. In: Proceedings of 10th International conference on structural dynamics Eurodyn-2017 (Vestroni, F., Romeo, F. and Gatutulli, V. (eds)), Procedia Engineering, 199, 2396-2401.